

REFERENCE USE ONLY

# STATISTICAL REPRESENTATIONS OF TRACK GEOMETRY

## VOLUME II—APPENDICES



**MARCH 1980**

Document is available to the U.S. public through  
The National Technical Information Service,  
Springfield, Virginia 22161

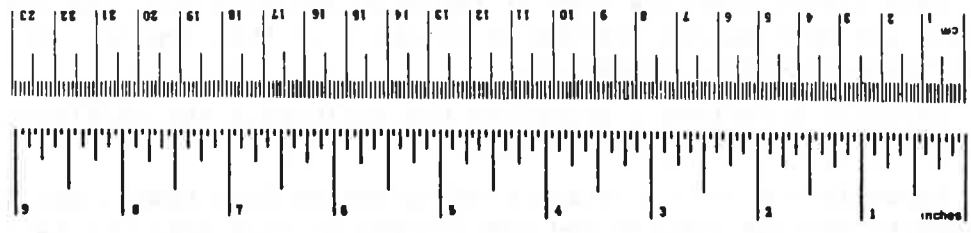
**U.S. DEPARTMENT OF TRANSPORTATION  
FEDERAL RAILROAD ADMINISTRATION  
Office of Research and Development  
Washington, D.C. 20590**



1. Report No. FRA/ORD-80/22.2		2. Government Accession No. PB81-179038		3. Recipient's Catalog No.	
4. Title and Subtitle STATISTICAL REPRESENTATIONS OF TRACK GEOMETRY Volume II -- Appendixes				5. Report Date March 1980	
				6. Performing Organization Code	
7. Author(s) John C. Corbin				8. Performing Organization Report No. DOT-TSC-FRA-80-4,II	
9. Performing Organization Name and Address ENSCO, Inc.* Transportation and Instrumentation Sciences Division 5408A Port Royal Road Springfield VA 22151				10. Work Unit No. (TRAIS) RR019/R0323	
				11. Contract or Grant No. DOT-TSC-1211-2	
12. Sponsoring Agency Name and Address U.S. Department of Transportation Federal Railroad Administration Office of Research and Redevelopment Office of Rail Safety Research Washington DC 20590				13. Type of Report and Period Covered Final Report May 1976 to April 1978	
				14. Sponsoring Agency Code	
15. Supplementary Notes *Under contract to: U.S. Department of Transportation Research and Special Programs Administration Transportation System Center Cambridge MA 02142					
16. Abstract This volume contains some of the more detailed data and analyses to support the results and conclusions reached in Volume I of this report. It is divided into appendixes lettered A through J.  Appendix A defines a procedure for evaluating the statistical parameters from field-collected track-geometry data.  Appendixes B and C contain track-geometry data traces and descriptive text used to support various results and conclusions as they apply to rail joints and track anomalies, respectively.  Appendix D contains the curve fits obtained for processed PSD data.  Appendixes E and F describe the analyses used to determine instrument and quantization noise, respectively.  Appendix G is a history of research preceding the effort described in this report.  Appendix H describes formal mathematical procedures needed for complete characterization of a periodically modulated random process.  Appendix I contains data on railhead wear. Appendix J reports on new technology.  Volume I -- Main Text has 208 pages.					
17. Key Words Track Geometry, Track Irregularities, Track Inspector Cars, Simulation Models, Railhead Profile, Statistical Analyses, Statistical Models			18. Distribution Statement  DOCUMENT IS AVAILABLE TO THE PUBLIC THROUGH THE NATIONAL TECHNICAL INFORMATION SERVICE, SPRINGFIELD, VIRGINIA 22161		
19. Security Classif. (of this report) Unclassified		20. Security Classif. (of this page) Unclassified		21. No. of Pages 202	22. Price

# METRIC CONVERSION FACTORS

Approximate Conversions to Metric Measures		Approximate Conversions from Metric Measures	
Symbol	When You Know	Multiply by	To Find
<b>LENGTH</b>			
in	inches	2.5	centimeters
ft	feet	30	centimeters
yd	yards	0.9	meters
mi	miles	1.6	kilometers
<b>AREA</b>			
sq in	square inches	6.5	square centimeters
sq ft	square feet	0.09	square meters
sq yd	square yards	0.8	square meters
sq mi	square miles	2.6	square kilometers
ac	acres	0.4	hectares
<b>MASS (weight)</b>			
oz	ounces	28	grams
lb	pounds	0.45	kilograms
	short tons (2000 lb)	0.9	tonnes
<b>VOLUME</b>			
teaspoon	teaspoons	5	milliliters
tablespoon	tablespoons	15	milliliters
fluid ounce	fluid ounces	30	milliliters
cup	cups	0.24	liters
quart	quarts	0.95	liters
gallon	gallons	3.8	liters
cubic foot	cubic feet	0.03	cubic meters
cubic yard	cubic yards	0.76	cubic meters
<b>TEMPERATURE (exact)</b>			
Fahrenheit temperature		$\frac{5}{9}$ (after subtracting 32)	Celsius temperature
<b>LENGTH</b>			
mm	millimeters	0.04	inches
cm	centimeters	0.4	inches
m	meters	3.3	feet
km	kilometers	1.1	yards
		0.6	miles
<b>AREA</b>			
sq cm	square centimeters	0.16	square inches
sq m	square meters	1.2	square yards
sq km	square kilometers	0.4	square miles
ha	hectares (10,000 m <sup>2</sup> )	2.5	acres
<b>MASS (weight)</b>			
g	grams	0.035	ounces
kg	kilograms	2.2	pounds
t	tonnes (1000 kg)	1.1	short tons
<b>VOLUME</b>			
ml	milliliters	0.03	fluid ounces
l	liters	2.1	pints
		1.06	quarts
		0.26	gallons
m <sup>3</sup>	cubic meters	36	cubic feet
		1.3	cubic yards
<b>TEMPERATURE (exact)</b>			
Celsius temperature		$\frac{9}{5}$ (then add 32)	Fahrenheit temperature



## TABLE OF CONTENTS

<u>Appendix</u>		<u>Page</u>
A	Definition of Measurement Procedures to Identify Component Processes	A-1
B	Characterization of the Rail Joint	B-1
C	Characterization of Anomalies	C-1
D	Compendium of PSD's	D-1
E	System Noise Floors	E-1
F	Quantization Error	F-1
G	Historical Background	G-1
H	Procedures for System Identification of Periodically Modulated Random Processes	H-1
I	Railhead Wear Characteristics	I-1
J	Report of New Technology	J-1



## LIST OF ILLUSTRATIONS

<u>Figure</u>		<u>Page</u>
A-1	Data Collection Form - Field Measurement	A-2
B-1	Low Joint Environment and Associated Models	B-3
B-2	Shift Register Representation of Joint Simulator	B-5
B-3	Quadratic Simulation of 1.0 in. Amplitude Joint NA=4, M=13	B-7
B-4	Spectral Content of Low Joint Models	B-9
B-5	Comparative Profile Representations for Left Rail in Special Test Section	B-20
B-6	Comparative Profile Representations for Right Rail in Special Test Section	B-21
B-7	All Inertial Representation of Profile in Special Test Section	B-22
B-8	Profiles of CWR	B-27
C-1	Surface Geometry of Number 10 Spring Frog Turnouts as Seen from Main Line, Leading and Trailing Point Approach	C-3
C-2	Surface Geometry of Number 10 Spring Frog Turnouts as Seen from Main Line, Leading Point Approach	C-4
C-3	Surface Geometry of Number 10 Spring Frog Turnouts as Seen from Main Line, Trailing Point Approach	C-5
C-4	Interlocking Number 1, Negotiated Without Track Change	C-7
C-5	Interlocking Number 1, Negotiated in Opposite Direction and with Track Change	C-8
C-6	Interlocking Number 2, Negotiated Without Track Change, Turnout at Right is Newly Installed	C-9

LIST OF ILLUSTRATIONS (Cont'd)

<u>Figure</u>		<u>Page</u>
C-7	Interlocking Number 2, Negotiated in Opposite Direction, Without Track Change, and Showing Anomalous Details in the Surroundings	C-10
C-8	Tower Location Negotiated Without Track Change	C-12
C-9	Tower Location Negotiated in Opposite Direction and with Track Change	C-13
C-10	Series of Turnouts at Yard Approach	C-14
C-11	Anomalous Geometry at Bridges	C-15
C-12	Surface Geometry on Long Trestle	C-16
C-13	Miscellaneous Anomalous Geometries	C-18
C-14	Anomaly Associated with Use of Buffer Rails in CWR	C-19
D-1	Extremely Long Wavelength Profile PSD's	D-2
D-2	Extremely Long Wavelength Alignment PSD's	D-3
D-3	Extremely Short Wavelength Profile PSD's	D-4
D-4	Range of BR Mean Profile, Main Line CWR	D-7
D-5	Range of BR Mean Alignment, Main Line CWR	D-8
D-6	Range of BR Crosslevel, Main Line CWR	D-9
D-7	Range of Individual Rail Profile Spectra, NEA, Class 5	D-10
D-8	Range of Individual Rail Profile Spectra, NEA, Class 4	D-11
D-9	Range of Individual Rail Profile Spectra, NEA, Class 3	D-12
D-10	Range of Individual Rail Alignment Spectra, NEA, Class 5	D-13
D-11	Range of Individual Rail Alignment Spectra, NEA, Class 4	D-14



LIST OF ILLUSTRATIONS (Cont'd)

<u>Figure</u>		<u>Page</u>
D-12	Range of Individual Rail Alignment Spectra, NEA, Class 3	D-15
D-13	Range of Crosslevel Spectra, NEA, Class 5	D-16
D-14	Range of Crosslevel Spectra, NEA, Class 4	D-17
D-15	Range of Crosslevel Spectra, NEA, Class 3	D-18
D-16	Range of Gage Spectra, NEA, Class 5	D-19
D-17	Range of Gage Spectra, NEA, Class 4	D-20
D-18	Range of Gage Spectra, NEA, Class 3	D-21
D-19	Smoothed Individual Rail Profile PSD's for New Construction	D-22
D-20	Range of Individual Rail Profile Spectra, NEA, Freight and Passenger (Class 5)	D-23
D-21	Range of Profile Spectra from Florida Track Freight and Passenger (Class 4)	D-24
D-22	Range of Profile Spectra from Chicago Area, Freight and Passenger (Class 3)	D-25
D-23	Range of Profile Spectra from Pittsburgh Area, Unit Coal Train Operation (Class 2)	D-26
D-24	Smoothed Gage PSD's for New Construction	D-27
D-25	Range of Gage Spectra, NEA, Freight and Passenger (Class 5)	D-28
D-26	Range of Gage Spectra from Florida Track, Freight and Passenger (Class 4)	D-29
D-27	Range of Gage Spectra from Chicago Area, Freight and Passenger (Class 3)	D-30
D-28	Range of Gage Spectra from Pittsburgh Area, Unit Coal Train Operation (Class 2)	D-31
D-29	SNCF Alignment and Profile, Paris-Toulouse Line	D-32

## LIST OF ILLUSTRATIONS (Cont'd)

<u>Figure</u>		<u>Page</u>
D-30	Example of Two SNCF Alignment Spectra, Collected Via Mauzin 10m (32.8') MCO	D-33
D-31	Mean Profile, NEA, Various Classes	D-37
D-32	Crosslevel, NEA, Various Classes	D-38
D-33	Mean Profile, Class 6 and Better (TG-69)	D-39
D-34	Crosslevel Class 6 and Better (TG-69)	D-40
D-35	Mean Alignment, Class 6 and Better (TG-69)	D-41
D-36	Gage, Class 6 and Better (TG-69)	D-42
D-37	Mean Profile, Various Bolted (TG-69)	D-43
D-38	Crosslevel Various Bolted (TG-69)	D-44
D-39	Mean Alignment, Various Bolted (TG-69)	D-45
D-40	Gage, Various Bolted (TG-69)	D-46
E-1	Profilometer System	E-6
E-2	Concept of System for Two-plane Measurement of Curvature	E-11
E-3	Procedure for Collecting and Processing TSD Data	E-14
H-1	Partially Partitioned Generator of Periodically Modulated Random Process	H-6
H-2	Fully Partitioned Generator of Periodically Modulated Random Process	H-8
H-3	Form of Generator of Periodically Modified Random Process	H-13
H-4	Track Parameter Extractor	H-14
H-5	Stages of Mean Shape Extraction Processing for Periodic Deterministic Data	H-16

LIST OF ILLUSTRATIONS (Cont'd)

<u>Figure</u>		<u>Page</u>
H-6	Stages of Mean Shape Extraction Processing for Simulated Track Geometry Data	H-18
I-1	Railhead Wear, 15 April 1977, Track No. 1	I-6
I-2	Railhead Wear, 3 May 1977, Track No. 2	I-13
I-3	Maximum Rail Wear at Splice	I-16
I-4	Dimensions for Minimum Railhead Thickness in Common Rail Sections	I-17
I-5	Dimensions for Minimum Head Width in Common Rail Sections	I-18
I-6	Typical Wear Patterns	I-20

## LIST OF TABLES

<u>Table</u>		<u>Page</u>
A-1	Assumptions and Definitions	A-4
A-2	Field Procedure for Computing Means and Confidence Intervals - PDP	A-5
A-3	Field Procedure for Evaluating Second Order Statistics - HMP and PMMP	A-10
B-1	Moving Strip Algorithm for Simulating Low Joint	B-6
B-2	Sensitivity of Chord to Various Surface Features	B-24
C-1	Scaling Factor for Graphical Geometry Data	C-1
D-1	Synopsis of Older PSD Data	D-6
D-2	Synopsis of PSD's Data Generated Under this Program	D-35
D-3	Summary of Characteristics of TG-69 Zones	D-36
D-4	Continuum Parameters for Surface Geometry	D-48
D-5	Continuum Parameters for Line Geometry	D-49
D-6	Summary of SRP and PDP Geometry Impact on 62-Foot MCO	D-50
E-1	Summary of System Performance Data	E-5
F-1	Resolution as Function of A-D Bits and Inch Range (p-p)	F-4
F-2	Zero Level and Asymptotic Constant, B, Using Model Spectrum and Various Resolutions	F-4
G-1	Early PSD Models for Track Profile, Alignment, and Crosslevel	G-7
G-2	Recent PSD Models for Profile and Alignment	G-14
I-1	Railhead Wear, 15 April 1977, Track No. 1	I-2
I-2	Railhead Wear, 3 May 1977, Track No. 2	I-5

## APPENDIX A

### DEFINITION OF MEASUREMENT PROCEDURES TO IDENTIFY COMPONENT PROCESSES

#### A.1 MEASUREMENT PROCEDURE

Surface\* can be characterized by the following measurements:

- A Mid Chord Offset (MCO) whose length is half the rail length;
- A MCO whose length equals the rail length;
- A MCO whose length is twice the rail length; and
- A crosslevel measurement.

Note that if the MCO measurement is sufficiently accurate, it is possible to convert the half rail-length chord measurements to all of the other MCO measurements.

The profile and crosslevel data that are collected should be measured at the joint or weld, the rail mid-point, and at the quarter points. These represent *families* of measurements and the data should be preserved as such. Thus joint data represents family 1 and it should not be mixed with rail mid-point data, representing family 3. These in turn should not be mixed with quarter point data, representing families 2 and 4. Orderly data collection may be achieved by using a form such as Figure A-1.

Gathering of data should be performed over anomaly-free track sections. Prima facie evidence that the section has an anomaly is indicated by:

---

\*The procedure is readily applied to the line parameters, alignment and gage.

Loc	Prof	Align	XLev	Gage	Notes
1	J-1				
	2				
	3				
	4				
2	J-1				
	2				
	3				
	4				
3	J-1				
	2				
	3				
	4				
4	J-1				
	2				
	3				
	4				
5	J-1				
	2				
	3				
	4				

FIGURE A-1. DATA COLLECTION FORM - FIELD MEASUREMENT

- Change in rail length;
- Change in rail joining method;
- Change in joint stagger; or
- Presence of an anomaly.

Occasional short rails can be ignored or included in the data set. This is primarily a judgmental decision. However, rails from which data is collected should maintain the same cadence with respect to stagger.

## A.2 CONTRIBUTION OF THE PERIODIC DETERMINISTIC PROCESS

In the presence of the Periodic Deterministic Process (PDP) both  $\frac{1}{2}$  rail length and full rail length chords will exhibit family dependent mean values. The 2 rail length chords will be completely insensitive to the PDP. The evaluation of the PDP is carried out using a procedure that is described in Tables A-1 and A-2.

Some idea of the mean shape of the rail can be gathered from this data. Suppose that left and right rail data are averaged to give mean profile. Let  $\bar{\delta}_1$ ,  $\bar{\delta}_2$ ,  $\bar{\delta}_3$  and  $\bar{\delta}_4$  be the mean values of the four families of rail length chords. Then mean profile, will be given by:

$$\begin{aligned}
 \bar{z}_1 &= \frac{5}{8}\bar{\delta}_1 - \frac{3}{8}\bar{\delta}_3 - \frac{1}{8}(\delta_2 + \delta_4) && \text{(Joint or Weld)} \\
 \bar{z}_2 &= \frac{5}{8}\bar{\delta}_2 - \frac{3}{8}\bar{\delta}_4 - \frac{1}{8}(\delta_3 + \delta_1) && \text{(1<sup>st</sup> Q-Pt.)} \\
 \bar{z}_3 &= \frac{5}{8}\bar{\delta}_3 - \frac{3}{8}\bar{\delta}_1 - \frac{1}{8}(\delta_4 + \delta_2) && \text{(Half Point)} \\
 \bar{z}_4 &= \frac{5}{8}\bar{\delta}_4 - \frac{3}{8}\bar{\delta}_2 - \frac{1}{8}(\delta_1 + \delta_3) && \text{(2<sup>nd</sup> Q-Pt.)}
 \end{aligned}
 \quad \left. \vphantom{\begin{aligned} \bar{z}_1 \\ \bar{z}_2 \\ \bar{z}_3 \\ \bar{z}_4 \end{aligned}} \right\} \text{(A-1)}$$

TABLE A-1. ASSUMPTIONS AND DEFINITIONS

- Assumptions:
- Measured values are 1/2 rail length MCO, left rail profile and alignment, gage, and crosslevel.
  - M rail lengths of data are observed.

Definitions of Symbols over character:

< Left	$\overset{<}{z}$ = Left Profile
> Right	$\overset{>}{z}$ = Right Profile
- Mean	$\bar{z}$ = Mean Profile
^ Difference	$\hat{z}$ = Crosslevel

Definition of Superscripts -  $\delta$ :

$\delta$  without superscript:  $\frac{1}{2}$  rail length MCO  
 $\delta'$ : rail length MCO  
 $\delta''$ : 2 rail lengths MCO

Definition of Character Symbols:

$n$  = family number = 1,2,3,4. USE MODULO 4 COUNTING, i.e.,  $n=5 \rightarrow n=1$ ,  $n=0 \rightarrow n=4$ .

$n=1$  = centered at joint on left rail.

$m$  = rail length number = 1,2,...,M.

$z$  = profile.

$\delta$  = average of all  $\frac{1}{2}$  rail length MCO's.

$\delta_n$  = average MCO for  $n^{\text{th}}$  family.

$\delta_n(m)$  = specific MCO,  $n^{\text{th}}$  family,  $m^{\text{th}}$  rail length.

$\sigma$  = Homogeneous standard error for confidence limits.



TABLE A-2. FIELD PROCEDURE FOR COMPUTING MEANS AND CONFIDENCE INTERVALS - PDP

Means:

$$\bar{\delta}_n = \frac{1}{M} \sum_{m=1}^M \delta_n^{(m)} \quad (1)$$

$$\hat{z}_n = \frac{1}{M} \sum_{m=1}^M \hat{z}_n^{(m)} \quad (2)$$

$$\hat{\delta}_n = \hat{z}_n - \frac{1}{2}(z_{n+1} + z_{n-1}) \quad (3)$$

$$\bar{\delta}_n^+ = \bar{\delta}_n + \frac{1}{2}\hat{\delta} \quad (4)^\dagger$$

$$\bar{\delta}_n^+ = \bar{\delta}_{n-1} + 2\bar{\delta}_n + \bar{\delta}_{n+1} \quad (5)^\dagger$$

$$\bar{\delta}_n^{++} = \bar{\delta}_{n-1} + 2\bar{\delta}_n^+ + \bar{\delta}_{n+1}^+ \quad (6)^\dagger$$

$$\bar{\delta}_n^{++} = \bar{\delta}_{n-1} + 2\bar{\delta}_n + \bar{\delta}_{n+1} \quad (7)^\dagger$$

Mean Shape: Crosslevel - use Equation (2);

$$\bar{z}_n = \frac{5\bar{\delta}_n}{8} - \frac{1}{8}\bar{\delta}_{n+1} - \frac{3}{8}\bar{\delta}_{n+2} - \frac{1}{8}\bar{\delta}_{n+3} \quad (8)^*$$

Confidence Limits: Standard deviations are given by;

$$\bar{\sigma} = \left\{ \frac{1}{4M-1} \sum_{i=1}^M \sum_{m=1}^M [\bar{\delta}_n^{(m)} - \bar{\delta}_n]^2 \right\}^{1/2} \quad (9)$$

$$\hat{\sigma} = \left\{ \frac{1}{4M-1} \sum_{i=1}^M \sum_{m=1}^M [\hat{z}_n^{(m)} - \hat{z}_n]^2 \right\}^{1/2} \quad (10)$$

\* This equation applies to individual rail and difference computations by changing all over-symbols appropriately.

+ This equation applies to individual chords by adding (m) after each character.

One half of mean crosslevel is added (subtracted) to the above to get left (right) mean shapes. If  $z_2 \neq z_4$  to a statistically significant level, the mean shape is asymmetrical. At this point, the researcher should seek specific causes, such as predominant direction of traffic tonnage or an unusual joint stagger.

### A.3 CONTRIBUTION OF THE SRP TO MCO MEASUREMENTS

AN MCO of arbitrary length constructed on the Stationary Random Process (SRP) will include a randomly varying component. The magnitude of this component can be evaluated from the MCO variance provided a model is accepted for the process.

#### A.3.1 SINGLE POWER LAW MODEL

One approach is to represent the SRP in profile or alignment by a single Power Law PSD without break frequencies. Such a representation is given by:

$$S(\phi) = A_m \phi^{-m}, \quad (\text{A-2})$$

where

$A_m$  = a roughness constant = the PSD ordinate at frequency  $\phi = 1$ , and

$\phi$  = spatial frequency.

The variance of a MCO whose half length is S will be given by\*:

$$\text{Var}[\Delta(m,S)] = \frac{(2\pi)^m S^{m-1} A_m}{2\Gamma(m)} \left[ \frac{(2^{m-3} - 1)}{\cos(m\pi/2)} \right], \quad (\text{A-3})$$

for  $1 < m < 5$ ,  $m \neq 3$ .  $\Gamma(m)$  is the gamma function.

---

\*Found by evaluating the integral:  $\int_0^\infty \frac{\sin^4 x}{x^m} dx$ .

For  $m = 3$ , the expression in square brackets is undefined. By expanding numerator and denominator and taking the limit of  $m$  approaching 3, there results:

$$\text{Var}[\Delta(3,S)] = (2\pi S)^2 A_3 \ln(2). \quad (\text{A-4})$$

### A.3.2 CONTINUOUS PSD MODEL WITH BREAK FREQUENCIES

It has been found in this research that the PSD of profile and alignment SRP is well represented by a  $(-4, -2, -4)$  power law incorporated in a smooth continuous function with two break frequencies,  $\phi_3$  and  $\phi_4$ .\*

$$S(\phi) = \frac{A \phi_4^2 (\phi^2 + \phi_3^2)}{\phi^4 (\phi^2 + \phi_4^2)}. \quad (\text{A-5})$$

Here, the roughness parameter,  $A$ , defines the PSD ordinate where the  $(-2)$  asymptote intersects the  $\phi = 1$  abscissa.

The correlation function for a continuously measured MCO of half-length,  $S$ , is given by:

$$R(x) = \frac{1}{4}U(x - 2S) - U(x - S) + \frac{3}{2}U(x) - U(x + S) + \frac{1}{4}U(x + 2S), \quad (\text{A-6})$$

where,

$$U(x) = \frac{\pi^2 AS}{u} \left\{ \frac{1}{6}\rho |v|^3 - (1 - \rho) [ |v| - e^{-|v|} ] \right\}, \quad (\text{A-7})$$

and where,

$$u = 2\pi\phi_4 S; \quad (\text{A-8})$$

$$v = 2\pi\phi_4 x; \text{ and} \quad (\text{A-9})$$

$$\rho = (\phi_3/\phi_4)^2. \quad (\text{A-10})$$

\*Other break frequencies exist but these are sufficiently removed from the range of interest that they are ignored.

The variance of the mid-chord is given by  $R(0)$ :

$$\text{Var}[\Delta(\rho, u, S)] = R(0) = \frac{(2\pi)^2}{4} \text{ASP}(\rho, u), \quad (\text{A-11})$$

where,

$$P(\rho, u) = \frac{1}{3}\rho u^2 + (1 - \rho) \left\{ 1 - \frac{1}{u} \left[ \frac{3}{2} - 2e^{-u} + \frac{1}{2}e^{-2u} \right] \right\} \quad (\text{A-12})$$

Notice that  $\rho = 1$  causes the spectrum to degenerate to an inverse 4<sup>th</sup> power law. For this case  $P(1, u) = u^2/3$  and

$$\text{Var}[\Delta(1, u, S)] = \frac{(2\pi)^4}{12} A_4 S. \quad (\text{A-13})$$

This agrees with Equation (A-3) when the substitution,

$$A_4 = A\phi_4^2, \quad (\text{A-14})$$

is made. If, in Equation (A-12),  $\rho \rightarrow 0$  is followed by  $u \rightarrow \infty$ , the spectrum degenerates to an inverse square law. In this limit,  $P(0, \infty) = 1$ , and Equation (A-11) gives:

$$\text{Var}[\bar{\Delta}(0, \infty, S)] = \frac{(2\pi)^2}{4} AS. \quad (\text{A-15})$$

This also agrees with Equation (A-3) with,

$$A = A_2 \quad (\text{A-16})$$

Where the SRP is the only fluctuating component present, the expected MCO variance is a function of chord length only and it is independent of which chord family is used. Observed

fluctuations from family to family will be within the limit of statistical sampling error. The three different chord lengths can be used to estimate  $A$ ,  $\rho$ , and  $u$  by solving 3 simultaneous equations in three unknowns. These are nonlinear equations, and the computational scheme needed to evaluate the unknowns has not been identified.

#### A.4 CONTRIBUTION OF RANDOM JOINT AMPLITUDES

The inclusion of random joint amplitudes modifies the above picture considerably. These are fluctuating components and without the special handling of chords by families, it would mix in with the SRP in a manner that simply elevates SRP statistics. At the same time, a form of fluctuation that is dynamically severe is ignored--that is, it is ascribed to the SRP which implies a lesser dynamic impact on vehicle responses.

By separating the chords into families, four variances per chord length will be found. Even in slightly degraded track, variances for a given chord length will fluctuate significantly from family to family. If a sufficient number of joints are included in the survey, these fluctuations will be well above the fluctuation levels implied by statistical sampling error.

An estimate of the additional fluctuation caused by joints is found by observing how much the largest MCO variance (invariably centered at the joints) exceeds the minimum variance. The procedure is described in Table A-3. An estimate of the distributional properties of the estimators is given.

Note that no attempt is made to characterize the random joint amplitudes except to quantify its variance. An examination of field data reveals that:

TABLE A-3. FIELD PROCEDURE FOR EVALUATING 2<sup>nd</sup> ORDER STATISTICS - HMP AND PMMP

Definitions of Character Symbols - In addition to those listed in Table H-1:

- w = Variance of space curve about the mean-crosslevel only.
- v = Variance of MCO about the mean → v' and v'' also.
- p = Minimum of v<sub>n</sub> as a function of n.
- P(ρ, u), See text, Equation (H-12). u<sub>0</sub> = 2πφ<sub>u</sub>X, X=rail length.
- f = Estimator of joint variances.

Variances about Means:

$$\hat{w}_n = \frac{1}{M-1} \sum_{m=1}^M [\hat{z}_n(m) - \hat{z}_n] \quad (1) \quad \bar{v}_n = \frac{1}{M-1} \sum_{m=1}^M [\bar{z}_n(m) - \bar{z}_n] \quad (1)^*$$

$$\bar{v}'_n = \frac{1}{M-1} \sum_{m=1}^M [\bar{z}'_n(m) - \bar{z}'_n] \quad (3)^* \quad \bar{v}''_n = \frac{1}{M-1} \sum_{m=1}^M [\bar{z}''_n(m) - \bar{z}''_n] \quad (2)^*$$

Determining the SRP, Mean Profile -Extendable to individual rails:

$$\left. \begin{aligned} \bar{p} &= \text{Min} \{ \bar{v}_1, \bar{v}_2, \bar{v}_3, \bar{v}_4 \} = \frac{1}{2} \pi^2 \bar{A} X P(\bar{p}, \frac{1}{2} \bar{u}_0) \\ \bar{p}' &= \text{Min} \{ \bar{v}'_1, \bar{v}'_2, \bar{v}'_3, \bar{v}'_4 \} = \pi^2 \bar{A} X P(\bar{p}, \bar{u}_0) \\ \bar{p}'' &= \text{Min} \{ \bar{v}''_1, \bar{v}''_2, \bar{v}''_3, \bar{v}''_4 \} = 2 \pi^2 \bar{A} X P(\bar{p}, 2 \bar{u}_0) \end{aligned} \right\} \left\{ \begin{aligned} \bar{A} &= A(\bar{p}, \bar{p}', \bar{p}'') \\ \bar{p} &= p(\bar{p}, \bar{p}', \bar{p}'') \\ \bar{u}_0 &= u_0(\bar{p}, \bar{p}', \bar{p}'') \end{aligned} \right. \quad (3)$$

Determining the Extent of the presence - 50% stagger assumed:

$$\begin{matrix} < & < & < \\ f & = & v_1/p \end{matrix} \quad (4)$$

$$\begin{matrix} > & > & > \\ f & = & v_3/p \end{matrix} \quad (5)$$

Distribution of Estimators - Gaussian Inputs Assumed:

v<sub>n</sub>, v'<sub>n</sub> and v''<sub>n</sub>: χ<sup>2</sup>, M-1 degrees of freedom.

f, f̄: F-distribution, Ratio of two χ<sup>2</sup>, M-1 degrees of freedom random variables.

Evidence supports a Gaussian distribution for SRP Γ-distribution for the joint amplitudes.

\*This equation applies to individual rail and difference computations by changing all over-symbols appropriately.

- A low joint on one rail produces a correlated depression on the opposite rail that is quite evident in highly degraded track where 50% stagger of joints is used;
- It is quite conceivable that consecutive joints on one rail and adjacent joints on opposite rails correlate with one another; and
- It is also suspected that consecutive shop welds anti-correlate with one another.

The ability to quantify these properties is probably beyond the computational limits of the field approach and is best left for the parameter extractor described in Appendix G.

Again, it is emphasized that the procedure outlined above can be applied to rail line geometry. In this mode, profile is replaced by alignment, and crosslevel is replaced by gage.





APPENDIX B  
CHARACTERIZATION OF THE RAIL JOINT

B.1 MATHEMATICAL DESCRIPTION OF JOINTS

B.1.1 JOINT SHAPE

Modeling the joint-related geometry consists of:

- Identifying the analytic functions needed to represent the universe of joint geometries that are found in field data.
- Identifying the distinguishing parameters that describe the universe of variations in joint geometry, e.g., joint depth, derivative discontinuity, etc.

Some features that are observable in the profile space curves of bolted splices in rail are:

- The profile exhibits a negative cusp at the joint.
- The depression at the joint dies away or is eventually obfuscated by the SRP within about 10 feet on either side.
- Other joint features, such as rail-end-mismatch, and batter depressions do exist and can be modeled. However, they are not observable in track geometry data collected at 2.4- to 0.6-foot sample intervals. Even with more frequent sampling, they may be masked by wheel diameter filtering or by wheel/rail dynamic interaction of the measuring vehicle.

As a first effort, the joint was represented by a symmetric function of the form:

$$z(x) = Cf(|kx|), \quad (B-1)$$

where  $z(x)$  = profile as a function of longitudinal distance,  $x$ , and  $k$  = decay rate. The joint shape function  $f(|kx|)$  is chosen so that  $f(0)=1$  so that  $C$  represents the joint amplitude.

Joint severity is defined as the instantaneous change of derivative at the cusp and is given by:

$$\text{Joint Severity} \equiv \left. \frac{dz}{dx} \right|_{0+} - \left. \frac{dz}{dx} \right|_{0-}, \quad (\text{B-2})$$

where,

$$\left. \frac{dz}{dx} \right|_{0\pm} = \lim_{x \rightarrow 0\pm} \frac{dz}{dx} = \pm C \left. \frac{df}{dx} \right|_{0+}. \quad (\text{B-3})$$

If  $\left. \frac{df}{dx} \right|_{0\pm} = \pm k$ , then joint severity is twice the product of amplitude and decay rate. Empirical observations indicate that as  $C$  increases,  $k$  decreases so that severity does not increase as dramatically as  $C$ .

Figure B-1A shows how the amplitude and the severity are related to analytical models of joints. The remainder of Figure B-1 defines several different mathematical formulations for low joints all normalized for equal amplitude and severity.

Figure B-1B shows an exponential form, one that matches physical intuition very well. However, simulation of these joints in a computer program is cumbersome since its convolution sequence is doubly infinite. The sequence elements are eventually sufficiently small so that the series can be truncated without introducing significant error. Still it cannot be simulated by stable recursive algorithms. Each sampled output must be obtained by the multiplication of as many joint causative impulses as fall within the range of the convolution sequence! (See Appendix H, Figure H-1.)

Figure B-1C shows a sinusoidal joint model. In the case where this depression is repeated identically every distance  $L$ , the traditional rectified sine wave results. The associated convolution sequence is of finite duration so that its simulation is simpler than the exponential form. Generally, only one joint causative impulse appears within the range of the sequence.

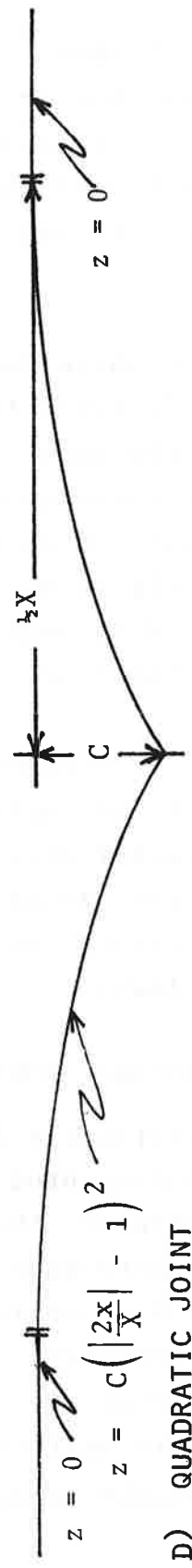
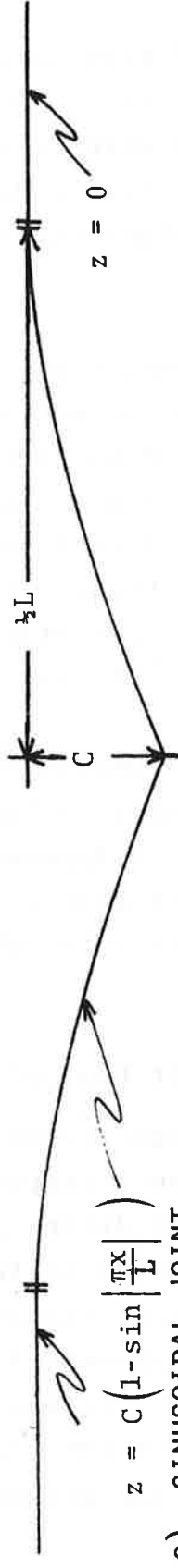
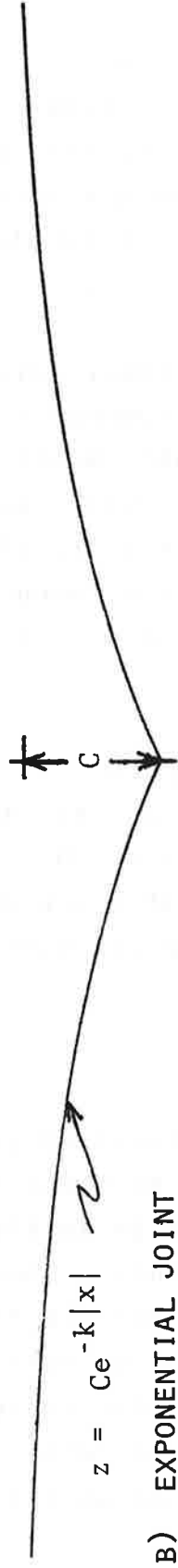
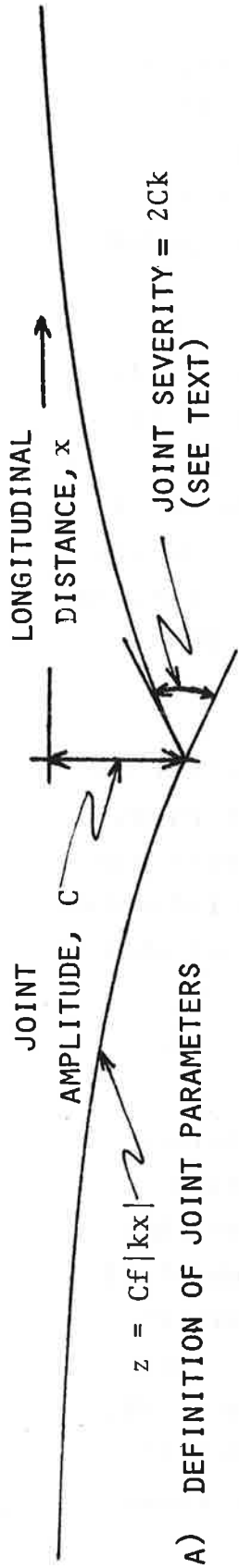


FIGURE B-1. LOW JOINT ENVIRONMENT AND ASSOCIATED MODELS

Figure B-1D shows a quadratic joint model. Its principal feature is that it is readily simulated. Figure B-2 shows how this is accomplished using a shift-register approach, and Table B-1 shows how this is done using a moving strip algorithm. Figure B-3 shows the resultant impulse response of both.

All of the above forms represent symmetrical joints. It is quite conceivable that an asymmetrical component should be added to the above. There is considerable multiple track territory where traffic on a given track will tend to be unidirectional. Even on bi-directional track, traffic load can be primarily in one direction. The most pronounced asymmetry is expected in unit train territory where dynamic responses to track input are always the same.

The need for asymmetrical models will appear as an output of both the Field-Implementable Techniques and the Track Parameter Extractor described in Appendices A and H, respectively. However, preliminary observations of real track data indicate that symmetrical models will be adequate for most track characterizations.

#### B.1.2 SPECTRAL CONTENT OF LOW JOINTS

Three analytically different representations of low joints have been presented. Visual inspection of their spatial shapes indicates that they differ primarily in the way they return to zero on either side of the joint. The sinusoidal model has a concentration of curvature near the transitions to level geometry. The exponential form concentrates the curvature near the joints. In the quadratic representation, curvature is uniform out to the transition points where it drops suddenly to zero. The obvious question is: *Is there*

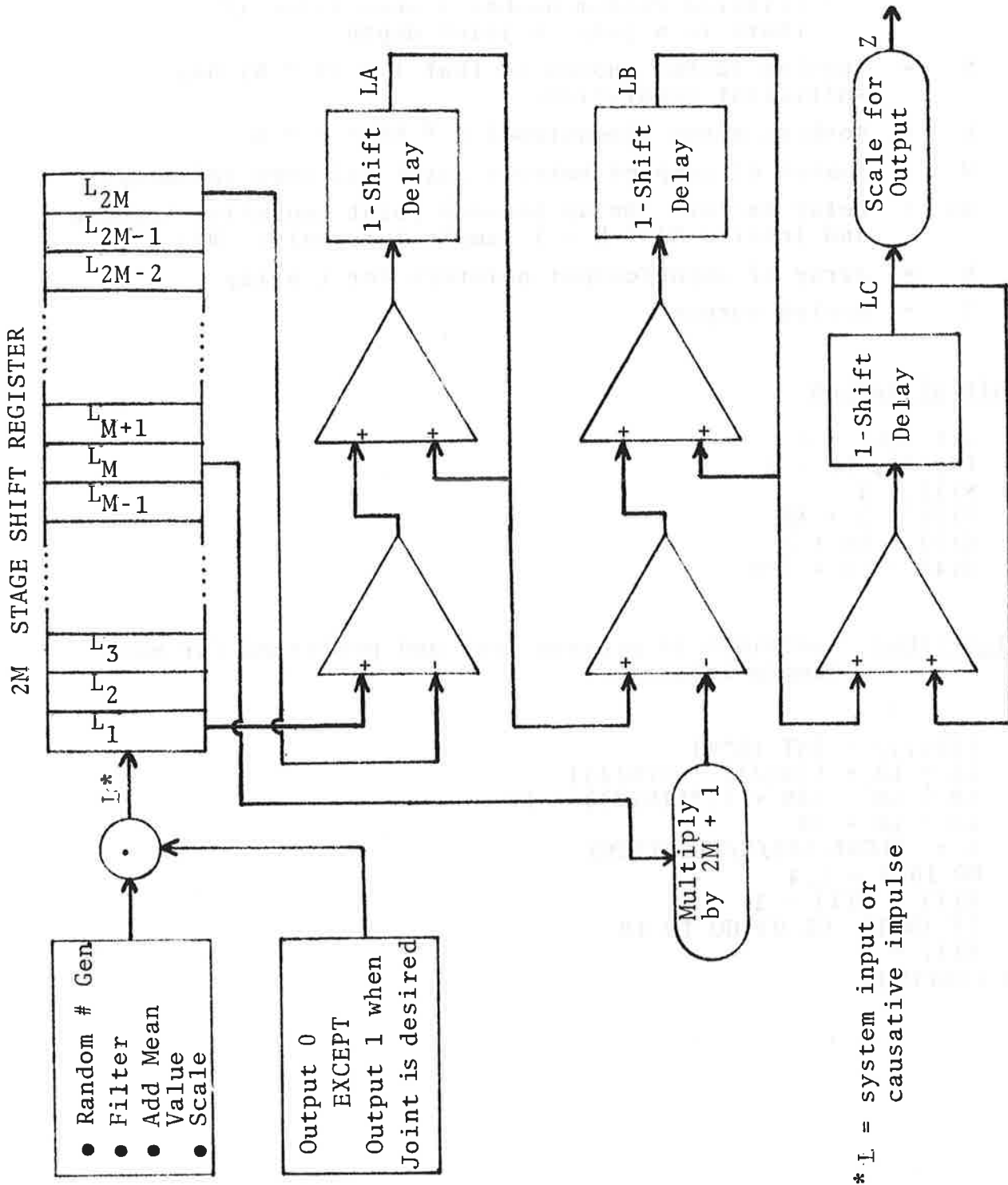


FIGURE B-2. SHIFT REGISTER REPRESENTATION OF JOINT SIMULATOR

TABLE B-1. MOVING STRIP ALGORITHM FOR SIMULATING  
LOW JOINT

Definitions:

- W = Output of generator (joint causative impulse)  
       = 0 if there is no joint  
       = filtered random number + mean value if  
       there is a joint = joint depth
- S = Scaling factor chosen so that INT (S \* W) has  
sufficient resolution.
- L = Working array dimensioned  $K \geq NA + 2 * M$
- M = Number of samples between joint and zero influence
- NA = Delay factor: Delay between joint causative impulse  
and joint =  $NA + M - 1$  sample intervals:  $NA \geq 0$
- N = Array of input/output pointers for L-array
- Z = Scaled output

Initialization

A11 L(K) = 0  
LA, LB, LC = 0  
N(1) = 1  
N(2) = 1 + NA  
N(3) = NA + M  
N(4) = NA + 2\*M

Algorithm: Contained in program loop and performed for each  
sample interval.

```

      :
      L(N(1)) = INT (S*W)
      LA = LA + L(N(2)) - L(N(4))
      LB = LB - (2M + 1)*L(N(3)) + LA
      LC = LC + LB
      Z = FLOAT(LC)/S/FLOAT(2M)
      DO 10 I = 1,4
      N(I) = N(I) - 1
      IF (N(I) .GT. 0) GO TO 10
      N(I) = K
10 CONTINUE
      :

```

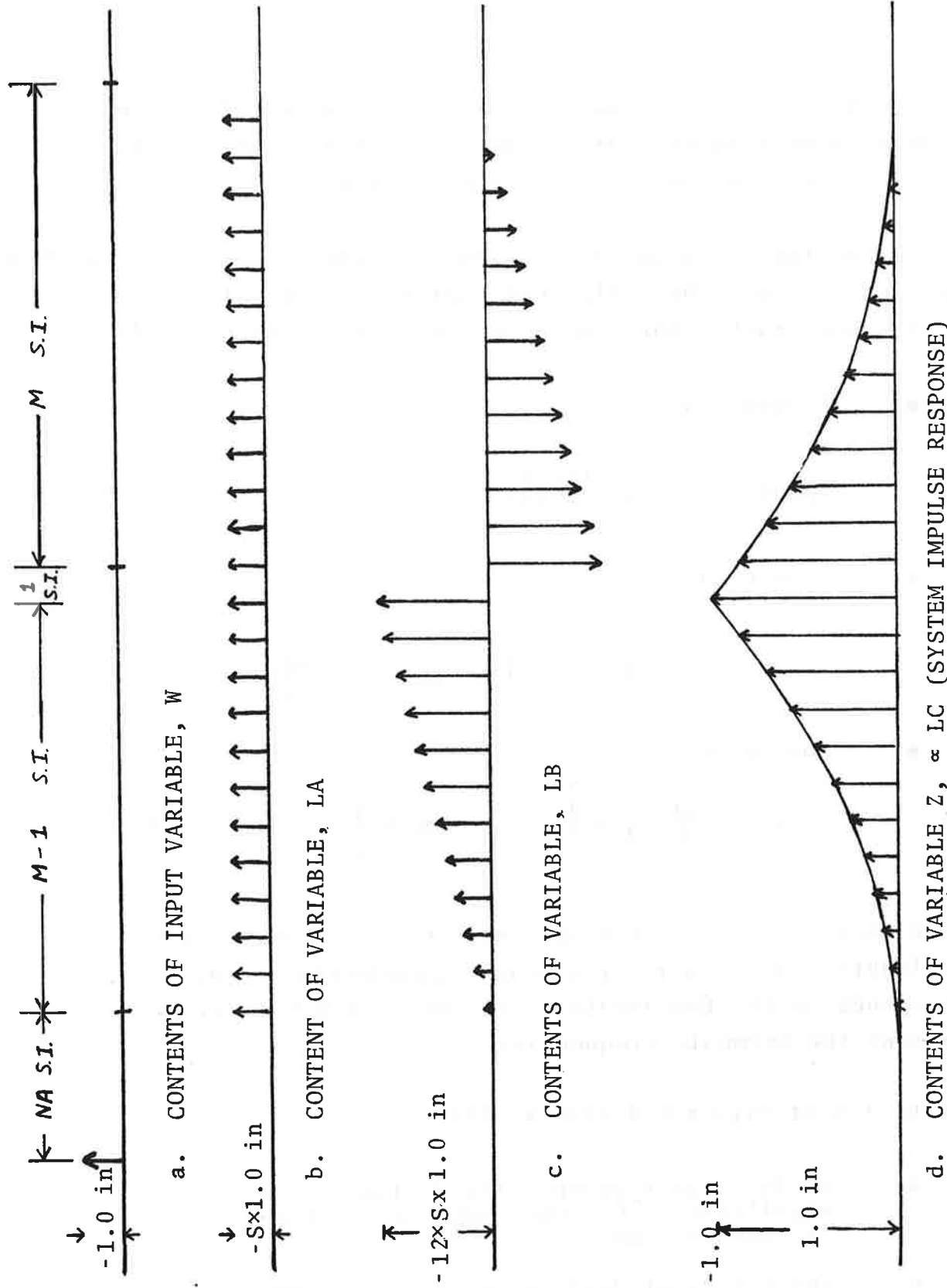


FIGURE B-3. QUADRATIC SIMULATION OF 1.0 INCH AMPLITUDE JOINT  
 $NA = 4, M = 13$

any cogent reason to choose one analytical representation of the joint over another? Or is the difference between these representations buried in the "noise" of the SRP.

To help resolve these questions, the frequency spectra of the three forms are derived. The analytical expressions are listed below and they are graphed for comparison purposes in Figure B-4.

- Exponential:

$$z_e(n) = \frac{2L}{\pi} \frac{(KL/\pi)}{4n^2 + (KL/\pi)^2}, \quad (B-4)$$

- Sinusoidal:

$$z_s(n) = \frac{2L}{\pi} \frac{1}{4n^2 - 1} \left[ 1 - \frac{1}{2n} \sin \pi n \right], \quad (B-5)$$

- Quadratic:

$$z_q(n) = \frac{2L}{\pi} \frac{1}{4n^2} \left[ 1 - \frac{1}{4n} \sin 4n \right], \quad X = 4L/\pi \quad (B-6)$$

In the above  $n = \phi L/2\pi$ ,  $\phi$  = spatial frequency, and  $L$  is the rail length. Thus in the periodic deterministic case,  $n = 1$  corresponds to the fundamental frequency and  $n = 2, 3, 4 \dots$  represent the harmonic frequencies.

Examination of Figure B-4 reveals that

- In the high frequency limit, there is no significant difference between the three representations.
- The principal difference is in the low frequency long wavelength limit. In this limit, the joint-related SRP processes are indistinguishable from SRP's.



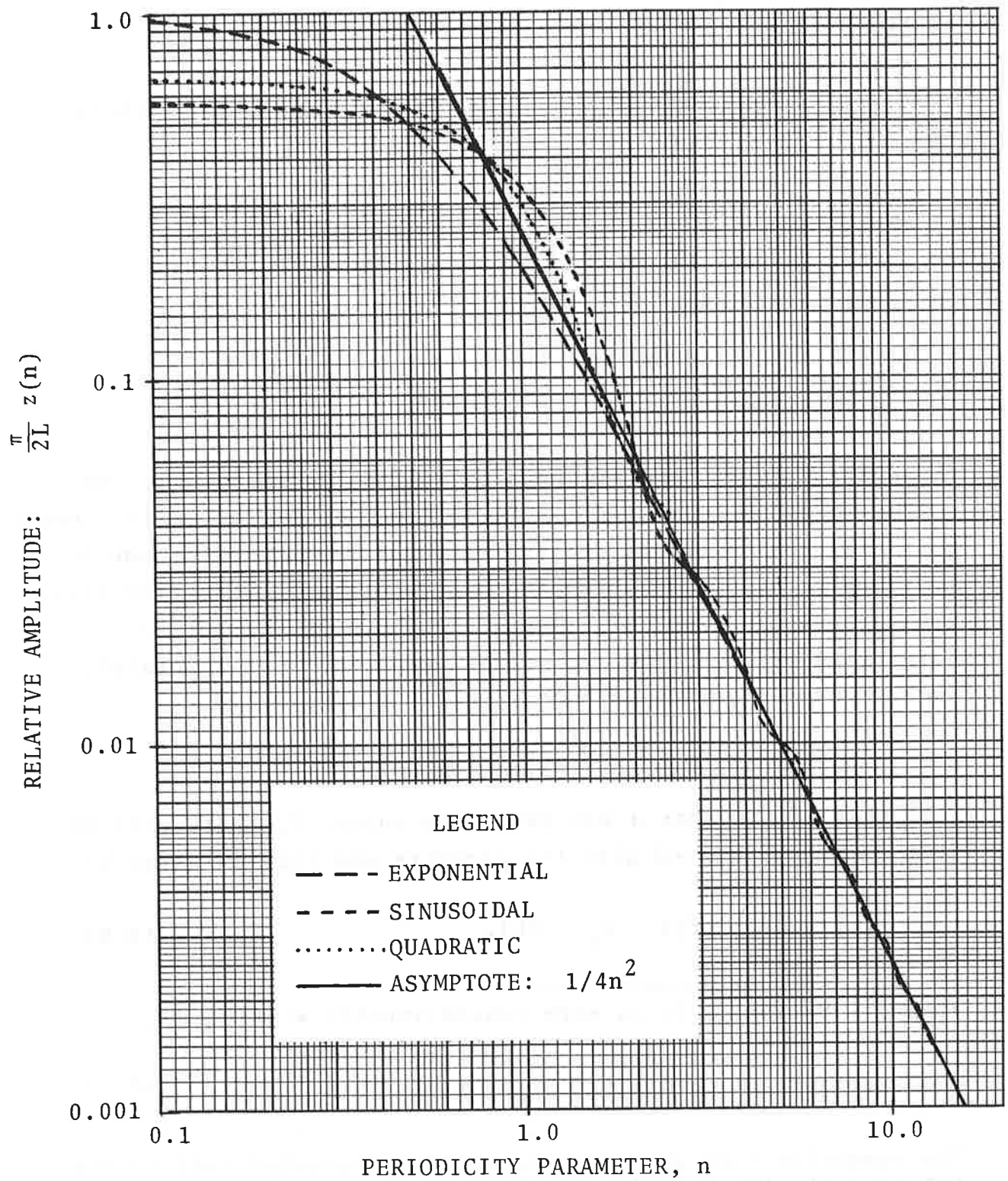


FIGURE B-4. SPECTRAL CONTENT OF LOW JOINT MODELS

## B.2 SYSTEMS OF JOINTS

The combination of SRP and random joint amplitudes is represented by the series,

$$z(x) = C(n) f(x - x_c - nL), \quad (B-7)$$

where

$z(x)$  = profile or alignment as a function of longitudinal distance,  $x$ .

$C(n)$  = depth of the  $n^{\text{th}}$  joint, a random variable,

$x_c$  = distance to 1<sup>st</sup> joint,

$L$  = rail length,

$n$  = running index,  $-\infty$  to  $+\infty$ .

In Equation (B-7), the Einstein convention is assumed to apply to the repeated running index,  $n$ .<sup>\*</sup> For the time being, the treatment will deal with one rail. The joint depth  $C(n)$  is now a stationary random variable with non-zero mean. This simplified treatment will serve to illustrate the applicable methods. Later, the effects of a second rail and other joint-related variations (severity, asymmetry) will be introduced.

### B.2.1 MEAN SHAPE AND CORRELATION FUNCTION

Note that if  $C(n)$  has a non-zero mean value,  $\bar{C}$ , there will be a mean shape associated with the geometry and this is given by,

$$\overline{z(x)} = \bar{C} \sum_{n=-\infty}^{\infty} f(x - x_c - nL), \quad (B-8)$$

---

\*Thus, Equation (B-7) is more conventionally written as,

$$z(x) = \sum_{n=-\infty}^{\infty} C(n) f(x - x_c - nL). \quad (B-7)$$

The summation sign will be used whenever repeated indices are not present, for example, Equation (B-8).

where  $\bar{C}$  is the mean of the  $C(n)$ . For the sinusoidal and the quadratic low joints discussed in the previous Section, mean shapes are simple to compute since the individual joint shape deviations do not overlap at all or only slightly. The amplitude of the mean shape is the average of the amplitudes and its shape is cyclic repetition of the individual joint shape. For the exponential joint,

$$\overline{z(x)} = \bar{C} \sum_{n=-\infty}^{\infty} e^{-k|x-nL|}, \quad (\text{B-9})$$

where  $x_c$  is taken as 0. Performing the manipulations implied in Equation (B-9) gives the following representation, valid over 2 rail lengths:

$$\overline{z(x)} = \bar{C} \frac{\cosh(k|x-\frac{1}{2}L|)}{\sinh(\frac{1}{2}kL)}, \quad |x| < L. \quad (\text{B-10})$$

By averaging over the second moment, the correlation function for  $z(x)$  is found to be

$$\begin{aligned} V(x) &= \overline{C(n)f(x'+nL) C(n+m) f(x'+x+nL+mL)}, \\ &= r(n) \xi(x-nL), \end{aligned} \quad (\text{B-11})$$

where, the overbar represents a time average over  $x'$  and where:

$$r(n) = \langle C(m) C(m+n) \rangle, \quad (\text{B-12})$$

$$\xi(x) = \frac{1}{L} \int f(x') f(x'+x) dx'. \quad (\text{B-13})$$

Equation (B-11) represents a convolution in  $n$ . Therefore the resultant PSD will be the product of PSD's associated with periodic Dirac delta-functions (impulses),  $r(n)$ , and  $\xi(x)$ .

Hence,

$$S_z(\phi) = R(\phi) W(\phi), \quad (\text{B-14})$$

where,

$$R(\phi) = r(n) \int \delta(x-nL) e^{i2\pi\phi x} dx = r(n) e^{i2\pi\phi nL}, \quad (\text{B-15})$$

$$W(\phi) = 2 \int \xi(x) e^{i2\pi\phi x} dx. \quad (\text{B-16})$$

The factor of 2 converts to single-sided PSD's.

### B.2.2 EXAMPLES

CASE 1: The joint depth is an uncorrelated random variable:

$$r(n) = \begin{cases} 0 & n \neq 0, \\ \Sigma^2 & n = 0, \end{cases}; \quad (B-17)$$

This represents the uncorrelated fluctuation of the joint depths with zero mean and standard deviation,  $\Sigma$ . For this case,

$$R(\phi) = \Sigma^2, \quad (B-18)$$

so that,

$$S_z(\phi) = \Sigma^2 W(\phi), \quad (B-19)$$

describes the spectrum of completely uncorrelated periodically spaced joints.

CASE 2: The joint depth is constant (PDP):

$$r(n) = \bar{C}^2 \text{ for all } n; \quad (B-20)$$

Hence:

$$\left. \begin{aligned} R(\phi) &= \bar{C}^2 \sum_{n=-\infty}^{\infty} e^{-i2\pi\phi nL}, \\ &= \bar{C}^2 \lim_{N \rightarrow \infty} \sum_{n=-N}^N e^{-i2\pi\phi nL}, \\ &= \bar{C}^2 \lim_{N \rightarrow \infty} \frac{\sin[\pi\phi(2N+1)L]}{\sin(\pi\phi L)} = \frac{\bar{C}^2}{L} \sum_{n=-\infty}^{\infty} \delta(\phi - n/L). \end{aligned} \right\} (B-21)$$

The last expression produces a periodic string of Dirac delta functions in  $\phi$  at intervals of  $n/L$ ,  $n = 0, \pm 1, \pm 2 \dots$ . This produces the line spectrum that is associated with the PDP.

The strength of each line component is proportional to  $W(\phi)$ , evaluated at  $\phi = n/L$ . Hence,

$$S(\phi) = \frac{1}{L} \bar{C}^2 W(\phi) \sum_{n=-\infty}^{\infty} \delta(\phi - n/L). \quad (\text{B-22})$$

Equation (B-5) gives the spectrum for a single sinusoidal low joint as:

$$z_s(n) = \frac{2L}{\pi} \frac{1}{4n^2 - 1} \left[ 1 - \frac{1}{2n} \sin n\pi \right], \quad (\text{B-5})$$

where spatial frequency is expressed in dimensionless units of  $n = \phi L$ . The delta-functions of Equation (B-22) vanish except at integer  $n$ , so that the term,  $\sin n\pi$ , of Equation (B-5) vanishes.  $W(\phi)$  becomes  $W(n)$  and is related to  $z_s(n)$  by:

$$W(n) = \frac{1}{L} z_s^2(n). \quad (\text{B-23})$$

If Equations (B-22), (B-5), and (B-23) are combined, the line component of the power spectrum can be found and it is given by

$$[S(\phi)]_s = \left[ 2 \left( \frac{2\bar{C}}{\pi(4n^2 - 1)} \right)^2 \right] \delta(\phi - n/L). \quad (\text{B-24})$$

The term in the square brackets is recognized as the expression for spectral line strengths of the rectified sine wave.  $n = 1$  gives the strength of the fundamental and  $n = 2, 3, 4 \dots$  gives the strengths of the harmonics.

The procedures outlined above can be applied to the exponential and the quadratic expressions as defined by Equations (B-4) and (B-6). These give:

$$[S_z(\phi)]_e = 2 \left[ \frac{2C(kL/\pi)}{\pi [4n^2 + (kL/\pi)^2]} \right]^2 \delta(\phi - n/L), \quad (B-25)$$

and

$$[S_z(\phi)]_q = 2 \left[ \frac{2C}{4n^2\pi} \left( 1 - \frac{1}{4n} \sin 4n \right) \right]^2 \delta(\phi - n/L). \quad (B-26)$$

CASE 3: Exponentially damped joint-to-joint correlation.

For this example, the correlation coefficients are given by:

$$r(n) = r(0)\gamma^{-|n|} \quad (B-27)$$

By varying  $\gamma$ , a gradual transition from completely correlated to completely uncorrelated random joints can be effected. For example

$$\begin{aligned} \lim_{\gamma \rightarrow 1} & \rightarrow \text{completely correlated random joint amplitudes} \\ \lim_{\gamma \rightarrow -1} & \rightarrow \text{completely anti-correlated random joint} \\ & \text{amplitudes} \quad (B-28) \\ \lim_{\gamma \rightarrow 0} & \rightarrow \text{completely uncorrelated joint amplitudes} \end{aligned}$$

Intermediate values of  $\gamma$  produce amplitudes with more or less correlation.

Further theoretical, graphical and textual explanation of this example is provided in Paragraph 2.3.1, Volume I of this report.

### B.2.3 GENERALIZATION: TWO RAILS AND ADDITIONAL JOINT DESCRIBING FUNCTIONS

The inclusion of an additional processes in the track and a second rail gives the following mean profile and crosslevel representations:

$$\bar{z}(x) = \frac{1}{2}C(\alpha, n) f(\alpha, x - x_c - nL) + \frac{1}{2}D(\alpha, n) f(\alpha, x - x_d - nL), \quad (B-29)$$

$$\theta(x) = G(\alpha, n) f(\alpha, x - x_c - nL) - H(\alpha, n) f(\alpha, x - x_d - nL), \quad (B-30)$$

where:

$\alpha$  = counting index describing the shape function list;

$f(\alpha, x)$  = function list, describing the joint shape (depth, asymmetry, severity, etc.);

$C, D, G, H$  = amplitudes associated with the above;

$x_c, x_d$  = distance to first joint on left/right rail.

Note that different amplitudes were used to represent crosslevel\*. This is done intentionally to reflect the possibility that joint related activity on one rail is observed to produce perturbations in the opposite rail. Left and right profiles are now given by:

LEFT RAIL:

$$\left. \begin{aligned} Z_c(x) &= \frac{1}{2}\theta(x) + \bar{z}(x), \\ &= \frac{1}{2}[C(\alpha, n) + G(\alpha, n)] f(\alpha, x - x_c - nL) \\ &\quad + \frac{1}{2}[D(\alpha, n) + H(\alpha, n)] f(\alpha, x - x_d - nL), \end{aligned} \right\} \quad (B-31)$$

RIGHT RAIL:

$$\left. \begin{aligned} Z_d(x) &= \frac{1}{2}\theta(x) + \bar{z}(x), \\ &= \frac{1}{2}[C(\alpha, n) - G(\alpha, n)] f(\alpha, x - x_c - nL) \\ &\quad + \frac{1}{2}[D(\alpha, n) - H(\alpha, n)] f(\alpha, x - x_d - nL). \end{aligned} \right\} \quad (B-32)$$

---

\*Alternatively, this can be achieved by adding to the function list.

#### B.2.4 CORRELATION RELATIONSHIPS BETWEEN JOINT DESCRIBING PARAMETERS

The correlation functions for mean profile and crosslevel, and the cross-correlation function for mean profile with crosslevel will be given by:

$$\begin{aligned}
 R_{\bar{z}}(x) = & \frac{1}{2} \rho_C(\alpha, \beta; n) \xi(\alpha, \beta; x - nL) \\
 & + \frac{1}{2} \rho_{CD}(\alpha, \beta; n) \xi(\alpha, \beta; x - nL - x_0) \\
 & + \frac{1}{2} \rho_D(\alpha, \infty; n) \xi(\alpha, \beta; x - nL);
 \end{aligned}
 \tag{B-33}$$

$$\begin{aligned}
 R_{\theta}(x) = & \rho_G(\alpha, \beta; n) \xi(\alpha, \beta; x - nL) \\
 & + 2\rho_{GH}(\alpha, \beta; n) \xi(\alpha, \beta; x - nL + x_0) \\
 & + \rho_H(\alpha, \beta; n) \xi(\alpha, \beta; x - nL);
 \end{aligned}
 \tag{B-34}$$

$$\begin{aligned}
 R_{\bar{z}\theta}(x) = & \frac{1}{2} \rho_{CG}(\alpha, \beta; n) \xi(\alpha, \beta; x - nL) \\
 & + \frac{1}{2} \rho_{CH}(\alpha, \beta; n) \xi(\alpha, \beta; x - nL - x_0) \\
 & + \frac{1}{2} \rho_{DG}(\alpha, \beta; n) \xi(\alpha, \beta; x - nL + x_0) \\
 & + \frac{1}{2} \rho_{DH}(\alpha, \beta; n) \xi(\alpha, \beta; x - nL).
 \end{aligned}
 \tag{B-35}$$

In the above, for example,

$$\rho_C(\alpha, \beta; n) = \langle C(\alpha, m) C(\beta, m + n) \rangle, \tag{B-36}$$

$$\rho_{CD}(\alpha, \beta; n) = \langle C(\alpha, m) D(\beta, m + n) \rangle, \tag{B-37}$$

$$\xi(\alpha, \beta; x) = \frac{1}{L} \int f(\alpha, x') f(\beta, x' + x) dx, \tag{B-38}$$

$$x_0 = x_d - x_c; \quad |x_0| < \frac{1}{2} L. \tag{B-39}$$



Obvious simplifications take place if the set of functions,  $f(\alpha, x)$ , are chosen to be orthogonal to one another. This will be particularly simple when the stagger is 0% or 50%, and slightly more difficult for  $\pm 25\%$  stagger.

Another point worthy of note: For sampled data, no more functions,  $f(\alpha, x)$ , can be used than there are samples/half rail length. Also, if the same number of functions are used as are allowed by this criterion, the rail geometry is completely specified, and there are no deviations left over for a stationary random process! Therefore, the list of  $f(\alpha, x)$  should be selective, and should reflect only those joint related processes that are seen to be present at joints. For example, it is tempting to add two functions that would represent rail end mismatch and rail end batter. However, track dynamics in the presence of measurement car loading, combined with the sample intervals normally used in the collection of track data will tend to obfuscate these conditions. Geometry data has been examined that includes abundant examples of both, yet tracings do not reveal their presence.

### B.3 CHARACTERIZATION OF JOINTS FROM REAL DATA

Most of the foregoing discussion proceeded on the basis of limited observation, the limitations being

- Faithful space curves of fairly good track via the T-3 profilometer (speeds high);
- Highly distorted space curves of degraded track via the T-3 profilometer (speeds too slow);
- Faithful space curves of limited territory and not in the best format from the TSD; and
- Highly colored profiles from chord systems.

During the latter part of the program, some T-6 data has been available to support the track characterization effort. Since the lower speed range of older profilometers is of the order of 25 mph, little profile data has been collected from track in very poor condition. T-6 incorporates a low speed profile system that collects multi-chordal data at speeds to 0 mph. Also the application of new processing techniques to the profilometer greatly improves its noise floor, so that valid data is available at 10 mph or less. With the availability of low-speed data in an easy-to-handle format, a considerable improvement in joint characterization is possible.

In the paragraphs that follow the statistical distribution of low joints is characterized. This investigation centers on a homogeneous section of track that has 156 joints in each rail. Also, a section of highly degraded jointed track is examined. Finally, it is shown that CWR also has some joint related activity that is not a residue of ballast deformation under bolted joints.

#### B.3.1 PROBABILITY DISTRIBUTIONS OF LOW JOINTS

A statistic that is just as important as the correlations for low joint behavior, is their frequency versus amplitude density for a homogeneous track section. To find how the amplitudes of low joints are distributed, a section of T-6 collected data was examined. 16' MCO's centered at joints were tabulated and their magnitudes converted into a histogram. Details of this exercise are present in Paragraph 2.1.3.1, Volume 1 of this report.

Based on its geometry, the zone from which the data has been collected was estimated at class 3 track. Construction characteristics were 132 lb. RE rail, 39' lengths with bolted joint bars, good ballast, good ballast shoulder profile, undisturbed wood ties and excellent drainage. The right of way is a main line section of two tracks, the left rail of the track surveyed being towards the edge of the embankment.

### B.3.2 HIGHLY DEGRADED JOINTS

In a second effort to characterize the joint from real data, attention focused on a special, highly degraded section of track. Geometry from this track is shown in the surface data of Figures B-5 through B-7.

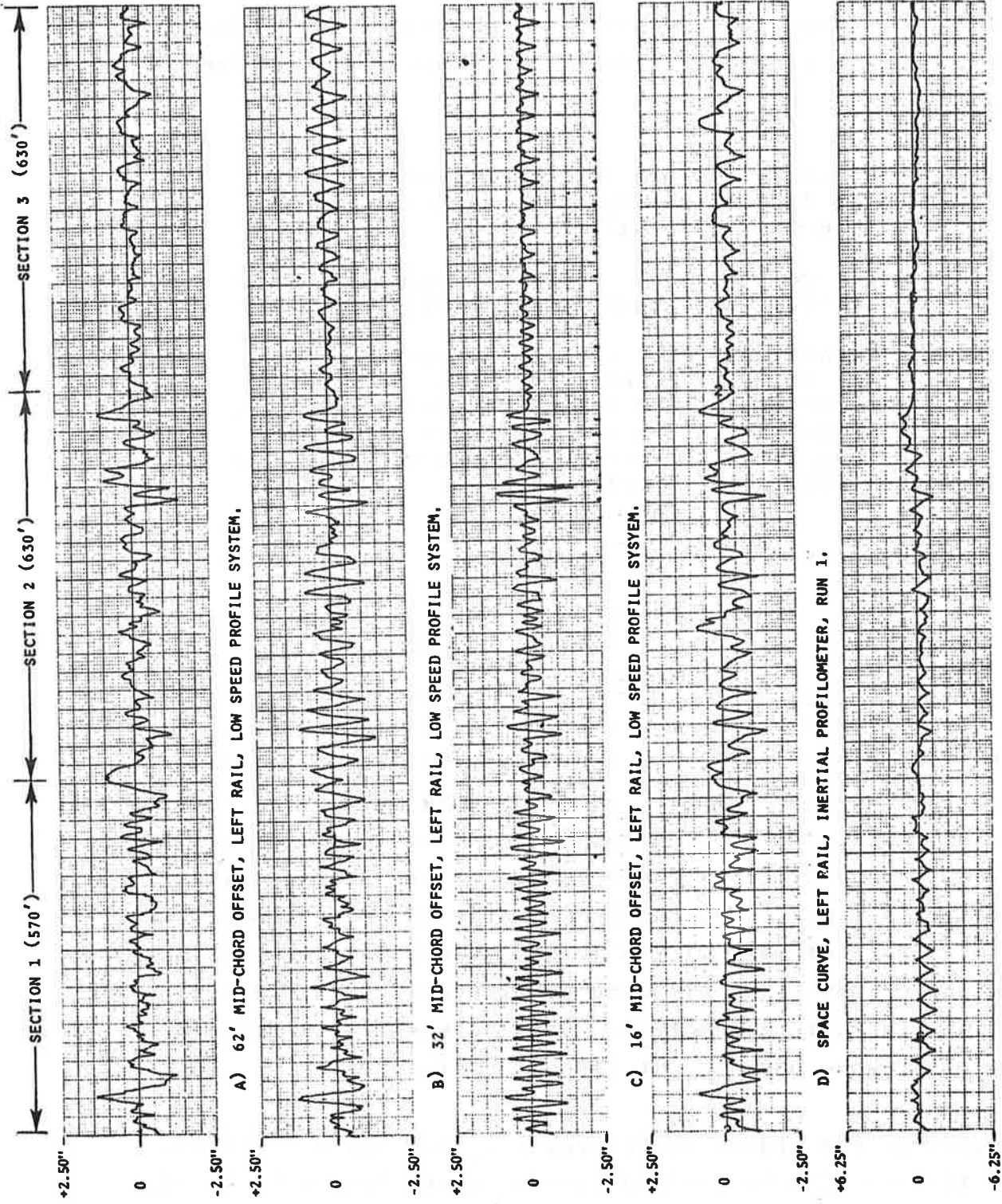
- Figure B-5 shows low speed profile (LSP) chords and inertially derived space curve from the left rail.
- Figure B-6 shows LSP chords and vertically derived space curve for the right rail.
- Figure B-7 shows inertially derived chords for right rail for comparison with LSP chords in Figure B-6. Also left and right space curves are included from runs other than shown in Figures B-5 and B-6 to demonstrate repeatability.

The data was taken from runs at speeds of 9 mph or less.

#### B.3.2.1 Description of the Special Test Section

The track whose geometry is displayed in Figures B-5 through B-7, is representative of a section of 33' rail which has a high level of joint related activity with little SRP evident. It is replete with examples of crushed rail heads, loose and missing bolts, crushed and rotten ties, rail end batter (not evident in the traces), fouled ballast, etc. At one joint a horizontal split head had broken away and 5" of rail head was missing. At many of the joints, two bolts were missing from one of the rails allowing considerable vertical weakness and longitudinal rail motion. Gaps between rails ends as long as 4" were observed at these locations.

A glance at the traces in Figures B-5, B-6 and B-7 reveals that the zone can be divided into 3 subsections with fairly uniform characteristics:



AMPLITUDE, IN

FIGURE B-5. COMPARATIVE PROFILE REPRESENTATIONS FOR LEFT RAIL IN SPECIAL TEST SECTION

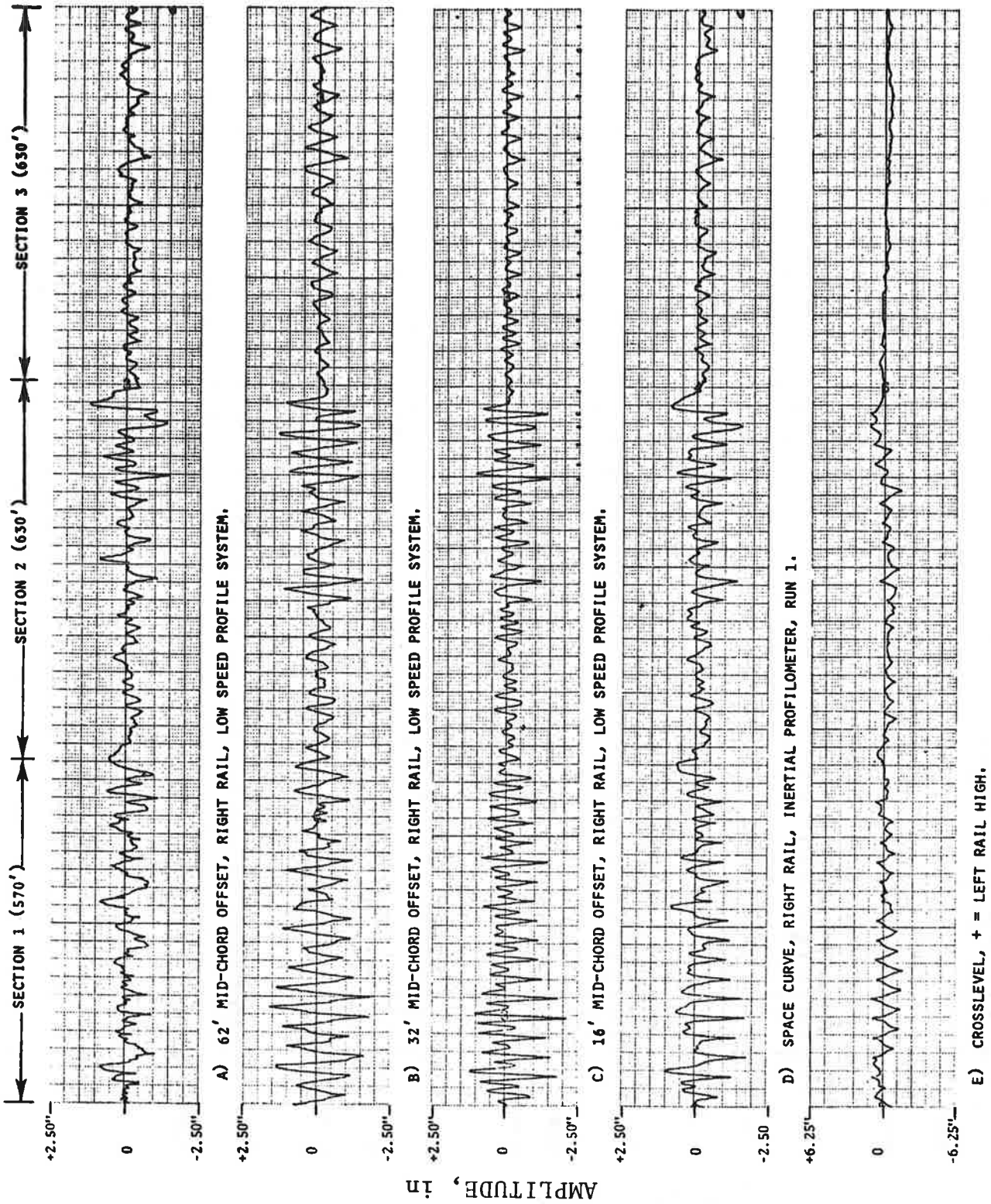
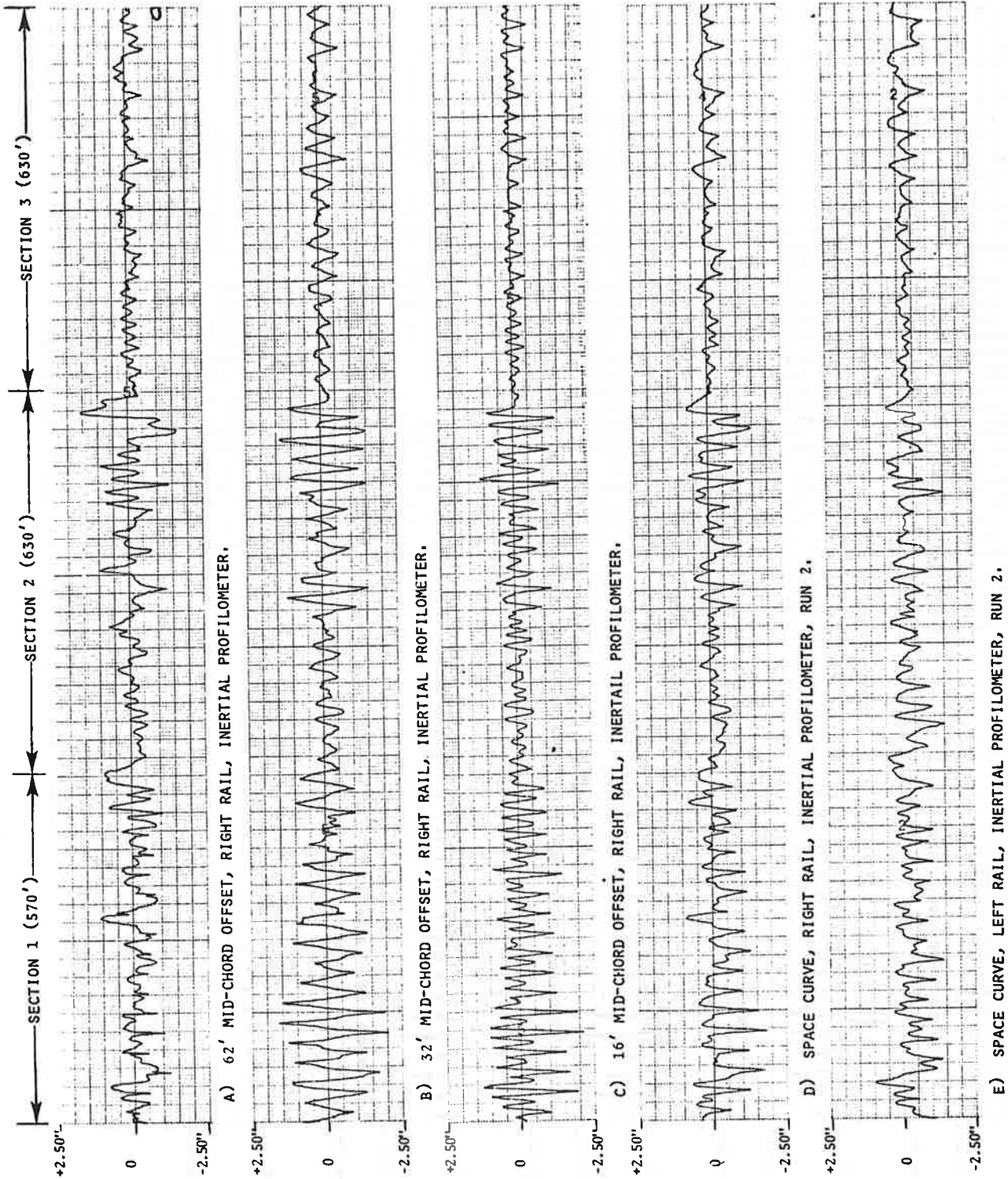


FIGURE B-6. COMPARATIVE PROFILE REPRESENTATIONS FOR RIGHT RAIL IN SPECIAL TEST SECTION



AMPLITUDE, in

FIGURE B-7. ALL INERTIAL REPRESENTATION OF PROFILE IN SPECIAL TEST SECTION

- Section 1 has a 50% stagger of joints;
- Section 2 has a 25% stagger of joints; and
- Section 3 has a 0% stagger.

Rail length throughout the zone is typically 33 ft. long. Section 1 and 2 are 100 lb. rail, section 3 is 132 lb rail in panel track sections. Section 3 is an area where work was begun to rehabilitate the entire zone.

#### B.3.2.2 Test Section Measurements

Surface Measurements over the zone included

- Profile space curve
- 62' MCO (nearly 2 rail lengths)
- 32' MCO (nearly 1 rail length)
- 16' MCO (nearly  $\frac{1}{2}$  rail length)
- Crosslevel

Table B-2 summarizes some observable features and the relative sensitivity of each surface measurement to these features. Note that 62' (2 rail-length) chord is almost totally insensitive to the PDP.

As mentioned earlier, the primary characteristic of a low joint is its depth below the mean profile of a rail. Space curve, the half rail MCO and the full rail MCO provide such estimates. A regression analysis was performed to determine which of these representations would provide the best information on the location and amplitude of a joint. Preliminary findings indicate that:

- The space curve is the most unequivocal indication that a joint is present. The 16 ft. MCO is a good second choice if there are only occasional broken rails to interrupt the joint cadence.

TABLE B-2. SENSITIVITY OF CHORD TO VARIOUS SURFACE FEATURES

	<u>62'</u> <u>MCO</u>	<u>32'</u> <u>MCO</u>	<u>16'</u> <u>MCO</u>	<u>SPACE</u> <u>CURVE</u>	<u>CROSS-</u> <u>LEVEL</u>
Sensitivity to:					
Low Joints Sec. 1	N	V/Q	V	V	V
Low Joints Sec. 2	N	V/Q	V	V	M
Low Joints Sec. 3	M	V/Q	V	V	N
Sec. 1-2 Transition	M	V	V	V	V
Sec. 2-3 Transition	V	V	V	V	V
Difference Between L&R Rail Sec. 1	N	V	V	V	N/A
General Random Behavior	V	M	M	V	V

V Very Sensitive  
M Marginally Sensitive  
N Not Very Sensitive  
V/Q Very Sensitive (But in a Way Requiring Careful Interpretation)



- Regressions of peak values found at joints reveal that the 16-ft. MCO and the 32-ft. MCO give almost identical indications of joint amplitude, particularly when there are no short or broken rails: And
- If an envelope is drawn through the maxima of the space curve values and if the envelope is then used as a reference line for evaluating joint amplitudes, these results are in excellent agreement with the 16-ft. MCO and the 32-ft. MCO.

#### B.4 GEOMETRY OF WELDS IN CWR

The introduction of CWR was supposed to eliminate the problems associated with bolted joints. It was to approach the ideal in track geometry - one in which only the SRP and anomalies would continue to play a role. Accordingly, one of the big surprises was the appearance of a strong component at 39-foot and harmonic intervals when CWR profiles were processed for PSD's. At first this was ascribed totally to a phenomenon called ballast memory - a weakness in the ballast and subgrade at the site of joints before the bolted rail was removed. Subsequent observations revealed that ballast memory is not the only source of a periodic component.

- The 39-foot wavelength appears in new construction where the CWR is composed of 39-foot rail.
- When 39-foot CWR is installed where 33-foot bolted rail was removed, both wavelengths appear in the PSD's.

Thus, where 39-foot CWR has replaced 39-foot bolted rail, the periodic component may be a resultant of two independent processes, ballast memory and a new component from the CWR itself.

The development of a space curve technology revealed the new source for the 39-foot component. Profile traces of a typical section of CWR were chosen at random. A characteristic upward cusp frequently occurred at 1/4-inch intervals on the plots. This is equal to a 39-foot interval on the track. Two such plots are shown in Figure B-8.

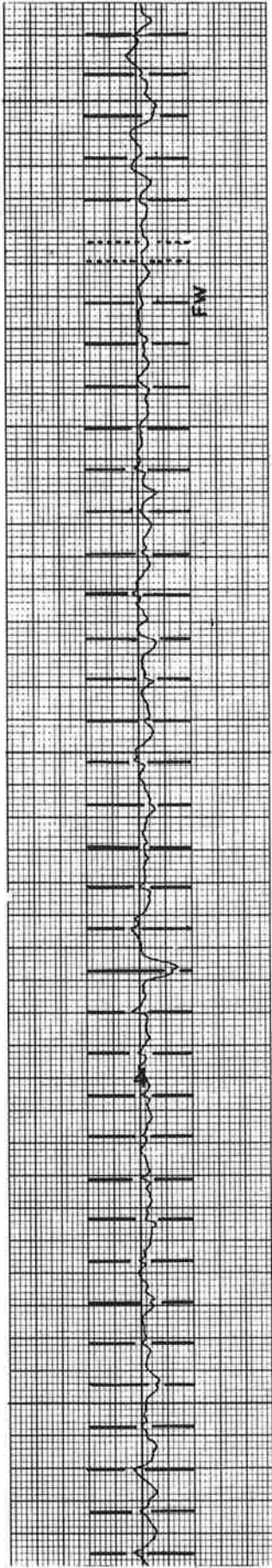
In Figure B-8, the locations of welded joints are indicated by solid vertical lines. An "FW" indicates a field weld where two long strings of CWR are joined. Near the FW on the right rail, two dotted lines appear. A short rail had been installed somewhere between the shop welds (solid lines) on either side. The data did not reveal these weld locations, and they were established by a subsequent site visit.

Additional features are evident in Figure B-8. There are many characteristic turns and cusplings that occur over the rail length, often at specific locations in the rail. Two possible causes for these features are:

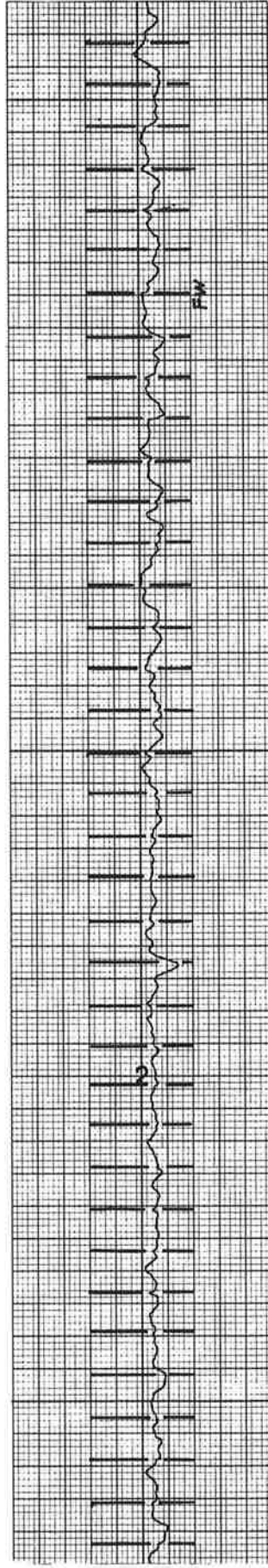
- They are caused by rail straightening operations by the manufacturer; or
- They are caused by rail head grinding in surfacing operations.

The cause of specific features in the plots may be determined by examining rail head wear data.

It should be pointed out that the section of track represented by Figure B-8 is not in any way unusual. Similar weld signatures may be seen in the CWR traces in Appendix C.



RIGHT PROFILE SPACE CURVE,  $\pm 2.5''$  FULL SCALE



LEFT PROFILE SPACE CURVE,  $\pm 2.5''$  FULL SCALE

FIGURE B-8. PROFILES OF CWR



## APPENDIX C

### CHARACTERIZATION OF ANOMALIES

#### C.1. INTRODUCTION

The effort to characterize anomalies was greatly enhanced by the development of a phase distortionless space curve algorithm for processing T-6 profilometer data. This represents a substantial advance over other profile algorithms since:

- Previous space curves from profilometers were not free of phase distortion. They gave different responses to the same profiles that depended on speed and direction:
- Chordal representations of anomalies, while freer of the phase distortion problem, confuse the perception of complex anomalies because of their wavelength discriminating characteristics. (See Figures B-5 through B-7 of Appendix B.)

The space curve and chordal data from T-6 profilometer are free of the phase distortion problems. Above a minimum speed, wave shapes remain constant regardless of the direction or speed of the car. *All space curves used in this section are scaled as shown in TABLE C-1.*

TABLE C-1. SCALING FACTOR FOR GRAPHICAL GEOMETRY DATA

	Minor Division	Intermediate Division	Major Division or Full Scale
Profile	0.10"	0.50"	2.50"
Crosslevel	0.25"	1.25"	6.25"
Longitudinal Distance	6'	30'	600'

## C.2 TURNOUTS

The turnout deserves special attention because of its prevalence, and because of its weakness as a track structure. Quite frequently, it also presents drainage problems. Three turnout scenarios have been identified and these are described below.

### C.2.1 MAIN LINE TURNOUTS TO SIDE TRACKS

Eleven turnouts are included in the geometry processed through the space curve algorithm. Rail profiles and cross-levels at these turnouts are shown in Figures C-1, C-2 and C-3. All are Number 10 turnouts\* with spring frogs. These are located in CWR track and the main line stock rail is usually uninterrupted by bolted joints.

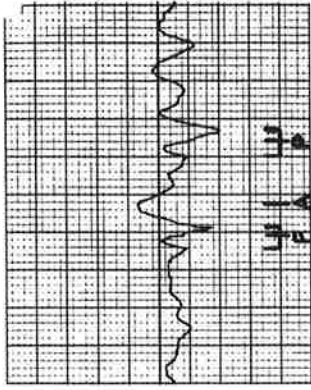
Principal features of these turnouts in Figures C-1, C-2 and C-3 are indicated as follows:

- A trident-shaped symbol above a "P" indicates point features. The center marker indicates the location where the wheel tread transfers from/to the stock rail to/from the split switch. This is usually accompanied by a mild downward cusp riding on the profile. The outside marker locates the joint connecting the divergent stock rail to main line CWR. The inside marker locates the split switch heel joint to the closure rail. For #10 turnouts, 16'-6" split switches are used.
- A single marker above an "A" indicates where the divergent closure rail is at the center of the track. This corresponds to the location of maximum automatic location detector output.
- A trident shaped symbol above an "F" indicates frog features. The center marker locates the point of the frog. The inside marker locates the toe joint connection to the closure rail. The outside marker locates the heel joint connection to CWR.

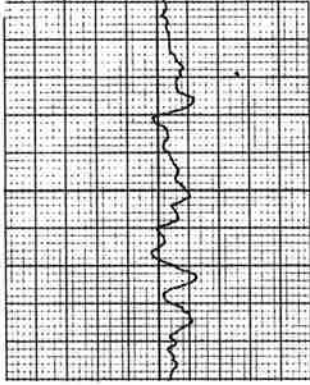
---

\*Frog angle =  $2 \tan^{-1}(1/2N)$ , N = Frog or turnout number.

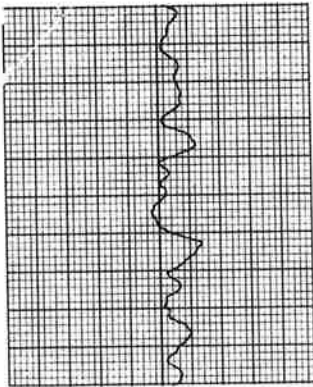
TURNOUT #4



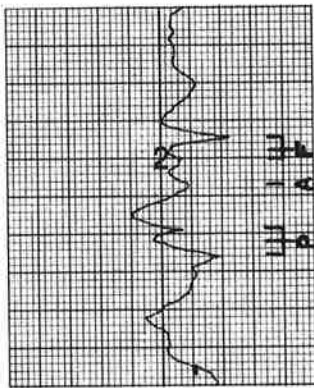
TURNOUT #3



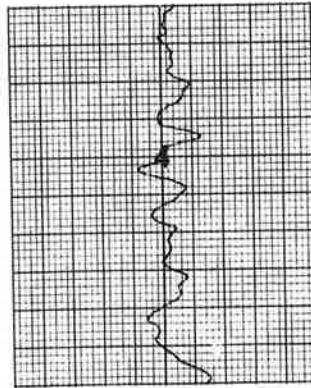
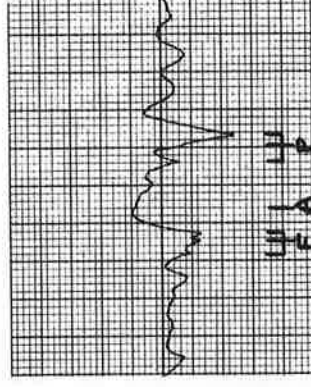
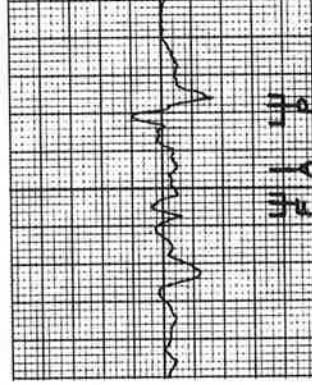
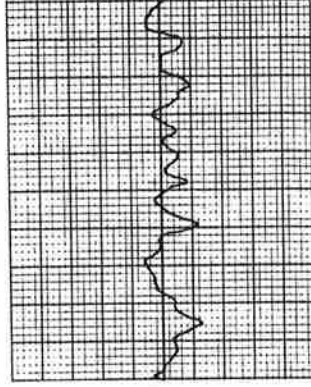
TURNOUT #2



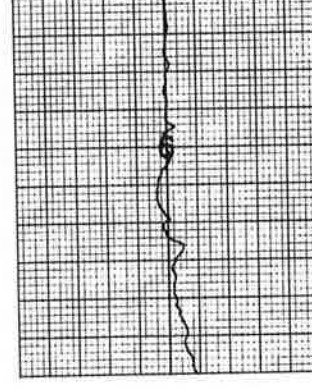
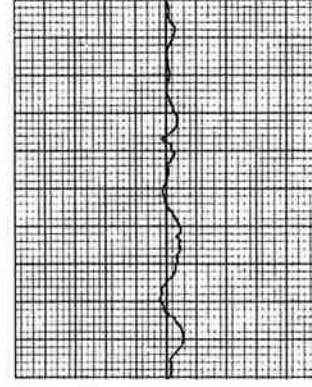
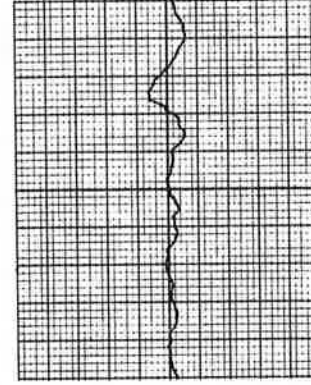
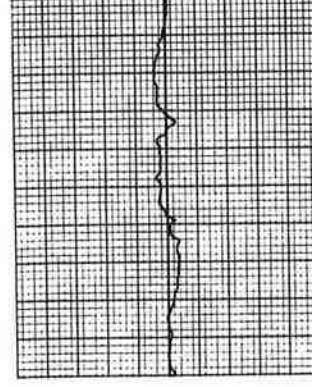
TURNOUT #1



LEFT PROFILE SPACE CURVE, ±2.5" FULL SCALE



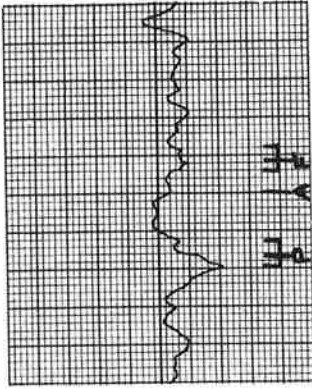
RIGHT PROFILE SPACE CURVE, ±2.5" FULL SCALE



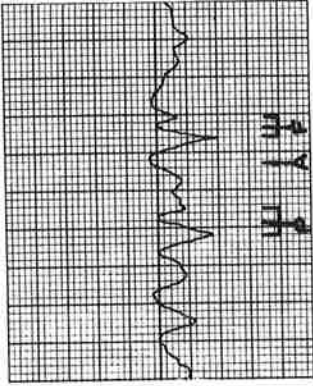
CROSSLEVEL, ±6.25" FULL SCALE

FIGURE C-1. SURFACE GEOMETRY OF NUMBER 10 SPRING FROG TURNOUTS AS SEEN FROM MAIN LINE, LEADING AND TRAILING POINT APPROACH

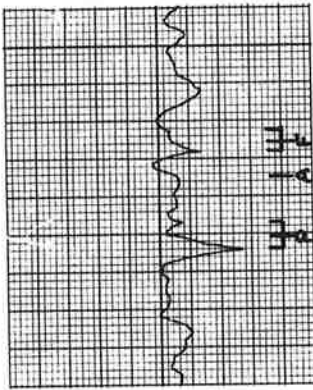
TURNOUT #8



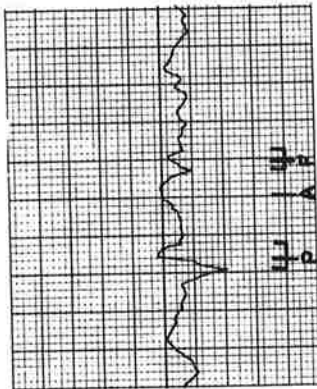
TURNOUT #7



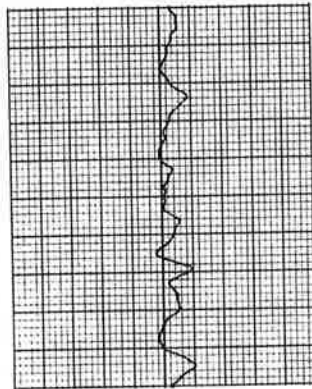
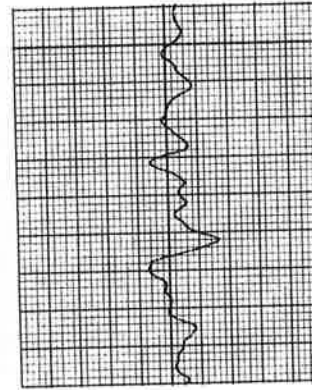
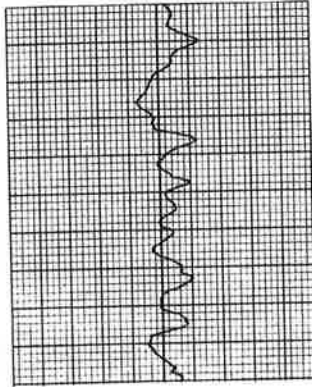
TURNOUT #6



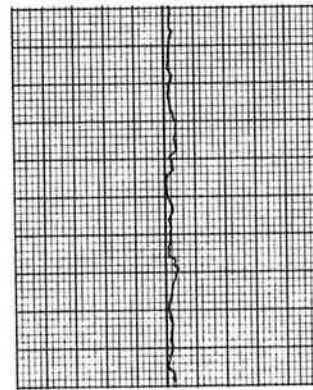
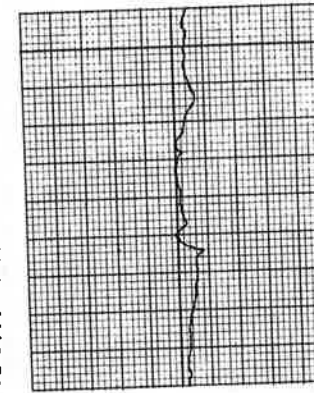
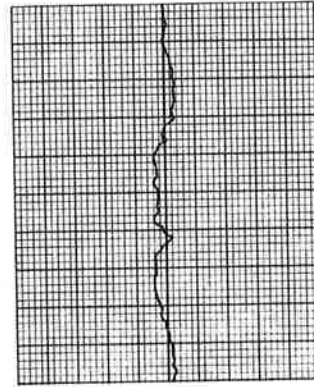
TURNOUT #5



LEFT PROFILE SPACE CURVE,  $\pm 2.5''$  FULL SCALE



RIGHT PROFILE SPACE CURVE,  $\pm 2.5''$  FULL SCALE



CROSSLEVEL,  $\pm 6.25''$  FULL SCALE

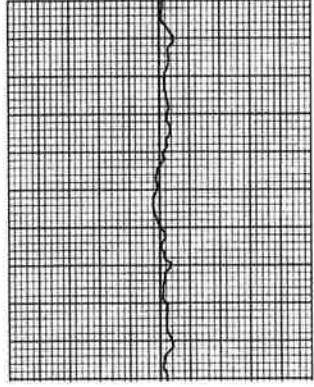


FIGURE C-2. SURFACE GEOMETRY OF NUMBER 10 SPRING FROG TURNOUTS AS SEEN FROM MAIN LINE, LEADING POINT APPROACH



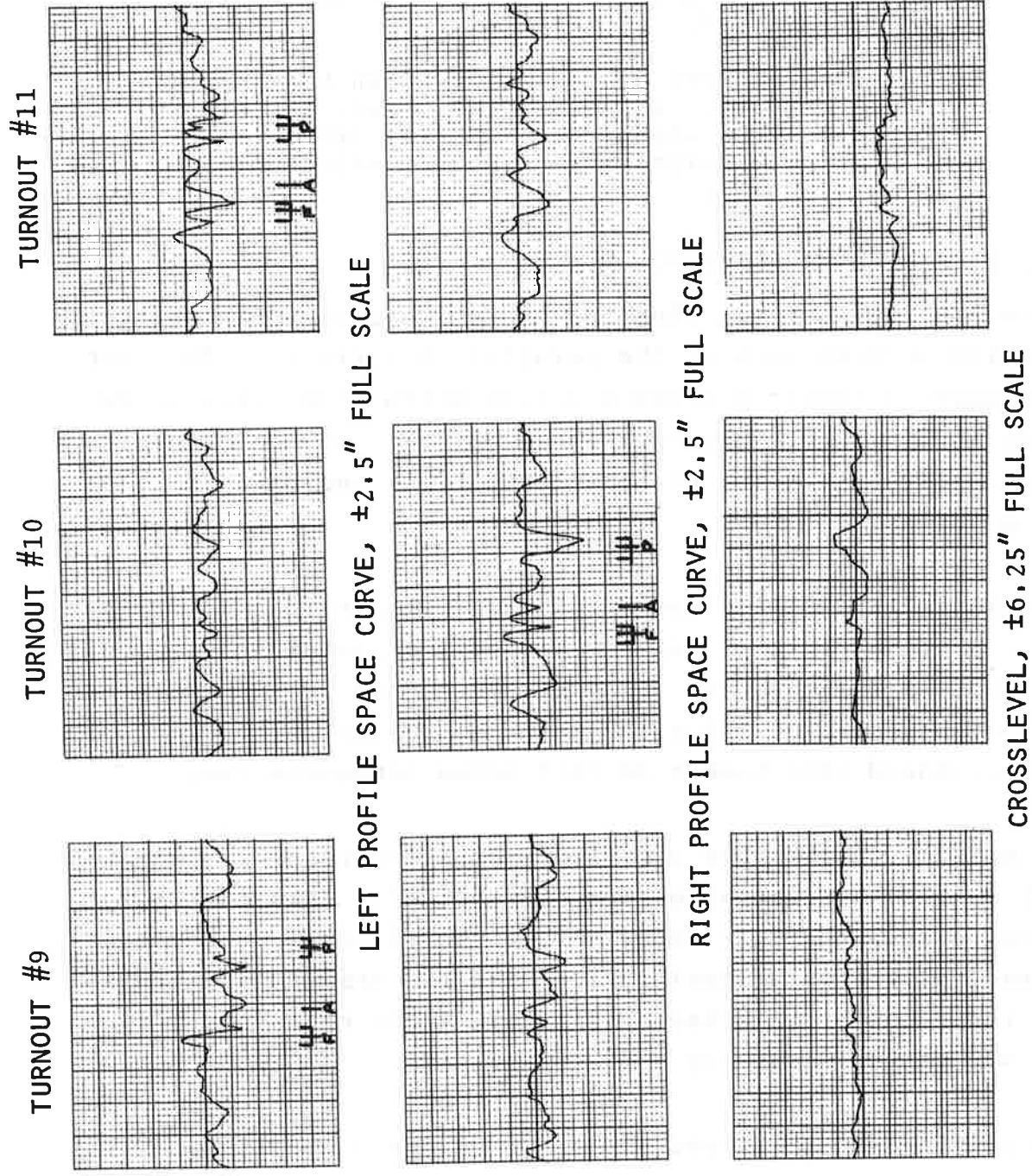


FIGURE C-3. SURFACE GEOMETRY OF NUMBER 10 SPRING FROG TURNOUTS AS SEEN FROM MAIN LINE, TRAILING POINT APPROACH

A survey of the figures reveals that:

- A weak spot on one rail promotes a low spot on the other, even though there is no joint on the latter\*.
- Most features of the turnout can be represented as an assemblage of joints suitably positioned along the track and otherwise properly correlated and/or coordinated with one another.

### C.2.2 MAIN LINE INTERLOCKINGS

Interlockings on main line track provide crossover interconnection between each of the parallel main tracks. They are intended to impose a minimum deceleration from track speed when track changes are required. For this reason, they are typically constructed of heavy components and have small frog angles.

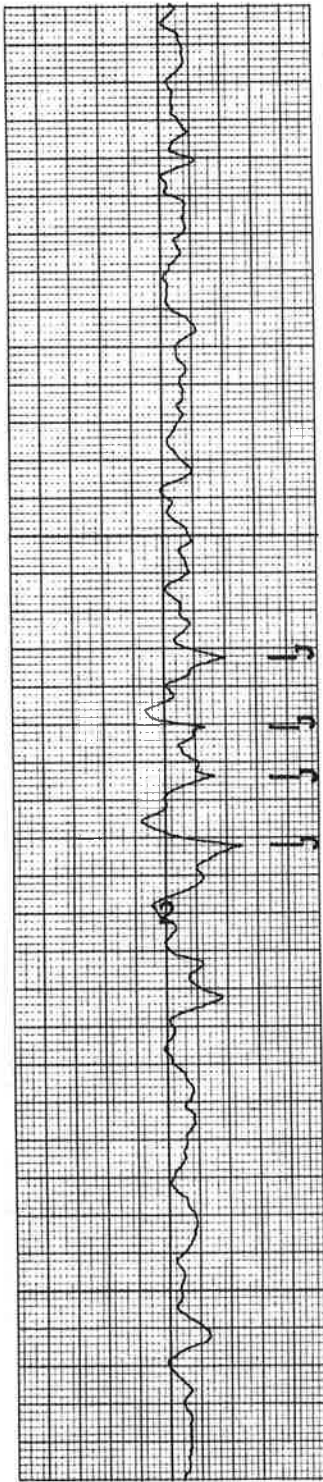
Interlocking profiles are displayed in Figures C-4 through C-7. Titles of these figures are self-explanatory. In all cases, the interlocking turnouts are Number 20 incorporating a 39-foot split switch with graduated risers. The frog is the standard AREA Number 20 rail-bound manganese frog.

Principal features are indicated as in Figures C-1, C-2 and C-3 with an additional marker over an "F". This marker locates a cusp that may occur at the transition from the manganese insert to the heel rail. Also the presence of joints is indicated by a marker over a "J", grade crossings by a GX, and bridges by a BR.

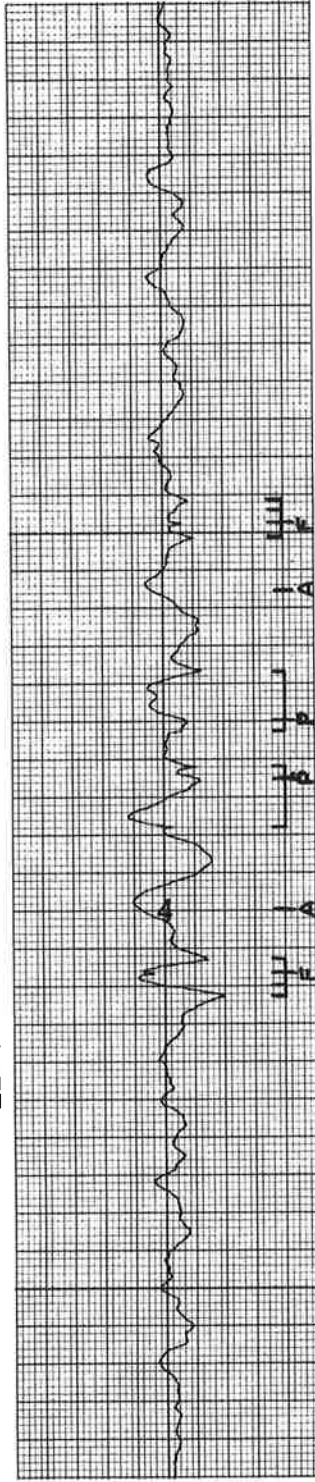
Surprising as it may seem, there are a pair of joints in the tangent stock rail of most of the interlocking turnouts that

---

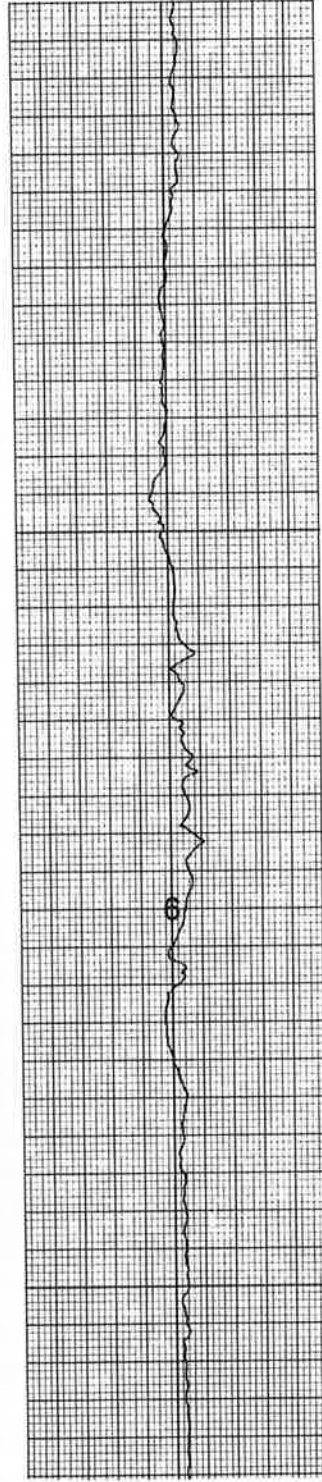
\*As pointed out in Appendix B, this is a general phenomenon. A loose or highly depressed joint invariably couples through to the opposite rail to produce a depression at that location.



LEFT PROFILE SPACE CURVE,  $\pm 2.5''$  FULL SCALE

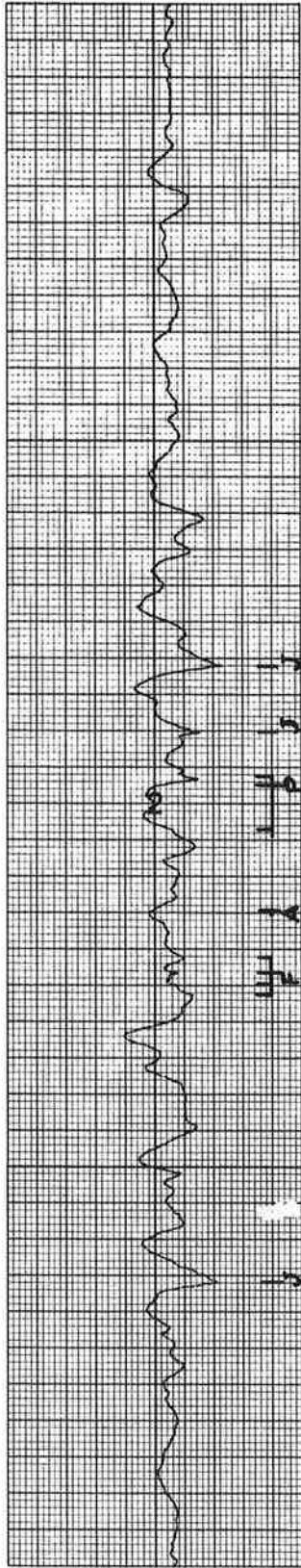


RIGHT PROFILE SPACE CURVE,  $\pm 2.5''$  FULL SCALE

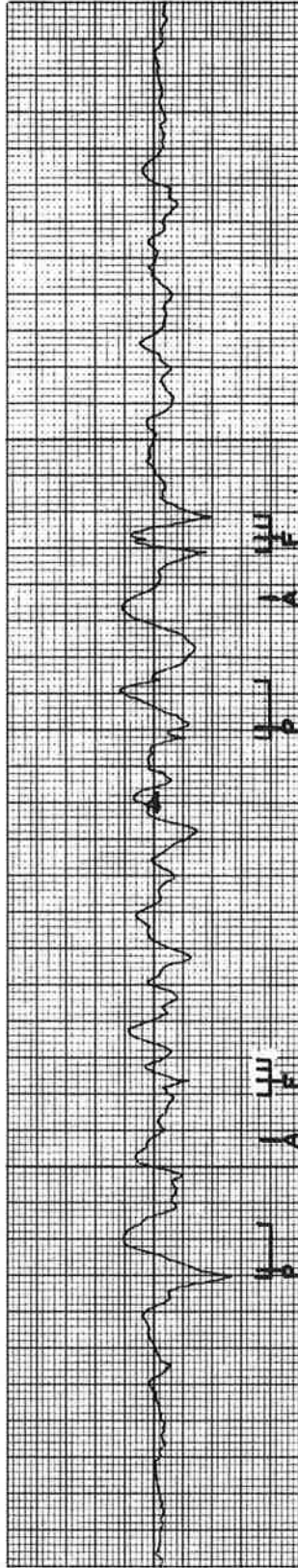


CROSSLEVEL,  $\pm 6.25''$  FULL SCALE

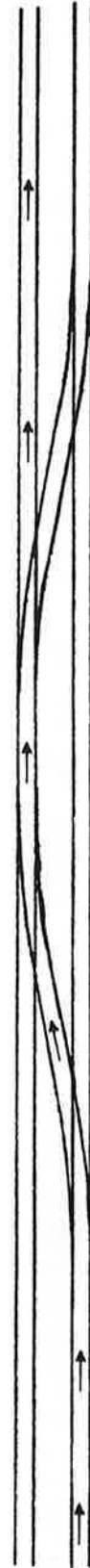
FIGURE C-4. INTERLOCKING NUMBER 1, NEGOTIATED WITHOUT TRACK CHANGE



LEFT PROFILE SPACE CURVE,  $\pm 2.5''$  FULL SCALE

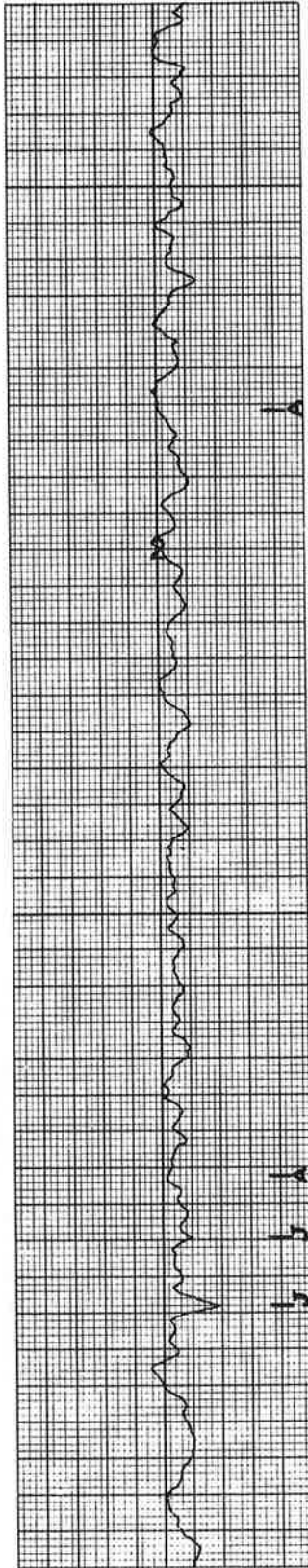


RIGHT PROFILE SPACE CURVE,  $\pm 2.5''$  FULL SCALE

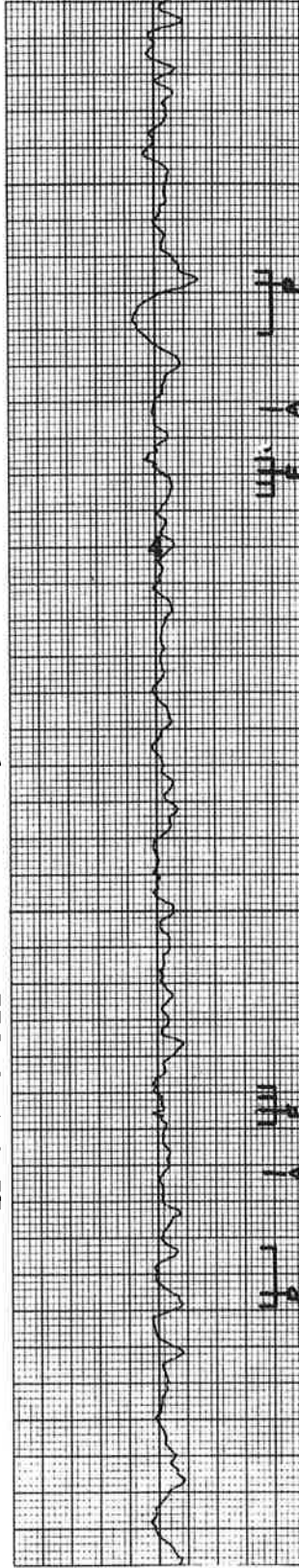


TRACK PLAN IN AREA

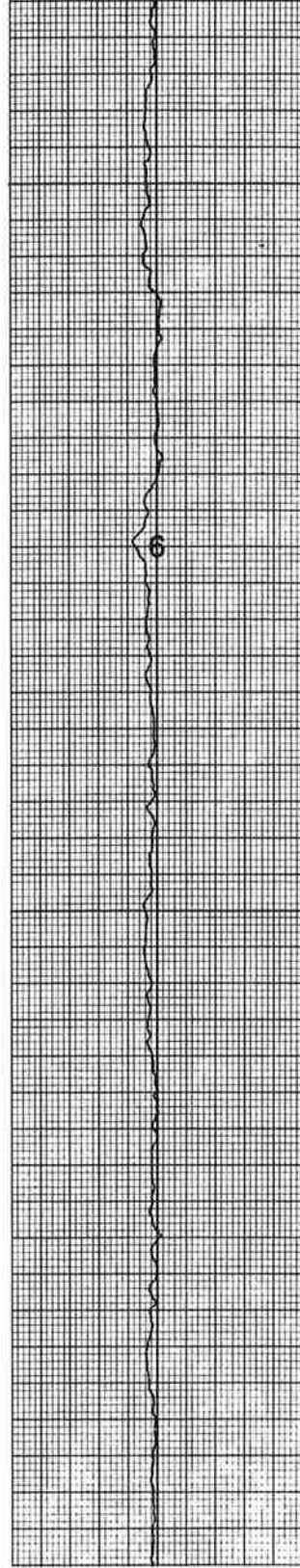
FIGURE C-5. INTERLOCKING NUMBER 1, NEGOTIATED IN OPPOSITE DIRECTION AND WITH TRACK CHANGE



LEFT PROFILE SPACE CURVE,  $\pm 2.5''$  FULL SCALE



RIGHT PROFILE SPACE CURVE,  $\pm 2.5''$  FULL SCALE



CROSSLEVEL,  $\pm 6.25''$  FULL SCALE

FIGURE C-6. INTERLOCKING NUMBER 2, NEGOTIATED WITHOUT TRACK CHANGE, TURNOUT AT RIGHT IS NEWLY INSTALLED

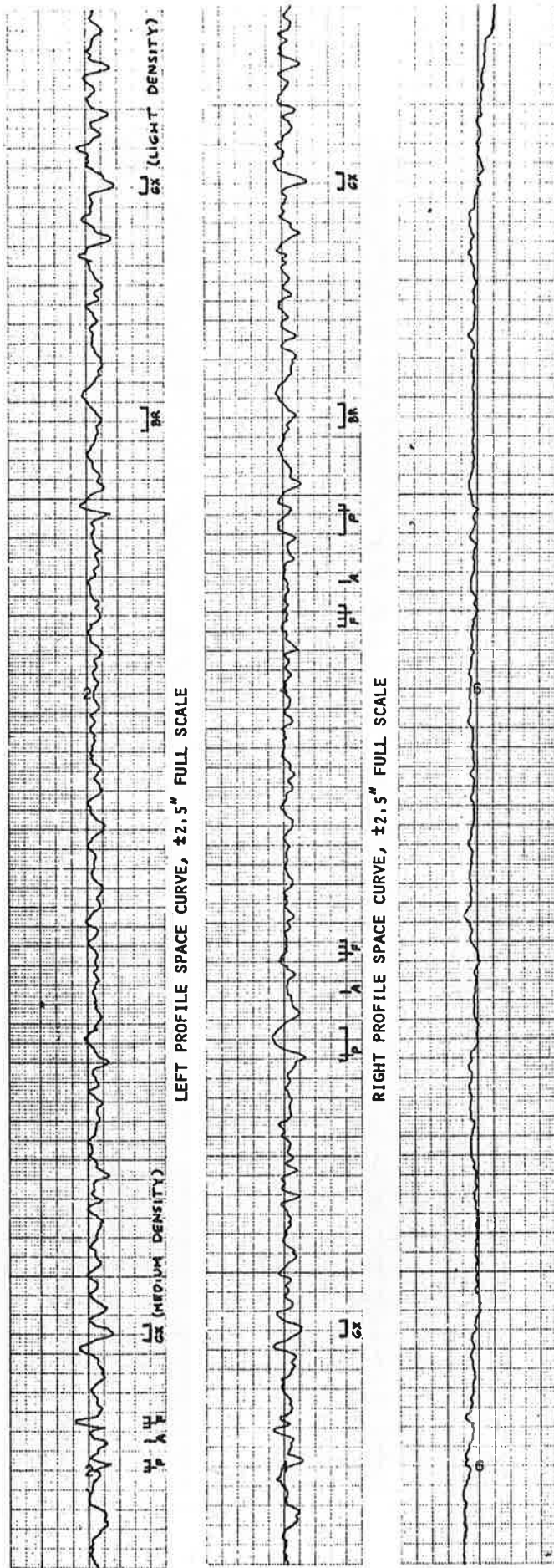


FIGURE C-7. INTERLOCKING NUMBER 2, NEGOTIATED IN OPPOSITE DIRECTION, WITHOUT TRACK CHANGE, AND SHOWING ANOMALOUS DETAILS IN THE SURROUNDINGS

were examined. The reason for this is that trains enter from the curved leg at high speed. This inflicts considerable lateral forces and causes rapid degradation on the tangent stock rail. When changeout is necessary, the replacement rail is bolted rather than welded in place. The replacement stock rail is 1-1/2 rail lengths. This allows free split switch movement. Another method to allow switch movement is to install regular 39-foot rail lengths with specially ground joint bars.

### C.2.3 TOWER LOCATIONS

Tower and yard approaches have very complex assemblages of turnouts. They facilitate interlocking, branching, siding, train sorting, and car storage in a relatively compact area. Examples of these are shown in Figures C-8, C-9 and C-10. As is evident in these figures, a wide range of conditions of track degradation can be expected.

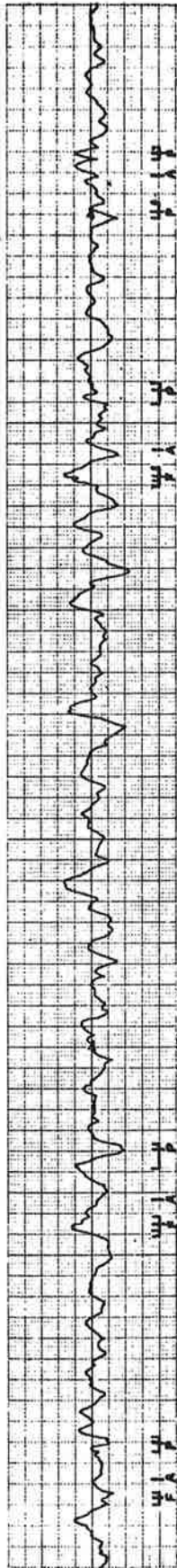
### C.3 BRIDGE STRUCTURES

Next to turnouts, bridge structures present some of the most difficult problems in the control of track geometry. The primary difficulties occur at the embankment to bridge transitions. Both settling of bridge abutments and changes in the track support stiffness may contribute to the problems. Examples of rail profiles at bridges are shown in Figure C-11.

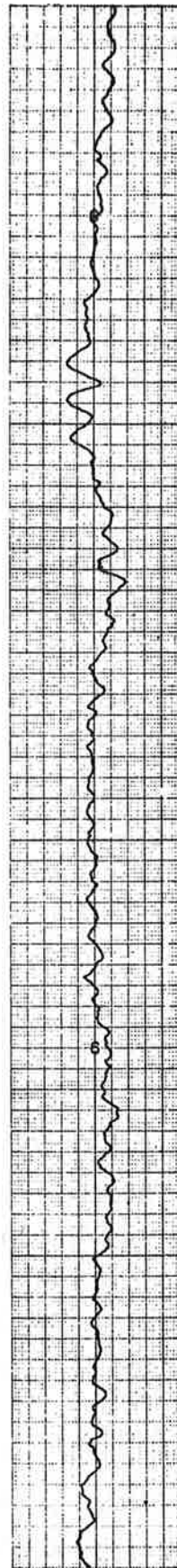
In longer bridges, the design of the bridge itself may contribute to geometry deviations. The profiles in Figure C-12 show an upward cusp every 90 feet. A subsequent visit to the bridge site revealed that it was a multiple span deck girder supported by piers on 90-foot centers.



LEFT PROFILE SPACE CURVE,  $\pm 2.5''$  FULL SCALE



RIGHT PROFILE SPACE CURVE,  $\pm 2.5''$  FULL SCALE



CROSSLLEVEL,  $\pm 6.25''$  FULL SCALE

FIGURE C-8. TOWER LOCATION NEGOTIATED WITHOUT TRACK CHANGE



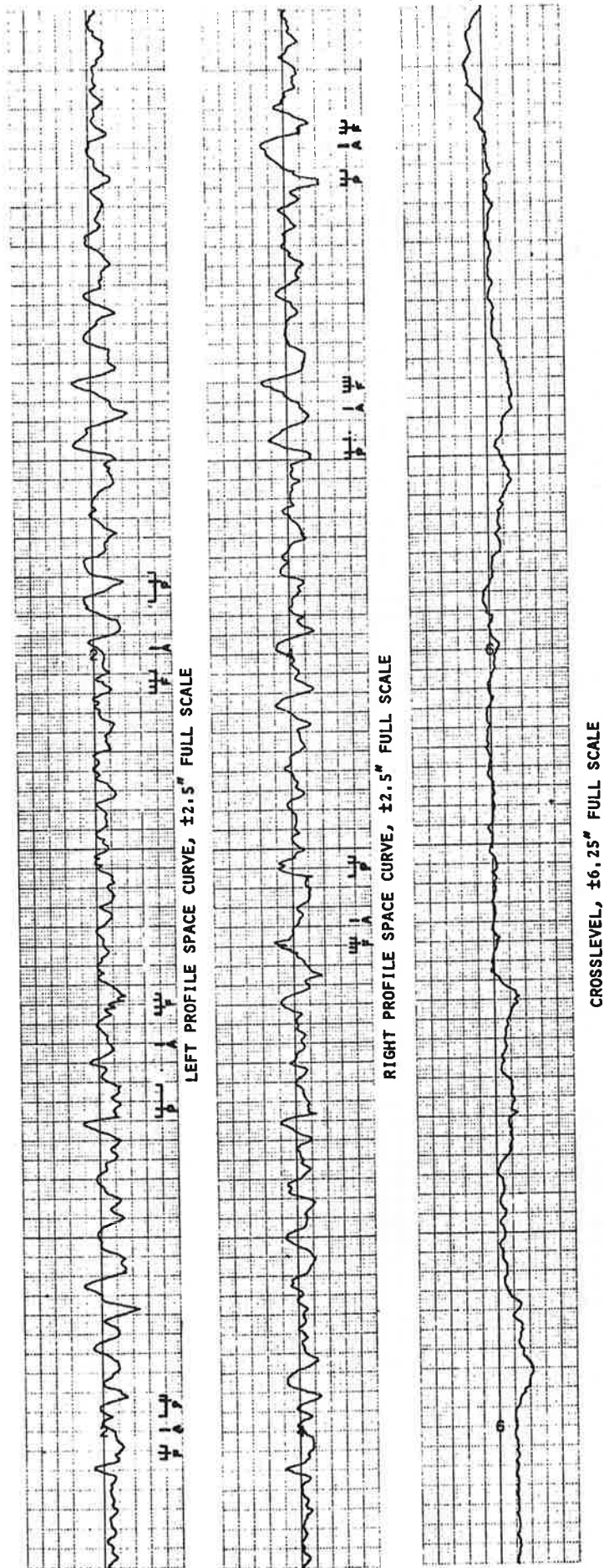


FIGURE C-9. TOWER LOCATION NEGOTIATED IN OPPOSITE DIRECTION AND WITH TRACK CHANGE

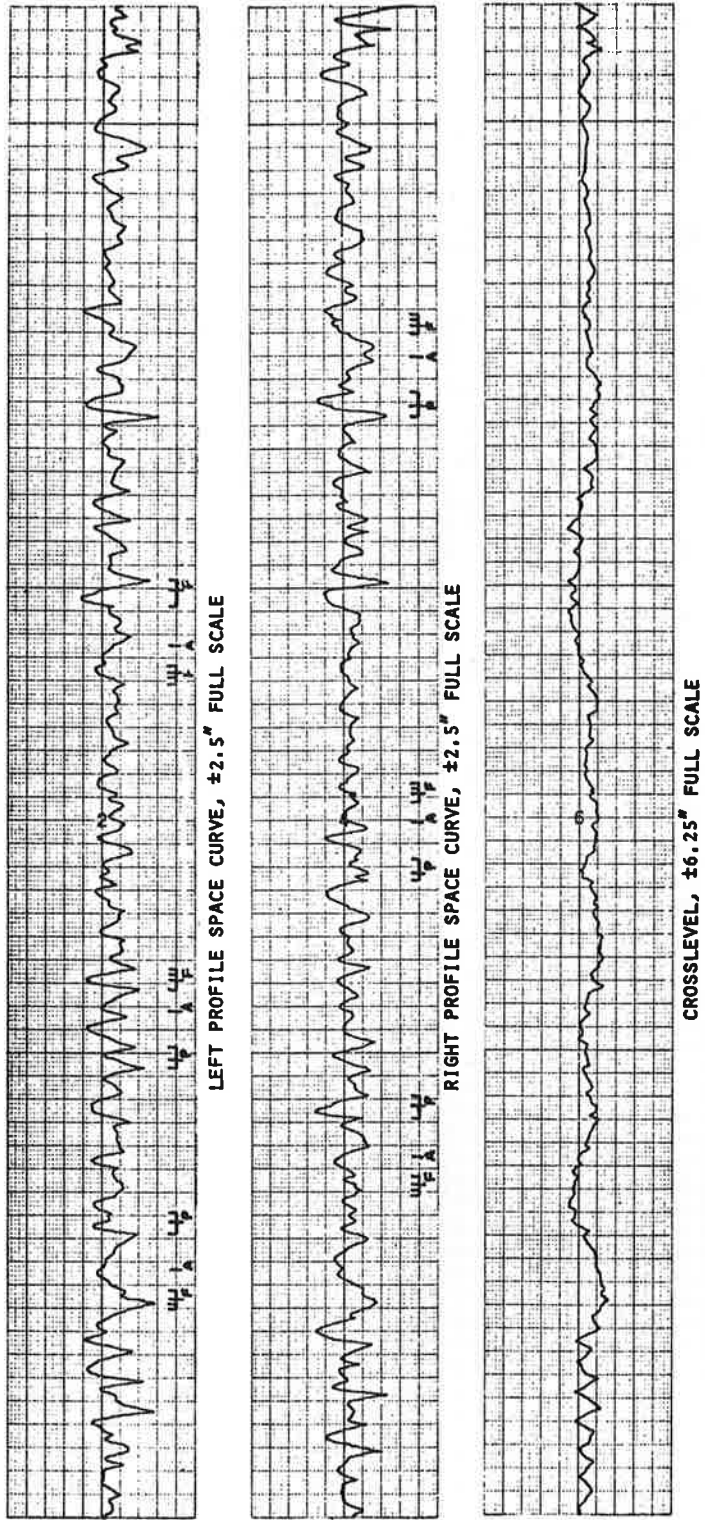
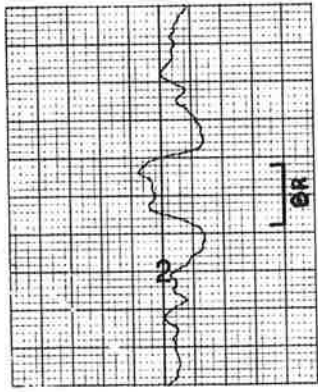
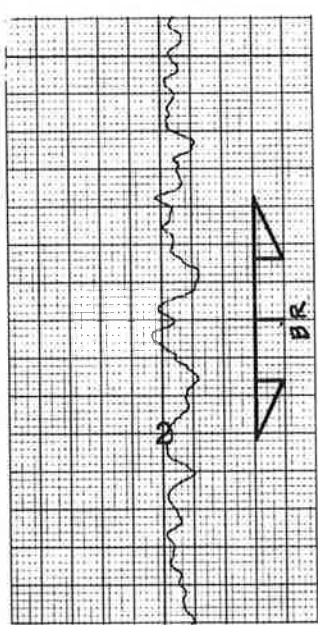


FIGURE C-10. SERIES OF TURNOUTS AT YARD APPROACH

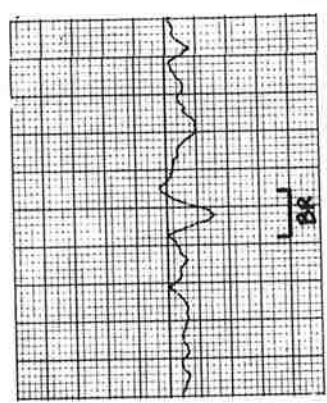
BRIDGE #3



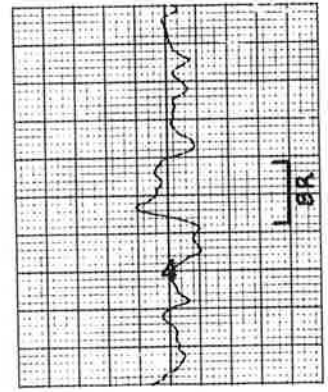
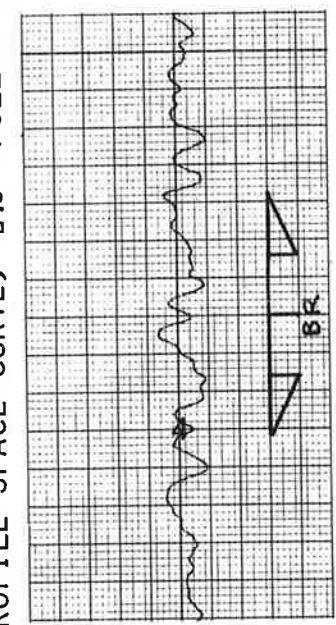
BRIDGE #2



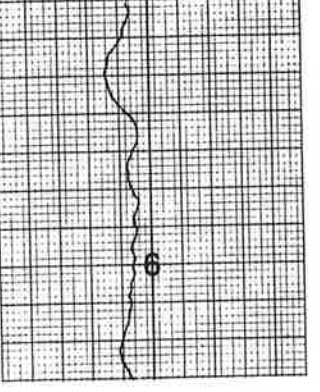
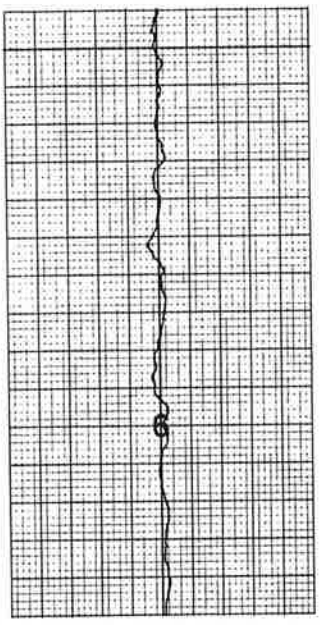
BRIDGE #1



LEFT PROFILE SPACE CURVE,  $\pm 2.5''$  FULL SCALE



RIGHT PROFILE SPACE CURVE,  $\pm 2.5''$  FULL SCALE



CROSSLEVEL,  $\pm 6.25''$  FULL SCALE

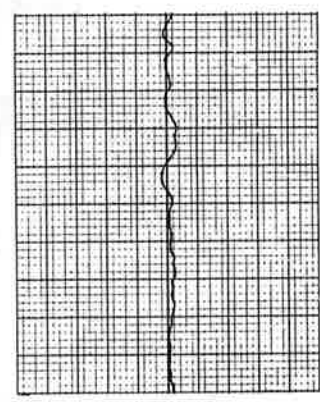
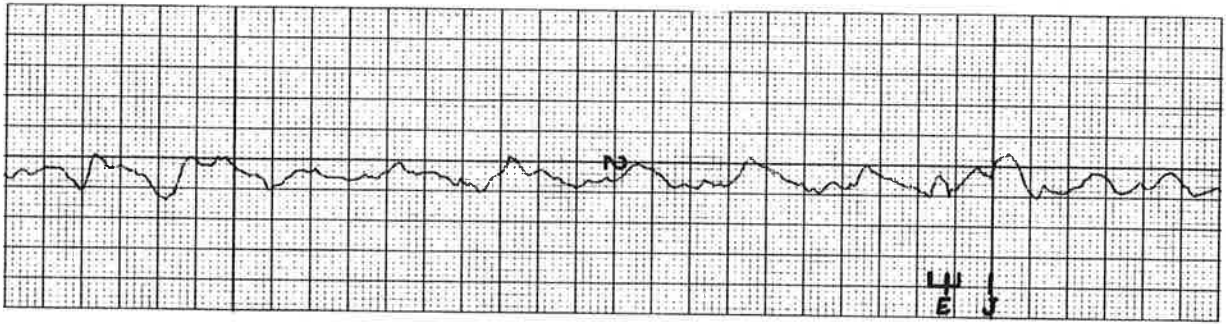
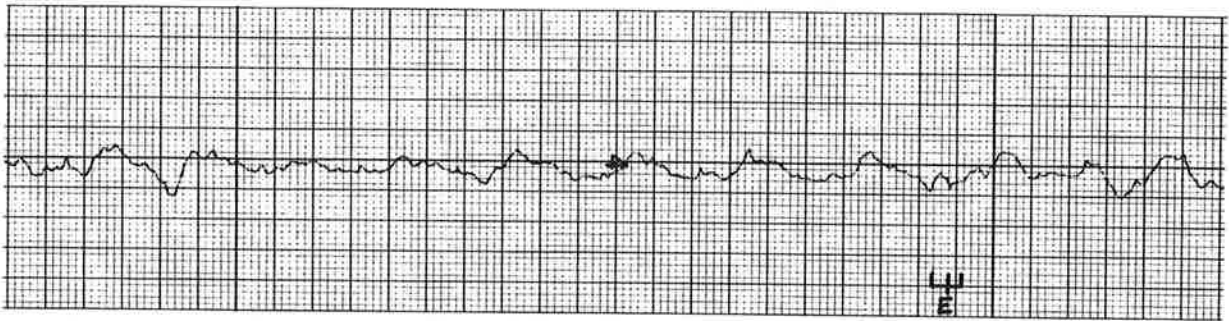


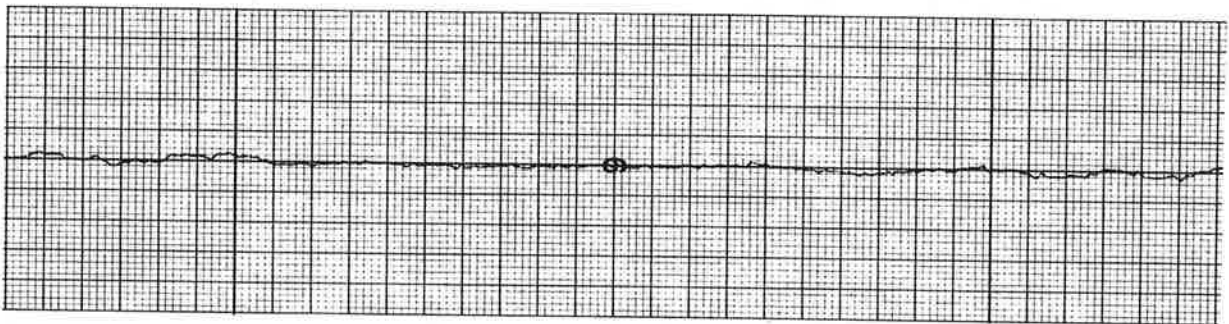
FIGURE C-11. ANOMALOUS GEOMETRY AT BRIDGES



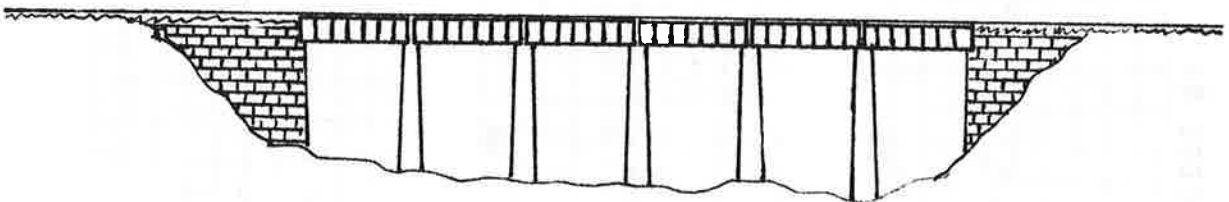
LEFT PROFILE SPACE CURVE,  $\pm 2.5''$  FULL SCALE



RIGHT PROFILE SPACE CURVE,  $\pm 2.5''$  FULL SCALE



CROSSLEVEL,  $\pm 6.25''$  FULL SCALE



SIDE VIEW MULTIPLE SPAN DECK GIRDER BRIDGE

FIGURE C-12. SURFACE GEOMETRY ON LONG TRESTLE

Another feature of long bridges, particularly in CWR territory, is a track fixture installed to allow thermal expansion. Such a fixture was used on the trestle shown in Figure C-12. Its location is indicated by a trident shaped marker over an "E". All of the bridge anomalies shown can be incorporated in a geometry simulator.

#### C.4. GRADE CROSSINGS

Because of the difficulty and inconvenience of maintenance, grade crossings present a combination of stiffness and geometry problems. Typically, these problems are exacerbated by poor drainage. A typical example is shown in the first set of tracings in Figure C-13. Some additional examples are shown in Figure C-7.

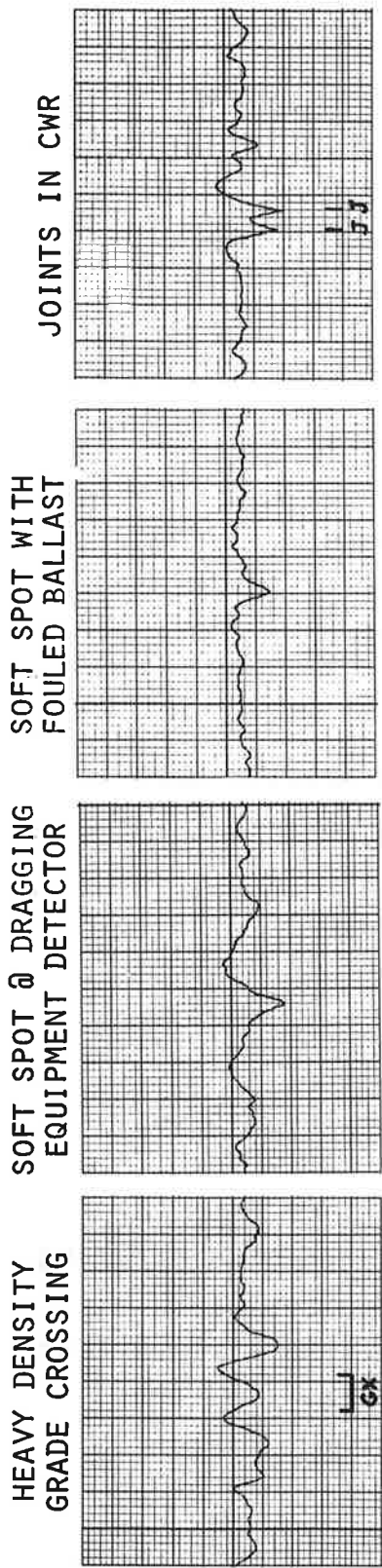
The grade crossings shown present an anomalous profile that is easily incorporated into a geometry simulator. However these examples represent a very limited sampling of two lane roads. Vehicular traffic densities do vary considerably as noted.

#### C.5. LOW SPOTS

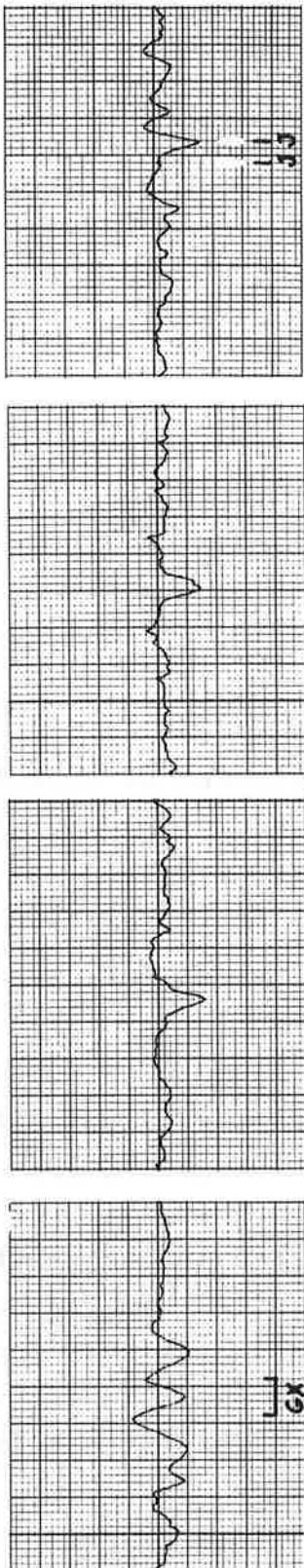
Isolated low spots develop because of some softness in the track support. Two examples are illustrated in the second and third set of tracings of Figure C-13.

The first of these was located in the neighborhood of a dragging equipment detector. Apparently tamping equipment could not insert sufficient ballast near this device. As a result the track sank into the void. A visit to the site revealed that this profile has assumed a permanent set in the rails.

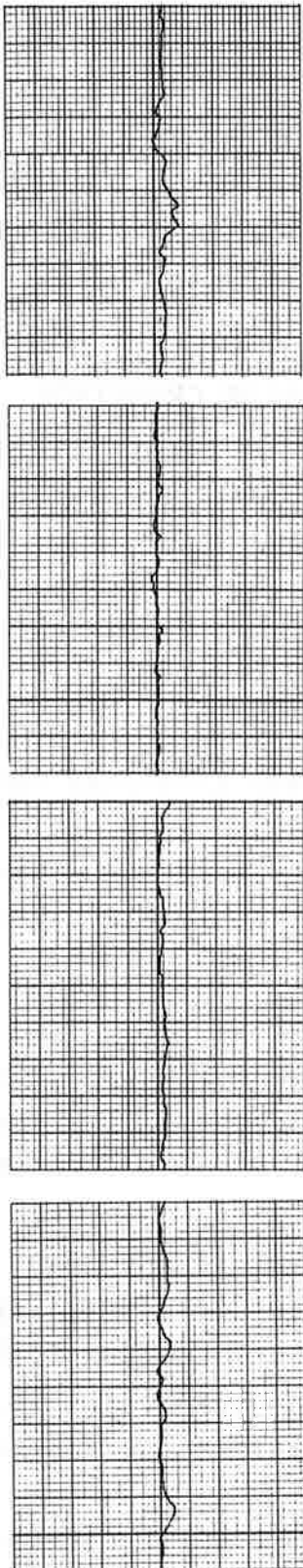
The cause of the second low spot was not immediately apparent. A visit to the site revealed that drainage in the area was quite



LEFT PROFILE SPACE CURVE,  $\pm 2.5''$  FULL SCALE



RIGHT PROFILE SPACE CURVE,  $\pm 2.5''$  FULL SCALE



CROSSLEVEL,  $\pm 6.25''$  FULL SCALE

FIGURE C-13. MISCELLANEOUS ANOMALOUS GEOMETRIES

good. Whatever the cause, considerable ballast fouling has taken place. It was also noted that the profile deformation has assumed a permanent set.

As is evident from the traces, the profile associated with the low spots shown is a relatively simple form that is readily simulated.

#### C.6. ISOLATED JOINTS IN CWR

Isolated joints were observed to occur frequently in CWR of some railroad properties. The practice on these is to join the 1400'+ strings of CWR using joint bars and a 39-foot buffer rail. A situation such as that shown in Figure C-14 results. Typically,  $A = 0.4$  to  $0.6$ ".

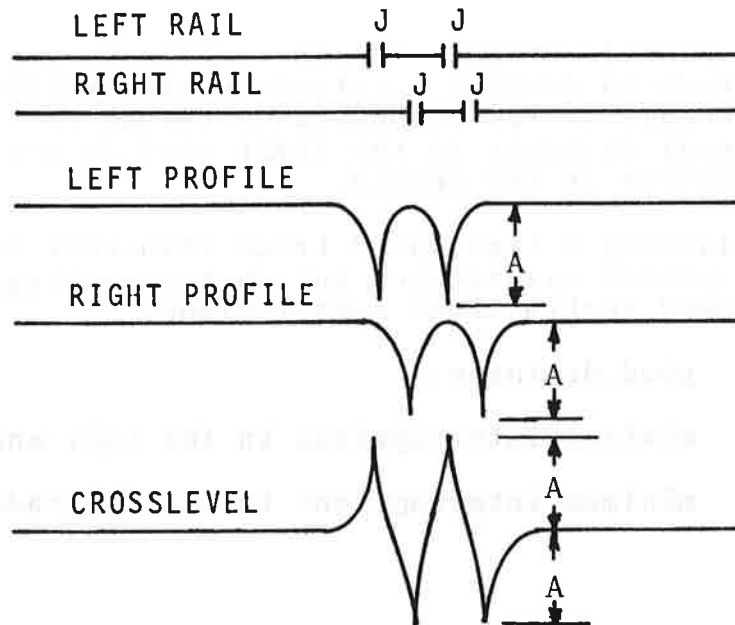


FIGURE C-14. ANOMALY ASSOCIATED WITH USE OF BUFFER RAILS IN CWR

A similar configuration is shown in the profile and crosslevel plots of Figure C-13. Based on the pattern of the welds seen in the track, it appeared that bolted sections were inserted to repair a break in the rail.

#### C.7. SUMMARY OF OBSERVATIONS

A cursory examination of the anomalies discussed in this appendix reveals what virtually every trackmaster knows already. However for the sake of completeness, the observations are summarized as follows:

- Most profile geometry anomalies are related to vertical stiffness anomalies. Quite likely, they started as stiffness anomalies before they developed into profile geometry problems.
- A profile anomaly in one rail (e.g. a joint) tends to develop a corresponding profile anomaly in the second, even though the structural weakness in the first rail is not present in the second.
- Planning a high speed track structure to minimize maintenance and energy wasting speed restrictions must include:
  - good drainage;
  - minimum interruptions in the CWR; and
  - minimum interruptions in the subgrade.



APPENDIX D  
COMPENDIUM OF PSD'S

D.1 EXTREMELY LONG AND SHORT WAVELENGTHS

Some empirical PSD's have been generated for Extremely Long Wavelengths (approximately 100,000 ft.) and Extremely Short Wavelengths (0.01 ft.). These establish some confidence that trends exhibited by the Intermediate Wavelength PSD's are indeed valid and not biased by processing techniques.

- Extremely Long Wavelength Profile PSD's are shown in Figure D-1. These were generated by processing track chart data. The shortest valid wavelength is estimated at 250 ft.
- Extremely Long Wavelength Alignment PSD's are shown in Figure D-2. They are generated in the same manner as Profile.
- Extremely Short Wavelength or Roughness PSD's are shown in Figure D-3. They are generated by transcribing some data contained in Remington et al.\*

Details on the generation of Figures D-1 and D-2 are given in Paragraph 2.5.1, Volume 1 of this report.

---

\*P. J. Remington, et al, "Wheel/Rail Noise and Vibration," Final Report (2 Vols), UMTA-MA-06-0025-75-10 and UMTA-MA-06-0025-75-11, May 1975.

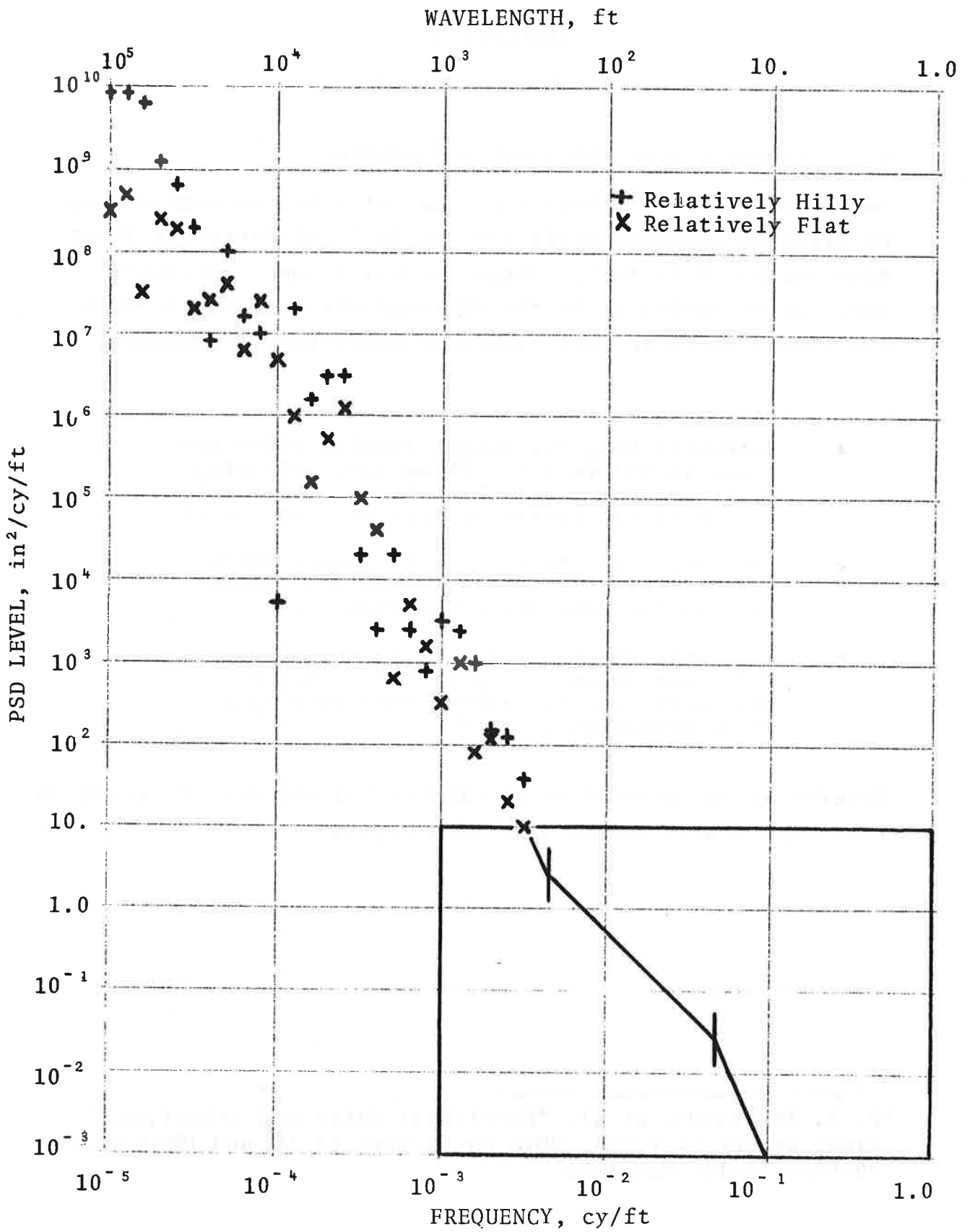


FIGURE D-1. EXTREMELY LONG WAVELENGTH PROFILE PSD'S

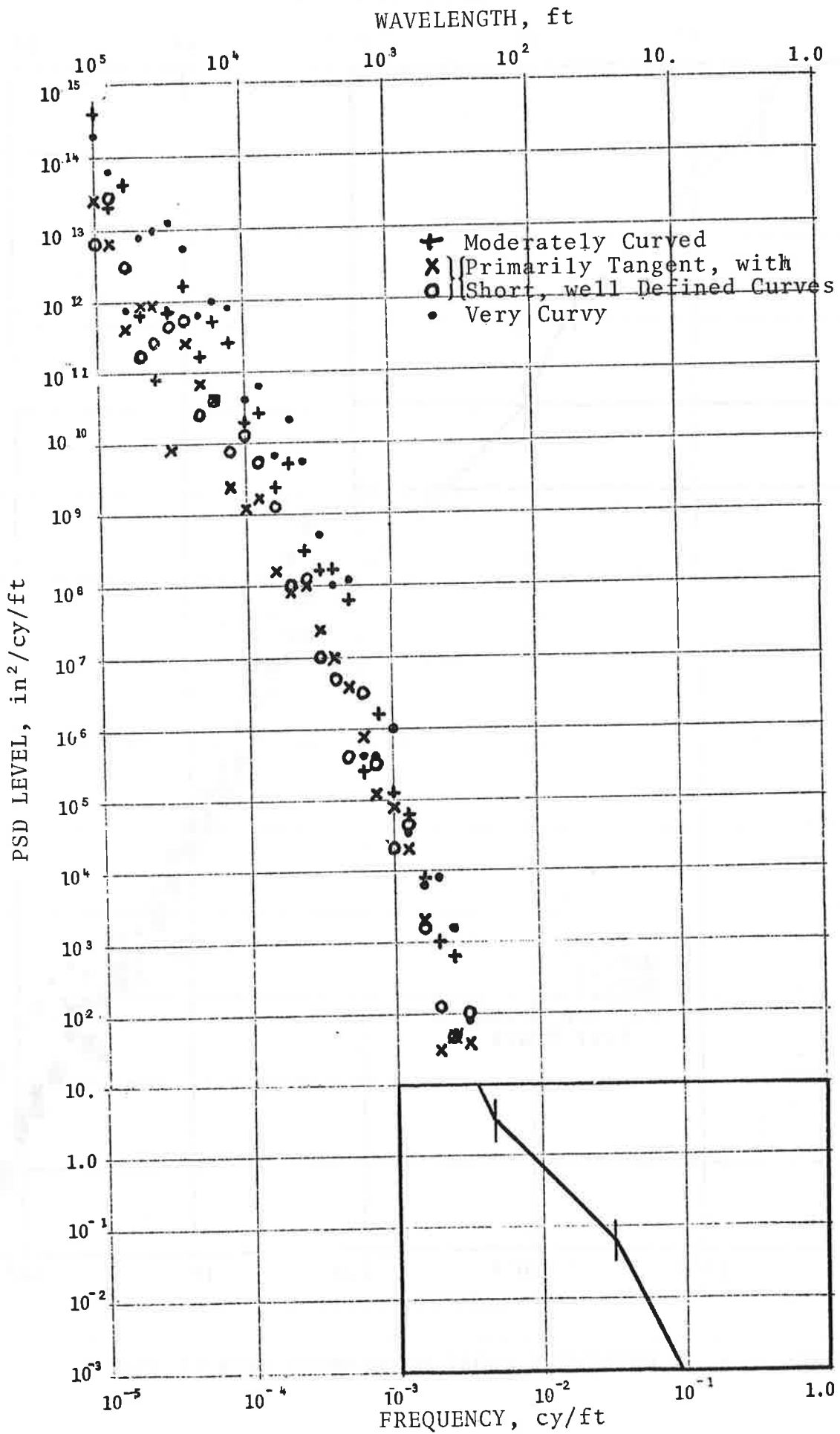


FIGURE D-2. EXTREMELY LONG WAVELENGTH ALIGNMENT PSD'S

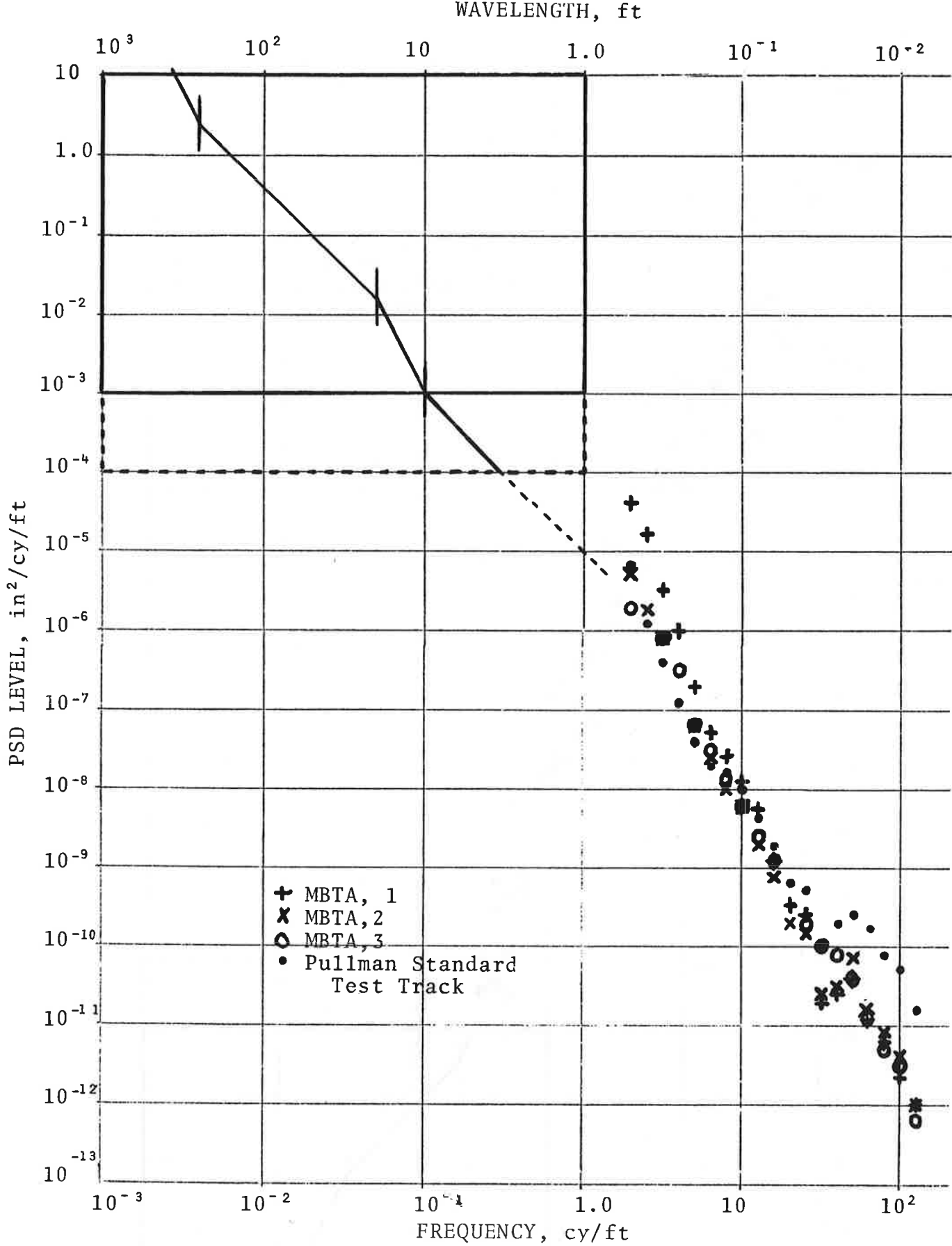


FIGURE D-3. EXTREMELY SHORT WAVELENGTH PROFILE PSD'S

## D.2 HISTORICAL PSD's

In this section, a collection of track PSD's having historical interest are presented. Methods of measurement, vintage, territory, and other pertinent details are summarized in Table D-1. Included are:

- The British Rail ranges of PSD's for main line track, Figures D-4 through D-6.
- Early ENSCO PSD ranges covering a wide variety of track are presented in Figures D-7 through D-28.
- Some PSD's generated by the French National Railways (SNCF) using data collected by their Mauzin track measurement car are contained in Figures D-29 and D-30.

TABLE D-1. SYNOPSIS OF OLDER PSD DATA

	RANGE OF BR SPECTRA	ENSCO 1971	ENSCO 1973
Mean Profile	TMM-1 Survey	-	-
Individual Rail Profile	-	14.5' MCO Capacitive	14.5' MCO Capacitive
Mean Alignment	TMM-1 Survey	-	-
Individual Rail Alignment	-	14.5 MCO Capacitive	Capacitive
Crosslevel	TMM-1 Survey	Self-erecting gyro	-
Gage	-	Capacitive	Capacitive
Broken Down by Track Class	Class 5 & better Main Line CWR	5, 4, 3	5, 4, 3, 2
Territory Covered	Great Britian	Northeastern Area U.S. (NEA)	New Construction NEA, Chicago Pittsburgh, Chicago
Resolution of Peaks	Unknown	0.05 Decade	0.05 Decade
No. Diagrams	3	12	10
Number of PSD's per Range Diagram	12	3 (average)	3 (average)
Typical Length of Data/PSD	1 mi. (average)	3 mi. (average)	3 mi. (average)

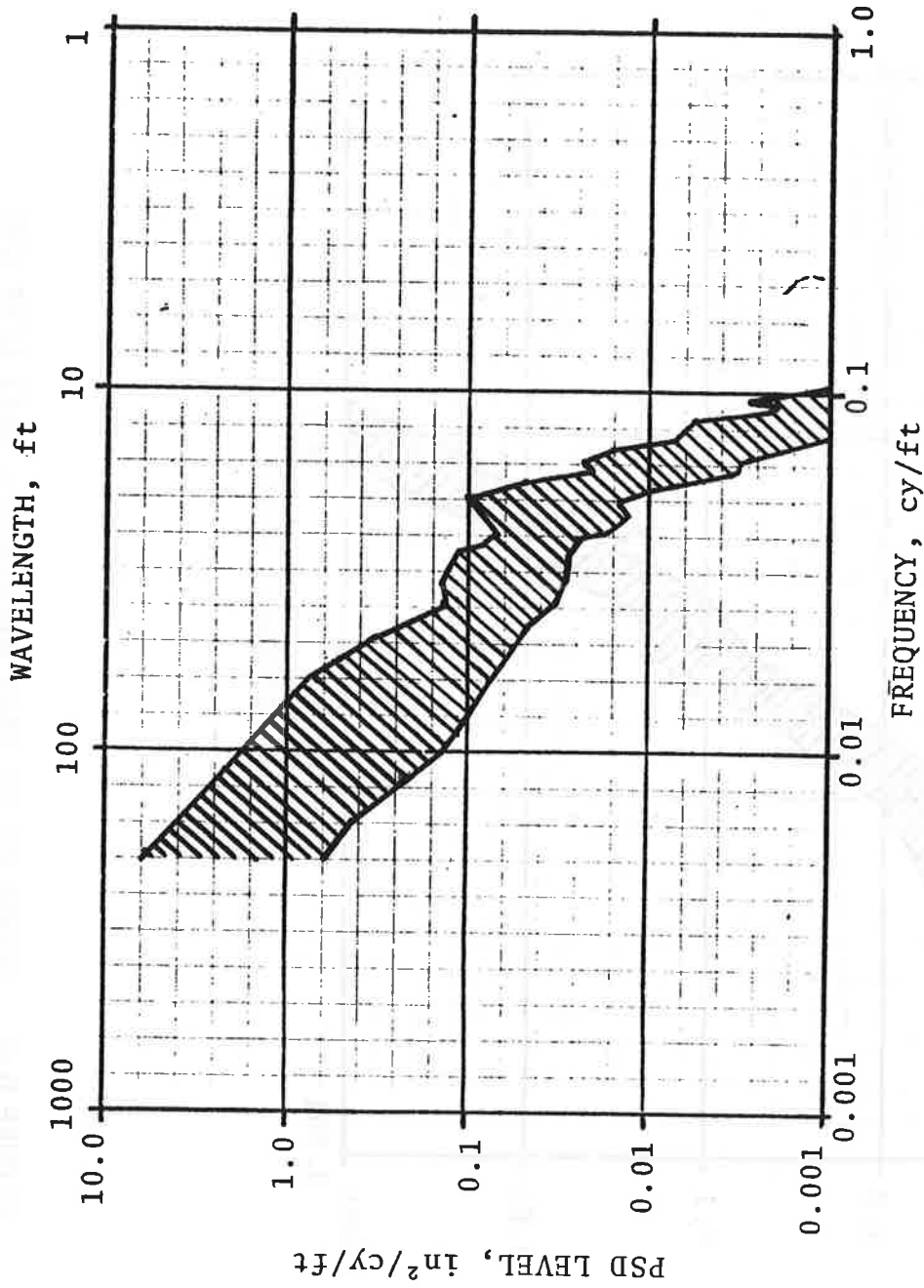


FIGURE D-4 . RANGE OF BR MEAN PROFILE, MAIN LINE CWR

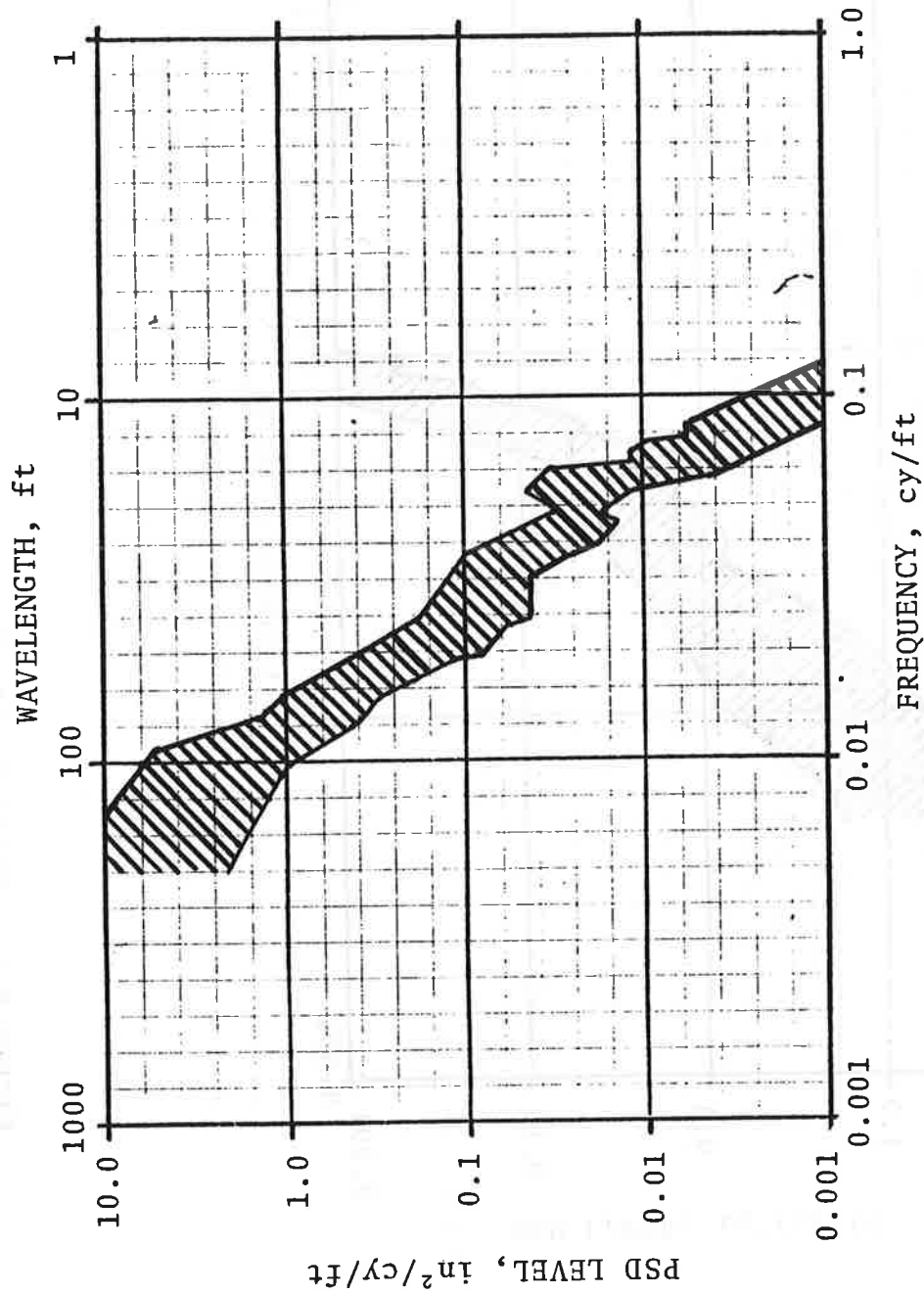


FIGURE D-5. RANGE OF BR MEAN ALIGNMENT, MAIN LINE CWR



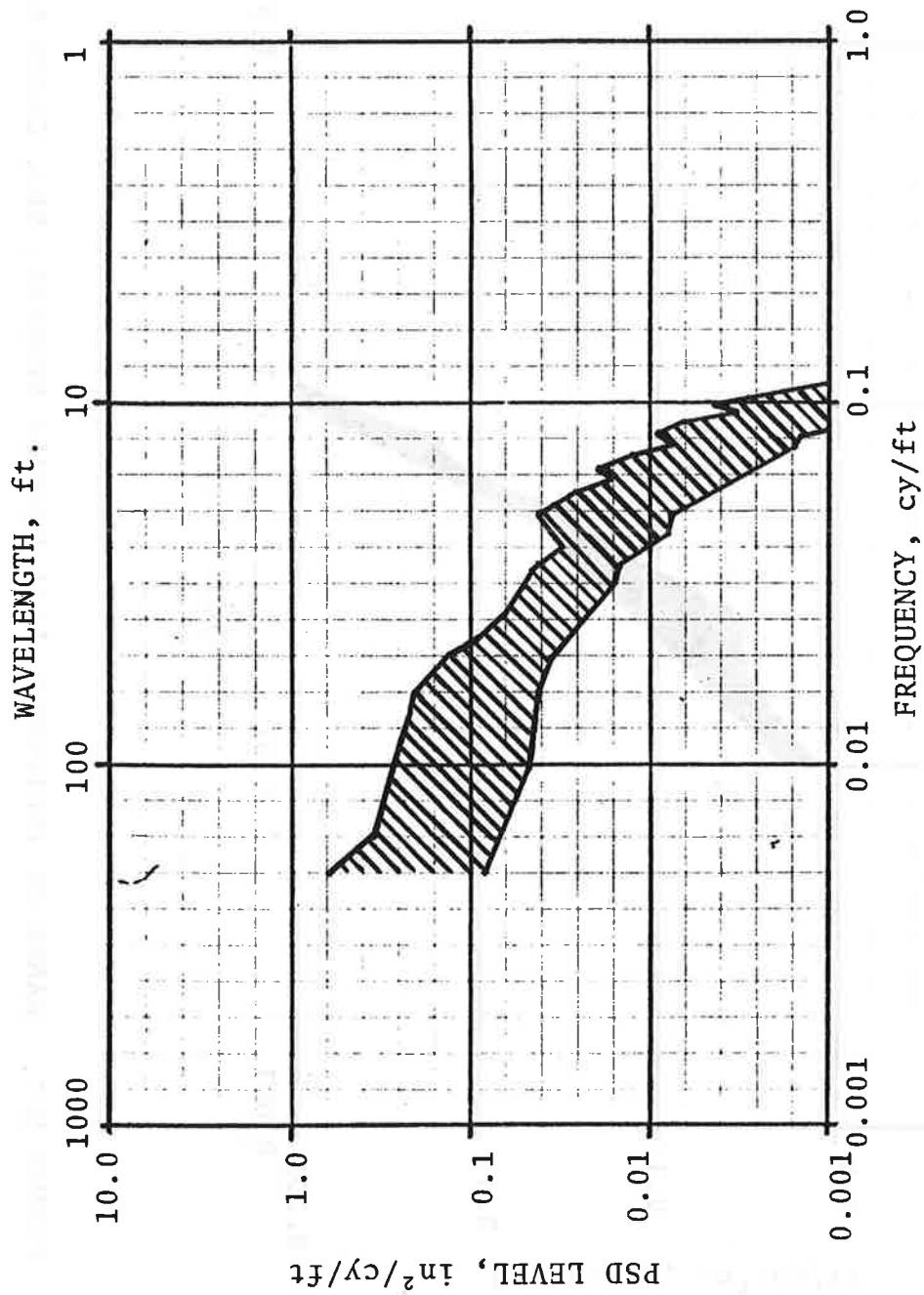


FIGURE D-6. RANGE OF BR CROSSLEVEL, MAIN LINE CWR

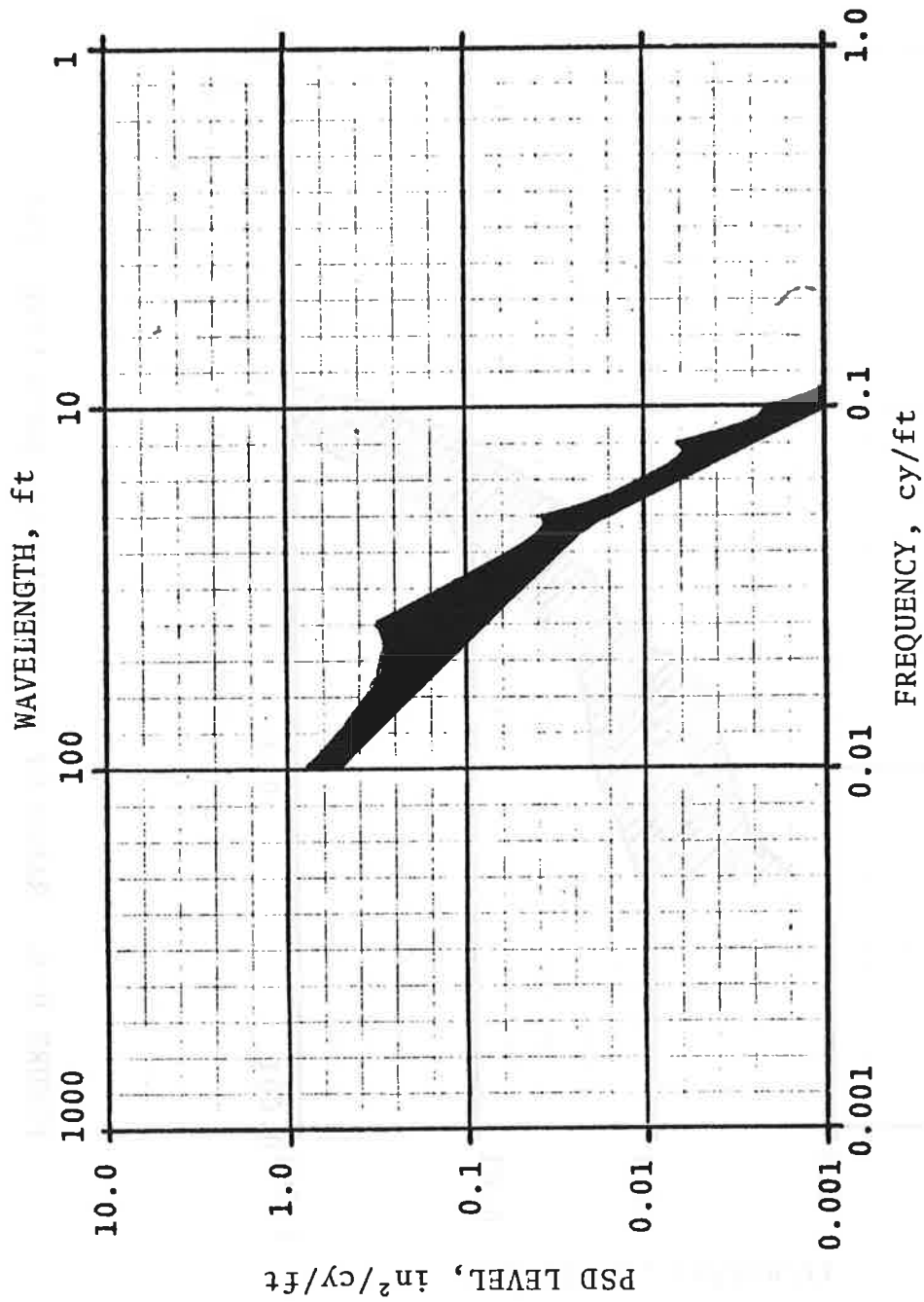


FIGURE D-7. RANGE OF INDIVIDUAL RAIL PROFILE SPECTRA, NEA, CLASS 5

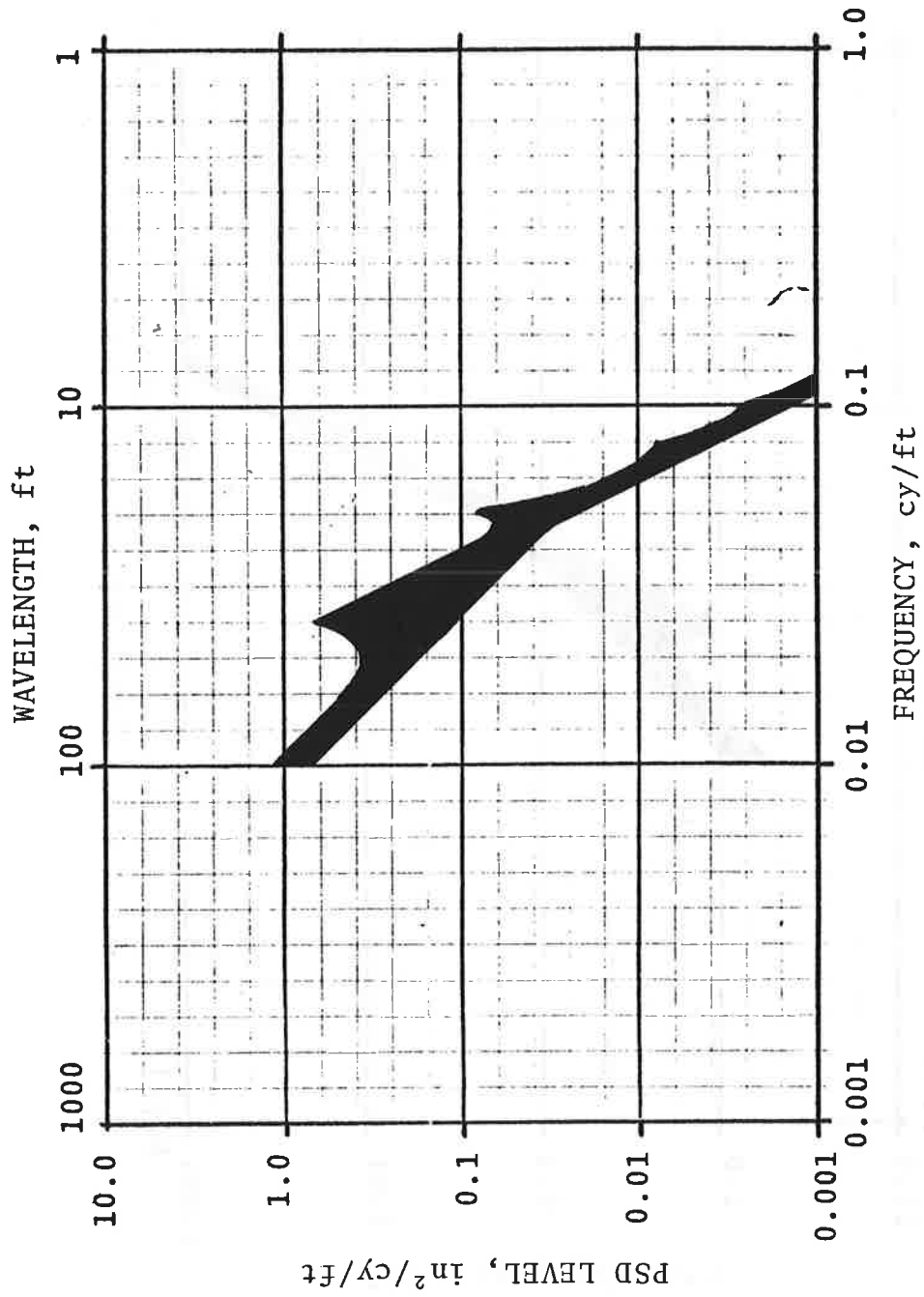


FIGURE D-8. RANGE OF INDIVIDUAL RAIL PROFILE SPECTRA, NEA, CLASS 4

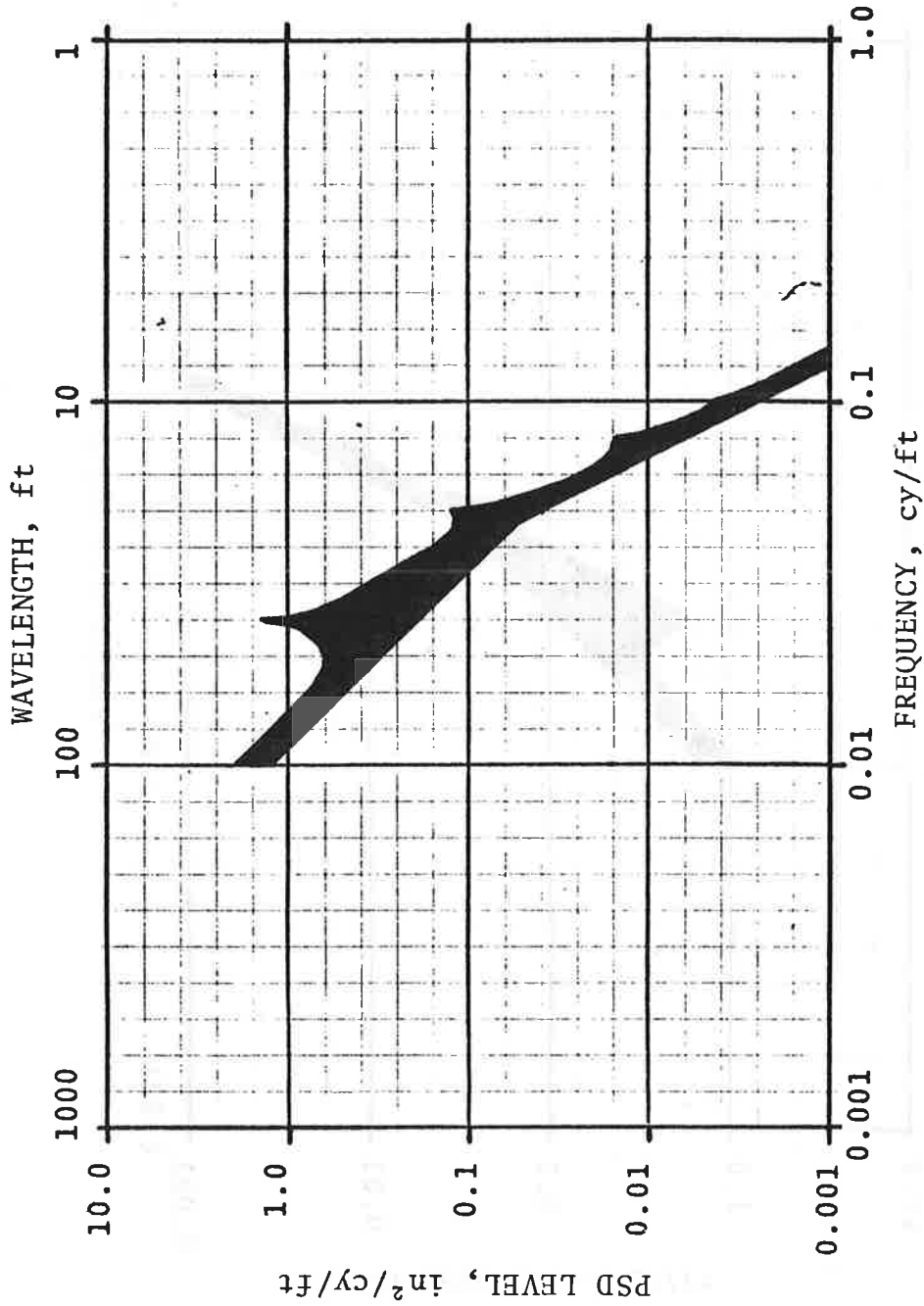


FIGURE D-9. RANGE OF INDIVIDUAL RAIL PROFILE SPECTRA, NEA, CLASS 3

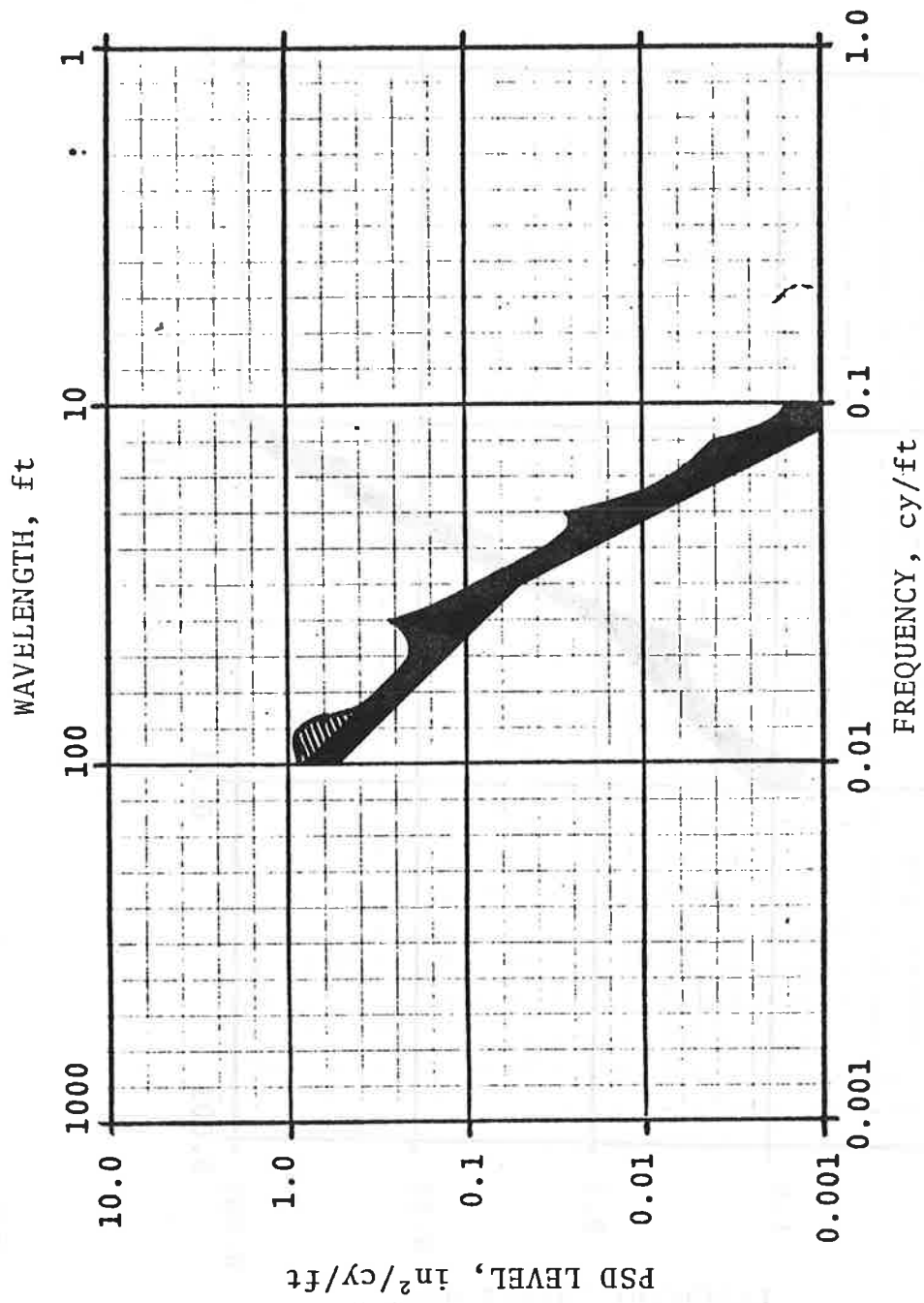


FIGURE D-10. RANGE OF INDIVIDUAL RAIL ALIGNMENT SPECTRA, NEA, CLASS 5

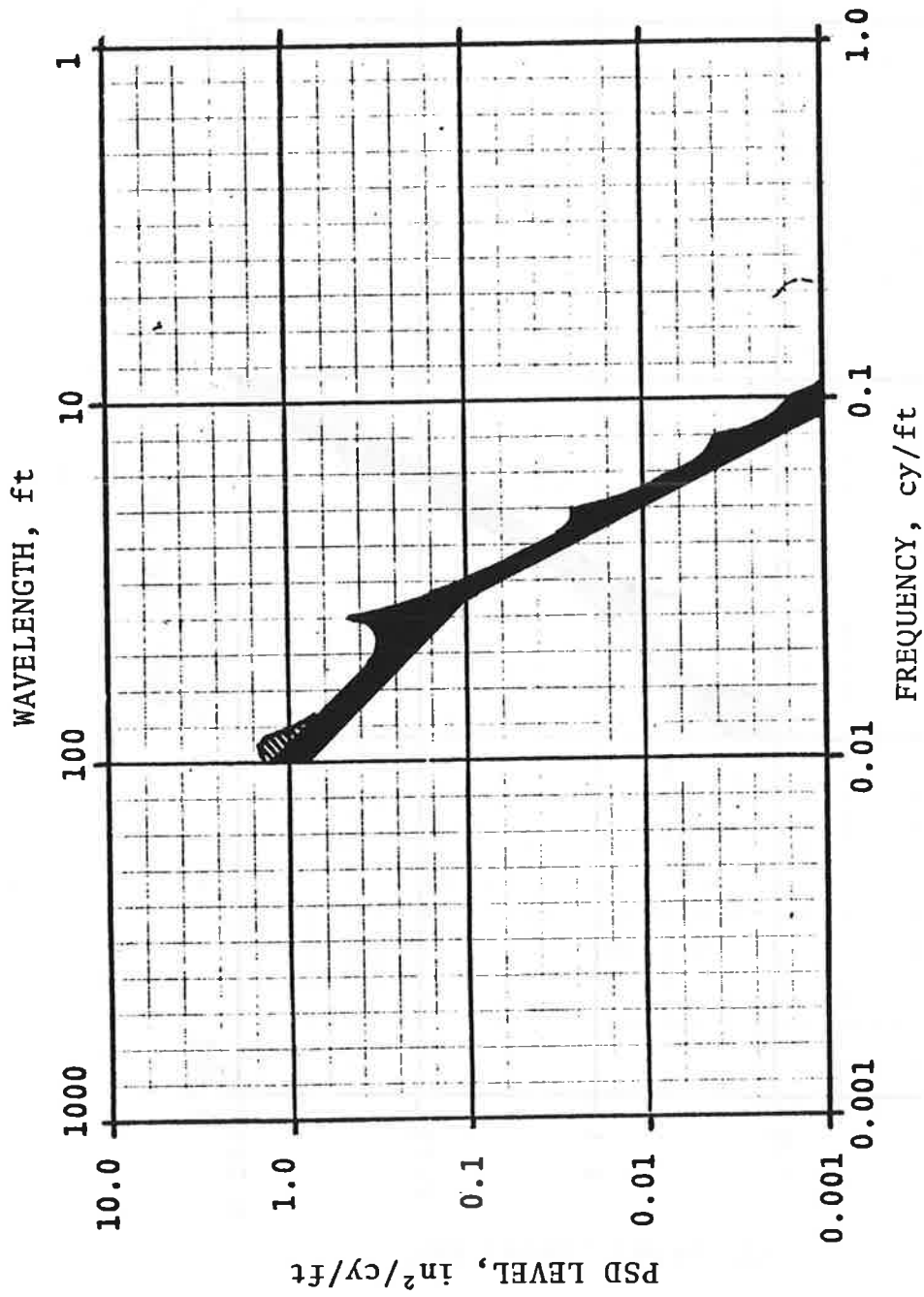


FIGURE D-11. RANGE OF INDIVIDUAL RAIL ALIGNMENT SPECTRA, NEA, CLASS 4

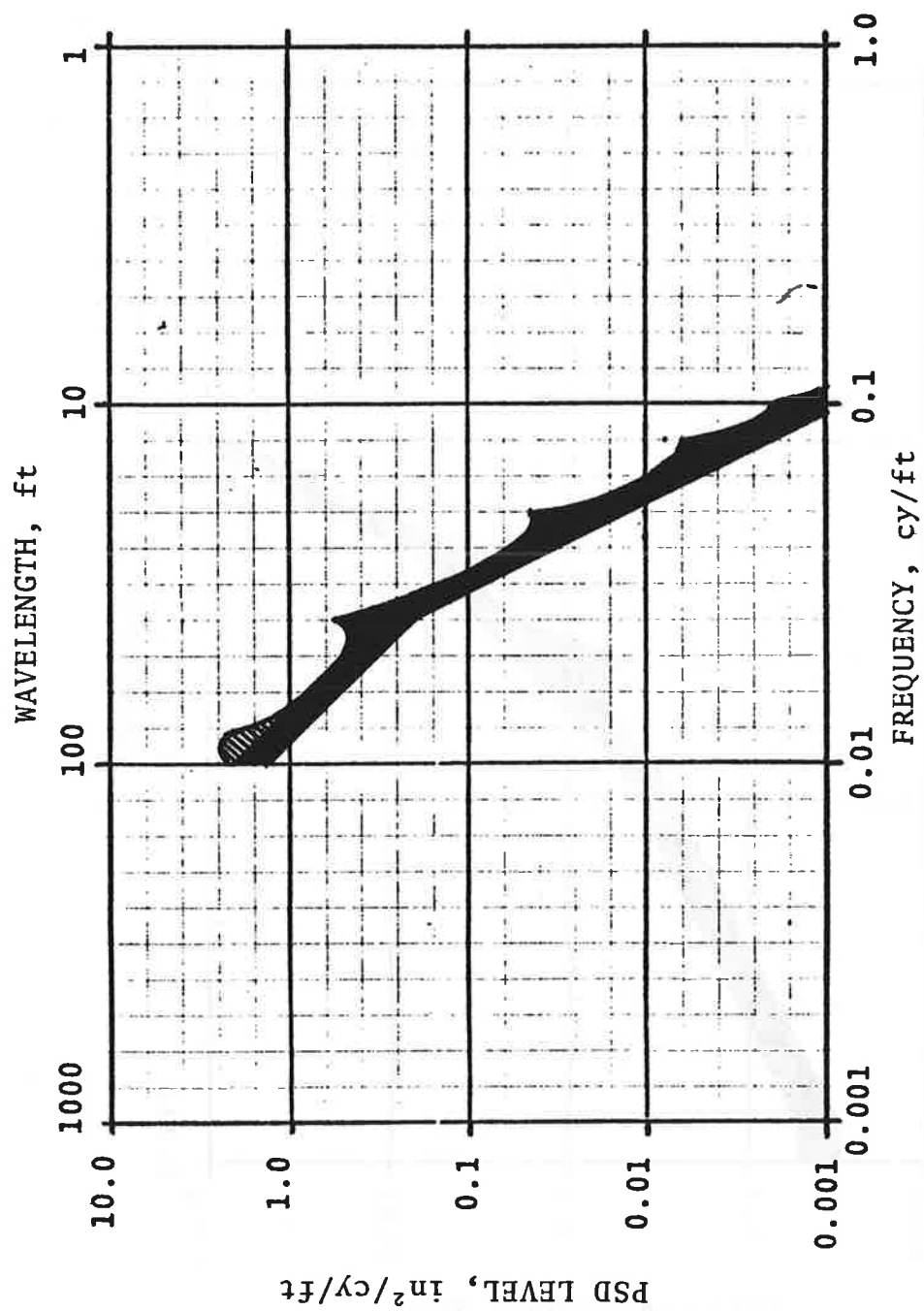


FIGURE D-12. RANGE OF INDIVIDUAL RAIL ALIGNMENT SPECTRA, NEA, CLASS 3

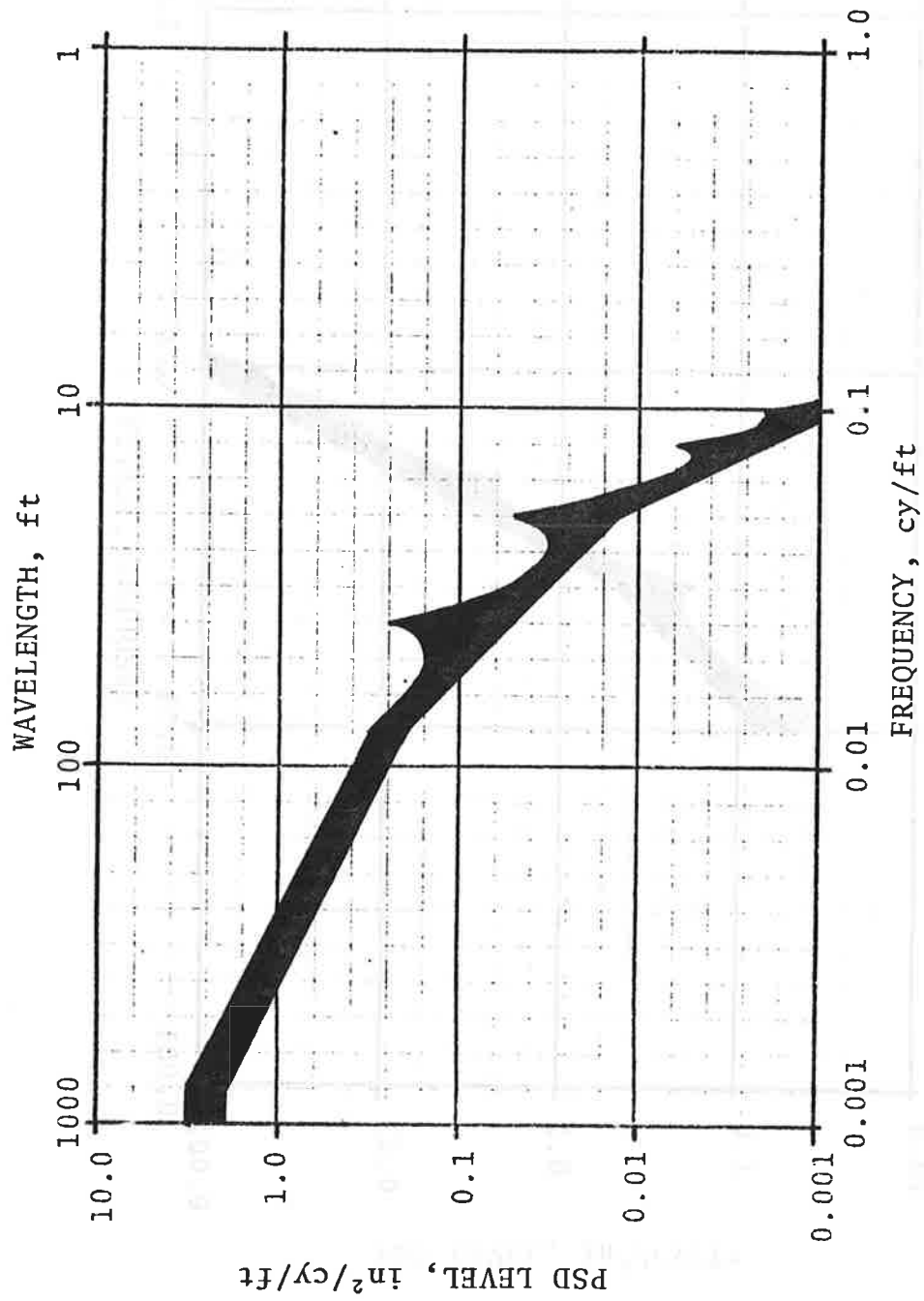


FIGURE D-13. RANGE OF CROSSLEVEL SPECTRA, NEA, CLASS 5



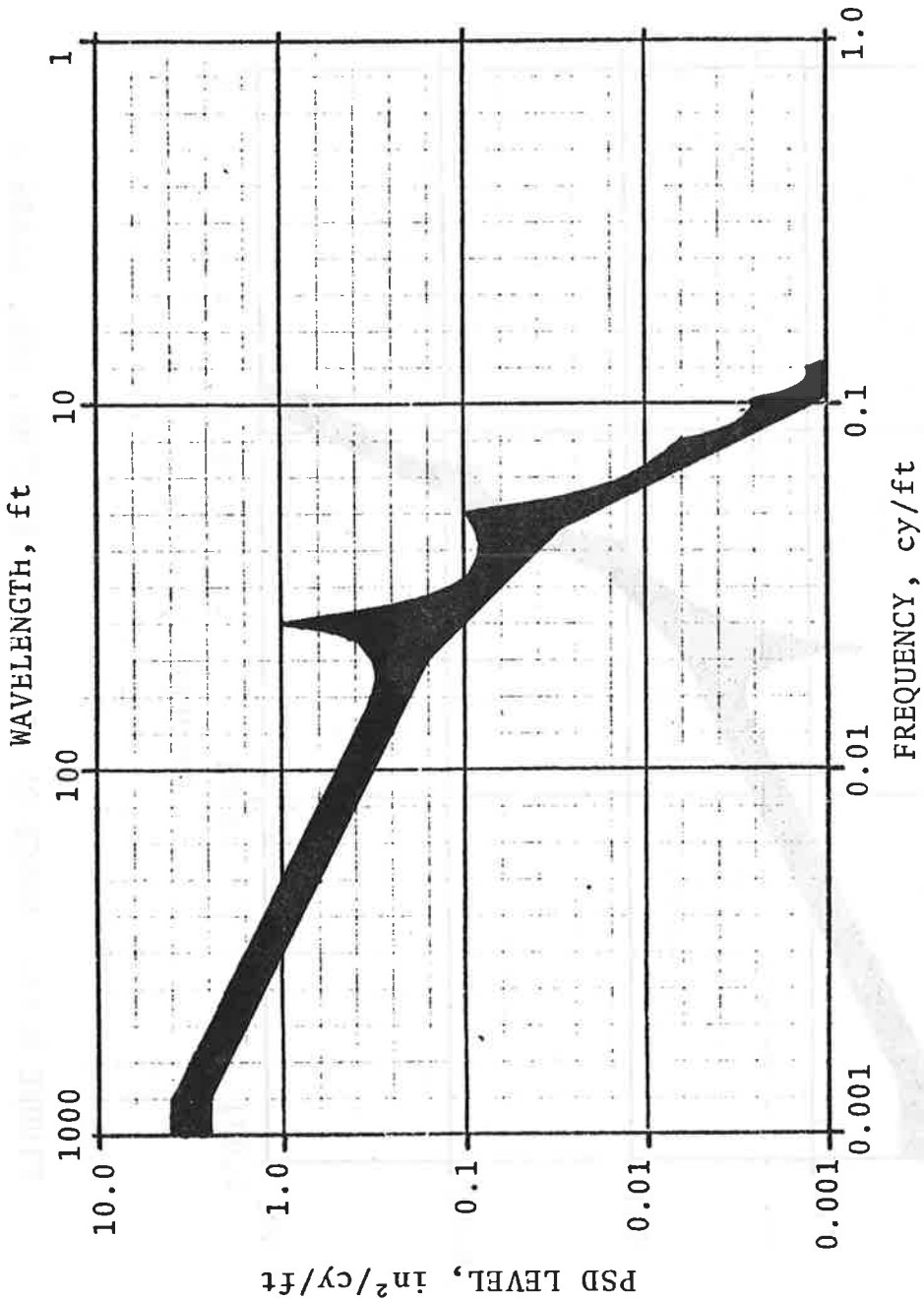


FIGURE D-14. RANGE OF CROSSLLEVEL SPECTRA, NEA, CLASS 4

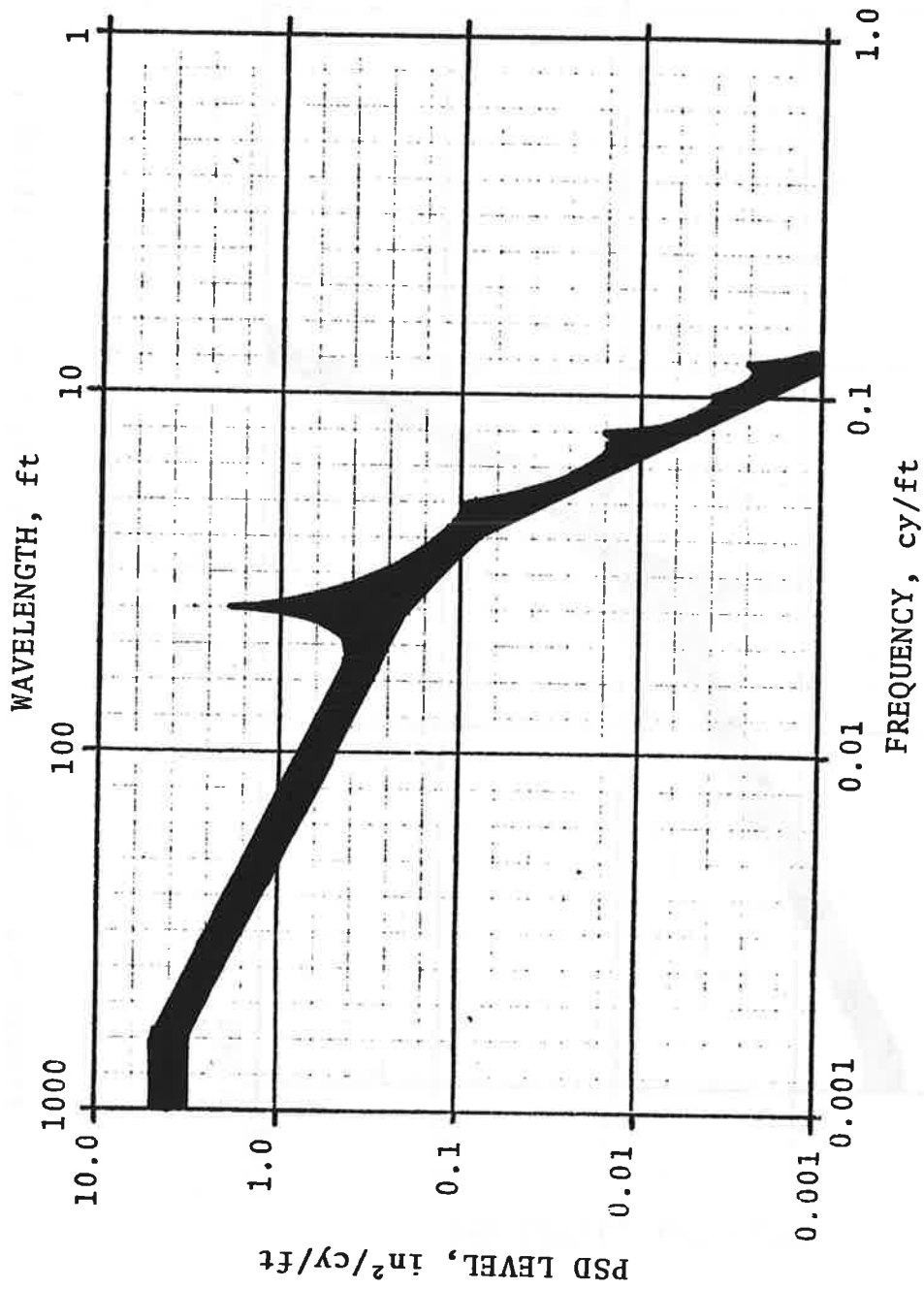


FIGURE D-15. RANGE OF CROSSLEVEL SPECTRA, NEA, CLASS 3

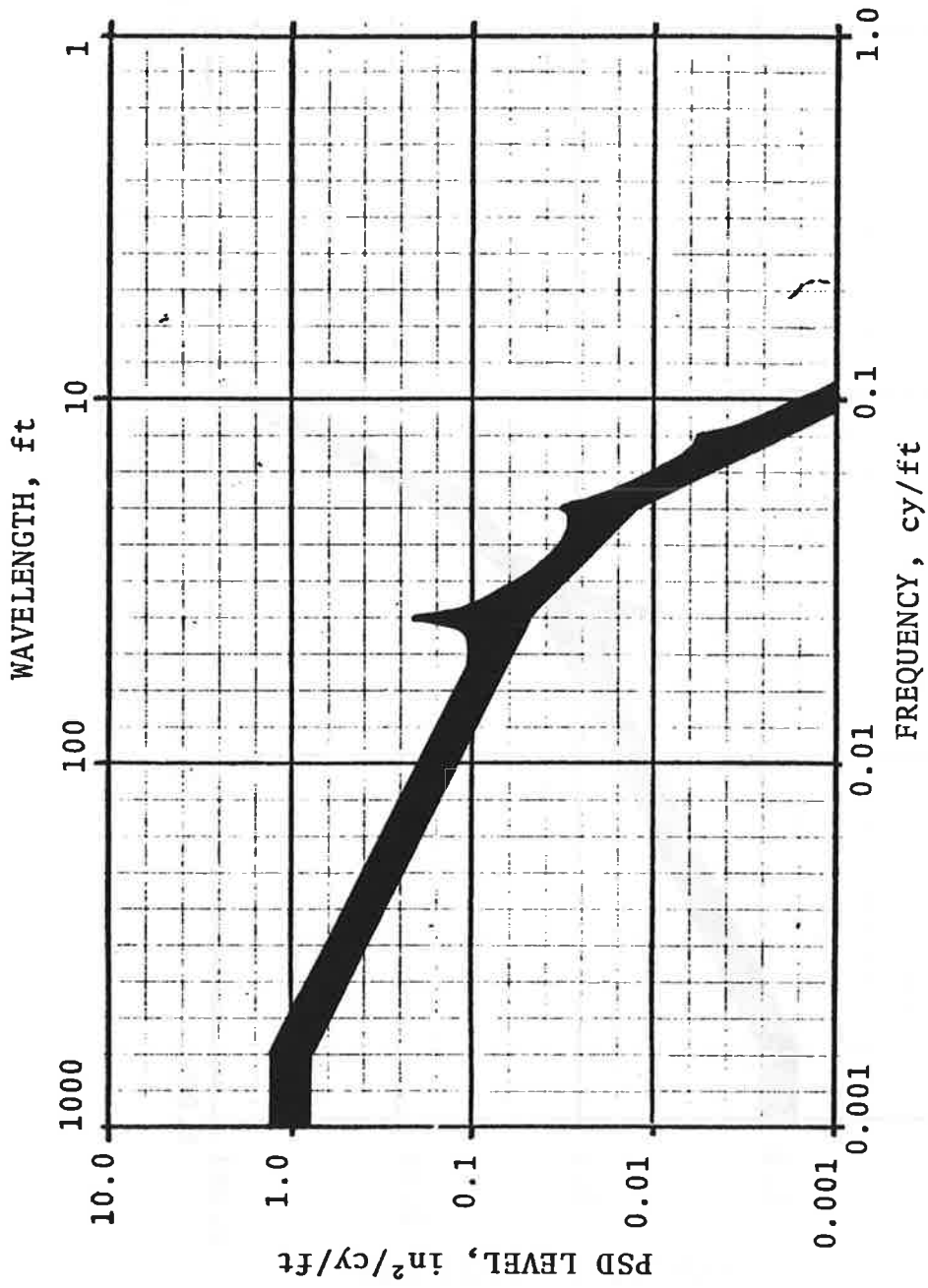


FIGURE D-16. RANGE OF GAGE SPECTRA, NEA, CLASS 5

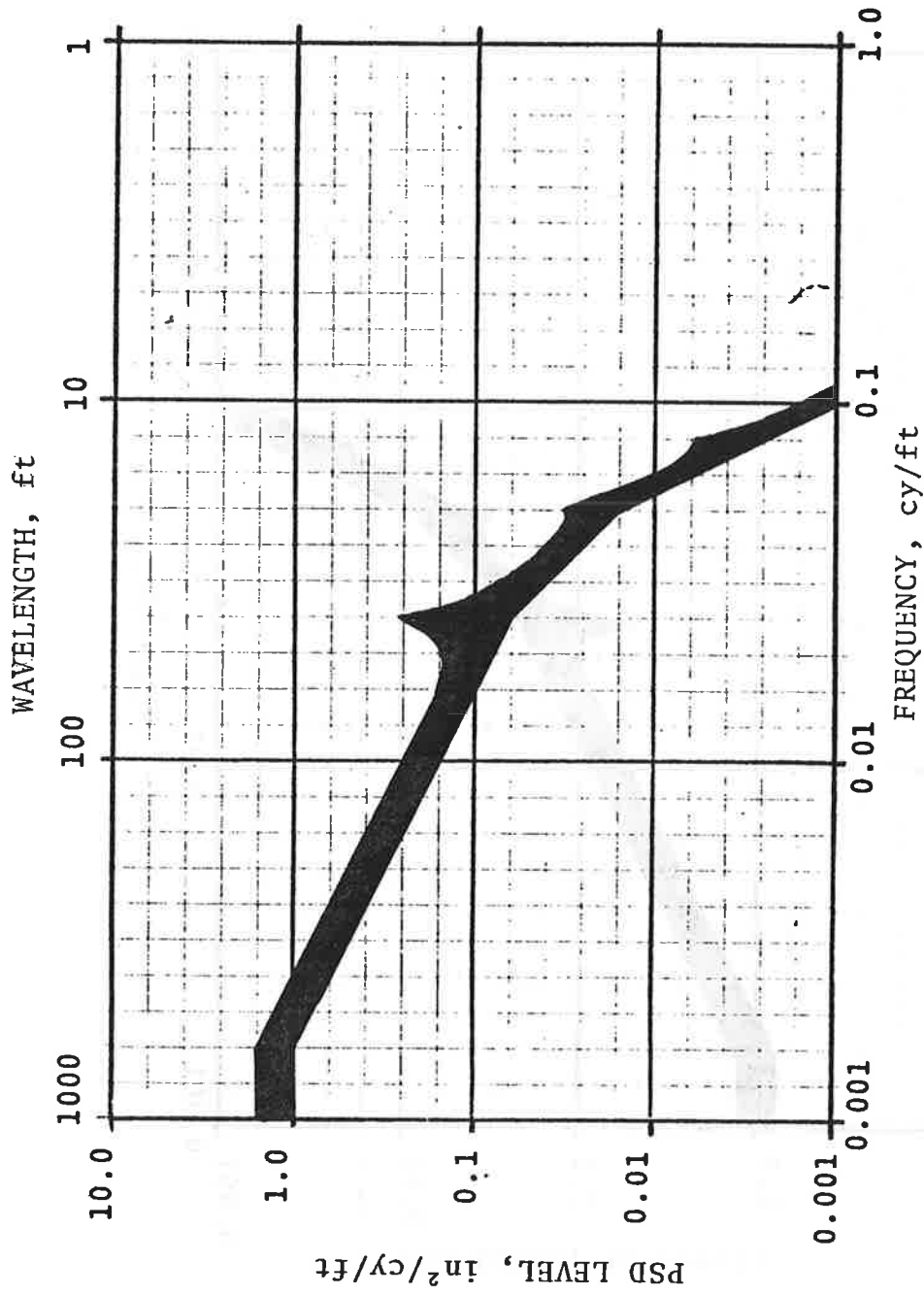


FIGURE D-17. RANGE OF GAGE SPECTRA, NEA, CLASS 4

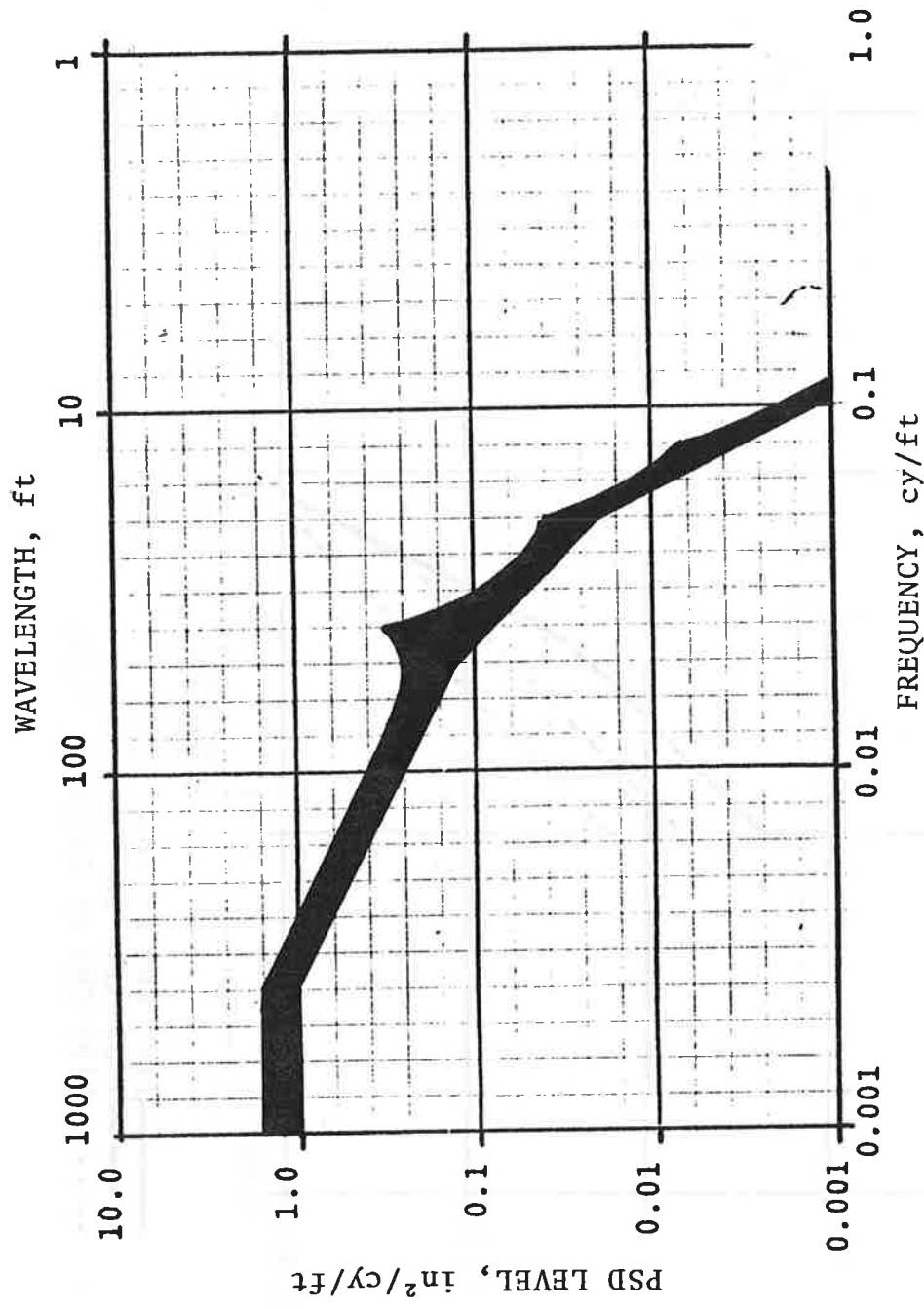


FIGURE D-18. RANGE OF GAGE SPECTRA, NEA, CLASS 3

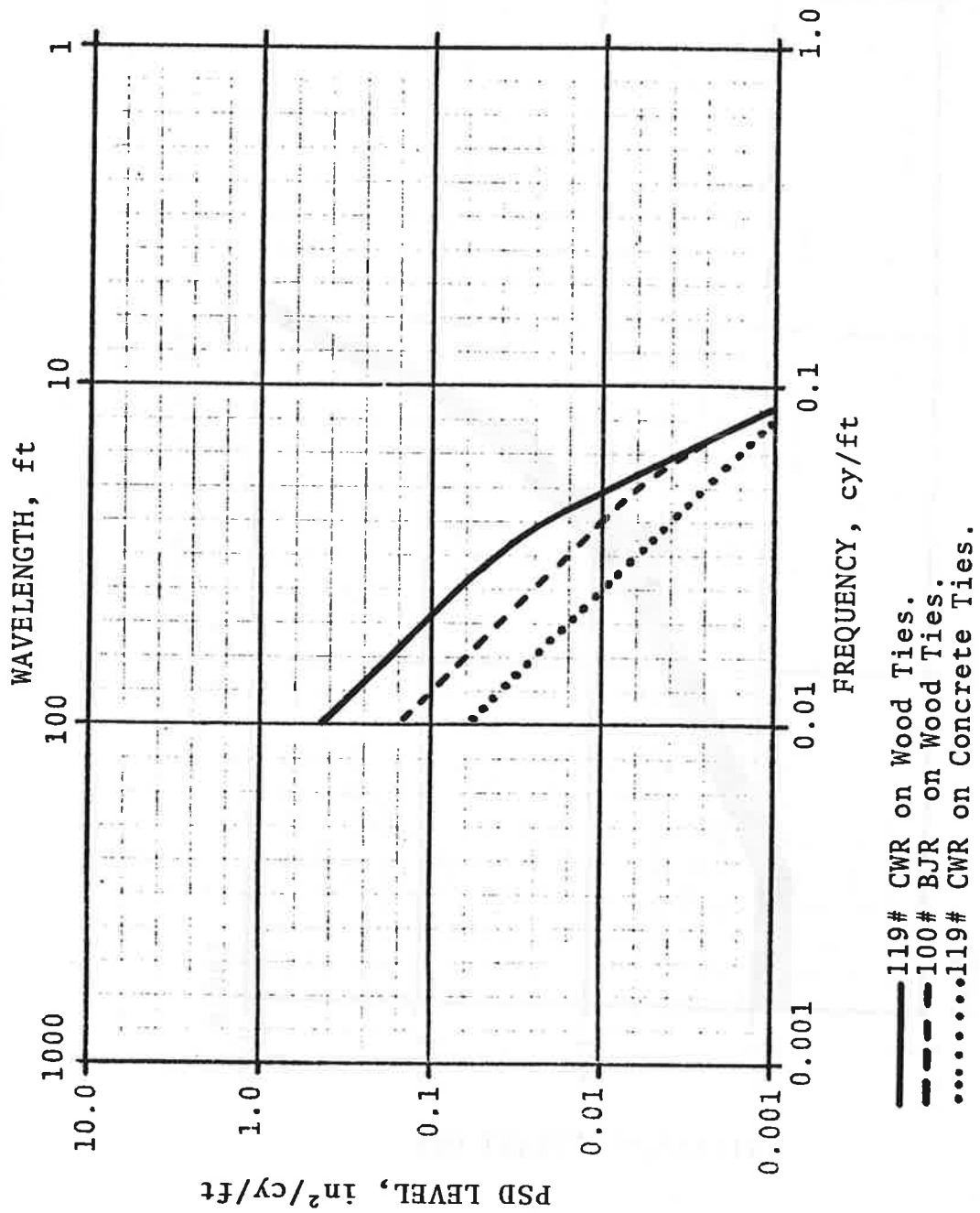


FIGURE D-19. SMOOTHED INDIVIDUAL RAIL PROFILE PSD'S FOR NEW CONSTRUCTION

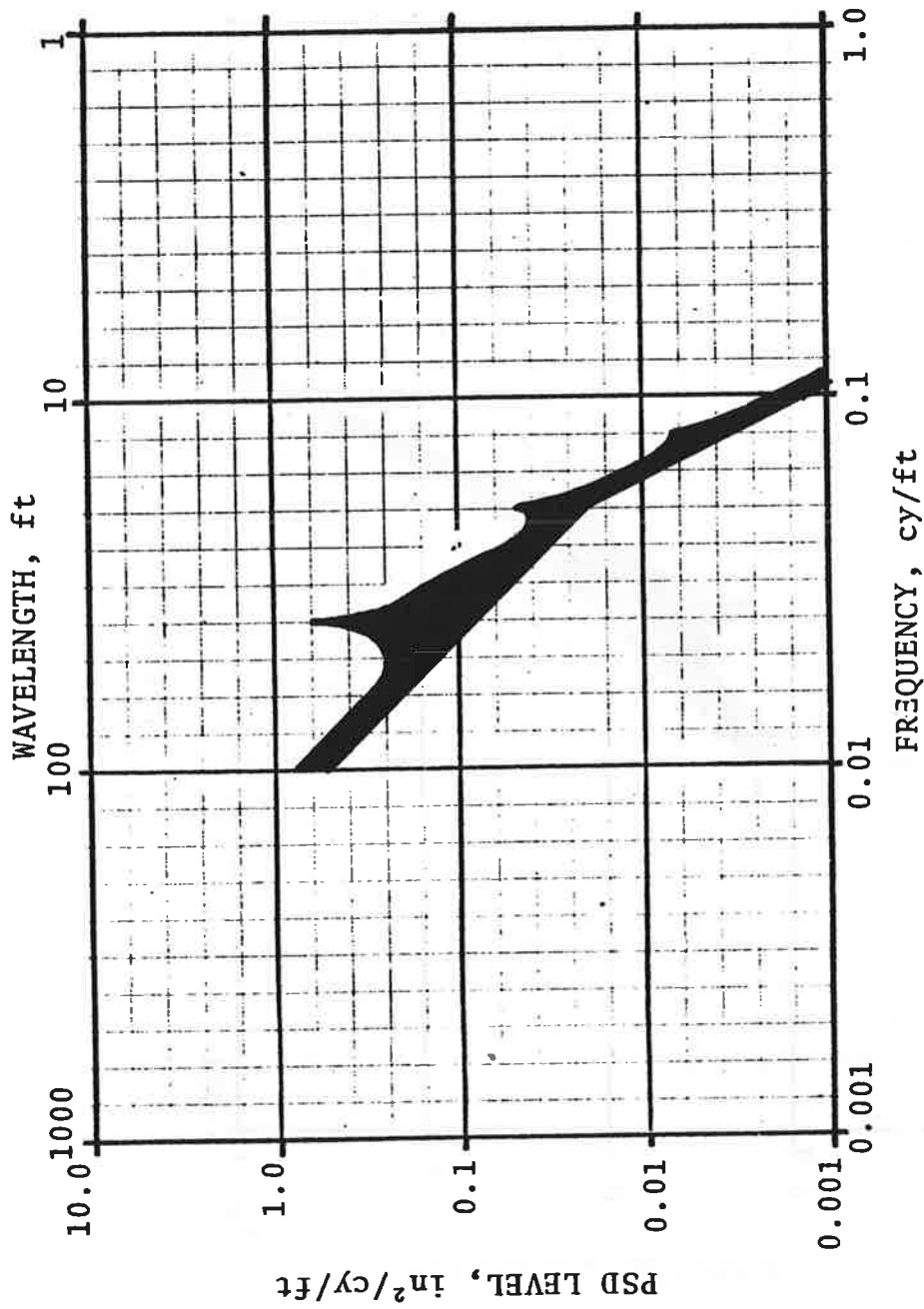


FIGURE D-20 . RANGE OF INDIVIDUAL RAIL PROFILE SPECTRA, NEA, FREIGHT AND PASSENGER (CLASS 5)

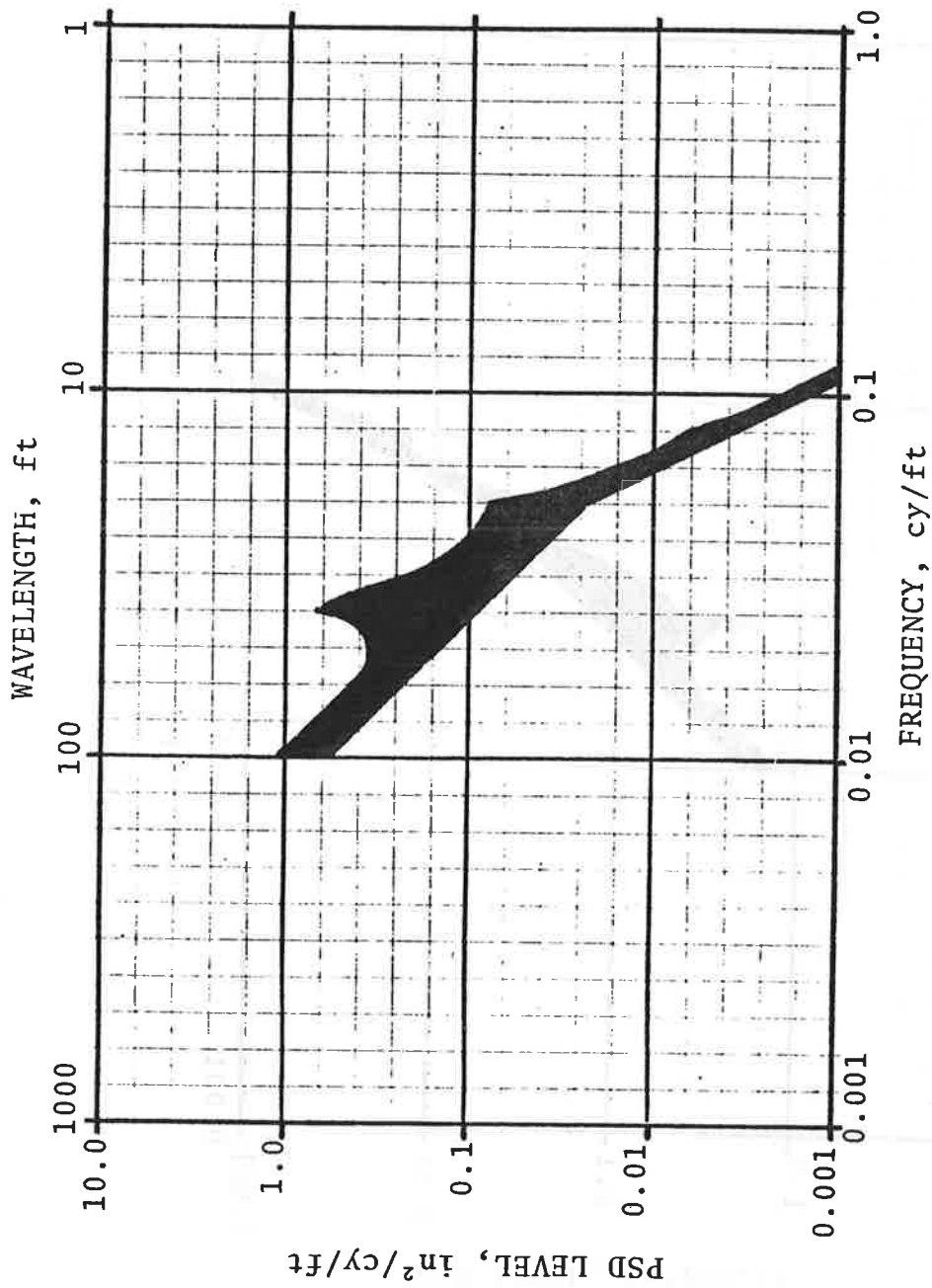


FIGURE D-21 . RANGE OF PROFILE SPECTRA FROM FLORIDA TRACK FREIGHT AND PASSENGER (CLASS 4)



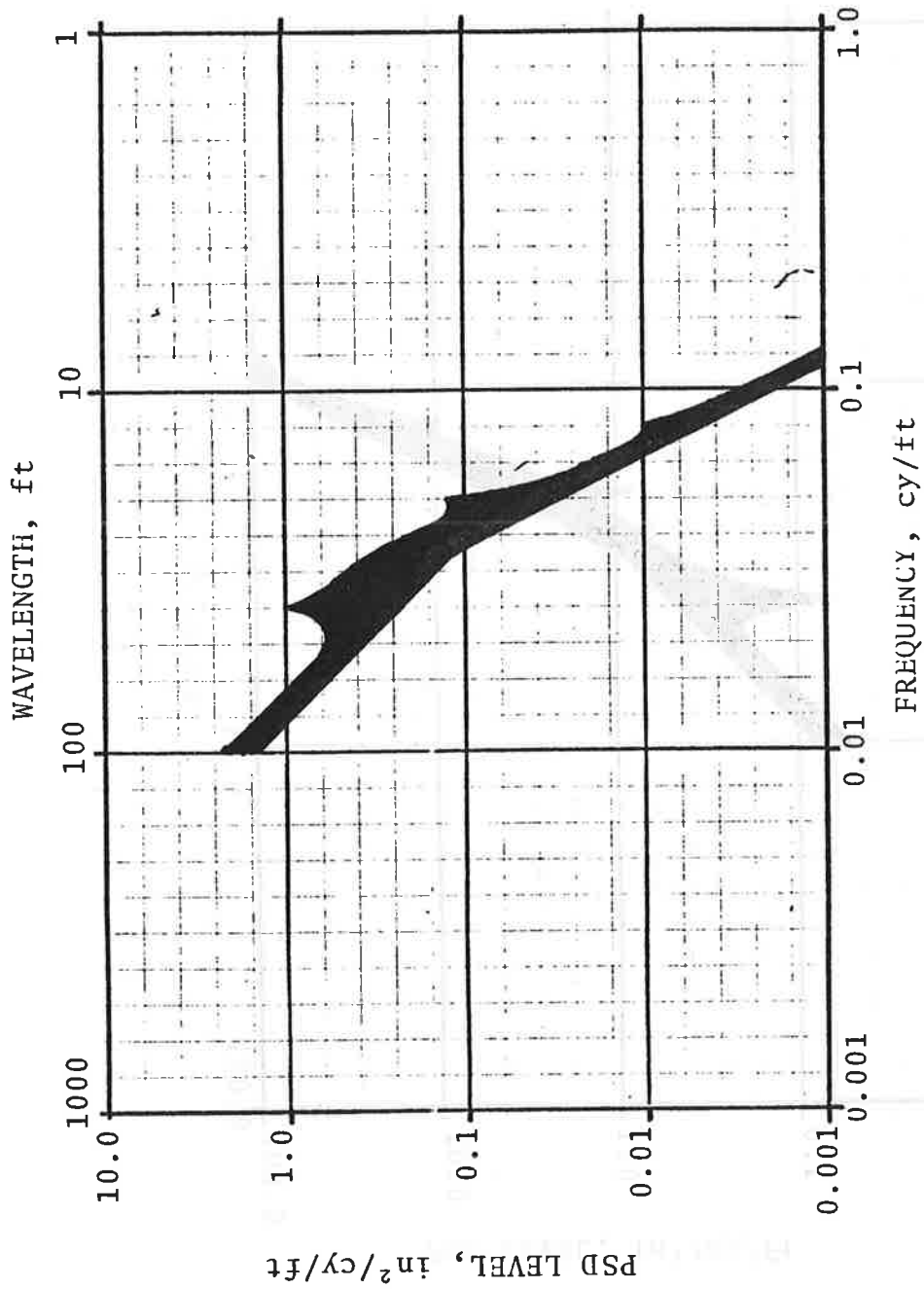


FIGURE D-22. RANGE OF PROFILE SPECTRA FROM CHICAGO AREA, FREIGHT AND PASSENGER (CLASS 3)

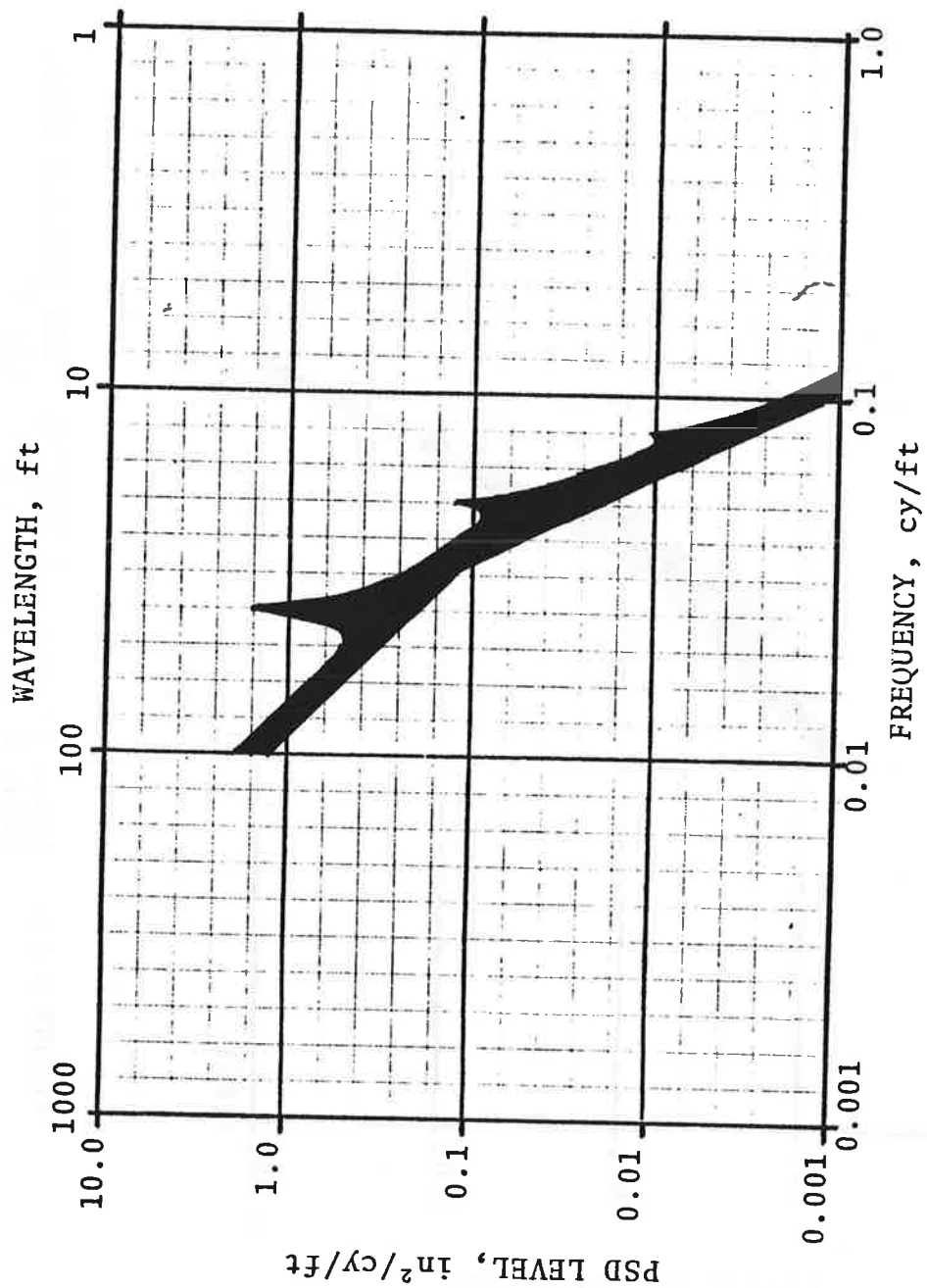
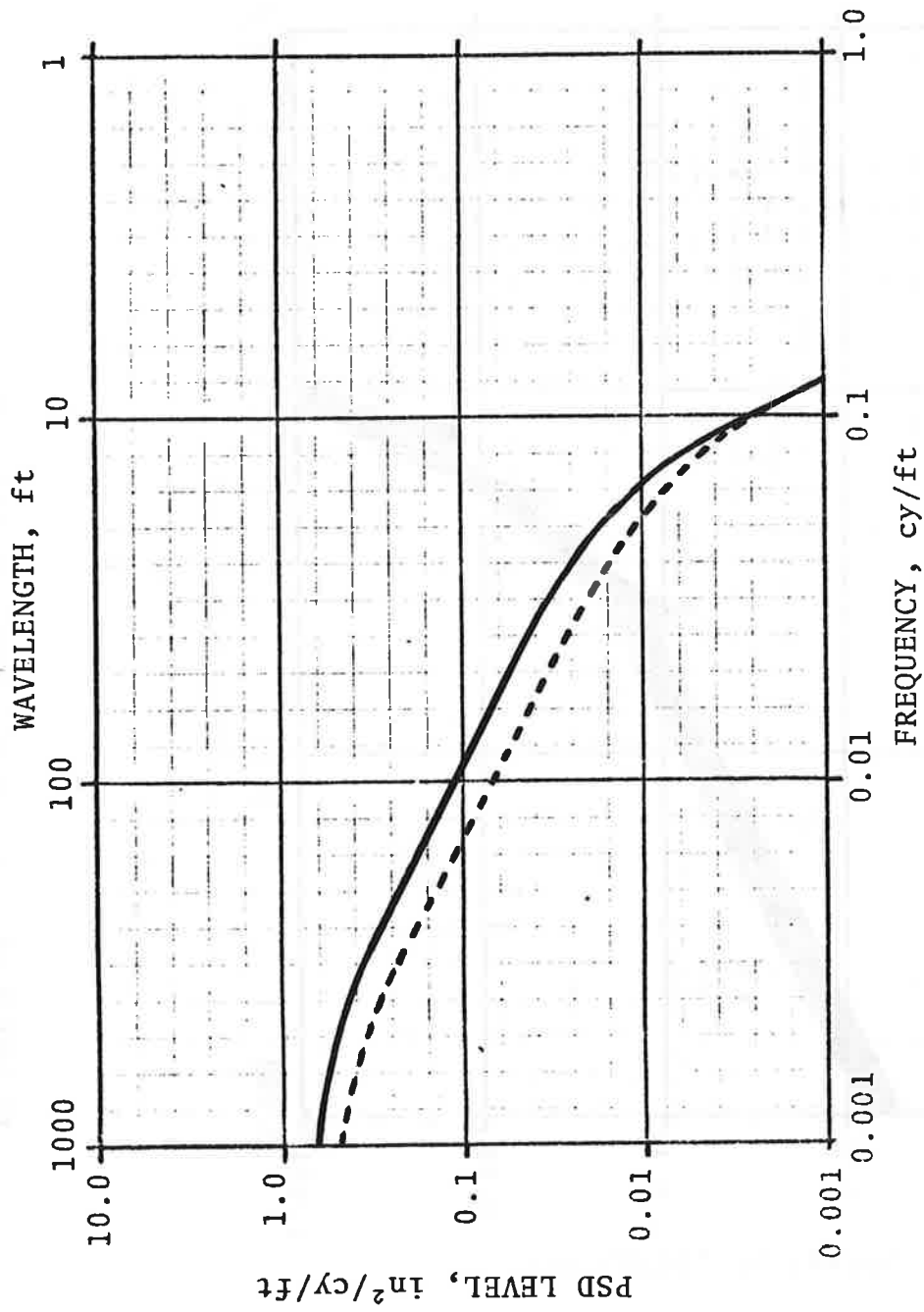


FIGURE D-23. RANGE OF PROFILE SPECTRA FROM PITTSBURGH AREA, UNIT COAL TRAIN OPERATION (CLASS 2)



119# CWR on Wood Ties  
 100# BJR on Wood Ties and  
 119# CWR on Concrete Ties

FIGURE D-24 . SMOOTHED GAGE PSD'S FOR NEW CONSTRUCTION

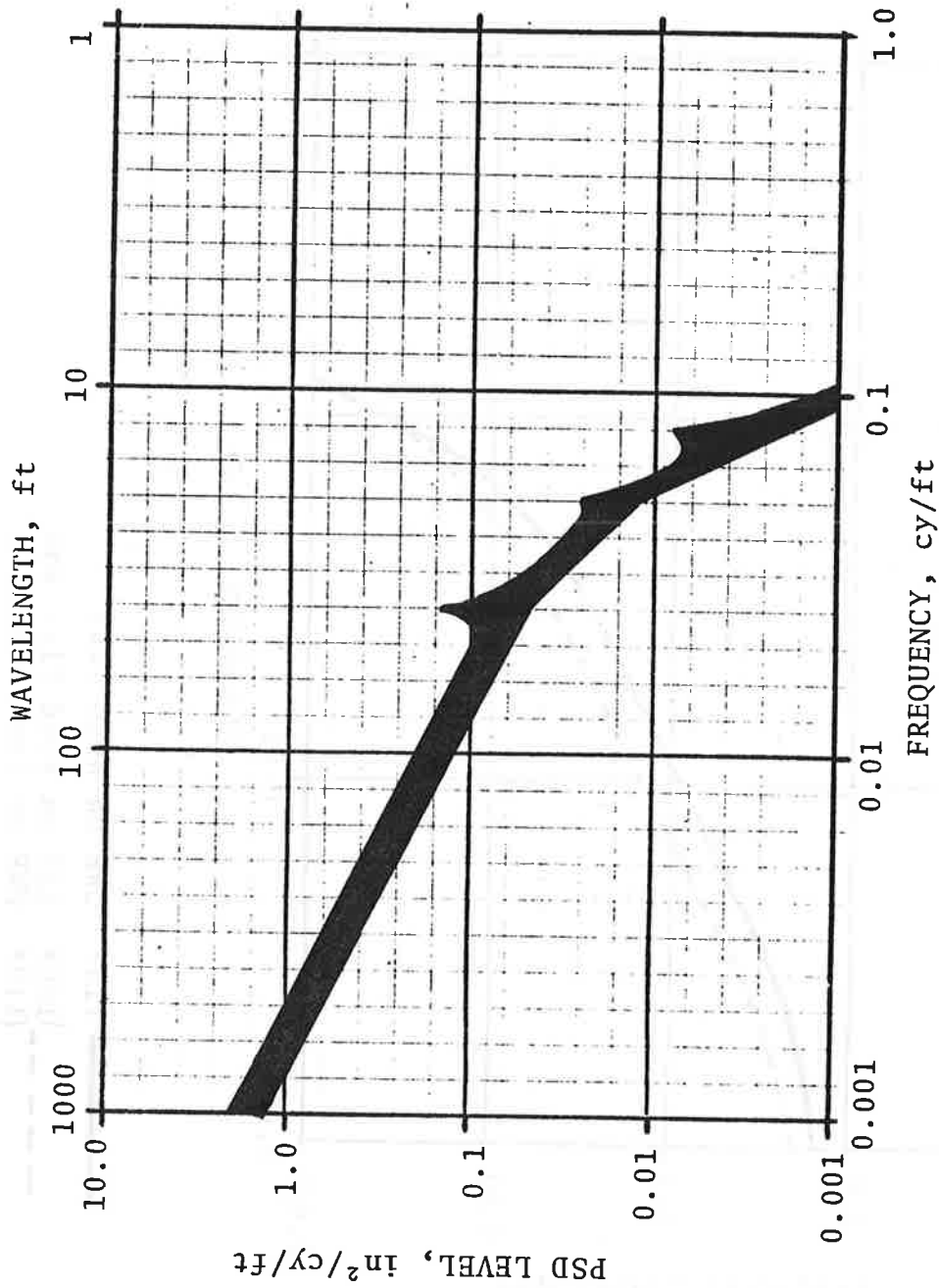


FIGURE D -25 . RANGE OF GAGE SPECTRA, NEA, FREIGHT AND PASSENGER (CLASS 5)

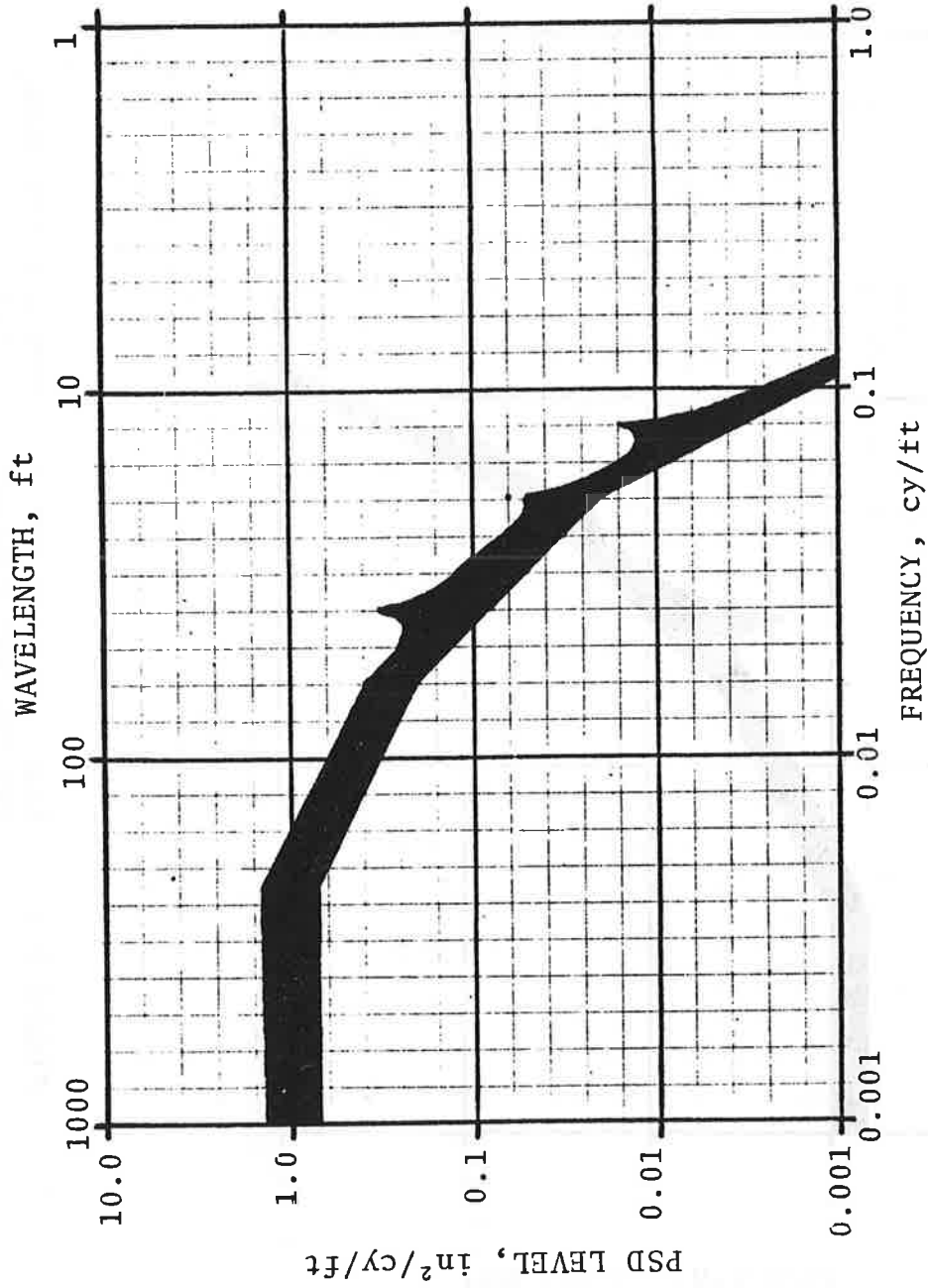


FIGURE D-26 . RANGE OF GAGE SPECTRA FROM FLORIDA TRACK, FREIGHT AND PASSENGER (CLASS 4)

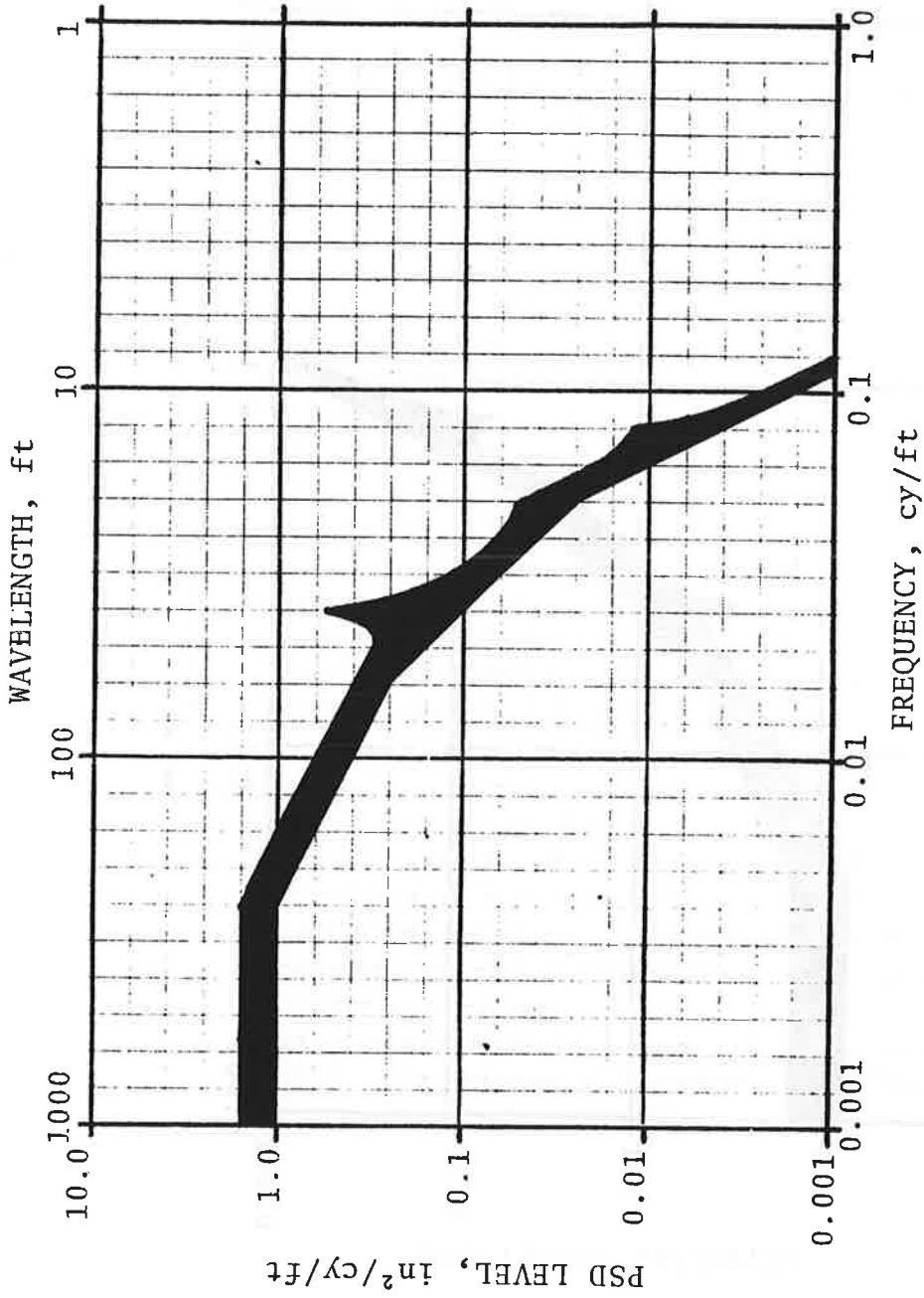


FIGURE D-27. RANGE OF GAGE SPECTRA FROM CHICAGO AREA, FREIGHT AND PASSENGER (CLASS 3)

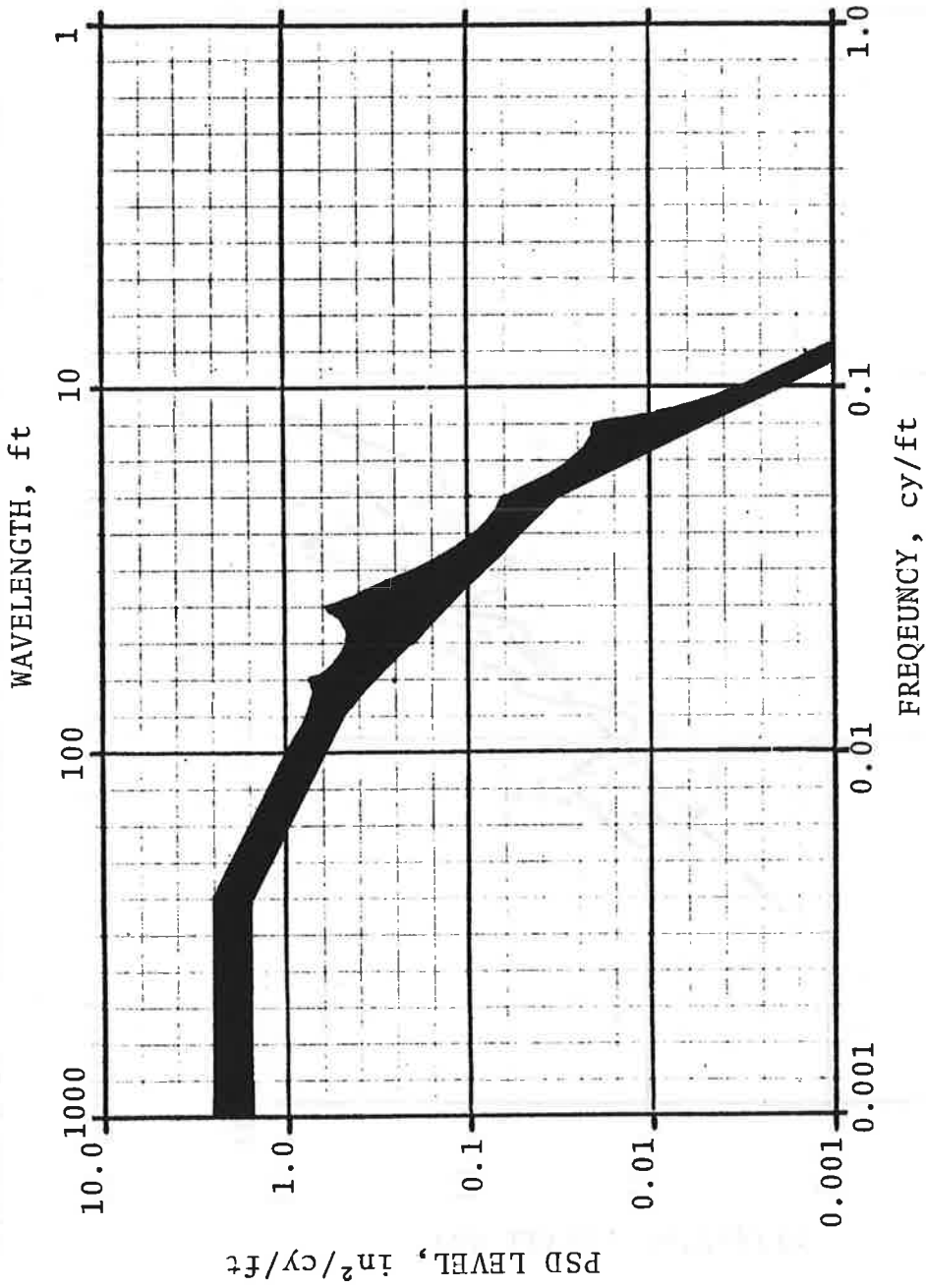
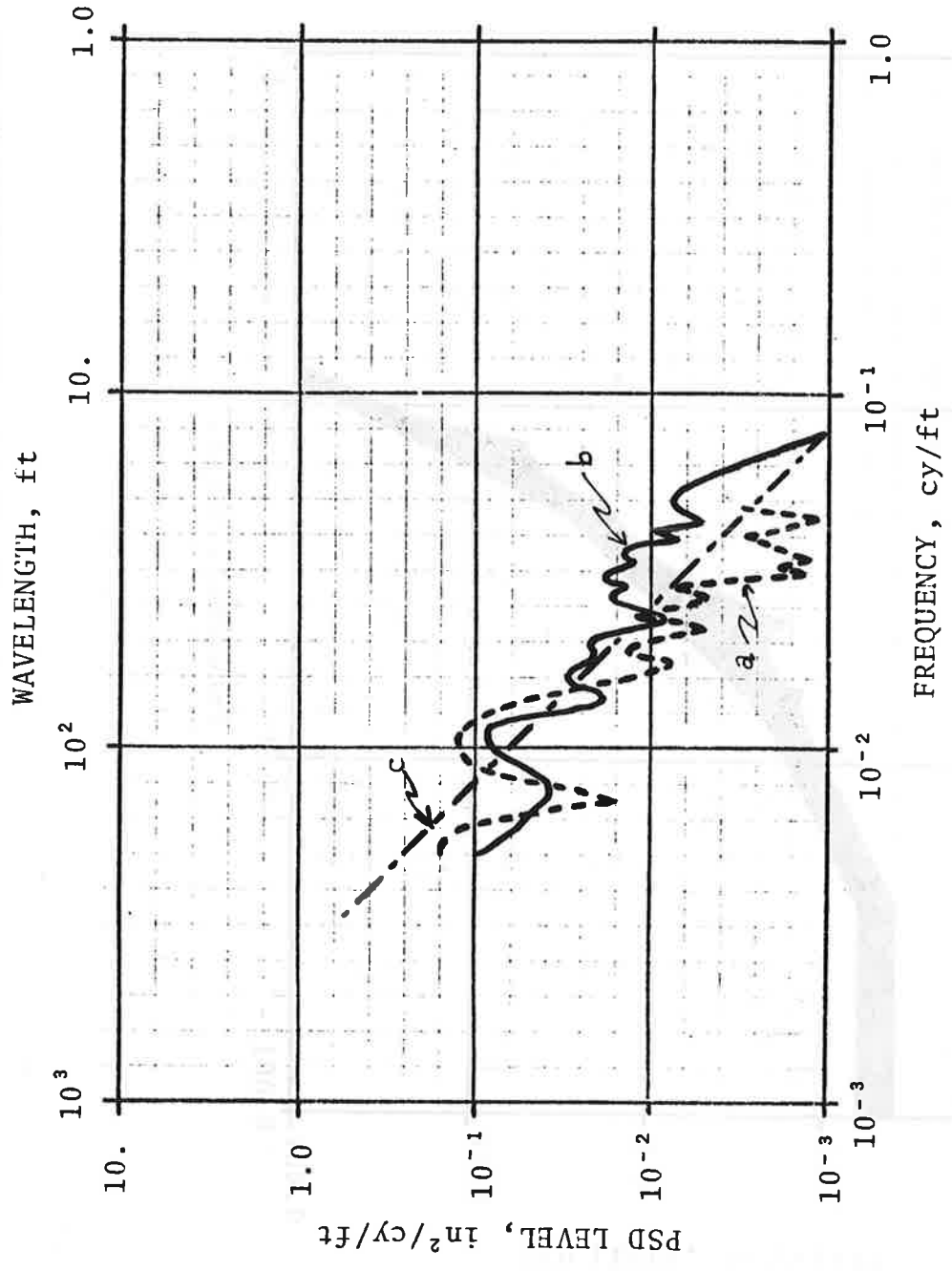


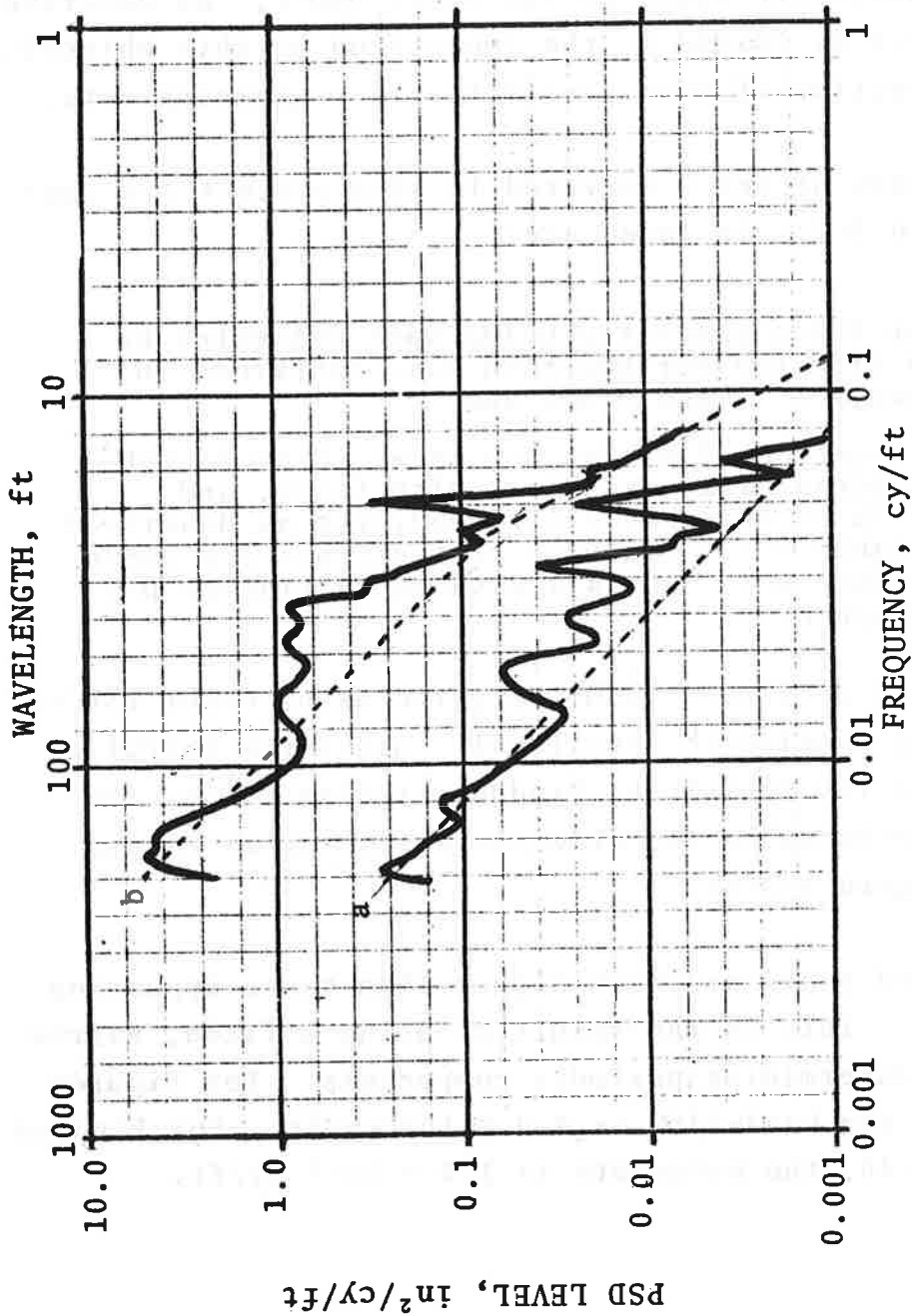
FIGURE D-28. RANGE OF GAGE SPECTRA FROM PITTSBURGH AREA, UNIT COAL TRAIN OPERATION (CLASS 2)



a) Profile, b) Crosslevel, c) Design PSD; 1 Km sample

FIGURE D-29 . SNCF ALIGNMENT AND PROFILE, PARIS-TOULOUSE LINE





- a) Laid 1967, upgraded prior to processing, 100 lb CWR, 2 Km sample.
- b) Laid 1933, 95 lb. CWR installed over original subgrade, metal ties, 1 Km sample.

FIGURE D-30. EXAMPLE OF TWO SNCF ALIGNMENT SPECTRA, COLLECTED VIA MAUZIN 10m (32.8') MCO

### D.3 PSD's GENERATED BY RAINBO

This section contains PSD's generated on this project. These PSD's satisfy the objective that they improve upon the reliability and the wavelength range of the older PSD's. As described in Paragraph 4.4.4, Volume 1, the imposition of this objective forced the rejection of most available track geometry data.

Some descriptions of track surveyed in this project are contained in Table D-2. Included are:

- Some PSD's generated using data collected by T-3 from the Northeastern U.S. contained in Figures D-31 and D-32, and
- Data collected by the TSD under TG-69.\* TSD collected data has a low noise floor, and the TG-69 data has a high pedigree as described in Table D-3. Features of the zones are shown in Table D-3. PSD's are shown in Figures D-33 through D-40.

The only notable departure from the patterns of older PSD's appears in long wavelength crosslevel. Since the output of T-3 CAS and the TSD crosslevel produce similar PSD's, the problem is attributed to the slave/de-slave action in the self-erecting gyro system.

Rainbo-generated peaks are much higher than those appearing in older PSD's. This is the result of using a fixed, narrow bandwidth for determining periodic components. For Figures D-31 and D-32, the bandwidth is  $8.0 \times 10^{-4}$  cy/ft. For Figures D-33 through D-40, the bandwidth is  $1.0 \times 10^{-3}$  cy/ft.

---

\*These data were processed in a previous exercise but profile and alignment were not handled properly.

TABLE D-2. SYNOPSIS OF PSD's DATA GENERATED UNDER THIS PROGRAM

	NEC and ENVIRONS 1977	Track Survey Device, Data from TG-69 (1973)
Mean Profile	Avg. T-3 Profilometers	Laser Tracker + Corrections
Individual Rail Profile	T-3 Profilometer	Laser Tracker + Crosslevel + Measurement Frame Dimensions
Mean Alignment	N/A	Laser Tracker + Corrections
Individual Rail Alignment	N/A	Laser Tracker + Gage + Crosslevel + Measurement Frame Dimensions
Crosslevel	Compensated Accelerometer System	Electronic Pendulum (Low Speed)
Gage	N/A	Hydraulically Loaded Wheels
Broken Down by Track Class	Class 6 thru Class 3	Class 6 thru Class 1
Territory Covered	Northeastern Area U.S. (NEA)	Area of Pueblo, Colorado
Resolution of Peaks	$8.0 \times 10^{-4}$ cy/ft	$1.0 \times 10^{-3}$ cy/ft
No. of Diagrams	2	8
Number of PSD's Per Range Diagram	4	5
Typical Length of Data/PSD	5 mi. to 25 mi.	700 ft. to 7000 ft.

TABLE D-3, SUMMARY OF CHARACTERISTICS OF  
TG-69 ZONES

<u>Zone</u>	<u>Speed Class by Geometry</u>	<u>Rail Weight, Mfr. &amp; Year</u>	<u>Joints</u>	<u>Rail Length, Stagger</u>	<u>Tie Centers &amp; Cond.</u>	<u>Ballast Depth &amp; Shoulders</u>	<u>Zone Length, Application &amp; History</u>
1	6++	1360 RE CC CF&I 1973	B6	39', 50%	19½"	S&, 22", 12" C	1.70 mi, Nh
2	6	10025 RE CC CF&I 1972	B6	39', 50%	23"	Gr, 17", 21" C	0.40 mi, U&
3	6+	1190 CC CF&I 1970	W	39', 18%	24"	Gr, 15", 12" P	0.36 mi, Nh
4	6+	1190 CC CF&I 1971	W	39', 36%	24"	Gr, 15", 21" C	0.59 mi, U&
5	6	1190 CC CF&I 1971	W	39', 50%	19½"	Gr, 18", 10" C	0.63 mi, Mh
6	4	1121 RE H COL. 1941	B4 LBFR	39', 50%T	23" CR	Gr, 6", N MW	0.30 mi, Ah
7	4	1121 RE OH COL. 1943	B4 LMB	36', 50% 39', 50%	20" BC	S&, 10", N MSW	0.57 mi, TMh
8	3	1150 RE CC CF&I 1951	B4 LMB	38', 45%	21½" CR	S&, N", N MSW	0.13 mi, Mh
9	2	COL. SEC903 1912-29 OH CF&I SEC 851 1905-08 8504 ILL. STEEL S. WKS 1904-06 CAMBRIA 85 1896-1903	B4 LM	33', V½	20" M	S&, 8", 6" L	0.64 mi, TS&
10	1	7506 ILL. STEEL S. WKS 1896-99	B4 LMBRX	28', 50%	20"	N, N", N" MCS	0.63 mi, S&

Legend

<u>Joints</u>	<u>Rail Lengths</u>	<u>Ballast</u>	<u>Applications &amp; History</u>
W Welded	T Typical	Gr Granite	N New
B4 Jointed, 4-hole	V Variable	S& Slag	U Slightly used
B6 Jointed, 6-hole		N Nondescript/None	M Main
L Loose Bolts	<u>Ties</u>	M Fouled with Mud	A Yard Approach
M Missing Bolts	B Battered	S Fouled with Sand	B Branch
B Battered Joints	R Rotten	P Polymer Stabilized	S Siding
R Broken Rails	C Crushed	W Asperities Worn	Y Yard
J Broken Joint Bus	M Missing	C Compacted	h Heavy
F Joint Bars applied at Rail Flaw		L Loose	ℓ Light
			T Taken out of service

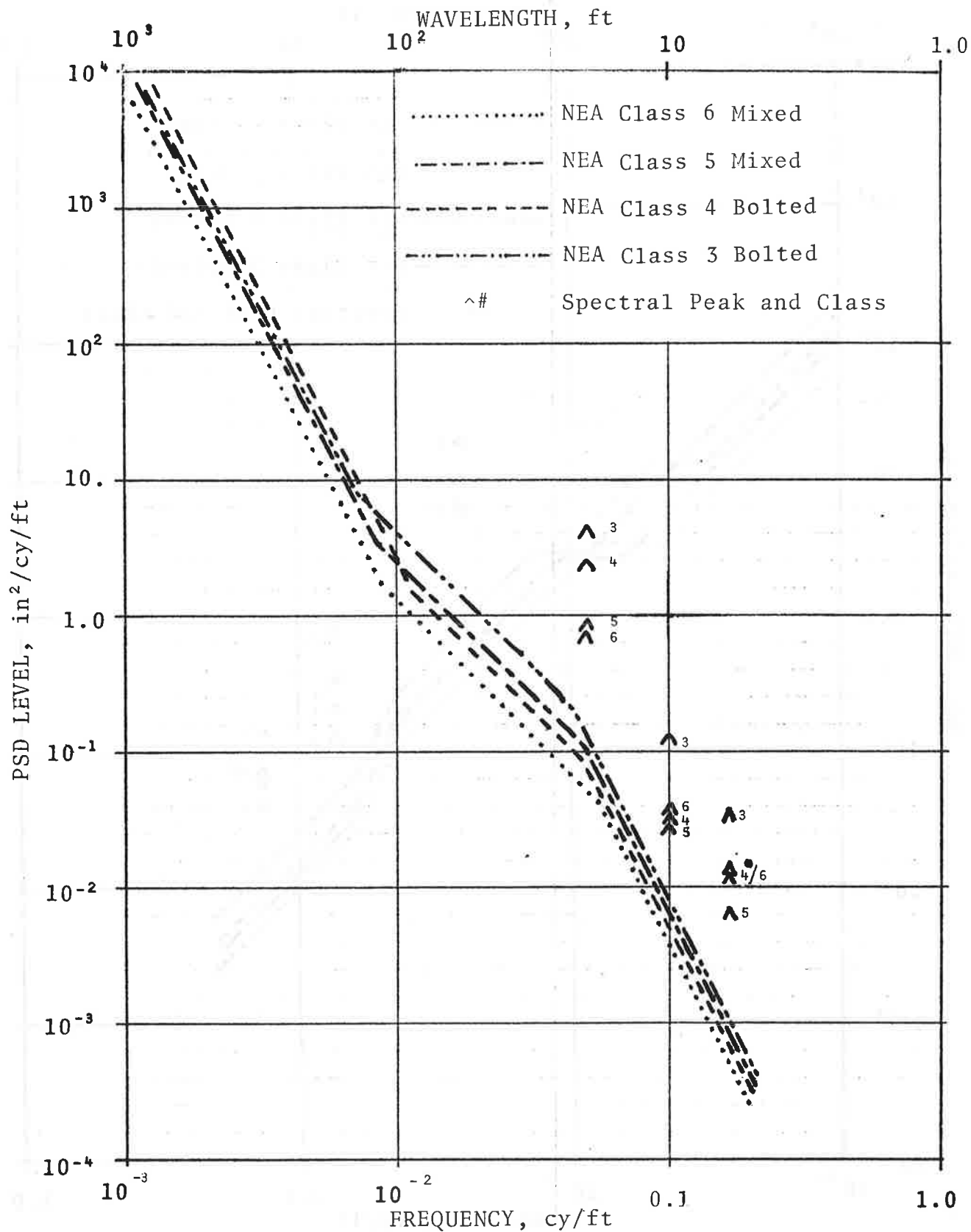


FIGURE D-31. MEAN PROFILE, NEA, VARIOUS CLASSES

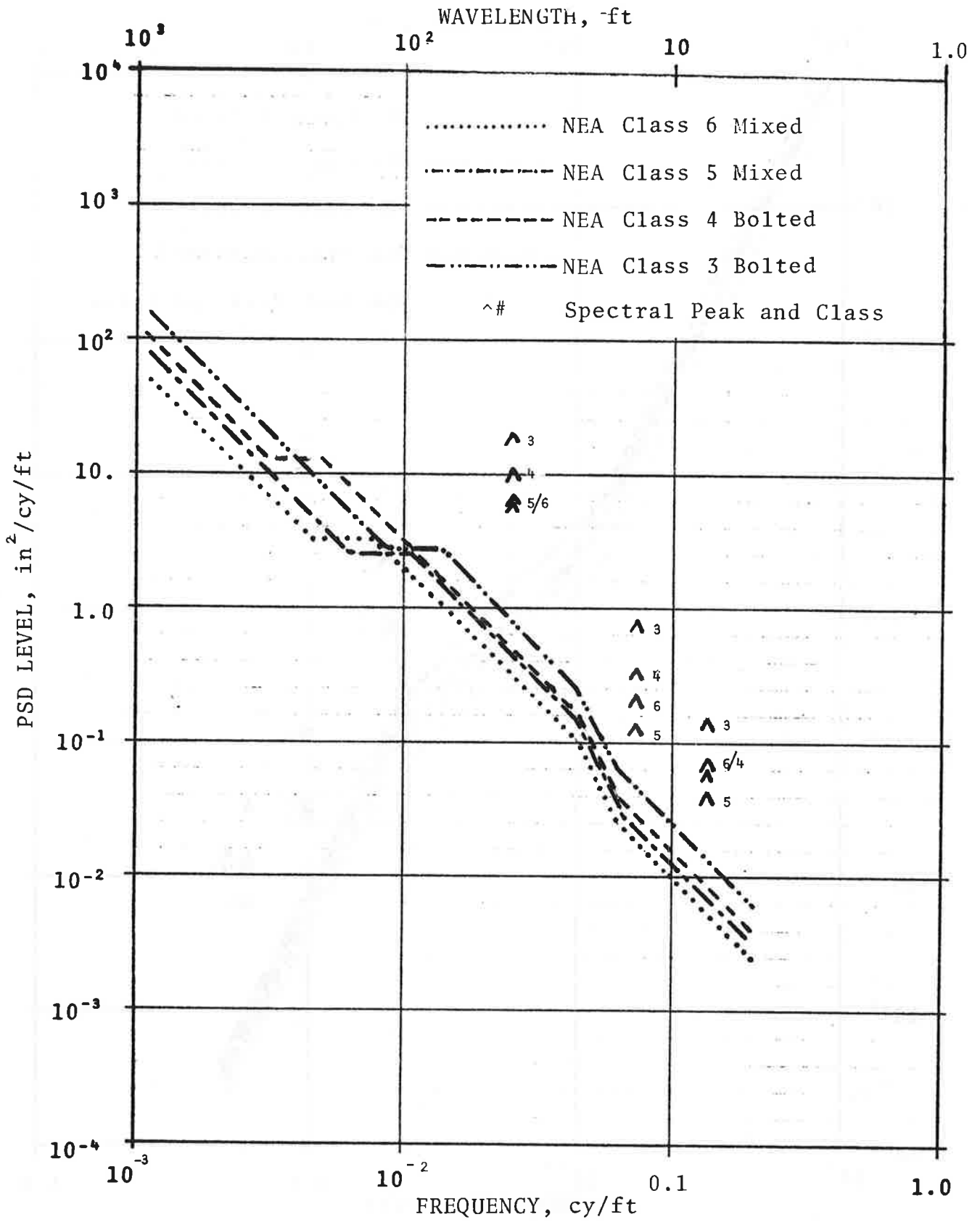


FIGURE D-32. CROSSLEVEL, NEA, VARIOUS CLASSES

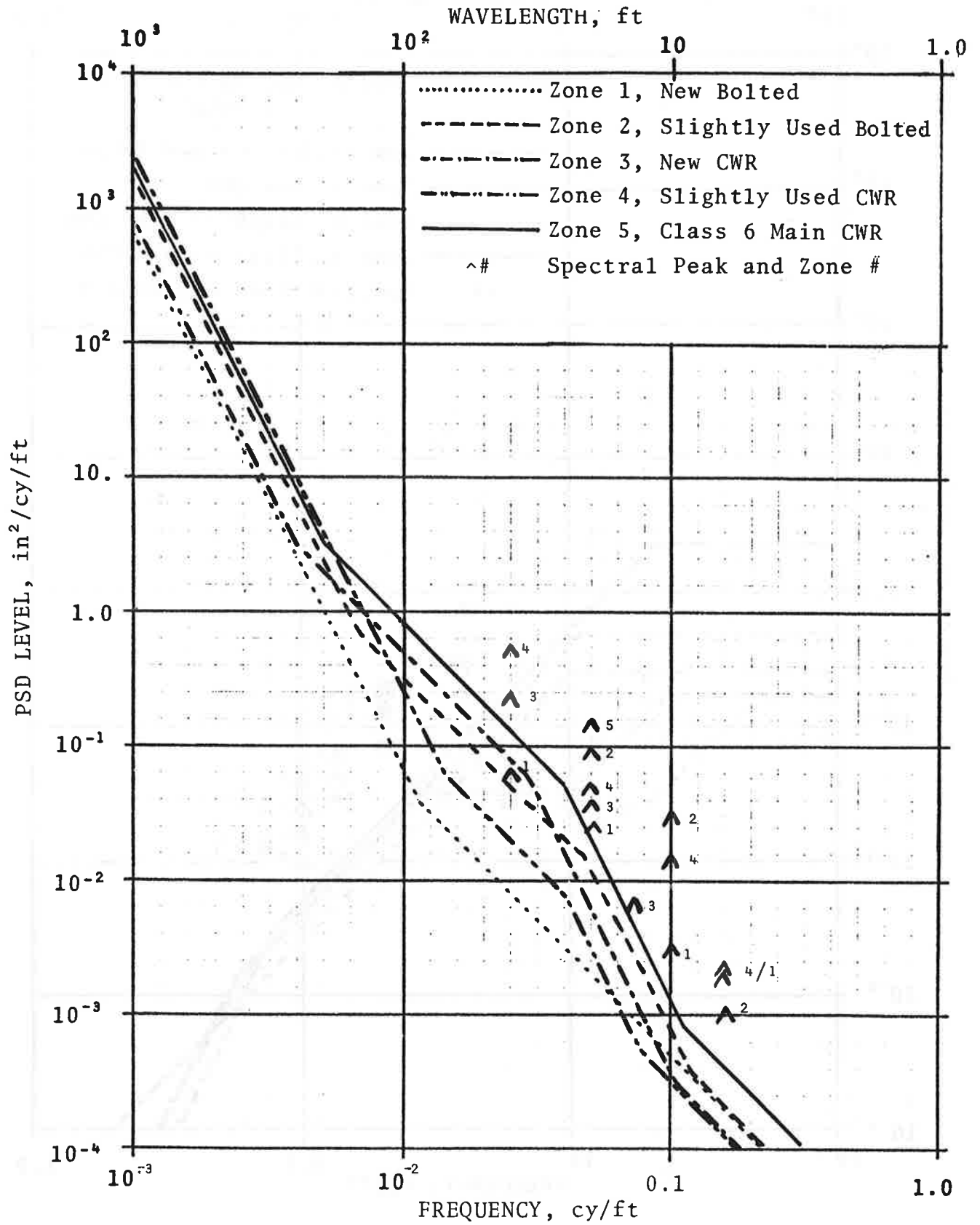


FIGURE D-33. MEAN PROFILE, CLASS 6 AND BETTER (TG-69)

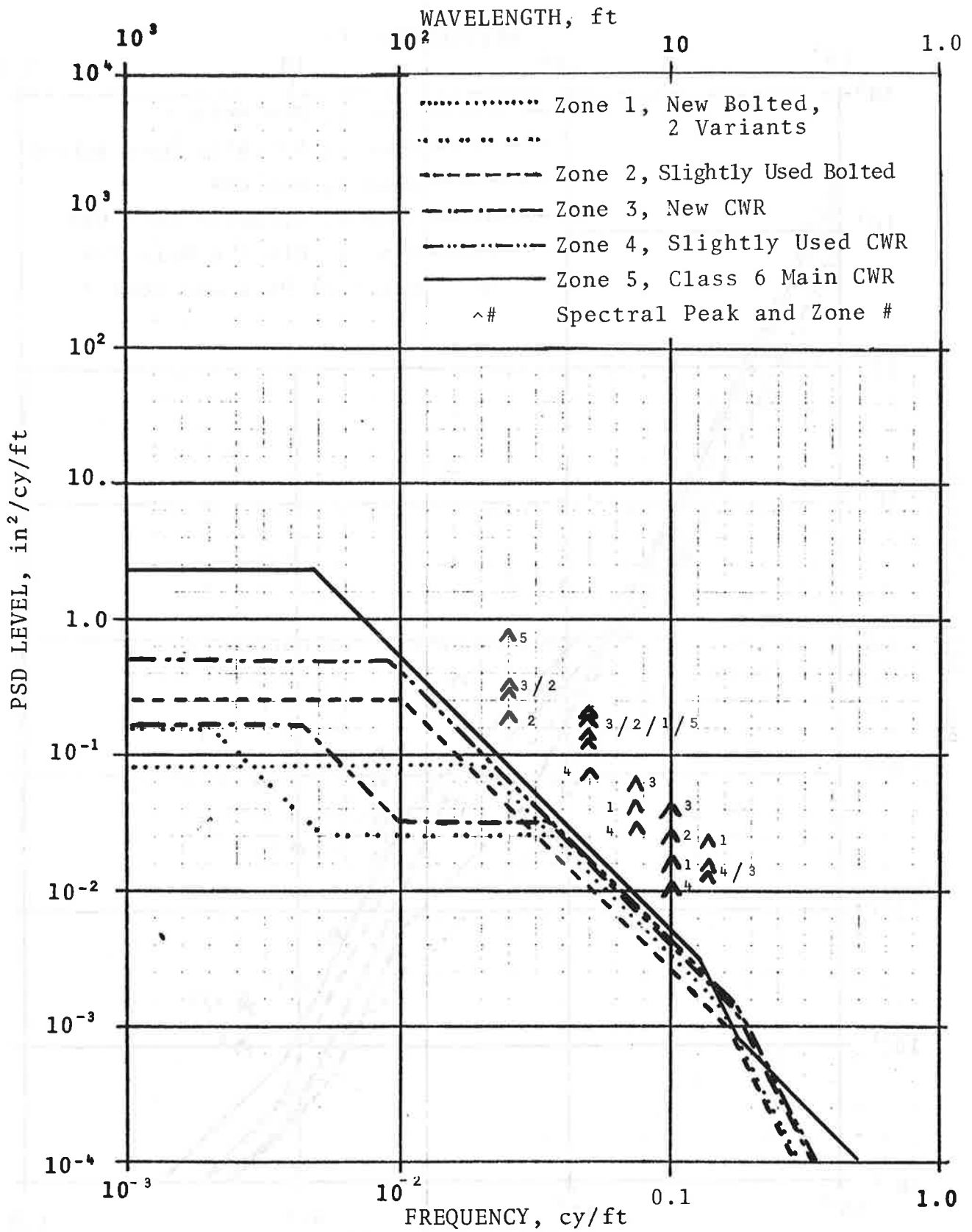


FIGURE D-34. CROSSLEVEL CLASS 6 AND BETTER (TG-69)



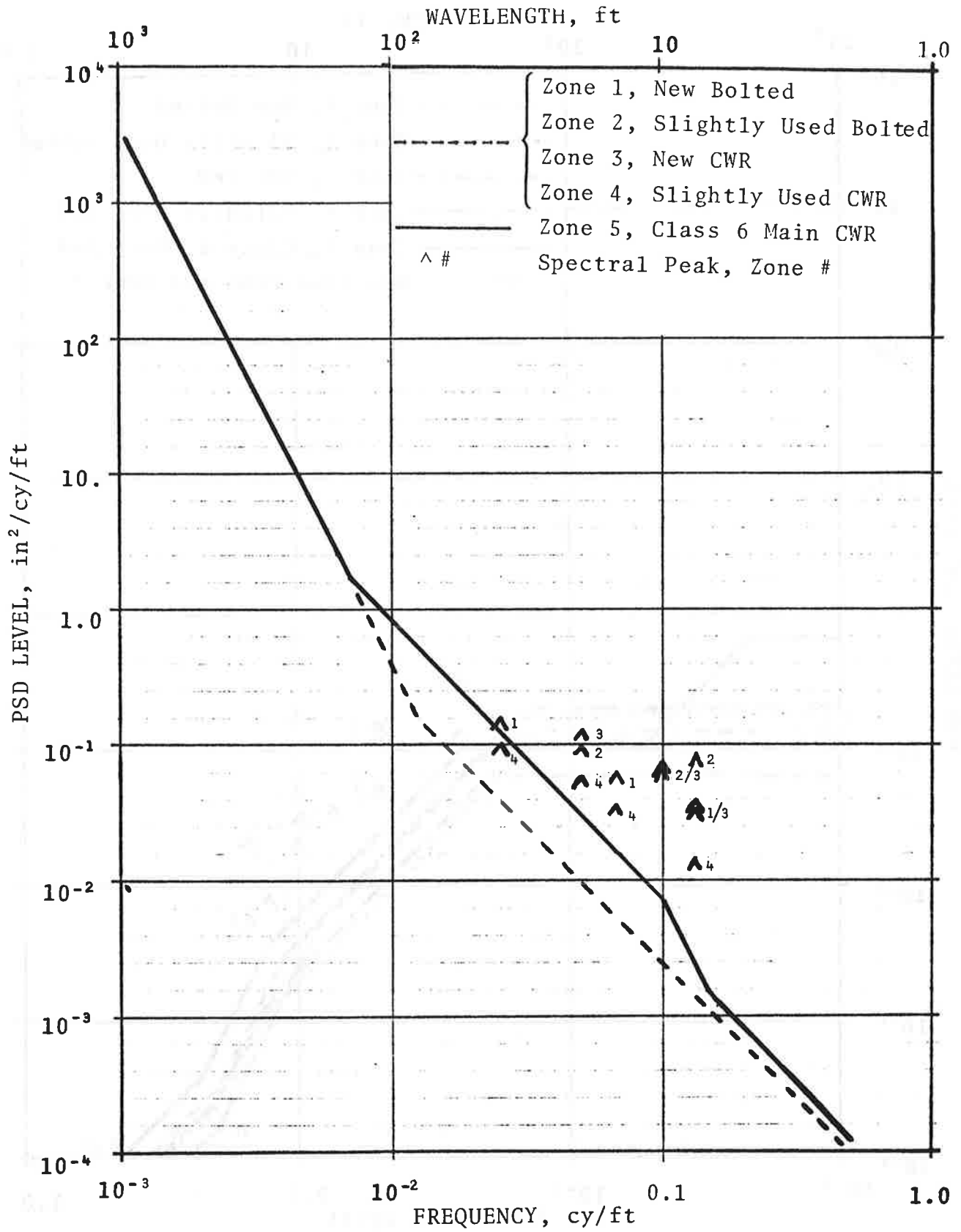


FIGURE D-35. MEAN ALIGNMENT, CLASS 6 AND BETTER (TG-69)

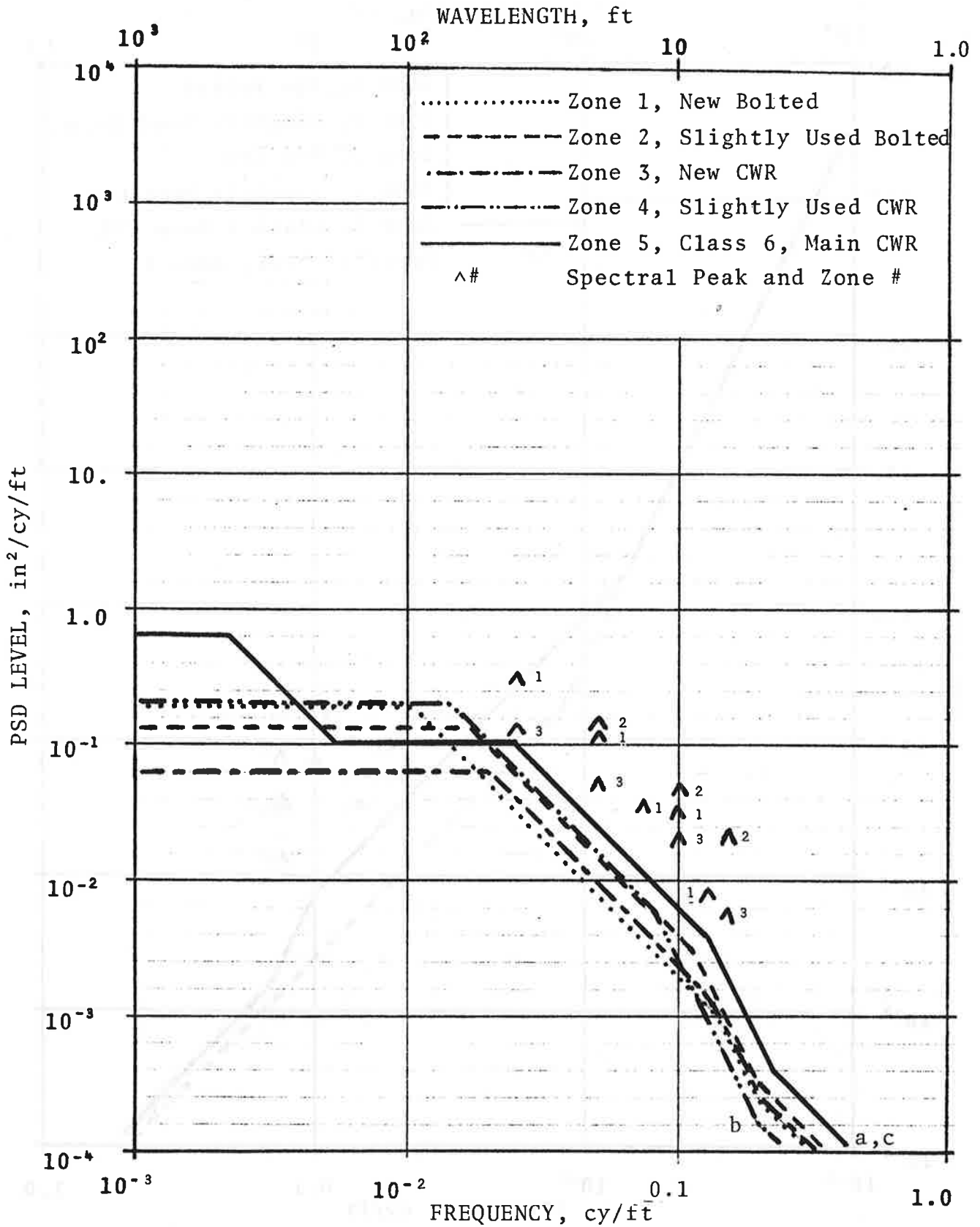


FIGURE D-36. GAGE, CLASS 6 AND BETTER (TG-69)

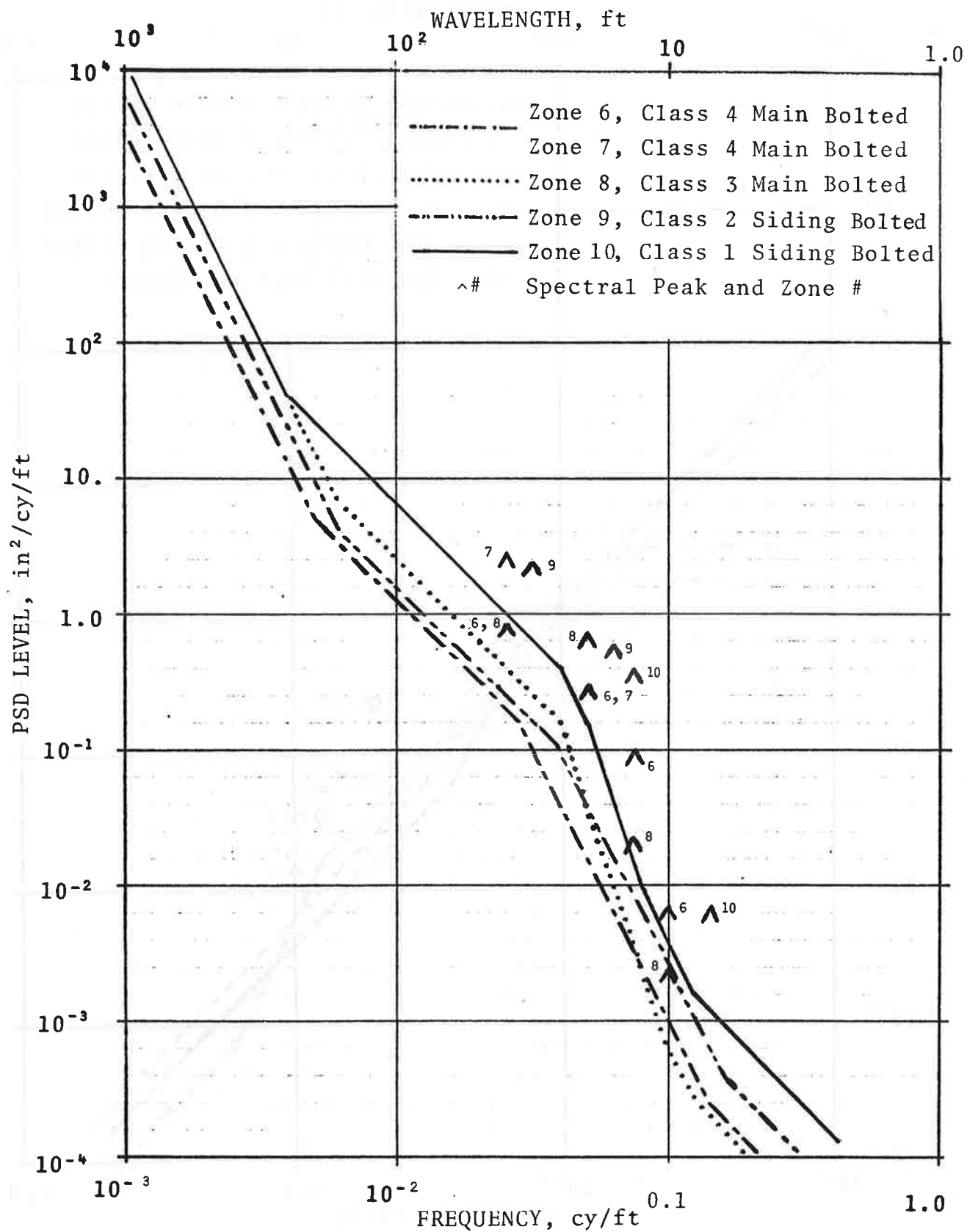


FIGURE D-37. MEAN PROFILE, VARIOUS BOLTED (TG-69)

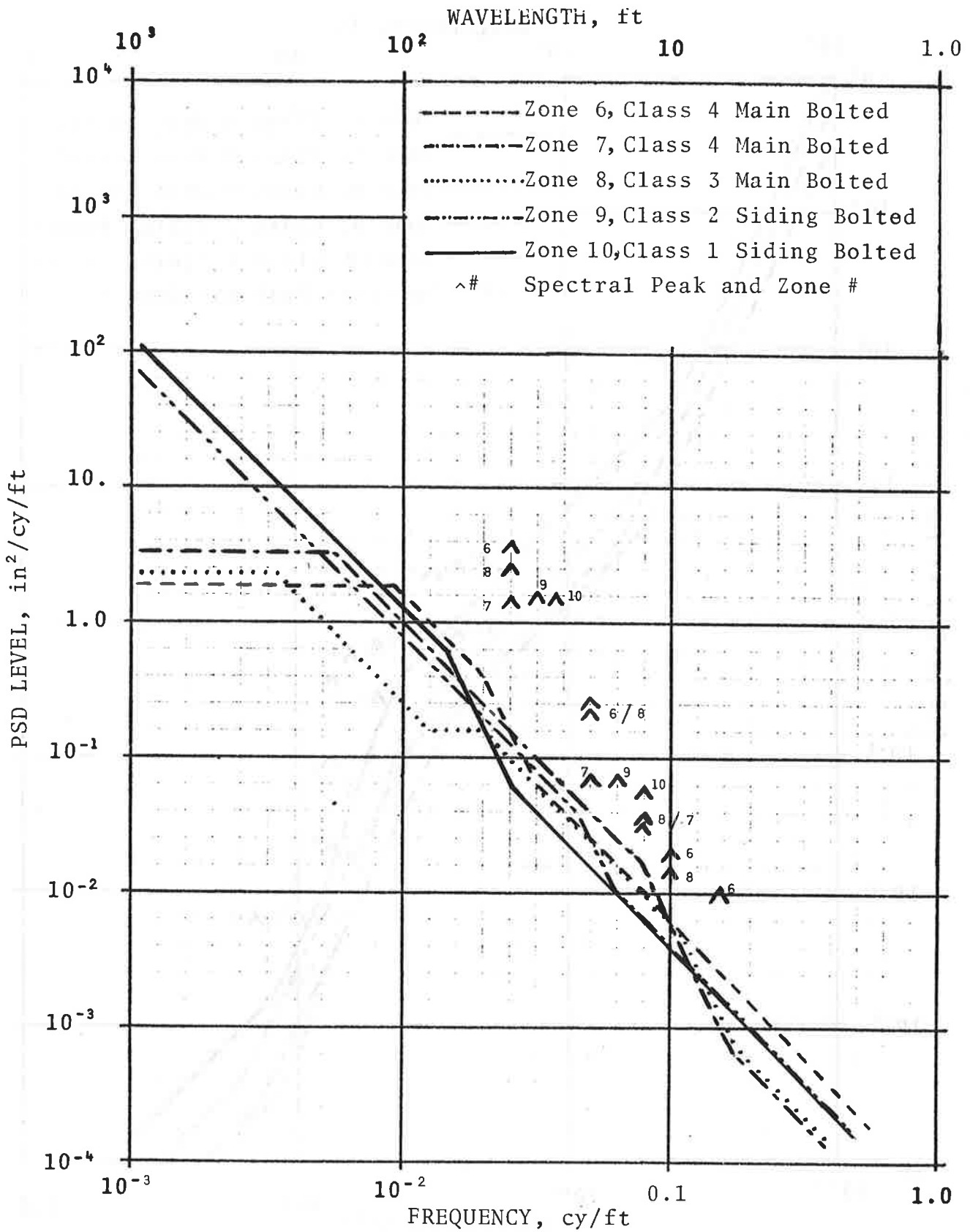


FIGURE D-38. CROSSLEVEL VARIOUS BOLTED (TG-69)

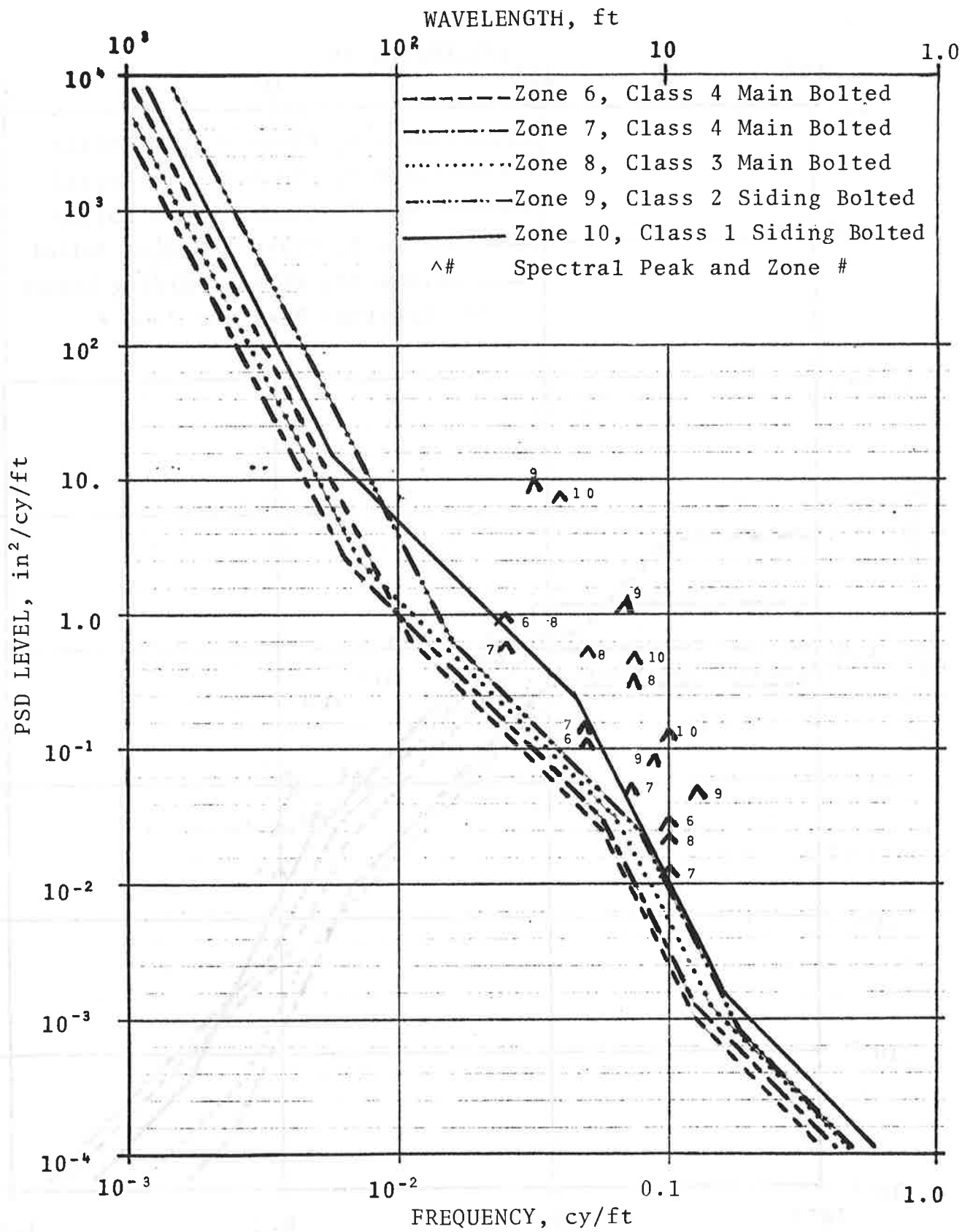


FIGURE D-39. MEAN ALIGNMENT, VARIOUS BOLTED (TG-69)

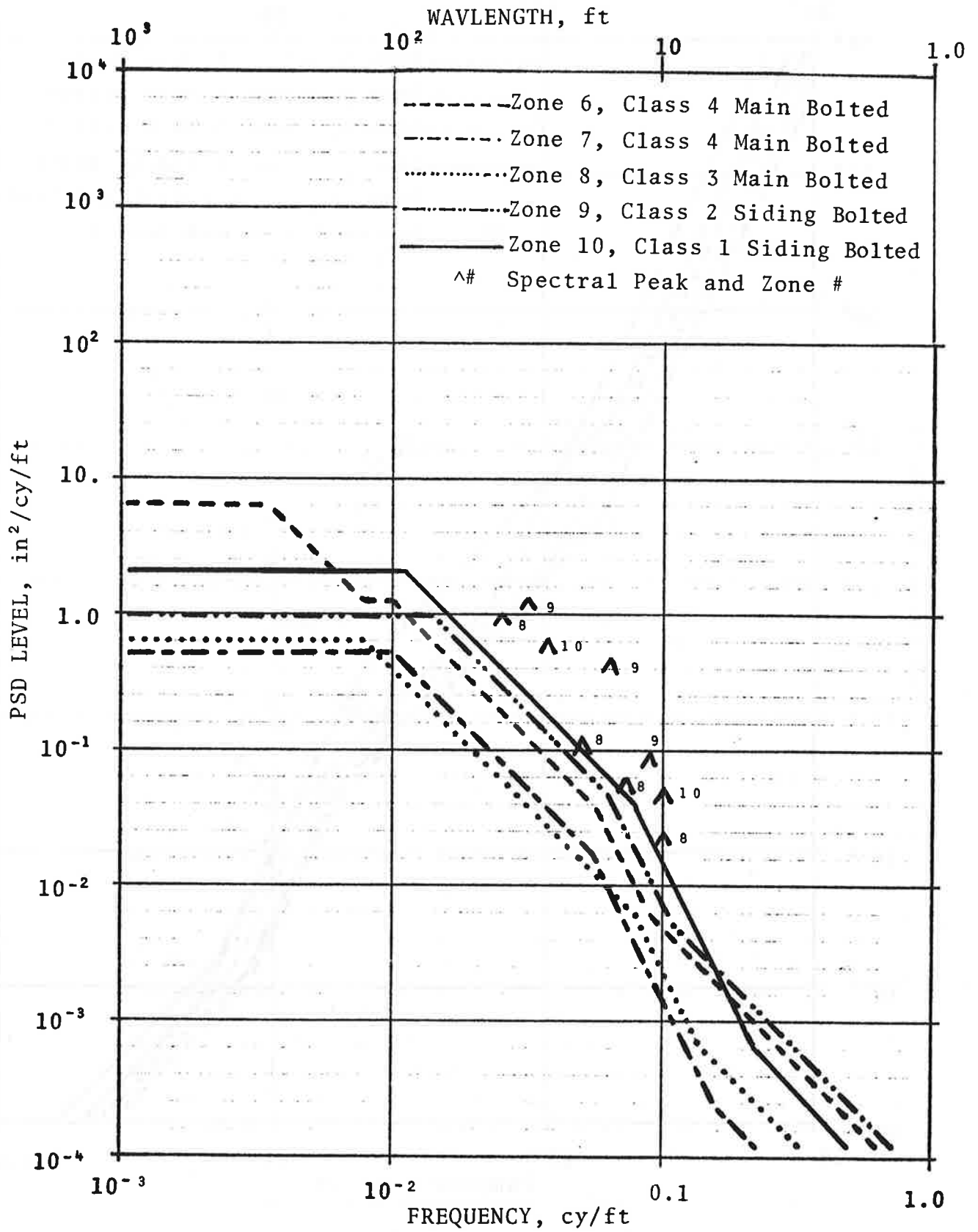


FIGURE D-40. GAGE, VARIOUS BOLTED (TG-69)

#### D.4 TABULATION OF AMPLITUDES, BREAK FREQUENCIES AND GEOMETRY MEASUREMENT PROPERTIES

The amplitudes and break frequencies of the continuum portion of the spectra shown in Figures D-31 through D-40 were evaluated. These are summarized in Tables D-4 for surface variables, and D-5 for line variables.

The continua for mean profile and alignment are attributed to a random walk. MCO's constructed on such random variations are best characterized by their standard deviations. These are listed in the first part of Table D-6.

Also recognizable in the PSD's of Figures D-31 through D-40 are the line spectral components that are associated with the PDP. The characteristics of this process were evaluated by applying the procedure described in Section 3.2, Volume 1, to individual rail profile and alignment PSD's (not shown). The mean joint amplitude, C, and the decay rate, k, were obtained and these are listed in Table D-6.

Using the formula:

$$\hat{\Delta} = \bar{C} [1 - e^{-k|S-L|}]$$

the worst case, 62 foot MCO,  $\hat{\Delta}$ , is evaluated. In the above,

S = 31 feet =  $\frac{1}{2}$  chord length

L = rail length (ft)

These results are summarized in Table D-6.

A regression analysis was performed on this data to ascertain the existence of any correlation between parameters and track class. Using these results, the characteristics of generic track classes implied by the FRA Track Safety Standards were derived. These results are summarized in Table 2 and Figure 1 of the main text, Vol I.

TABLE D-4. CONTINUUM PARAMETERS FOR SURFACE GEOMETRY

Zone Designator	Geometry Class	Profile				Crosslevel						
		$\phi_{13}$ , CY/ft $\times 10^{-3}$	$\phi_{14}$ , CY/ft $\times 10^{-3}$	$\phi_{15}$ , CY/ft $\times 10^{-2}$	$\bar{A}_1$ in <sup>2</sup> -CY/ft $\times 10^{-4}$	$\phi_{41}$ , CY/ft $\times 10^{-3}$	$\phi_{42}$ , CY/ft $\times 10^{-3}$	$\phi_{43}$ , CY/ft $\times 10^{-3}$	$\phi_{44}$ , CY/ft $\times 10^{-2}$	$\phi_{45}$ , CY/ft $\times 10^{-2}$	$\bar{A}_4$ in <sup>2</sup> -CY/ft $\times 10^{-4}$	
NEC	6	8.9	5.6	U	1.3	T	4.5	7.1	4.5	6.3	2.0	
NEC	5	7.9	5.0	U	2.0	T	6.3	11.2	4.5	7.1	3.2	
NEC	4	11.2	5.0	U	2.5	T	3.2	5.0	4.5	6.3	3.2	
NEC	3	7.1	4.5	U	4.0	T	8.9	14.1	4.5	6.3	5.0	
TG-69 Zone #	1	6++	11.2	A	A	0.05	{ A 2.0	{ A 5.0	{ 20.0 35.5	15.8	U	0.25
	2	6	7.1	5.0	12.6	0.32	A	A	10.0	17.8	U	0.32
	3	6+	4.0	2.8	10.0	0.50	4.5	10.0	35.5	17.8	U	0.40
	4	6+	14.1	4.0	7.9	0.13	A	A	8.9	17.8	U	0.40
	5	6	5.0	4.0	11.2	0.79	A	A	5.0	12.6	17.8	0.50
TG-69 Zone #	6	4	5.0	2.8	14.1	1.3	A	A	8.9	2.0	3.2	1.6
	7	4	5.0	2.8	14.1	1.3	A	A	5.6	7.9	17.8	1.0
	8	3	6.3	4.0 <sup>†</sup>	12.6	2.5	3.5	12.6	20.0	10.0	17.8	0.63
	9	2	6.3	4.0	15.8	1.6	T	A	A	4.5	6.3	0.8
	10	1	4.0	4.0 <sup>†</sup>	12.6	6.3	T	A	A	1.4	2.5	1.3

NOTES:

A - Degenerate case - set both frequencies to arbitrary but equal values.

T - Frequency below PSD range, set to  $10^{-3}$  cy/ft.

U - Frequency above folding, set to 0.5 cy/ft.

† - Best fit value - spectrum does not obey usual model.



TABLE D-5. CONTINUUM PARAMETERS FOR LINE GEOMETRY

Zone Designator	Geometry Speed/Class	Alignment				Gage						
		$\phi_{53}$ , CY/ft $\times 10^{-3}$	$\phi_{54}$ , CY/ft $\times 10^{-2}$	$\phi_{55}$ , CY/ft $\times 10^{-1}$	$A_5$ in <sup>2</sup> -CY/ft $\times 10^{-4}$	$\phi_{81}$ , CY/ft $\times 10^{-3}$	$\phi_{82}$ , CY/ft $\times 10^{-3}$	$\phi_{83}$ , CY/ft $\times 10^{-2}$	$\phi_{84}$ , CY/ft $\times 10^{-2}$	$\phi_{85}$ , CY/ft $\times 10^{-1}$	$A_8$ in <sup>2</sup> -CY/ft $\times 10^{-4}$	
69-GI	1	6++	12.6	A	A	0.25	A	A	1.0	14.1	2.0	0.20
	2	6	12.6	A	A	0.25	A	A	1.8	11.2	2.0	0.40
	3	6+	12.6	A	A	0.25	A	A	2.0	12.6	2.0	0.25
	4	6+	12.6	A	A	0.25	A	A	1.4	7.9	2.0	0.40
	5	6	7.1	10.0	1.4	0.63	2.2	5.6	2.5	12.6	3.2	0.63
69-GI	6	4	11.2	5.6	1.3	0.8	3.5	7.9	1.0	5.6	1.1	1.26
	7	4	6.3	5.6	1.3	1.0	A	A	1.0	5.6	0.9	0.50
	8	3	7.1	6.3	1.4	1.3	A	A	0.8	7.9	1.4	0.40
	9	2	15.8	7.9	1.8	1.6	A	A	1.4	6.3	1.1	2.00
	10	1	5.6	4.5	1.6	5.0	A	A	1.1	7.9	2.2	2.50

NOTES:

A - Degenerate case - set both frequencies to equal arbitrary values.

TABLE D-6. SUMMARY OF SRP AND PDP GEOMETRY IMPACT ON 62-FOOT MCO

				62 ft MCO, Continuum		PDP Characterization						
						Profile			Alignment			
						Joint Amplitude $\bar{C}$ (in)	Decay Rate, $k$ (ft <sup>-1</sup> )	62' MCO (in)	Joint Amplitude, $\bar{C}$ (in)	Decay Rate, $k$ (ft <sup>-1</sup> )	62' MCO (in)	
Zone Designator	Geometry Class	Rail Length (ft)	Joint Stagger %	Profile, Standard Error (in)	Alignment, Standard Error (in)							
NEC	6	39	50	0.27	N	0.19	0.20	0.15	N	N	N	
NEC	5	39	50	0.32	N	0.19	0.14	0.13	N	N	N	
NEC	4	39	50	0.43	N	0.18	0.16	0.13	N	N	N	
NEC	3	39	50	0.42	N	0.27	0.22	0.22	N	N	N	
# zone 69-GI	1	6++	39	50	0.06	0.15	0.06	0.25	0.05	0.09	0.40	0.09
	2	6	39	50	0.08	0.15	0.10	0.40	0.10	0.17	0.71	0.17
	3	6+	39	18	0.12	0.15	0.09	0.40	0.09	0.16	0.89	0.16
	4	6+	39	36	0.11	0.15	0.07	0.35	0.07	0.08	0.45	0.08
	5	6	39	50	0.16	0.17	0.10	0.22	0.08	0.13	0.40	0.13
# zone 69-GI	6	4	39	50	0.20	0.24	0.18	0.18	0.13	0.15	0.16	0.11
	7	4	{36 39}	50	0.20	0.20	0.23	0.10	0.08	0.11	0.28	0.09
	8	3	38	45	0.31	0.24	0.26	0.13	0.16	0.19	0.22	0.15
	9	2	33	Var.	0.25	0.44	0.21	0.13	0.05	0.27	0.18	0.08
	10	1	28	50%	0.44	0.43	0.15	0.16	0.06	0.17	0.25	0.13

APPENDIX E  
SYSTEM NOISE FLOORS

E.1 LIST OF SYMBOLS

- d = displacement, (in)
- f = temporal frequency, (Hz)
- $f_c$  = folding frequency, (Hz)
- $f_o$  = bandwidth
- L = MCO length, (ft)
- $M(f), N(\phi)$  = noise PSD's as a function of f or  $\phi$ . Subscripts indicate parameter.  $N(\phi) = vM(f)$ , (in<sup>2</sup>/cy/ft)
- $\hat{M}(f), \hat{N}(\phi)$  = noise PSD's after allowing for folding
- N = number of samples per overlapping sequence
- n = counting index
- $n_o$  = number of sample intervals between TSD and closest approach to laser
- $P(\phi)$  = instrument power response as a function of  $\phi$ . Super/subscripts indicate Input/Output.
- R = sequence overlap range, (ft)
- r = wheel radius roughness, (in)
- s = space curve offset, (in)
- u, u', u'' = composite, first pass, and second pass error contaminations of x, x', and x'', respectively usually subscripted.
- $V(n)$  = variance of TSD error as a function of sample intervals from laser, (in<sup>2</sup>).
- $V_\delta(L)$  = variance of MCO, length L, (in)<sup>2</sup>
- v = train speed, (ft/sec)
- W = distance between two measurement planes, (ft)

$X$  = sample interval, (ft)  
 $x, x', x''$  = composite, first pass, and second pass profile values - usually subscripted (TSD).  
 $\alpha$  = weighting coefficient - usually subscripted  
 $\delta$  = MCO, (in)  
 $\delta, \delta', \delta''$  = composite, first pass, and second pass profile short MCO's - usually subscripted (TSD)  
 $\delta$  = Kronecker delta =  $\begin{cases} 0, & m \neq n \\ 1, & m = n \end{cases}$   
 $\epsilon, \epsilon', \epsilon''$  = composite, first pass, and second pass error contaminations of  $\delta, \delta',$  and  $\delta''$  respectively, usually subscripted (TSD)  
 $\theta$  = crosslevel, (in)  
 $\rho$  =  $\phi_c / f_0$ , (sec/ft)  
 $\sigma$  = standard error (units of parameter). Subscripts indicate parameter.  
 $\sigma_\delta(L)$  = standard error, MCO of length L, (in)  
 $\phi$  = spatial frequency, (cycles/ft)  
 $\phi_c$  = folding frequency, (cycles/ft)  
 $\omega$  = angular velocity  
 $[ ]$   $\Rightarrow$  Mod by 2N

## E.2 SINGLE PLANE MEASUREMENTS

### E.2.1 DISPLACEMENT NOISE FLOORS

Typical displacement measurements performed in the FRA track survey cars include:

- Truck to rail distances as used in the discontinued capacitive beam and in all gage systems;

- Car body to truck distances as used in cross-level systems; and
- Journal to inertial platform distance as used in the profilometer.

All of these systems experience random noise fluctuations typified by a noise spectrum that is white below  $f_0$  and given by

$$M_d(f) = \begin{cases} M_d(0) & 0 \leq f \leq f_0, \\ 0 & f_0 < f < \infty. \end{cases} \quad (E-1)$$

By Parseval's theorem, the standard error is related to  $M_d(0)$  and  $f_0$  by,

$$\sigma_d^2 = \int_0^{\infty} M_d(f) df = M_d(0)f_0. \quad (E-2)$$

Data is sampled on the FRA track measurement cars without the benefit of anti-alias filtering. This does not cause a serious problem, since noise levels are generally low, and the spectra of measurable rail defects at folding rolls off at  $f^{-2}$  or better. Since  $f_0 \gg f_c$ , the energy,  $\sigma_d^2$ , is distributed uniformly over the range of frequencies  $(0, \phi_c)$ ; and the noise floor is given by,

$$\hat{N}_d(\phi) = \hat{N}_d(0) = \frac{\sigma_d^2}{\phi_c} = 2X\sigma_d^2, \quad 0 \leq \phi \leq \phi_c. \quad (E-3)$$

Note that the noise floor is sample interval dependent.

Incorporating anti-alias filtering can improve the noise floor. If a constant wavelength corner frequency is matched to the folding frequency,  $\phi_c$ , then

$$\hat{N}_d(\phi) = V\phi_c N_d(0) = v\rho\sigma_d^2, \quad 0 \leq \phi \leq \phi_c. \quad (\text{E-4})$$

represents a speed-dependent noise floor where the increased time-between-samples at lower speeds allows noise reduction by signal averaging.

Typical  $\sigma$ 's for FRA displacement measurements are tabulated in Table E-1. These values are based on the Validation Report\*, and on recent repeatability tests. Graphical representations of the associated PSD's for currently employed sample rates are shown in Figure 33, Volume I of this report.

### E.2.2 ACCELEROMETER NOISE FLOOR

Profile and alignment can be determined by single-plane inertial measurements. Conceptually, the output of a transverse accelerometer is double integrated to give an uncolored space curve. As pointed out in Paragraph 3.1.3, Volume I of this report, such a simplistic view is fraught with fallacy. Spatial and temporal double integration is an abstract operation. However, for spectral analysis, it is easily modeled in the frequency domain.

The violent environment of the truck is a source of problems. Direct-mount accelerometers must be rugged and have excessively high noise floors. To help overcome the problems, the profilometer concept was developed.

The profilometer design is shown in Figure E-1. It consists of an isolated massive platform on which an accelerometer is placed. The platform is suspended on a spring-damped linear bearing system which allows only vertical movement relative to rolling axle and which cushions the accelerometer against shocks. Vertical motion between mass and axle is measured with a Linear Voltage Displacement Transducer (LVDT).

---

\* T-L. Yang, "FRA Track Geometry System Validation Report," FRA Report No. FRA-ORD&D-73-08, June 1974.

TABLE E-1. SUMMARY OF SYSTEM PERFORMANCE DATA

		STANDARD DEVIATIONS											
		Gage			Profile			Alignment			Crosslevel		
		MainLine	Yard	MainLine	Yard	MainLine	Yard	MainLine	Yard	MainLine	Yard	MainLine	Yard
Loaded Manual Versus Electronic	High	0.055"	0.130"	0.060"	0.275"	0.065"	0.255"	0.100"	0.190"				
	Avg.	0.045"	0.100"	0.035"	0.250"	0.050"	0.245"	0.075"	0.140"				
	Low	0.035"	0.070"	0.025"	0.225"	0.035"	0.220"	0.040"	0.080"				
Electronic System Repeatability	High	0.035"		0.045"		0.065"		0.045"					
	Avg.	0.025"		0.025"		0.030"		0.030"					
	Low	0.010"		0.005"		0.015"		0.015"					
Unloaded Manual Repeatability	High	0.045"		0.030"		0.035"		0.080"					
	Avg.	0.040"		0.020"		0.030"		0.035"					
	Low	0.010"		0.010"		0.015"		0.015"					

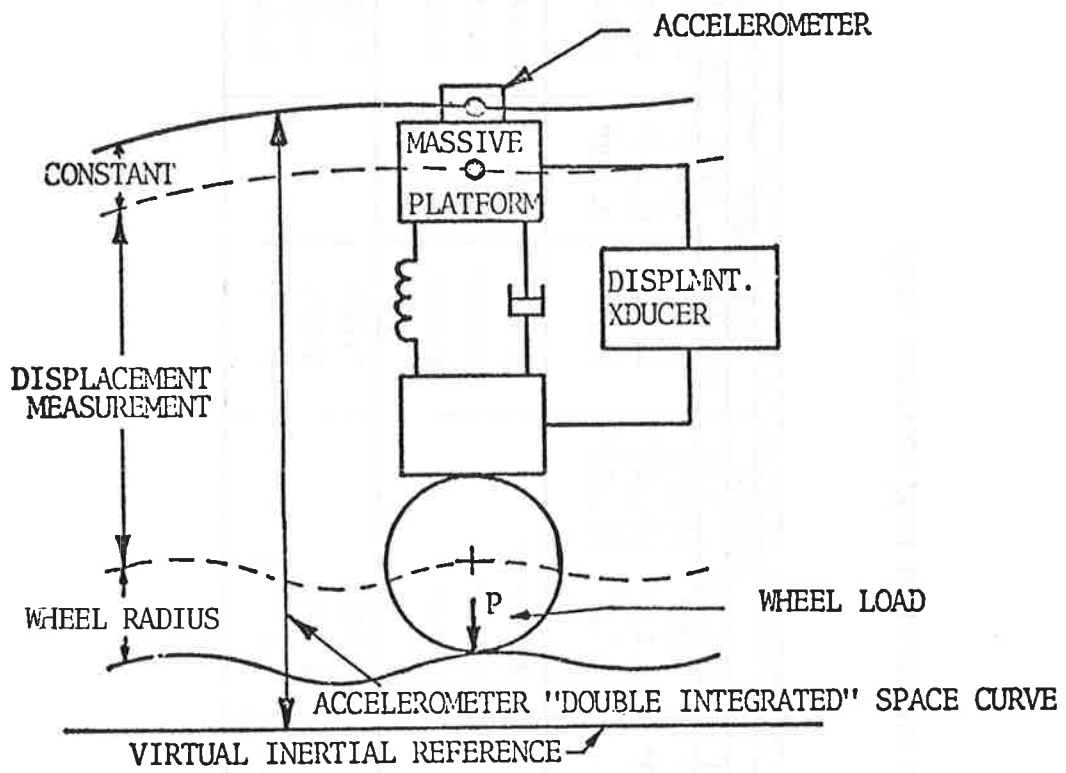


FIGURE E-1. PROFILOMETER SYSTEM



In concept, the output of the accelerometer is "double integrated" and the LVDT is subtracted to obtain an inertial measurement of the rail surface. At present, the profilometer utilizes  $\pm 10g$  servo accelerometer. Effective noise consists of random components whose rms level is  $\sigma = 5.0 \times 10^{-3} g$  for a bandwidth of  $f_0 = 150$  Hz. Other errors not included in this analysis are non-linearity and cross-axis/rotational sensitivity. Hysteresis is not a problem, because the units are mounted on the truck, and the high frequency environment found there "dithers" the accelerometer jewel bearings.

Experimentally, the noise spectrum for the accelerometer output is:

$$M_a(f) = \frac{\sigma_a^2}{f_0} = M_a(0), \quad 0 \leq f \leq f_0, \quad (E-5)$$

$$M_a(0) = 0.025 \text{ (in/sec}^2\text{)}^2/\text{Hz}. \quad (E-6)$$

The accelerometer output is double integrated to obtain space curves so that:

$$M_{ffa}(f) = \frac{M_a(0)}{(2\pi f^4)}. \quad (E-7)$$

When converted to distance-based, or  $\phi$  spectra, there results,

$$N_{ffa}(\phi) = \frac{N_a(0)}{v^3(2\pi\phi)^4}. \quad (E-8)$$

After the data is sampled, power at frequencies over  $\phi_c$  combines with power at frequencies less than  $\phi_c$ . Since  $\phi_c \ll \phi_0$ , this results in a noise spectrum given by,

$$N_{ffa}(\phi) = \frac{N_a(0)}{v^3(2\pi)^4} \left[ \frac{1}{\phi^4} + \frac{1}{(2\phi_c - \phi)^4} \right], \quad 0 \leq \phi \leq \phi_c. \quad (E-9)$$

This is the noise spectrum of the accelerometer data only. Ignoring the folding term, its noise spectrum varies as  $\phi^{-4}$  and  $v^{-3}$ . Thus low speeds adversely affect long wavelength performance. The accelerometer's contribution, as a function of speed and sample interval, is displayed in Figure 34, Volume I of this report.

The total profilometer noise floor includes accelerometer noise, LVDT (displacement) noise, wheel eccentricity, bearing and wheel tread roughness, and tread conicity effects. Equation (E-9) modified to account for all errors gives a space-curve noise spectrum,

$$\hat{N}_s(\phi) = \hat{N}_{ffa}(\phi) + \hat{N}_d(\phi) + \hat{N}_r(\phi), \quad (\text{E-10})$$

where statistical independence of noise sources is assumed. The combined effects of  $N_{ffa}(\phi)$  and  $N_d(\phi)$  (from the previous paragraph) are shown in Figure 34, Volume I of this report. It reveals that useful profilometer output can be obtained at about 10 mph. It also confirms that an accelerometer, by itself, is the ideal tool for characterizing the very short rail roughness wavelengths. Some discussion, along with empirical noise spectra for  $N_r(\phi)$ , are provided in Paragraph 3.1.5, Volume I of this report.

### E.2.3 GRAVITATIONAL ANGLE

The variable error components from instruments used to establish the gravitational vertical, differ little from those found in the displacement measurements. For a properly calibrated system, this will be the primary component of noise. The noise floor PSD can be found by using data from Table E-1 together with Figure 33, Volume I.

Detailed analysis of crosslevel systems is quite involved, since they depend on inertial components. The older self-erecting gyro system is examined in the Yang Validation Report. In addition to its other faults, data were collected with it for many years while an incorrect sign applied to two sensor contributions went undiscovered. This anomaly was rediscovered as described in Paragraph 3.1.5, Volume I. Paragraph 3.1.3 in Volume I describes some conceptual errors in the Compensated Accelerometer System (CAS) that were recently corrected.

### E.3 MULTI-PLANE MEASUREMENTS

Multi-plane measurements are those that are distributed longitudinally along the track and which relate to the track at two or more points. The need for such measurements introduces chordal response functions which make the measurements totally unresponsive to certain wavelengths. Examples of systems used by FRA and other track survey cars include curvature, a 2-plane system, and Mid-Chord Offsets (MCO's), a 3-plane system. Warp and runoff are examples of other two-plane measurements.

#### E.3.1 THE CURVATURE SYSTEM

The heart of the curvature system is a rate of turn gyro. If the gyro axis could be aligned instantaneously tangent to the rail, the output of the gyro could be treated as a single plane measurement. However maintaining axis tangency with any degree of accuracy would require mounting the gyro on the truck. It is believed that the gyro could not survive the rugged environment were it placed so near to the rail.

Accordingly, the gyro is placed in the car body. Two displacements relate the gyro axis to the rail at each truck.

The relations are shown schematically in Figure E-2. Since the effects of displacement error are well defined, they will be ignored for the present.

Gyro noise is of the form,

$$M_{\omega}(f) = \begin{cases} M_{\omega}(0), & 0 \leq f \leq f_0, \\ 0 & f_0 < f < \infty. \end{cases} \quad (\text{E-11})$$

Power response of the measurement is given by a mixture of temporal and spatial terms:

$$P_{\omega}^S(f, \phi) = [4\pi f \sin(\pi\phi W)]^2. \quad (\text{E-12})$$

The noise spectrum for a space curve is given by

$$\begin{aligned} N_S(f, \phi) &= P_{\omega}^S(f, \phi) M_{\omega}(f), \\ &= \frac{36W^2 M_{\omega}(0)}{\{4\pi f \sin(\pi\phi W)\}^2}, \quad 0 < f < f_c. \end{aligned} \quad (\text{E-13})$$

Using forward velocity to convert  $f$  to  $\phi$  gives the following speed dependent noise floor:

$$N_S(\phi) = \frac{36W^2 M_{\omega}(0)}{v \{4\pi\phi \sin(\pi\phi W)\}^2}, \quad 0 < \phi < \frac{f_c}{v}. \quad (\text{E-14})$$

Note that for  $\phi$  small, the noise  $\phi$  floor is given by:

$$N_S(\phi) \sim \frac{1}{v\phi^4}. \quad (\text{E-15})$$

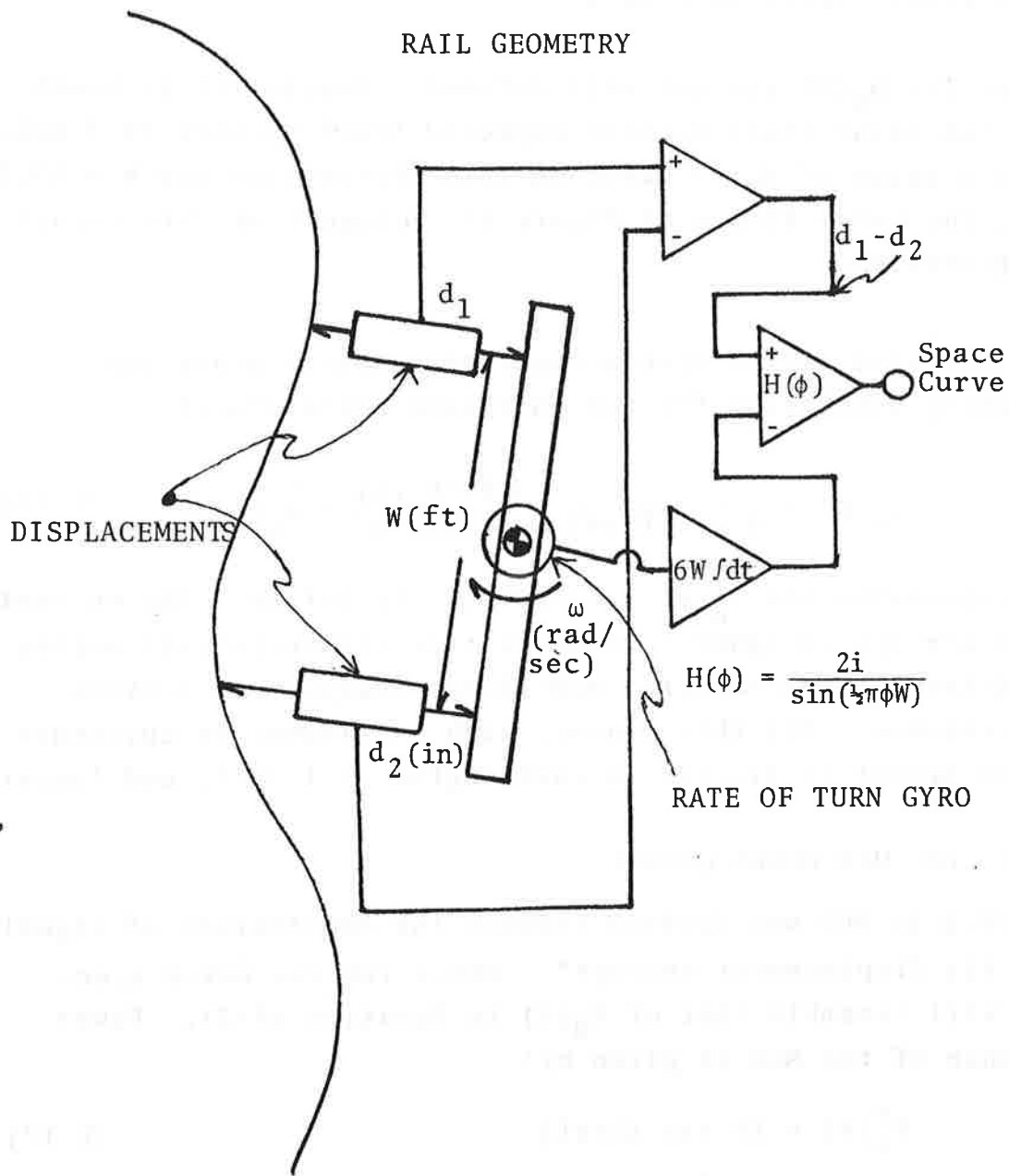


FIGURE E-2. CONCEPT OF SYSTEM FOR TWO-PLANE MEASUREMENT OF CURVATURE

Again, the  $\phi^{-4}$  noise floor is peculiar to all systems used to obtain long wavelength profile/alignment. Unlike the accelerometer derived space curve, the elevation of the noise floor varies only as  $v^{-1}$ .

Values for  $M_{\omega}(0)$  are not well defined. However it is known that the noise floor exceeds expected track spectra at 2 mph. Using a value of  $M_{\omega}(0)$  based on this observation and  $W = 59.5$  feet, the noise floors of Figure 35, Volume I of this report are generated.

The inclusion of the displacement transducers gives the following expression for the curvature noise floor:

$$\hat{N}_s(\phi) = \frac{1}{4 \sin^2(\pi\phi W)} \left[ \frac{9W^2 M_{\omega}(0)}{(X\pi\phi)^2 v} + \hat{N}_d(\phi) \right]. \quad (E-16)$$

The expression for  $\hat{N}_d(\phi)$  is difficult to define. The current curvature system ignores relative truck-track lateral motion. Its determination requires non-linear analysis of vehicle yaw response. For this reason, high confidence in curvature system output is limited to wavelengths of 150 ft. and longer.

### E.3.2 THE MID-CHORD OFFSET

The 14.5 ft MCO was derived through the combination of signals from six displacement sensors\*. Hence its raw noise spectrum will resemble that of  $\hat{N}_d(\phi)$  in Equation (E-3). Power response of the MCO is given by:

$$P_s^{\delta}(\phi) = 16 \sin(\frac{1}{2}\pi\phi L) \quad (E-17)$$

Hence

$$\hat{N}_s(\phi) = \frac{\hat{N}_d(0)}{16 \sin(\frac{1}{2}\pi\phi L)}, \quad 0 < \phi < \phi_c \quad (E-18)$$

---

\*W. W. Gunn, "DOT Test Train Program System Instrumentation Manual - Seventh Edition," Annual Report, FRA-OR&D-76-254, June 1976.

The noise floors are displayed in Figure 36, Volume I of this report. Typical values of  $N_{\delta}(0)$  data from Table E-1 were used. Performance is better on unworn rail, and poorer on highly worn rail.

#### E.4 THE TRACK SURVEY DEVICE

Within a range of approximately 200 feet along a track, the Track Survey Device (TSD) performs single plane displacement measurements. Over that range, the noise floor models for such measurements are quite adequate. Using special processing techniques, the longitudinal range of the TSD can be extended well beyond 200 feet. However in doing this, some elevation in the long wavelength noise floor must be anticipated. In the theory that follows, individual measurement errors are traced through the processing algorithm, and their impacts on long wavelength performance are predicted.

##### E.4.1 THEORY OF TSD MEASUREMENT

The current method of collecting and handling TSD data is illustrated in Figure E-3. Two surveys of the track are required to generate data for computing rail deviations. In the first survey (pass of the TSD) sequential sets of measurements are made, each within the range of the TSD. In the second pass of the TSD, sequential sets of measurements are made that overlap the first sets as shown in Figure E-3a, the overlaps being  $N = 6$  sample lengths while the sets of measurements are  $2N = 12$  sample lengths.

In data processing, sequential data are converted into short Mid-Chord Offsets (MCO). These are derived from triads of adjacent data points and, as a consequence, no data is lost in the MCO response nulls. Except for points near the end of a set, two MCOs are generated for each location of the survey. The process by which  $2N - 2 = 10$  MCOs

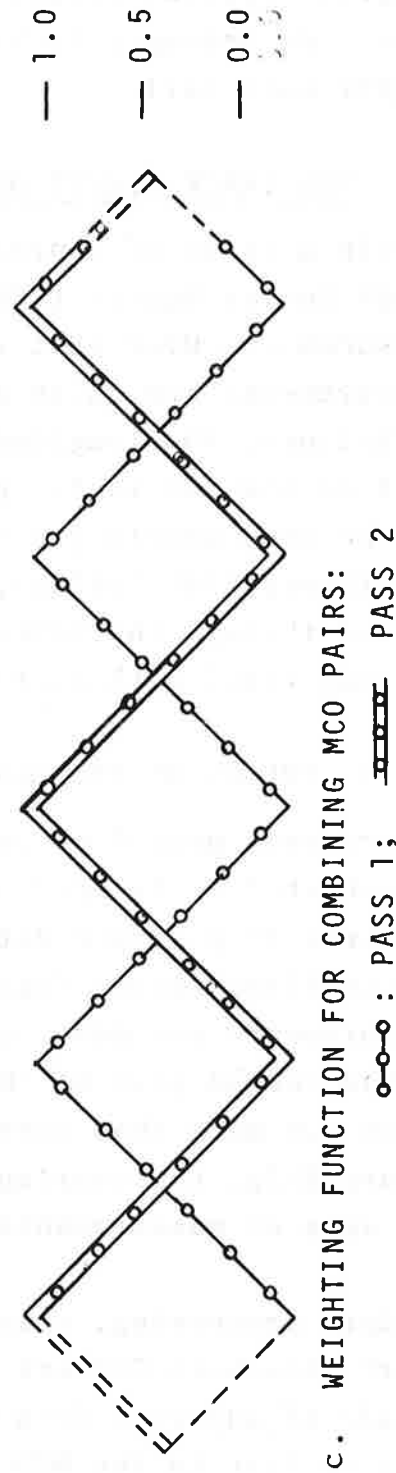
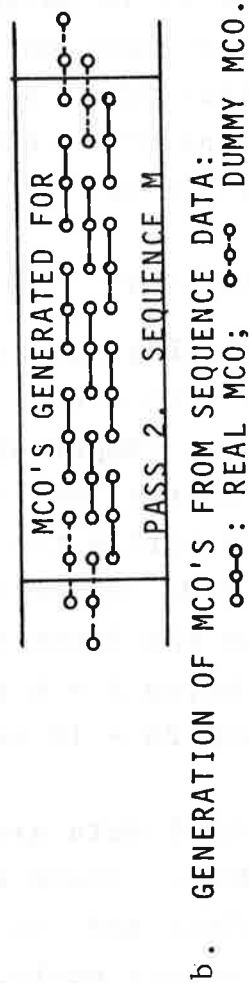
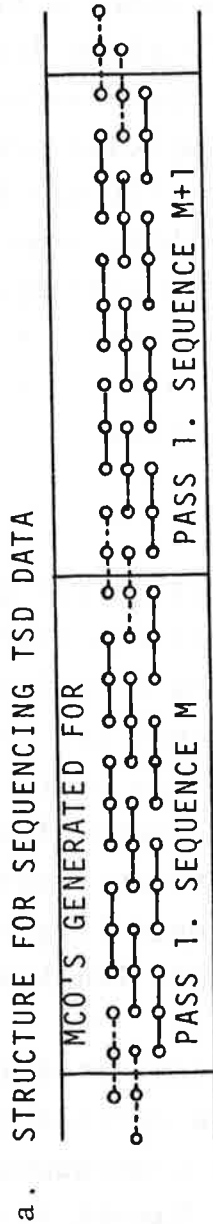
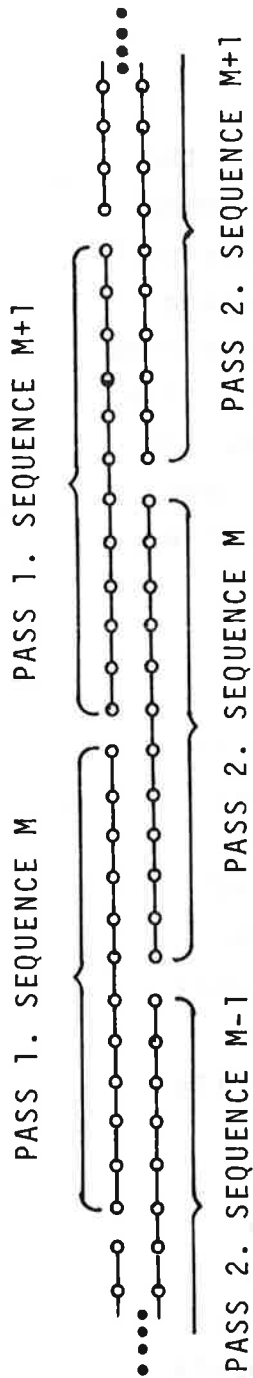


FIGURE E-3. PROCEDURE FOR COLLECTING AND PROCESSING TSD DATA



are generated for each set of measurements is shown in Figure E-3b.

A composite set of MCOs is constructed as the weighted sum of first pass and second pass MCOs. A weighting scheme that changes linearly with position in the sequence is used. It is shown in Figure E-3c. The sum of the first and second pass weights is always unity. Note that at locations where only one MCO is generated, the weighting function is unity for the measurements generating the MCO, and is null for the non-generated or "dummy" MCO.

Stated mathematically, let  $\{x'_n\}$  represent the sequence of first pass sampled profile values,  $n = 1, 2, 3, \dots$ . MCOs are generated by,

$$\delta'_n = x'_n - \frac{1}{2}(x'_{n-1} + x'_{n+1}), \quad n = 1, 2, 3, \dots \quad (E-19)$$

Note that the  $\delta'_n$  generated at  $n = 1, 2N, 2N+1, 4N, \dots$  are fictitious but that the weighting,  $\alpha_n$ , applied to these values is zero. Similarly,

$$\delta''_n = x''_n - \frac{1}{2}(x''_{n-1} + x''_{n+1}), \quad (E-20)$$

represent MCOs generated from the sequence of second pass profile values,  $\{x''_n\}$ . Then,

$$\delta_n = \alpha_n \delta'_n + (1 - \alpha_n) \delta''_n, \quad (E-21)$$

where,

$$\alpha_n = \frac{|[N - n + \frac{1}{2}] - N| + \frac{1}{2}}{N}, \quad (E-22)$$

with

$$[n] = \text{Mod } (n, 2N). \quad (\text{E-23})$$

Using the sequence of values,  $\{\delta_n\}$ , the profile is reconstructed by an inverse MCO process.

#### E.4.2 ERROR COMPUTATION FOR TSD

When measurements are made with the TSD, every  $x'_n$  and  $x''_n$  is contaminated by a  $u'_n$  or  $u''_n$  respectively, since errors are introduced from several sources. Sources of error are listed in order of seriousness:

- Atmospheric and scintillation effects of the laser,
- Instrumentation noise,
- Quantization noise in the A-D process, and
- Nonlinearities in measurements.

The first two sources are evaluated with the following assumptions regarding ensemble averages of the noise:

$$\langle u'_n u'_{n+m} \rangle = \delta_{m,0} V[n], \quad (\text{E-24})$$

$$\langle u''_n u''_{n+m} \rangle = \delta_{m,0} V[n+N], \quad (\text{E-25})$$

$$\langle u'_n u''_{n+m} \rangle = 0 \quad (\text{E-26})$$

These statements stipulate that:

- The error is derived from a white noise process,
- The standard deviation of the error is dependent on distance from the laser beam source, and
- The error is totally uncorrelated from one run to the next.

An error contamination of  $x_n$  by  $u_n$  generates an error contamination of  $\delta_n$ ,  $\epsilon_n$ . Applying ensemble averaging to the MCO errors gives:

$$\langle \epsilon'_n \epsilon'_{n+2} \rangle = \frac{1}{4} \langle u^2_{n+1} \rangle, \quad (E-27)$$

$$\langle \epsilon'_n \epsilon'_{n+1} \rangle = -\frac{1}{2} \langle u^2_n \rangle - \frac{1}{2} \langle u^2_{n+1} \rangle, \quad (E-28)$$

$$\langle \epsilon'^2_n \rangle = \frac{1}{4} \langle u^2_{n-1} \rangle + u^2_n + \frac{1}{4} \langle u^2_{n+1} \rangle, \quad (E-29)$$

$$\langle \epsilon'_n \epsilon'_{n-1} \rangle = -\frac{1}{2} \langle u^2_{n-1} \rangle - \frac{1}{2} \langle u^2_n \rangle, \quad (E-30)$$

$$\langle \epsilon'_n \epsilon'_{n-2} \rangle = \frac{1}{4} \langle u^2_{n-1} \rangle, \quad (E-31)$$

with similar results being obtained for the second pass. All other ensemble error averages vanish.

Finally,

$$\begin{aligned} \langle \epsilon_n \epsilon_{n+m} \rangle &= \langle \alpha_n \epsilon'_n \alpha_{n+m} \epsilon'_{n+m} \rangle \\ &+ \langle (1-\alpha_n) \epsilon''_n (1-\alpha_{n+m}) \epsilon''_{n+m} \rangle, \end{aligned} \quad (E-32)$$

or,

$$\langle \epsilon_n \epsilon_{n+2} \rangle = \frac{1}{4} \{ \alpha_n \alpha_{n+2} V[n+1] + (1-\alpha_n) (1-\alpha_{n+2}) V[n+N+1] \}, \quad (E-33)$$

$$\begin{aligned} \langle \epsilon_n \epsilon_{n+1} \rangle &= \frac{-\frac{1}{2} \{ \alpha_n \alpha_{n+1} (V[n] + V[n+1]) \\ &+ (1-\alpha_n) (1-\alpha_{n+1}) (V[n+N] + V[n+N+1]) \}}{2}, \end{aligned} \quad (E-34)$$

$$\begin{aligned} \langle \epsilon_n^2 \rangle &= \frac{\frac{1}{4} \{ \alpha_n^2 (V[n-1] + 4V[n] + V[n+1]) \\ &+ (1-\alpha_n)^2 (V[n+N-1] + 4V[n+N] + V[n+N+1]) \}}{2}, \end{aligned} \quad (E-35)$$

$$\langle \varepsilon_n \varepsilon_{n-1} \rangle = \frac{\overline{\alpha_n \alpha_{n-1} (V[n-1] + V[n])}}{\overline{(1-\alpha_n)(1-\alpha_{n-1})(V[n+N-1] + V[n+N])}} \quad (E-36)$$

$$\langle \varepsilon_n \varepsilon_{n-2} \rangle = \overline{\alpha_n \alpha_{n-2} V[n-1] + (1-\alpha_n)(1-\alpha_{n-2}) V[n+N-1]}. \quad (E-37)$$

where an overbar indicates that a cyclic average over  $n$  is to be performed.

The above equations can be used as the means of launching an analysis of error propagation through the entire TSD data collection and processing scheme. At present there is no detailed description of the  $V(n)$  needed for this analysis. However, it is known that  $V(n)$  will be the sum of four error components that include:

- A residual constant part that describes the basic measurement system error.
- A component that is proportional to  $(n+n_0)^2$  due to random angle output at the laser. Its causes are oscillation, structural/seismic vibration of the laser mount, and wind interaction with laser mount.
- A correlated component proportional to  $(n+n_0)^3$  due to atmospheric fluctuations in density gradient.
- A d-c component that represents a uniform thermal gradient across the laser path. This develops a curving bias whose variance increases as  $(n+n_0)^4$ .

#### E.4.3 RESULTS

In order to examine the noise floor, a nominal worst case value of  $V(n)$  is taken and it is treated as a constant.

Then

$$\overline{\alpha_n} = \frac{1}{2}, \quad (\text{E-38})$$

$$\overline{\alpha_n^2} = \frac{2N^3 - 3N^2 + N}{6N(N-1)^2}, \quad (\text{E-39})$$

$$\overline{\alpha_n \alpha_{n+1}} = \frac{2N^3 - 3N^2 - 2N + 3}{6N(N-1)^2}, \quad (\text{E-40})$$

$$\overline{\alpha_n \alpha_{n+2}} = \frac{2N^3 - 3N^2 - 11N + 18}{6N(N-1)^2}. \quad (\text{E-41})$$

The above give expressions for power response in the space domain. It is possible to convert this to power response in the frequency domain. An overall power response for TSD data collection and processing back to space curve is then given by:

$$P_S^d(\phi) = \frac{1}{4N(N-1)^2 \sin^4(\pi\phi X)} + \frac{3N-5}{N(N-1)^2 \sin^2(\pi\phi X)} + \frac{2N^3 - 3N^2 - 11N + 18}{3N(N-1)^2}. \quad (\text{E-42})$$

The resultant noise floor is given by:

$$\begin{aligned} \hat{N}_S(\phi) &= P_S^d(\phi) \hat{N}_d(0) \\ &= 2XP_S^d(\phi) \sigma_\phi^2. \end{aligned} \quad (\text{E-43})$$

This expression is evaluated for a number of standard operating conditions and for  $\sigma_d = 0.02''$  which has been observed in overlay differences. Results are shown in Figure 37, Volume I of this report.

In the long wavelength limits, this figure reveals that the performance of the TSD is the best of any instrument developed to date. The profilometer would have to operate at 120 mph to do as well.

The long wavelength behavior of the noise floor is characteristic of all self-contained profile/alignment systems when the wavelength greatly exceeds the system baseline:

$$N_s(\phi) \sim \frac{K}{\phi^4}, \quad \frac{1}{R} \gg \phi, \quad (\text{E-44})$$

where

$$K = \frac{\phi^2}{a\pi^4 R^3}. \quad (\text{E-45})$$

Equation (E-45) does give the misleading impression that increasing R will improve the long wavelength noise floor. For each R, a new effective  $\sigma_d$  must be computed that reflects the increase of V(n) with n. Also, K is not improved by more frequent sampling - a consequence of the linear form of  $\alpha_n$  currently used.

The long wavelength behavior can be used to provide a consistency check with an independent error observation. In processing KTT data, the error of an 800 ft. MCO was observed to be 0.18 in. The standard error for a MCO on a  $\phi^{-4}$  spectrum is given by:

$$\alpha_\delta(L) = \left( \frac{K\pi^4 L^3}{6} \right)^{\frac{1}{2}} = \left( \frac{L^3}{12R^3} \right)^{\frac{1}{2}} \sigma_\phi. \quad (\text{E-46})$$

For R = 100 ft., L = 800 ft., and  $\sigma_\phi = 0.25$ , a  $\sigma_m(L)$  of 0.16 in results.

The short wavelength behavior is inconsistent with the observed PSD's processed from TSD data. These indicate that the noise floor should be well below  $10^{-4}$  in<sup>2</sup>/cycle/ft. The reason for this discrepancy is associated with the way in which  $\sigma_d$  is observed. It is obtained from run to run differences which are not sampled at precisely the same locations. The effective  $\sigma_d$  of long wavelength behavior should include the effects of sample locations not being identical, whereas the effective  $\sigma_d$  that applies to short wavelength behavior should be much less. The dashed line in Figure 37, Volume I of this report, indicates the short wavelength noise floor as determined from PSD's of TSD data.





## APPENDIX F

### QUANTIZATION ERROR

#### F.1. LIST OF SYMBOLS

- A = Roughness related amplitude of model power spectrum  
(in<sup>2</sup>-cy/ft).
- $\alpha$  = Artificial, or effective limit of integration.
- B = Power law constant, noise floor, - see text.
- C = Constant defined in text.
- n = Counting index.
- R( $\tau$ ) = Correlation function associated with S( $\phi$ ), (in<sup>2</sup>).
- S( $\phi$ ) = Model power spectrum for track profile, (in<sup>2</sup>/cy/ft).
- u = Dummy variable defined in text.
- W( $\phi$ ) = Noise floor power spectrum for quantization error,  
(in<sup>2</sup>/cy/ft).
- W <sub>$\infty$</sub> ( $\phi$ ) = Asymptotic limit of W( $\phi$ ),  $\lim_{\phi \rightarrow \infty}$
- x<sub>0</sub> = Quantization resolution, (in).
- $\zeta(x)$  = Riemann Zeta-function.
- $\tau$  = Distance argument, (ft).
- $\phi$  = Spatial frequency, (cy/ft).
- $\Psi(\tau)$  = Correlation function associated with W( $\phi$ ), (in<sup>2</sup>).

#### F.2 THEORY

Deutsch\* derives a formulation that generates the correlation function for the quantization error in terms of the correlation function of the digitized process. Modifying this equation slightly to accommodate variables defined in the previous section gives:

---

\*R. Deutsch, "Non-Linear Transformations of Random Processes," Prentice-Hall, Englewood Cliffs NJ, 1972, p. 79-81.

$$\Psi(\tau) = \frac{x_0^2}{2\pi^2} \sum_{n=1}^{\infty} \frac{1}{n^2} \exp \left\{ -\frac{4\pi^2 n^2 [R(0) - R(\tau)]}{x_0^2} \right\} . \quad (F-1)$$

Note that

$$\Psi(0) = \frac{x_0^2}{2\pi^2} \sum_{n=1}^{\infty} \frac{1}{n^2} = \frac{x_0^2}{2\pi^2} \zeta(2) = \frac{x_0^2}{12} . \quad (F-2)$$

which is the variance of a uniformly distributed random variable over the interval  $(-\frac{1}{2}x_0, +\frac{1}{2}x_0)$ . The single sided power spectrum for the model profile is given by

$$S(\phi) = \frac{A}{\phi^2} , \quad 0 < \phi < \infty , \quad (F-3)$$

and the associated correlation function is given as,

$$R(0) - R(\tau) = \frac{A\pi|\tau|}{2} . \quad (F-4)$$

It is desired to compute the single sided power spectrum associated with  $\psi(\tau)$  which defined the noise floor for profile-type measurement. This will be given by,

$$W(\phi) = 2 \int_{-\infty}^{\infty} \psi(\tau) e^{-i2\pi\phi\tau} d\tau ,$$

Carrying out the implied operations gives:

$$W(\phi) = \frac{x_0^4}{A\pi^5} \sum_{n=1}^{\infty} \frac{1}{n^4 + C\phi^2} , \quad (F-5)$$

where,

$$C = \frac{x_0^4}{\pi^4 A^2} . \quad (F-6)$$

The sum indicated in Equation (F-5) does not have a closed form solution. However asymptotic forms can be calculated. In the limit that  $\phi \rightarrow 0$

$$W(0) = \frac{x_0^4}{A\pi^5} \quad \zeta(4) = \frac{x_0^4}{90\pi A} \quad (F-7)$$

In the limit of  $\phi \rightarrow \infty$ , the sum can be replaced by an integral giving,

$$W_\infty(\phi) = B\phi^{-3/2}, \quad (F-8)$$

where,

$$B = \frac{x_0}{4\pi} A^{1/2} \quad (F-9)$$

A typical value of A, corresponding to the short wavelength end profile and crosslevel spectrum is:

$$A = 10^{-5} \text{ in}^2\text{-cy/ft} \quad (F-10)$$

Some typical values of  $x_0$  encountered are evaluated in Table F-1. Using these values of  $x_0$ ,  $W(0)$  and B are evaluated in Table F-2.

Noise spectra corresponding to  $x_0 = 0.08$  and  $0.01$  inches were calculated and are plotted in Figure 38, Volume 1 of this report. As can be seen, slight improvements in resolution yield dramatic improvements in the noise floor.

For reference purposes, profilometer and crosslevel data was often collected by the FRA track survey car T-3 using an 8-bit A-D and a peak to peak scale of  $\pm 10$  inches for a resolution of 0.08 in. This gives a signal to noise ratio less than unity for wavelengths shorter than 8 feet.

TABLE F-1. RESOLUTION AS FUNCTION OF A-D BITS AND INCH RANGE (p-p)

P-p range (in.)	Number of A-D Bits		
	8	10	12
5	0.02	0.005	0.0012
10	0.04	0.01	0.0025
20	0.08	0.02	0.005
40	0.16	0.04	0.01

} Resolution,  $x_0$ , in.

TABLE F-2. ZERO LEVEL AND ASYMPTOTIC CONSTANT, B, USING MODEL SPECTRUM AND VARIOUS RESOLUTIONS

Values of $x_0$	$W(0)$ : $\text{in}^2/\text{cy}/\text{ft}$	B
0.16	$2.30 \times 10^{-1}$	$4.03 \times 10^{-5}$
0.08	$1.45 \times 10^{-2}$	$2.01 \times 10^{-5}$
0.04	$9.14 \times 10^{-4}$	$1.01 \times 10^{-5}$
0.02	$5.77 \times 10^{-5}$	$5.03 \times 10^{-6}$
0.01	$3.64 \times 10^{-6}$	$2.52 \times 10^{-6}$
0.005	$2.30 \times 10^{-7}$	$1.26 \times 10^{-6}$
0.0025	$1.45 \times 10^{-8}$	$6.29 \times 10^{-7}$
0.0012	$9.06 \times 10^{-10}$	$3.15 \times 10^{-7}$

APPENDIX G  
HISTORICAL BACKGROUND

G.1 EVALUATION OF TRACK SURVEY DATA

Many attempts have been made to obtain definitive information about track condition from track surveys. Information is needed not only to ensure safety and to plan track maintenance, but to assist in the design of new cars and locomotives that will ride safely and comfortably on existing track.

Lists of exceptions to prescribed limits for track geometry have been useful in determining whether or not a track meets standards for its speed class, but the exception reports have not been good indicators of overall track condition or the rate of deterioration of the track. Efforts to obtain more information from track surveys have centered on comparing graphs of track geometry measurements plotted against distance and on examining power spectral density (PSD) plots derived from track geometry measurements.

The comparison of graphs of track geometry measured at different times over the same track proved tedious and not very revealing. Prospects appeared poor both for simplification of the work and for accurate comparison of different tracks of the same speed class. The PSD's appeared more useful for track analysis and classification, since similarities seemed to be evident in the PSD's from different lengths of track that were in similar conditions. However, it has been difficult to separate the information in the PSD's on track roughness which is concentrated at joints (and at other discrete locations such as places where rail is damaged) from roughness which is distributed uniformly over the track length.

Definitive information on track roughness is critical, as the roughness coupled with the forward motion of the vehicle serves to excite transverse dynamic reactions in both track and vehicles. These reactions result in sharp impacts that cause rapid degradation of the track structure; they decrease ride comfort, cause excessive wear of vehicle components, and often result in lading damage. Hence the ability to identify problem track geometries, or geometries that affect problem vehicles, could yield important benefits in improved track reliability and reduced costs of maintenance for both track and vehicles.

From a theoretical standpoint, track irregularities produce forcing functions or input signals that serve to excite dynamic response in vehicles and track structures. The vehicles and track structures are governed by mechanical equations of motion, and they respond to the forcing functions in a predictable way. Accordingly, the prediction of vehicle response to track irregularities is a problem in dynamics that requires the specification of the input signals and the mechanical properties of the vehicle and track systems.

The input signals can be determined from the data collected by surveys of track geometry that measure variations in alignment, profile, gage and crosslevel. While it would be possible to survey a very large number of tracks, classify the track geometry variations and apply the data to many vehicles at many speeds, the work would be very burdensome and very expensive even with the most advanced computer processing. Accordingly, a statistical approach has been attractive for reducing the great mass of data that would have to be processed, and the PSD has appeared to be a very good tool for deriving salient statistics from track geometry variations.

The vehicle response to track variations is also statistical and can be described by a few parameters that relate to the track parameters on a one-to-one basis. An optimistic suggestion is that the track geometry random variable is some form of a stationary statistical process that can be completely characterized by its PSD, and its parameters can be identified by examining the PSD. Similarly, vehicle responses can be characterized by PSD's generated by a simple multiplication of the track PSD and the vehicle power response.

The minority of track segments that cannot be statistically represented by the parameters that describe the random variable are known as anomalies. Usually the presence of an anomaly is associated with a physical or structural condition in the track that makes it obviously different from its surroundings. A list of typical track anomalies is provided in Table 5, Volume I of this report.

The characterization of anomalies requires a specific definition of the track geometry variation in the neighborhood of the anomaly and, unlike the majority of the track segments, cannot be adequately described by frequency domain techniques. An optimistic approach to the characterization of anomalies holds that they can be represented by a series of transient variations in the track which occur randomly (but infrequently) with distance along the track. Then the vehicle response to an anomaly would consist of its own transient response to the deterministic component of the anomaly plus an additive random component.

## G.2 EARLY USE OF PSD'S

The nucleus of the PSD evaluation is the Discrete Fourier Transform (DFT). It prescribes the complex operations required to convert a series of time or distance sampled data into a sampled frequency spectrum. Individual operations in the DFT are both numerous and difficult, and the routine evaluation of PSD's was not feasible until the mid 1950's when digital processing capabilities became generally available.

Almost immediately the PSD was applied to airport runway roughness measurement.<sup>1</sup> This first effort examined two runways described as "rough" and "smooth". Both gave rise to similar spectra in which the rougher one had a PSD that was twice as intense for wavelengths shorter than 50 feet, growing to 10 times as intense for wavelengths longer than 300 feet. Among other things, it was postulated that the heights of the spectra could provide an initial guide toward the establishment of criteria for runway surfaces.

In a subsequent report,<sup>2</sup> the same research team confirmed and elaborated on its findings and concluded that a spectrum band may be established (based on the spectra of a series of acceptable runways) within whose limits all new runways must be built or all old runways maintained in order to insure satisfactory operation.

---

<sup>1</sup>J. H. Walls, J. C. Houbolt and H. Press, "Some Measurements and Power Spectra of Runway Roughness," Technical Note 3305, November 1954. National Advisory Committee for Aeronautics, Washington DC.

<sup>2</sup>J. C. Houbolt, J. H. Walls, and R. F. Smiley, "On Spectral Analysis of Runway Roughness and Loads Developed During Taxiing," Technical Note 3484, July, 1955, National Advisory Committee for Aeronautics, Washington DC.



In yet another paper,<sup>3</sup> Houbolt discussed the necessity for avoiding the inclusion of anomalies in a spectral estimate which characterizes the continuously distributed roughness of the runway. The appendix of this third paper contains an interesting discussion of the roughness PSD in relation to measurements that might be used to support maintenance activities. However in a later paper on runway roughness,<sup>4</sup> negative conclusions were reported. It was found that the PSD's did not distinguish between a series of high amplitude bumps and low amplitude bumps at the same wavelength. Thus, a PSD would indicate that a runway with very unsatisfactory roughness at a few discrete locations was just as smooth as a runway with only slight roughness continuously distributed over its entire length.

### G.3 USE OF PSD'S FOR EUROPEAN TRACK

The first effort to characterize the roughness of railway track was performed by Gilchrist<sup>5</sup> of the British Railways (BR) Research Department in support of rail vehicle dynamics research.<sup>6</sup> Tracks at four sites having welded and bolted joints in both good and poor condition were analyzed.

---

<sup>3</sup>J. C. Houbolt, "Runway Roughness Studies in the Aeronautical Field," *Proc. Am. Soc. Civil Engr.*, (*J. Air Transport Division*, AT 1), p. 11-31, March 1961.

<sup>4</sup>T. L. Coleman and A.W. Hall, "Implications of Recent Investigations on Runway Roughness Criteria," Report #416, Advisory Group for Aeronautical R&D Flight Mechanics Panel, Paris, France, Jan. 15-18, 1963.

<sup>5</sup>A. O. Gilchrist, "A Report on Some Power Spectral Measurements of Vertical Rail Irregularities," Technical Note DYN/8, August 1965, British Railways Research Department, Derby, England.

<sup>6</sup>A. H. Wickens, "General Aspects of the Lateral Dynamics of Railway Vehicles," Paper No. 68-WA/RR-3, Am. Soc. Mech. Engr., Winter Annual Meeting, Dec. 1968.

While Gilchrist was aware of the U.S. runway roughness research effort of Houbolt,<sup>3</sup> whom he cited as a reference, it is not clear that he was familiar with the later negative conclusions of Coleman and Hall.<sup>4</sup> Nonetheless, he observed that the appearance of the better tracks supported the treatment of the irregularities as continuous; while in poor tracks, the pronounced irregularities at the rail joints implied that a different treatment was required. The continuous events are well described by a PSD while the discrete events at the joints may not be.

The researchers at BR noted that track geometry PSD's follow a consistent pattern and advanced a formula for modeling the continuum portion of the PSD<sup>7</sup> as shown in the first part of Table G-1. No attempt was made to model the spectral peaks in PSD's that were associated with rail length disturbances in the track.

At the same time as the BR efforts, the French National Railways (SNCF) produced PSD's using data from their Mauzin track geometry measurement coach.<sup>8</sup> Desiring only to model and characterize the continuum part of their spectra, the periodic component associated with an 18 m (60 ft) rail length was removed, resulting in a smooth curve. SNCF used a cubic form for the curve as shown in Table G-1.

---

<sup>7</sup>T. G. Pearce and B. J. May, "A Study of the Stability and Dynamic Response of the Linear Induction Motor Test Vehicle," Final Report #FRA-RT-70-25, September 1969.

<sup>8</sup>A. Prud'Homme, "The Track," *French Railway Technique*, 2. p.67-79, January 1970.

TABLE G-1. EARLY PSD MODELS FOR TRACK PROFILE,  
ALIGNMENT, AND CROSSLEVEL

British Rail:

$$S(\phi) = \frac{C}{a + b\phi^2 + \phi^4}$$

SNCF (French National Railways):

$$S(\phi) = \frac{C}{(b + \phi)^3}$$

Battelle #1:

$$S(\phi) = \frac{C}{\phi^N}$$

Battelle #2:

$$S(\phi) = \frac{C}{b + \phi^N}$$

Battelle #3:

$$S(\phi) = \frac{C}{a + b\phi^N + \phi^{2N}}$$

In the above:

$S(\phi)$  = Power Spectral Density Level, (in<sup>2</sup>/cy/ft)

$\phi$  = Spatial frequency, (cy/ft)

C = Roughness amplitude

a,b = Corner frequency parameters

N = Power law parameter

The effects of welds were not considered important, and the contribution of welds and joints to vehicle body motion was considered to be reduced at higher speeds. However it was noted that on a track where identical trains operate at identical speeds, the risk of long undulatory wear of the rails might be a problem.

One of the most significant contributions to the statistical description of railway track geometry was made in a comprehensive study by Sauvage,<sup>9</sup> in which he noted two distinct features of track spectra:

- A continuous curve which drops off toward the high frequencies (short wavelengths).
- A collection of lines corresponding to rail joints and other periodic irregularities.

Sauvage also noted that the PSD of properly maintained rail without joints will show nothing except a continuous curve.

Unlike previous research efforts, Sauvage also addressed the amplitude distribution of rail defects. In particular, SNCF was interested in the statistical distribution of class  $k$  peaks, which were defined as rail defects with peak values between  $k$  mm and  $(k+1)$  mm. Sauvage's report states:

"Various analyses have shown that the statistical distribution of amplitudes (of classes  $k$ ) is exponential with base  $v$ :

$$p(k) = (1-v)v^k$$

where  $v$  is given constant between 0 and 1."

---

<sup>9</sup>M. Sauvage, "Statistical Study of Track Geometry," *Bulletin d'Information des Anciens Elèves de l'École Supérieure des Cadres de l'Équipement*, 16, June 1973, and 17, December 1973.

This is a  $\Gamma$  or Pearson type III distribution.

One of the more interesting applications of rail roughness PSD's is found in a paper by Cousty and Tro.<sup>10</sup> They developed a linear model that describes how initial rail roughness interacts with a rolling vehicle load to produce an incremental permanent change in the roughness. Here a statistical approach was applied for expressing the initial and subsequent degradations in terms of roughness PSD's.

The principal findings of this study<sup>10</sup> were:

- Track degradation is progressive in the sense that the residual permanent deformation develops incrementally with the passage of each wheel load.
- All other factors being equal, the increment of change is inversely proportional to the number of wheel passages. This produces a cumulative permanent deformation that follows a logarithmic law that is common to soil fatigue phenomena.
- For the passage of identical wheel loads at identical speeds, there will be a band of track wavelengths (corresponding to the primary suspension resonant frequency) at which degradation will occur, and another band of shorter track wavelengths at which smoothing will occur.

---

<sup>10</sup>R. Cousty and G. Tro, "A Theoretical Study of the Development of Progressive Permanent Deformation in Longitudinal Profile of Railway Track under the Influence of Repeated Rollings Loads," *Revue Generale des Chemins de Fer* 91, p. 205-216, March 1972.

#### G.4 USE OF PSD's FOR U.S. TRACK

In the U.S., the processing of track geometry data into statistical formats was not undertaken until the late 1960's. Even then, the use of PSD's awaited the low-cost availability of data collected by the FRA Track Survey Cars,<sup>11</sup> and the need to improve ride quality of the high-speed metroliner.<sup>12</sup> A PSD processing program<sup>13</sup> was developed to use the data tapes from the FRA Survey Cars, and statistically representative samples of track geometry data were produced routinely. An output plot of log PSD level versus log frequency facilitated characterization of the PSD's.<sup>13</sup>

Scientists at the Battelle Columbus Laboratories were among the first to define parameters for PSD data. They did so while applying PSD's to computer models of rail vehicles.<sup>14</sup> These models were not capable of accepting combined random and deterministic inputs. Accordingly, two program versions of the model were used: one to represent the vehicle response to a deterministic input (particularly the rectified sine-wave geometry typical of 39-foot bolted rail lengths with staggered joints), while the other generated vehicle response to the random component of track geometry.

---

<sup>11</sup>C. L. Gerhardt and J. T. May, "DOT Test Train Program System Instrumentation Manual," Annual Report DOT-FR-72-1, January 1972 (PB-748-286).

<sup>12</sup>J. M. Herring, "Metroliner Ride Improvement Program," Final Report, FRA-RT-73-30, February 1973 (PB-221-272).

<sup>13</sup>R. D. Burnes, "Power Spectral Density Program Manual," ENSCO Technical Study Report No. DOT-FR-72-4, May 1972.

<sup>14</sup>D. R. Ahlbeck, et al, "Comparative Analysis of Dynamics of Freight and Passenger Rail Vehicles," Final Report, FRA-ORD&D-74-39, March 1974 (PB-240-329).

This approach provided useful results for the two extreme cases of well-maintained or new track (which can be represented by a continuum alone) and a highly degraded bolted rail (which can be represented by a periodic deterministic process).

The earliest Battelle model shown in Table G-1 (converted to the frequency notation of this report) was similar to the concepts of other investigators who had found that runways, roads and tracks exhibit random variations. However, Battelle found that at long wavelengths, the measured amplitude of vehicle excitations were far less than the simple model would indicate. Accordingly, they developed the model shown as Battelle No. 2 in Table G-1, again converted to frequency notation.

Subsequent experience with this model revealed deficiencies at the short wavelength end of the spectrum for vertical forces when compared to measured tie plate loads. The model for alignment and profile was modified further and is shown as Battelle No. 3 in Table G-1 (converted to frequency notation) to represent a smoother track at wavelengths of less than 10 feet.

Early in this work, Battelle provided an incisive description of the deterministic behavior found in track:

"One of the salient facts-of-life of North America railroad track is the half-staggered, bolted 39-foot rail... After sufficient tonnage, the bolted rail lengths assume a permanently-set shape (service-bent rail) that can be well approximated by a rectified wave."

They also made an observation that had an important bearing on later consideration of the random aspects of rail behavior at joints and welds:

To establish some reasonable relationship between the rectified sinewave ... and the geometry deviations set forth in the Track Safety Standards (TSS) some random distribution of amplitudes must be assumed.

In the ENSCO work on PSD characterization or modeling, it was realized that profile and alignment spectra need not level off. At wavelengths,  $\lambda$ , much greater than the secondary suspension resonance, vehicle sensitivity to roughness diminishes as  $\lambda^{-4}$ . A spectrum that ultimately rises as  $\lambda^4$  in the long wavelength limit does not impart a significant contribution to the forces, accelerations and relative displacements experienced by a vehicle when  $\lambda$  is small compared to "vehicle-resonance" wavelengths.

Track specifications that are based on PSD models that level off at long wavelengths impose overly stringent and costly requirements on track construction and maintenance. A case in point was the specification developed for the 250 mph Linear Induction Motor Research Vehicle track located at the Transportation Test Center near Pueblo, Colorado.<sup>7</sup>



Here the application of this specification to the extremely long wavelengths (up to 700 feet) implied adjustments to the track of up to 20 inches in one area.<sup>15</sup> Further investigation revealed that a more realistic design spectrum consisted of a long wavelength behavior of  $\lambda^2$  rather than level. This spectrum is still compatible with acceptable vehicle dynamic behavior, yet it implies a substantially reduced long wavelength standard with significantly less adjustment to the track.

As a part of FRA-sponsored research in track maintenance planning, ENSCO defined a PSD model (ENSCO 1, Table G-2) that included two significant improvements:<sup>16</sup>

- It provided for an unbounded continuum for profile and alignment following a  $\lambda^2$  trend in the long wavelength limit.
- It included a provision for adding the line components of the periodic deterministic process.

In later work,<sup>17</sup> a model (ENSCO 2, Table G-2) was developed for the line component of the periodic process; and, in addition, a two-segment power law was substituted for the continuum model.

---

<sup>15</sup>J. C. Corbin, "Shim Plan: A Systematic Method of Realigning Railway Track for Dynamic Capability,"

<sup>16</sup>J. C. Corbin and T-L. Yang, "Application of Guideway Roughness Power Spectral Density as a Management Tool," American Society of Mechanical Engineers Paper 73-1CT-144, June 1973.

<sup>17</sup>J. C. Corbin and W. M. Kaufman, "Classifying Track by Power Spectral Density," *Mechanics of Transportation Suspension Systems*, Winter Annual Meeting ASME, Houston, December 1975.

TABLE G-2. RECENT PSD MODELS FOR PROFILE AND ALIGNMENT

ENSCO: GENERAL FORM

$$S(\phi) = AU(\phi) + B^2V(\phi)$$

$U(\phi)$  = Continuum Spectrum

A = Amplitude of Continuum

$V(\phi)$  = Line Components

B = Amplitude of Periodic Process

ENSCO 1. ( $V(\phi)$  not specified)

$$U(\phi) = \lim_{\phi_0 \rightarrow 0} \frac{\phi_1^2}{(\phi^2 + \phi_0^2)(\phi^2 + \phi_1^2)}$$

ENSCO 2.

$$U(\phi) = \begin{cases} \phi^{-2} & \phi < \phi_1 \equiv \phi_c \\ \phi_1^2 \phi^{-4} & \phi > \phi_1 \equiv \phi_c \end{cases}$$

$$V(\phi) = \sum_{k=1}^k J_k H_n(\phi)$$

where

$$J_k = \frac{2}{\pi^2(4n^2 - 1)} \quad (\text{Rectified Sine Wave})$$

$$H_k(\phi) = \begin{cases} 0, & |\phi - k/L| > \beta_k \\ 1/\beta_k, & |\phi - k/L| < \beta_k \end{cases}$$

$\beta_k$  = spectral resolution at the  $k^{\text{th}}$  peak

L = rail length

BATTELLE, CURRENT

$$U(\phi) = \begin{cases} \phi^{-n} & \phi \leq \phi_c \\ \phi_c^{n-m} \phi^{-m} & \phi \geq \phi_c \end{cases}$$

In the above

$\phi_0$  = Artificial corner frequency

$\phi_1, \phi_c$  = corner frequencies

m, n = power laws

Along the same lines, Battelle advanced a new model<sup>18</sup> which represented a generalization of the ENSCO, (-2, -4) power law representation of the continuum and incorporated a (-n, -m) power law model as summarized in Table G-2.

In the meantime, considerable success was being achieved with the "time domain" (time = longitudinal distance) approach to track geometry characterization.<sup>19</sup> The significant result of this research was that it appeared geometry of homogeneous track could be comprehensively represented by three component statistical processes:

- A stationary random process that accounts for the uniformly present randomness of the rail.
- A periodic deterministic process (PDP) that describes the regularly spaced rail joints having non-zero mean amplitude.
- A periodically modulated random process that accounts for randomness in the joint amplitudes.

Based on this, the primary objective of the present project was to further develop this concept and derive quantitative statistical descriptors which can comprehensively characterize track geometry.

---

<sup>18</sup>D. R. Ahleck and G. R. Doyle, "Comparative Analysis of Freight and Passenger Rail Vehicles," Summary Report FRA-ORD-77-04, November 1976.

<sup>19</sup>J. C. Corbin, "Statistical Characterization of Railway Track Behavior," ASME/IEEE, Joint Railroad Conference, Pittsburgh, IEEE Paper No. C74903-3IA, April 1974.



## APPENDIX H

### PROCEDURES FOR SYSTEM IDENTIFICATION OF PERIODICALLY MODULATED RANDOM PROCESSES

#### H.1 LIST OF SYMBOLS

- D,  $D(\Omega)$  -Diagonal matrix consisting of eigenvalues of Z.
- D,  $D(\beta; \Omega)$  - $\beta^{\text{th}}$  eigenvalue of Z.
- F -Fourier Transform.  $F^{-1}$  represents inverse transform. Subscripts indicate Hilbert spaces between which transformations occur.
- f,  $f(m)$  -Convolution sequence (filter) - see text.
- G,  $G(\omega)$  -Matrix of frequency response functions,  $G(\alpha, \beta; \Omega)$ .
- G,  $G(\omega)$ ,  
G( $\alpha, \beta; \Omega$ ) -Frequency response functions - see text.  
 $G(\omega)$  - Stationary random process.  
G( $\alpha, \beta; \Omega$ ) -  $N \times N$  input/output representation of periodically modulated random process.
- g,  $g(m)$ ,  $g(m, n)$  -Convolution sequences (filter and kernel functions  
g( $\alpha, m$ ),  $g(\alpha, \beta; \mu)$  to generate various random processes - see text.  
Upper line unpartitioned, lower line is partitioned).
- h,  $h(m)$  -Convolution sequence (filter) - see text.
- i, j, k, l,  
m, n -Counting indices for unpartitioned data on convolution sequences. Interval:  $(-\infty, \infty)$ .
- M, N -  $N$  = number of samples per rail segment.  $M = N - 1$ .
- p -Exponent - see text.
- w,  $w(n)$ ,  $w(\alpha, \mu)$  -Unpartitioned and partitioned white noise sources or inputs.
- X,  $X(\Omega)$  -Matrices containing the column eigenvectors,  $X(\beta, \Omega)$ .
- $X(\beta; \Omega)$  - $\beta^{\text{th}}$  eigenvector of  $Z(\Omega)$ .
- $X(\alpha, \beta; \Omega)$  - $\alpha^{\text{th}}$  component of  $\beta^{\text{th}}$  eigenvector of  $Z(\Omega)$ .
- Z,  $Z(\Omega)$  -Matrix comprising auto- and cross-power spectral density elements,  $Z(\alpha, \beta; \Omega)$ .
- Z,  $Z(\omega)$ ,  
Z( $\alpha, \beta; \Omega$ ) -Power Spectral Densities (PSD):  
 $Z(\omega)$  = PSD for stationary random process.  
 $Z(\alpha, \beta; \Omega)$  = Cross PSD's between  $\alpha^{\text{th}}$  and  $\beta^{\text{th}}$  sample locations within rail length.
- z,  $z(n)$ ,  $z(\alpha; \nu)$  -Unpartitioned and partitioned track geometry outputs.

- $\alpha, \beta, \gamma, \delta$  -Modulo N counting indices for partitioned representation designating position within a rail length. Interval:  $(0, N-1)$
- $\delta_{mn}$  -Kronecker delta:  $= \begin{cases} 0, & m \neq n \\ 1, & m = n \end{cases}$
- $\zeta, \zeta(n),$   
 $\zeta(\alpha, \beta; \nu)$  -Correlation functions:  
 $\zeta(n)$  = Auto-correlation for stationary random process.  
 $\zeta(\alpha, \beta; \nu)$  - Cross correlation between  $\alpha^{\text{th}}$  and  $\beta^{\text{th}}$  sample locations within rail length and separated by  $\nu$  rail lengths.
- $\Phi, \Phi(\omega)$  -Phase function - see text.
- $\kappa, \gamma, \mu, \nu$  -Counting indices for partitioned representations designating rail segment in which data is located. Interval:  $(-\infty, \infty)$ .
- $\sigma, \sigma(\alpha)$  -Standard deviation constants - see text.
- $\Omega$  -Spatial radian frequency for data sampled at rail length intervals (partitioned data).
- $\omega$  -Spatial radian frequency for data sampled at N samples per rail length.
- \*
- Indicates complex conjugate
- †
- Indicates transpose of a matrix.
- ⊗
- Indicates convolution.

## H.2 THEORY

### H.2.1 NON-STATIONARY AND STATIONARY RANDOM PROCESSES

The general non-stationary random process can be represented by:

$$z(m) = g(m, n) w(n) \quad (\text{H-1})$$

where the Einstein convention of summation over repeated integer indices is used. In the more familiar notation, equation (H-1) becomes:

$$z(m) = \sum_{n=-\infty}^{\infty} g(m,n) w(n) ,$$

$n$  being the repeated index, and its range being given in the table of symbols as  $(-\infty, \infty)$ .  $\{w(n)\}$  represents a sequence of independent random values also known as a white noise process. The statistical characteristics of  $w(n)$  under ensemble averaging are given by:

$$\begin{aligned} \langle w(n) \rangle &= 0 , \\ \langle w(n) w(m) \rangle &= \delta_{mn} . \end{aligned} \tag{H-2}$$

If the process to be represented by equation (H-1) is to be a Stationary Random Process (SRP),  $g(m,n)$  takes the following form:

$$g(m,n) = g(m-n) . \tag{H-3}$$

In other words, the process kernel is only a function of the difference between input and output location.

For the SRP, the ensemble average over  $m$ ,  $\langle z(m) z(m+n) \rangle$  describes the autocorrelation function  $\zeta(n)$  which is given by:

$$\begin{aligned} \zeta(n) &= \langle z(m) z(m+n) \rangle , \\ &= g(m-k) g(m+n-l) \langle w(k) w(l) \rangle , \\ &= g(m) g(m+n) , \end{aligned} \tag{H-4}$$

where equation (H-2) has been used to obtain the last result. Equation (H-4) can be converted to the frequency domain by Fourier transformation to give:

$$Z(\omega) = G(\omega) G^*(\omega), \quad (\text{H-5})$$

where,

$$\left. \begin{aligned} Z(\omega) &= F_{\omega,n}[z(n)], \\ \text{and,} \\ G(\omega) &= F_{\omega,n}[g(n)]. \end{aligned} \right\} (\text{H-6})$$

$Z(\omega)$  is the Power Spectral Density (PSD) of the sequence,  $\{z(m)\}$ .  $G(\omega)$  is the frequency and phase response of the filtering operation. For a filter having an even symmetry impulse response,  $G(\omega)$  is real and is related to  $Z(\omega)$  by,

$$Z(\omega) = G^2(\omega). \quad (\text{H-7})$$

Inverting the relationship gives

$$G(\omega) = \sqrt{Z(\omega)}, \quad (\text{H-8})$$

and,

$$g(n) = F_{\omega,n}^{-1}[G(\omega)]. \quad (\text{H-9})$$

Additionally, any filter of the form,

$$G(\omega) = \sqrt{Z(\omega)} e^{i\Phi(\omega)}, \quad (\text{H-10})$$

with,

$$\Phi(\omega) = -\Phi(-\omega), \quad (\text{H-11})$$

represents an allowable frequency response, and the associated asymmetrical (e.g., causal) convolution sequence,  $\{g(n)\}$ , yields



the desired power spectral density when operating on  $\{w(n)\}$ . Evidently, there are infinitely many filters which will produce the desired PSD.

### C.2.2 PERIODICALLY MODULATED RANDOM PROCESSES

The Periodically Modulated Random Process (PMRP) is a particularization of the general non-stationary case by which every  $N$ th value of  $\{z(m)\}$  is drawn from a stationary sub-process. Thus:

$$\{z(m)\} \longrightarrow \{z(\alpha;\mu)\}, \quad (\text{H-12})$$

where,

$$\alpha = \text{Mod}(m, N), \quad (\text{H-13})$$

$$\mu = \left( \frac{m - \alpha}{N} \right). \quad (\text{H-14})$$

In terms of sampled track data, there are  $N$  samples per rail length,  $\alpha$  designates a sample within a rail length, and  $\mu$  designates which rail contains the sample. The sequence  $\{z(\alpha,\mu)\}$  is given by

$$z(\alpha,\mu) = g[\alpha;N(\mu-\nu)-\beta] w(N\nu+\beta). \quad (\text{H-15})$$

Conceptually, this arrangement is described in Figure H-1. There is a single white noise generator producing  $\{w(n)\}$ . There are  $N$  parallel filters being fed by the generator. The output  $\{z(\alpha,\mu)\}$  is produced by a commutation operation in which the  $N$  filters are sequentially tapped, *each tapping operation being accompanied by the generation of a new value of  $w(n)$ .*

It is possible to repartition Equation (H-15) in a manner that simplifies analysis. Effectively this is equivalent to proposing an  $N$  input -  $N$  output model where the inputs are independent

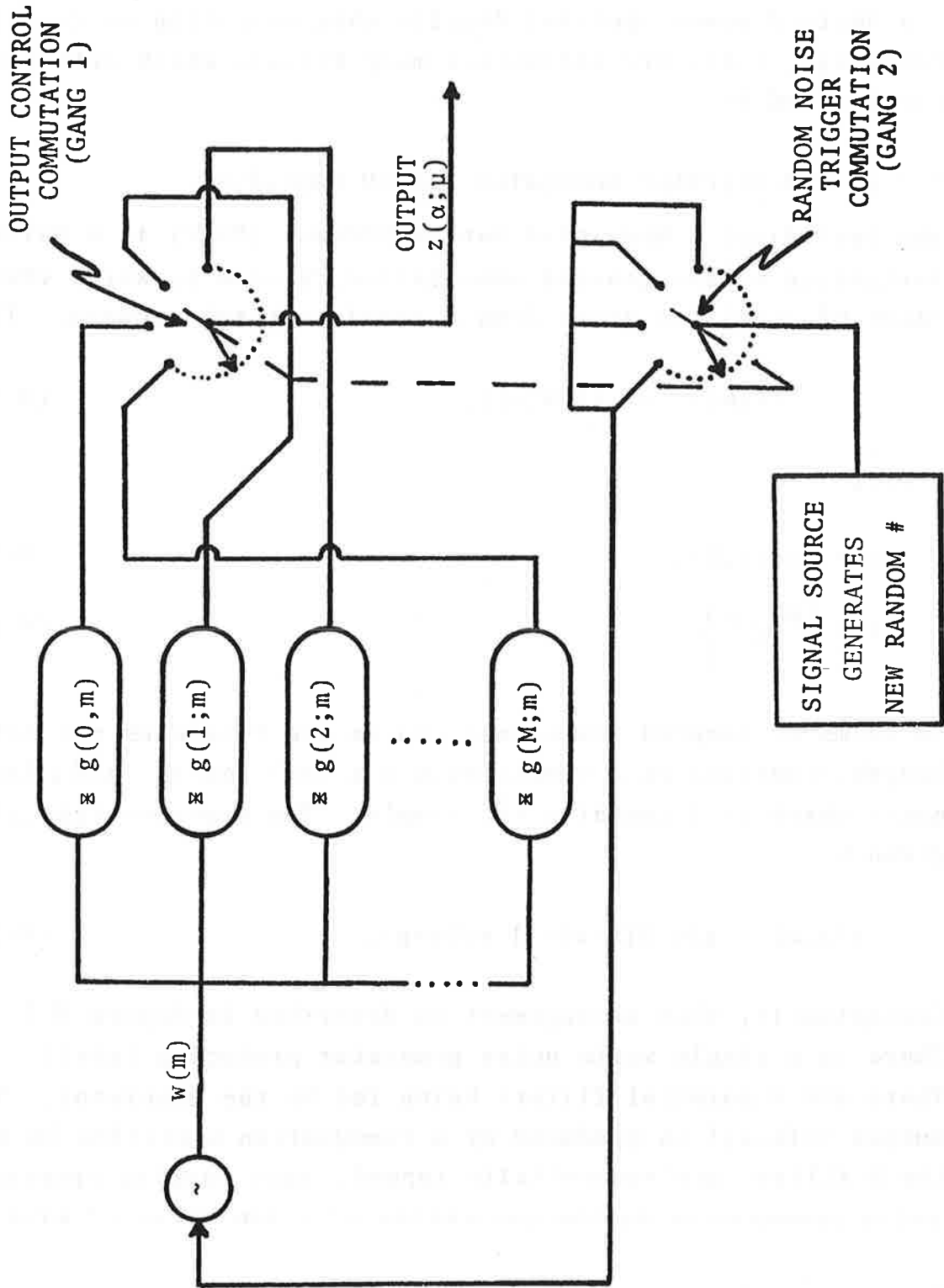


FIGURE H-1. PARTIALLY PARTITIONED GENERATOR OF PERIODICALLY MODULATED RANDOM PROCESS

random number generators that produce 1 sample per rail length. This new formulation of the model is illustrated in Figure H-2 where there are now N random number generators, N x N filters, and an N-terminal commutator, and the generators produce a new value for each time the commutator completes a rotation. Thus,

$$z(\alpha; \mu) = g(\alpha, \beta; \mu - \nu) w(\beta, \nu), \quad (\text{H-16})$$

with

$$\langle w(\alpha, \mu) w(\beta, \nu) \rangle = \delta_{\alpha\beta} \delta_{\mu\nu}. \quad (\text{H-17})$$

The ensemble average of second order statistics of  $z(\alpha; \mu)$  is given by  $\zeta(\alpha, \beta; \nu)$  as follows:

$$\begin{aligned} \zeta(\alpha, \beta; \nu) &\equiv \langle z(\alpha; \mu) z(\beta; \mu + \nu) \rangle, \\ &= g(\alpha, \gamma; \mu - \lambda) g(\beta, \delta; \mu + \nu - \kappa) \langle w(\gamma, \lambda) w(\delta, \kappa) \rangle, \\ &= g(\alpha, \gamma; \mu) g(\beta, \gamma; \mu + \nu). \end{aligned} \quad (\text{H-18})$$

The last step follows from an application of Equation (H-17). The physical interpretation of  $\zeta(\alpha, \beta; \nu)$  is that it is the correlation between what happens at the  $\alpha^{\text{th}}$  position in a rail segment and what happens at the  $\beta^{\text{th}}$  position in another rail segment,  $\nu$  rails removed. It has the symmetry property that,

$$\zeta(\alpha, \beta; \nu) = \zeta(\beta, \alpha; -\nu). \quad (\text{H-19})$$

Equation (H-18) is readily carried to the frequency, or the  $\Omega$  domain. There the use of the upper case for frequency is to indicate that data is effectively sampled every rail length:

$$Z(\alpha, \beta; \Omega) \equiv G(\alpha, \gamma; \Omega) G^*(\beta, \gamma; \Omega), \quad (\text{H-20})$$

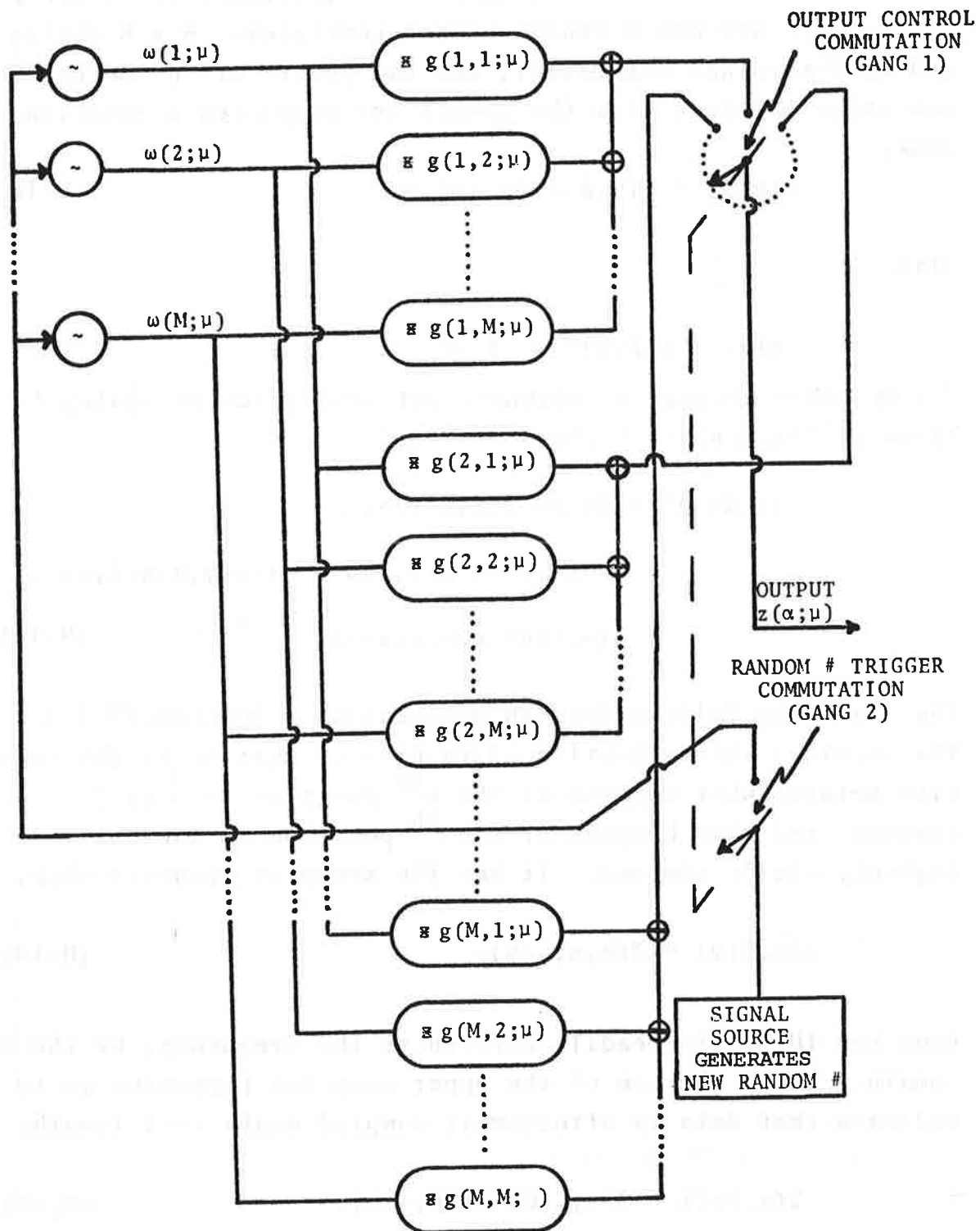


FIGURE H-2. FULLY PARTITIONED GENERATOR OF PERIODICALLY MODULATED RANDOM PROCESS

where,

$$Z(\alpha, \beta; \Omega) = F_{\Omega, \nu} [\zeta(\alpha, \beta; \nu)], \quad (\text{H-21})$$

and,

$$G(\alpha, \beta; \Omega) = F_{\Omega, \nu} [g(\alpha, \beta; \nu)]. \quad (\text{H-22})$$

In accordance with the fact that  $\zeta$  and  $g$  are real and that  $\zeta$  obeys the symmetry of Equation (H-19) it follows that:

$$Z(\alpha, \beta; \Omega) = Z^*(\alpha, \beta; -\Omega), \quad (\text{H-23})$$

$$Z(\alpha, \beta; \Omega) = Z^*(\beta, \alpha; \Omega), \quad (\text{H-24})$$

and,

$$G(\alpha, \beta; \Omega) = G^*(\alpha, \beta; -\Omega). \quad (\text{H-25})$$

### H.2.3 MATRIX EIGENVALUE FORMULATION

As in the stationary case, the correlation functions,  $Z(\alpha, \beta; \Omega)$  are obtained by processing track geometry data. Similarly it is desired to render a  $G(\alpha, \beta; \Omega)$  that will produce the required  $Z(\alpha, \beta; \Omega)$ . To visualize this, a matrix formulation for  $Z$  is given as follows:

$$Z(\Omega) = \begin{bmatrix} Z(0,0;\Omega) & Z(0,1;\Omega) & \dots & Z(0,M;\Omega) \\ Z(1,0;\Omega) & Z(1,1;\Omega) & \dots & Z(1,M;\Omega) \\ \vdots & \vdots & & \vdots \\ Z(M,0;\Omega) & Z(M,1;\Omega) & \dots & Z(M,M;\Omega) \end{bmatrix}, \quad (\text{H-26})$$

with,

$$M = N - 1. \quad (\text{H-27})$$

A similar structuring for  $G$  also exists and the matrix equivalent of Equation (H-20) becomes,

$$Z(\Omega) = G(\Omega) [G^*(\Omega)]^\dagger. \quad (\text{H-28})$$

Examining the expressions of Equation (H-20) and (H-24) reveals that the diagonal elements are rigorously real and that the off diagonal elements are Hermitian conjugate. Therefore  $Z(\Omega)$  admits to real eigenvalues.

Because of the phase indeterminacy of the elements,  $G$ , it is possible to stipulate that the matrix  $G$  is also Hermitian conjugate. Under these circumstances,

$$Z(\Omega) = [G(\Omega)]^2, \quad (\text{H-29})$$

a result that should be compared to Equation (H-7).

The elements of  $G(\Omega)$  are found by finding the equivalent of the square root of  $Z$ . This is done by solving the eigenvector equation,

$$Z(\Omega) \underline{X}(\beta; \Omega) = D(\beta; \Omega) \underline{X}(\beta; \Omega), \quad (\text{H-30})$$

where,

$D(\beta; \Omega) = \beta^{\text{th}}$  eigenvalue, and

$\underline{X}(\beta; \Omega) = \beta^{\text{th}}$  eigenvector composed of  $N$  elements,  $X(\alpha, \beta; \Omega)$ .

Let  $X(\Omega)$  represent a matrix comprising the  $N$  column eigenvectors and  $D(\Omega)$  represent a diagonal matrix comprising the  $N$  eigenvalues. Then Equation (H-30) expands to,

$$Z(\Omega) X(\Omega) = X(\Omega) D(\Omega), \quad (\text{H-31})$$

or

$$Z(\Omega) = X(\Omega) D(\Omega) X^\dagger(\Omega). \quad (\text{H-32})$$

$Z$  is raised to a power,  $p$ , by the following rule:

$$Z^p(\Omega) = X(\Omega) D^p(\Omega) X^\dagger(\Omega). \quad (\text{H-33})$$

Since  $D$  is diagonal,  $D^p$  is a new diagonal matrix found by taking the corresponding power of the original diagonal elements. Thus

$$\sqrt{Z(\Omega)} = X(\Omega) [D(\Omega)]^{\frac{1}{2}} X^\dagger(\Omega), \quad (\text{H-34})$$

with:

$$[D(\Omega)]^{\frac{1}{2}} = \begin{bmatrix} \sqrt{D(1;\Omega)} & 0 & \dots & 0 \\ 0 & \sqrt{D(2;\Omega)} & \dots & 0 \\ \vdots & \vdots & \dots & \vdots \\ 0 & 0 & \dots & \sqrt{D(M;\Omega)} \end{bmatrix}. \quad (\text{H-35})$$

As in the homogeneous case, arbitrary and independent phase response functions can be ascribed to each element of  $[D(\Omega)]^{\frac{1}{2}}$ . These can be used to achieve causal response functions if desired. Of course, the filters represented by  $g$  are found by inverse Fourier transforming the  $G$ , i.e.,

$$g(\alpha, \beta; \nu) = F_{\Omega, \nu}^{-1} [G(\alpha, \beta; \Omega)]. \quad (\text{H-36})$$

#### H.2.4 CONCLUSIONS

The identification procedure described above results in far too many parameters to represent a satisfactory statistical description and classification of the track. Further, there will be considerable statistical uncertainty surrounding the detailed correlation functions described herein when derived from realistic segments of track data. By this is meant samples that can be treated as stationary in terms of the expanded statistics described in this treatment. Accordingly development of system identification techniques should be oriented toward the following objectives:

- Advancing hypotheses concerning the nature of the  $g(\alpha, \beta; \nu)$  and  $g(\alpha, \nu)$  as used in Equations (H-15) and (H-16).
- Formulating analytic models to support simplification of the filter networks.

Such simplifications may result in a simpler PMRP generator such as one that is mathematically specified by:

$$z(m) = f(m-n) \sigma(\beta) h(m-n) w(n), \quad (\text{H-37})$$

where,

$$\beta = \text{Mod}(n, N). \quad (\text{H-38})$$

Implementation of this arrangement is illustrated in Figure H-3.

A filter,  $f$ , is needed to tie the rail data segments together to provide the short wavelength structure. It should be a finite impulse response filter, preferably symmetric, an odd number of points in duration, and its elements should be determined by a least squares procedure. Another filter,  $h$ , should be used for the long wavelength coherence. It should also deal with such phenomena as correlations and anti-correlations between adjacent and more removed joints. Using these concepts, a track simulator was developed as described in Paragraph 2.6.1, Volume I of this report.

### H.3 PROCESS IDENTIFICATION

The theory described in the previous sections of this appendix is readily applied to the identification of a general PMRP. Conceptually this can be accomplished via a Track Parameter Extractor (TPE) computer program or by the physical implementation of this program in some hardware device designed to duplicate the analytical procedures described above. A block diagram of the proposed TPE program flow is shown in Figure H-4.



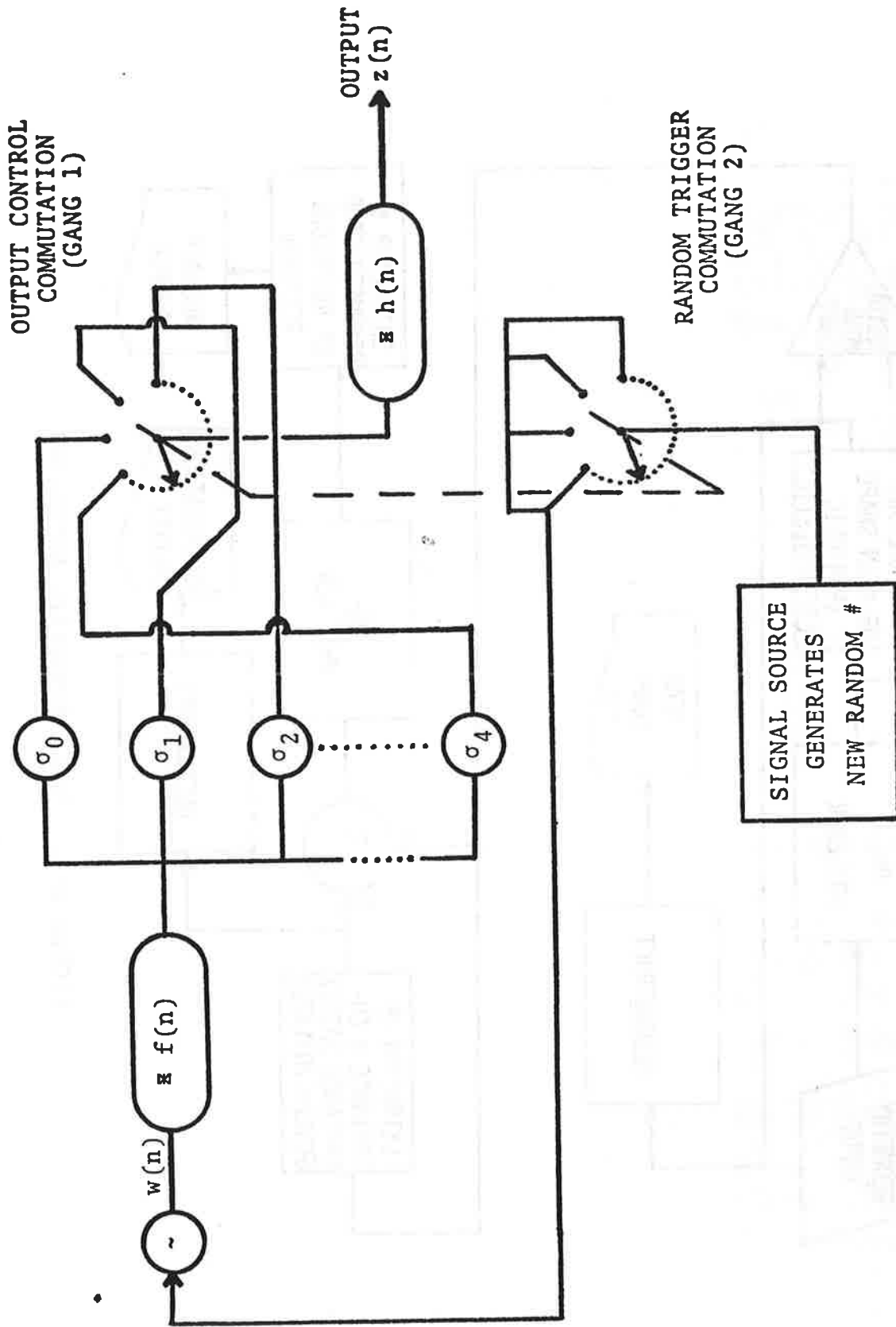


FIGURE H-3. FORM OF GENERATOR OF PERIODICALLY MODIFIED RANDOM PROCESS

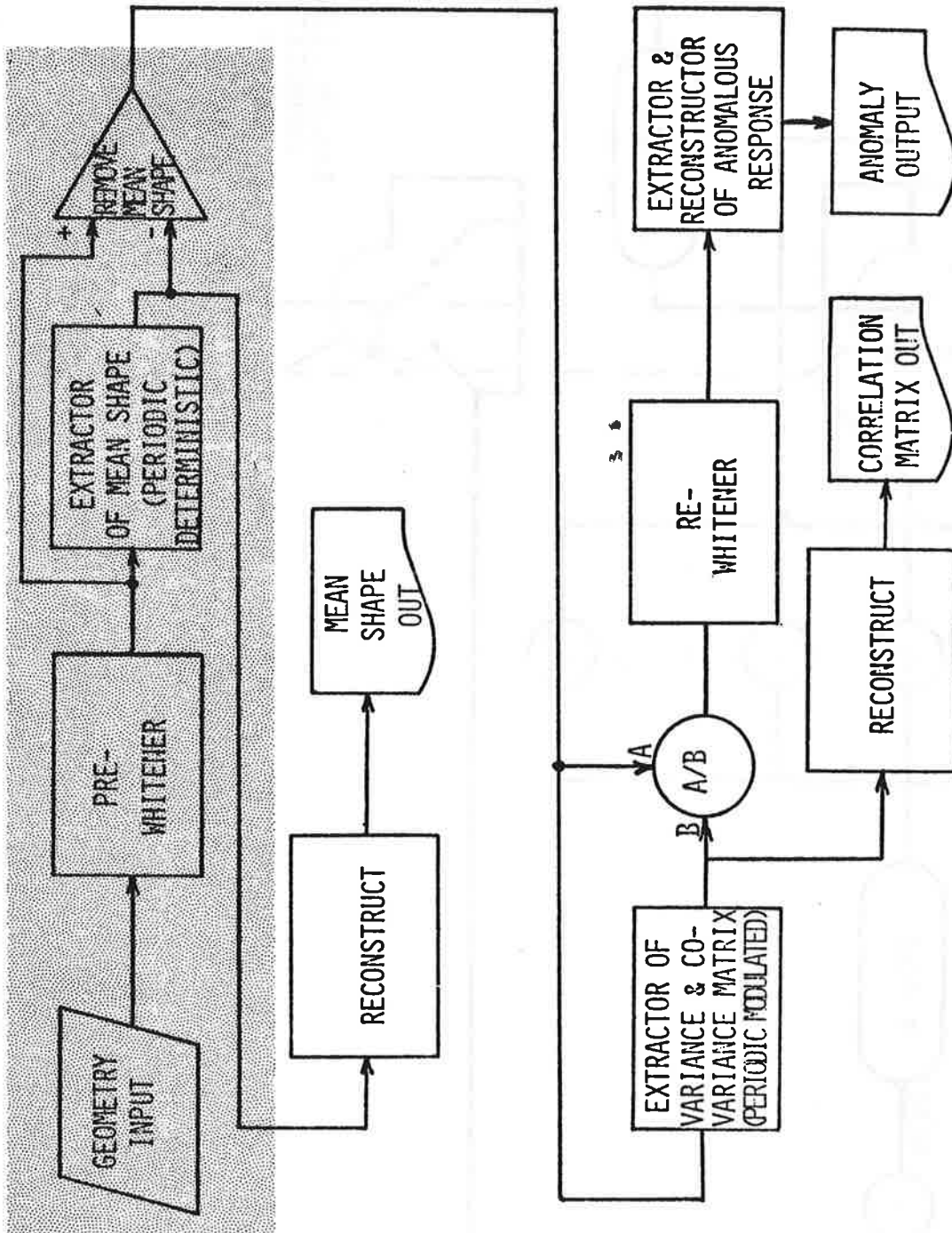


FIGURE H-4. TRACK PARAMETER EXTRACTOR

The shaded part of the TPE shown in Figure H-4 has been coded and is operational. It has entered the testing phase for the extraction of a periodic deterministic component from Track geometry data. For the purposes of the test, the input track geometry data was created by a geometry simulation program. Simulated data was chosen for its rigorously periodic joint structure. Experience thus far has demonstrated that a two-sample interval mid-chord offset is ideal both as a pre-whitener and as a joint detector. Later versions of the TPE will apply this principle to develop a generalized joint detector. This will provide the capability of handling varying rail lengths which can be expected in real track data.

Figure H-5 displays various stages of the processing of simulated periodic deterministic data in the mean shape extractor. The upper trace shows the input data. The second trace shows the result of the two-foot mid-chord offset pre-whitening process. The regular pattern of impulses is the response of the prewhitening process to the joint related activity. The third trace is the mean shape derived from the prewhitened data. This signal is the result of a convolution process over four rail lengths; consequently, the amplitude of this signal is greater than that of the original process. Start-up transients are apparent in the first four rail lengths of the signal. The final trace of Figure H-5 shows the result of removal of the mean shape from the original signal. As expected with periodic deterministic data, after the settling out of transients associated with the start-up of processing, the result of removing the mean shape is identically zero.

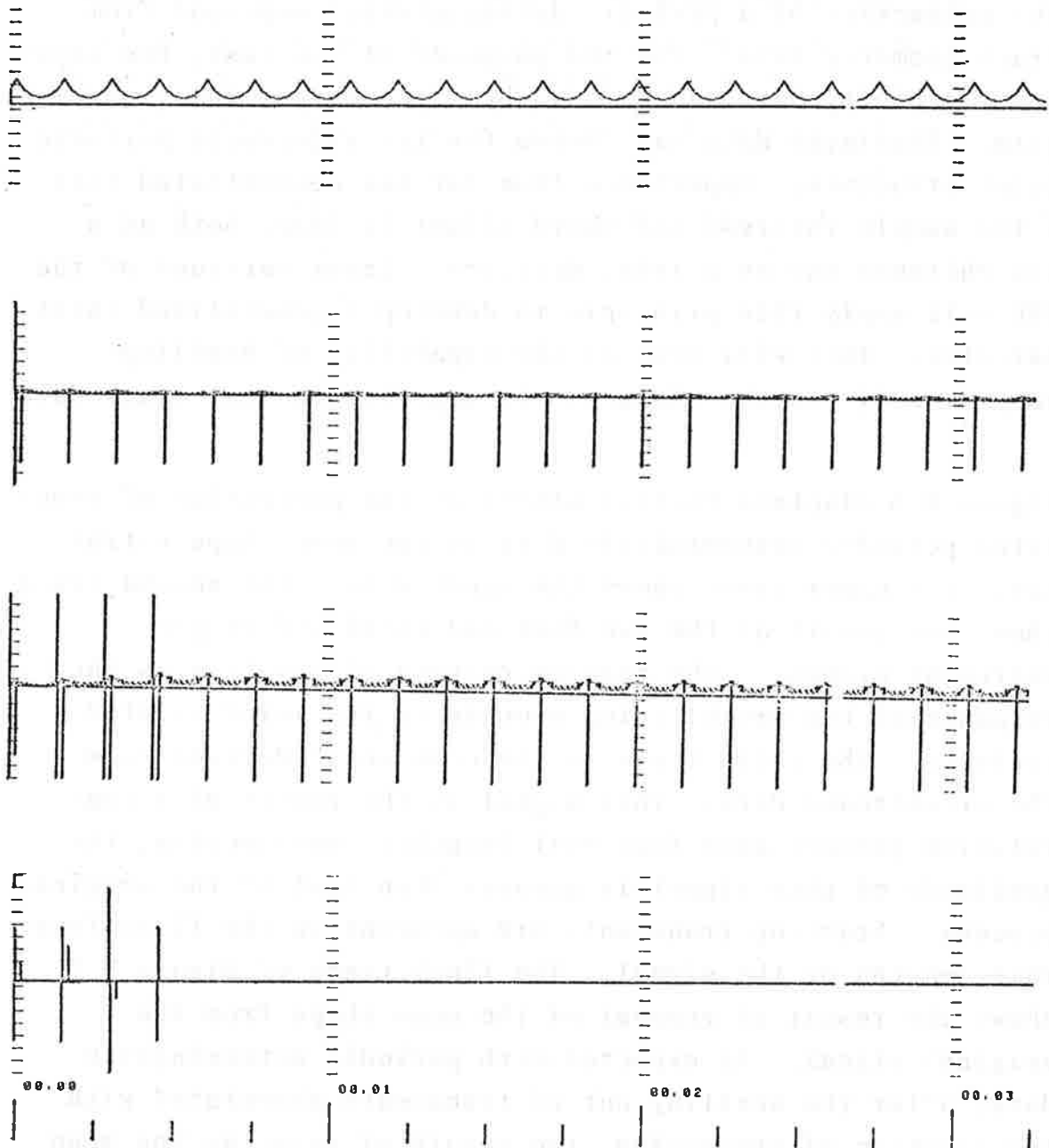


FIGURE H-5. STAGES OF MEAN SHAPE EXTRACTION  
 PROCESSING FOR PERIODIC  
 DETERMINISTIC DATA

Figure H-6 depicts the same series of processing steps for simulated data containing all three types of track processes. Joint-related behavior is again well pronounced in the two-foot mid-chord offset traces of the input data and the mean shape result. Again as expected, after the start-up transient has settled out, most of the joint-related behavior disappears from the signal from which the mean rail shape has been removed. Note that the resultant process has the appearance of white noise. All periodicities appear to have been removed.

6



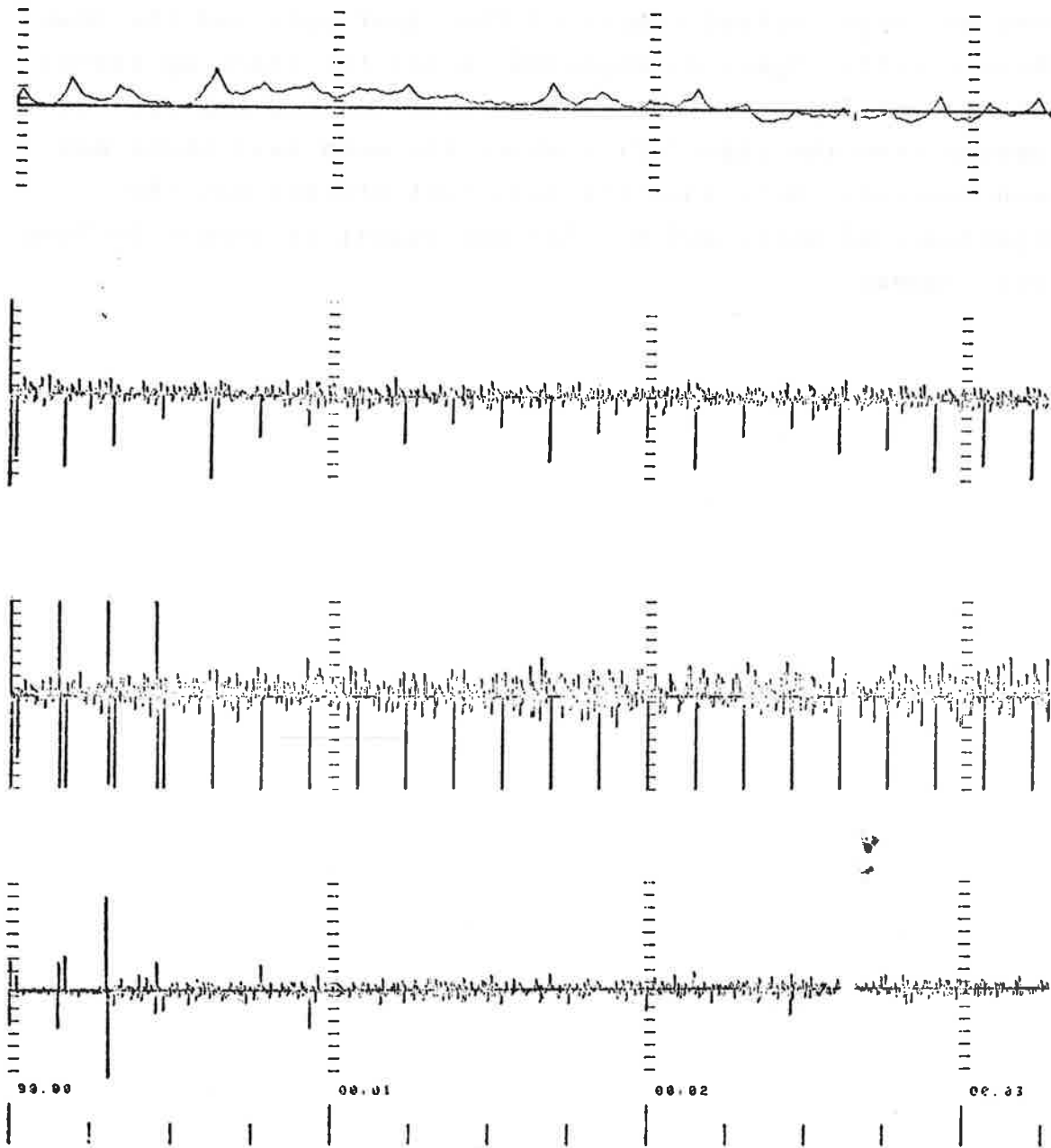


FIGURE H-6. STAGES OF MEAN SHAPE EXTRACTION PROCESSING FOR SIMULATED TRACK GEOMETRY DATA

## APPENDIX I

### RAILHEAD WEAR CHARACTERISTICS

#### I.1 RAILHEAD WEAR MEASUREMENT

Railhead wear was measured on a four-degree curve in mainline track of a cooperating railroad. Wear of the 132-pound AREA rail was measured with a special hand-held tool similar to tools used on other railroads. It gives one measurement of wear on the gage side of the head and one on the surface.

Transverse profiles of the railhead were also plotted using a contour tool fitted with thin, parallel rods, that show approximate contours when pressed against a curved surface.

#### I.2 DESCRIPTION OF ZONE AND RESULTS

The rail on track number 1 is almost five years old, while the rail on track number 2 is 14 years old. The wear on the high rail of track number 1 is seen to increase gradually from a point on the spiral at about C-300 and become fairly uniform in the body of the 4-degree curve. The high rail on track number 2 is scheduled to be changed out in a few months. This rail shows considerable loss of material from the gage area, which is characteristic of the high rails of curves after experiencing considerable tonnage.

Results of the measurements using the hand-held tool are tabulated in Tables I-1 and I-2. The small variations as seen in Figure I-1 are attributable to changes in the dynamic loading as trains travel through the curve. No cyclical patterns, related either to rail length or to peculiar dynamic wavelengths, were observed.

TABLE I-1. RAILHEAD WEAR, 15 APRIL 1977,  
TRACK NO. 1

WEAR IN UNITS OF 1/16 INCH

<u>STATION SPIRAL &amp; CURVE</u>	<u>HIGH RAIL</u>		<u>LOW RAIL</u>	
	<u>GAGE</u>	<u>SURFACE</u>	<u>GAGE</u>	<u>SURFACE</u>
C-475	0	1.0	0	0
C-450	0	1.0	0	0
C-425	0	1.0	0	1.0
C-400	0	1.0	0.5	1.0
C-375	0	1.0	0	1.0
C-350	0	1.0	0	1.0
C-325	0	1.0	0	1.0
C-300	0	1.0	0	1.0
C-275	0	1.0	0	1.0
C-250	1.0	2.0	0.5	1.0
C-225	0.5	1.5	0	1.0
C-200	0	1.5	0	1.0
C-180	0	1.0	0	1.0
C-160	0	1.0	1.0	1.0
C-140	0	1.0	1.0	1.5
C-120	0	1.0	1.0	1.5
C-100	0.5	1.5	0	2.0
C-80	0	1.5	0.5	1.0
C-60	0	1.0	0	1.0
C-40	0	1.0	0	1.0

Station distances on spiral and curve are in feet from an automatic location detector placed at a convenient location on curve C; - is distance north of C; + is distance south of C.



TABLE I-1. RAILHEAD WEAR, 15 APRIL 1977,  
TRACK NO. 1 (Cont'd)

STATION SPIRAL & CURVE	HIGH RAIL		LOW RAIL	
	GAGE	SURFACE	GAGE	SURFACE
C-20	0	1.0	0.5	1.0
C-10	0	1.0	0	1.0
C+0	0	1.0	0.5	1.0
C+2	0	1.0	1.0	2.0
C+4	1.0	2.0	1.0	2.0
C+6	1.0	2.0	0	1.0
C+8	0	1.0	0	1.0
C+10	0	1.0	0	1.0
C+12	0	1.0	1.0	2.0
C+14	0	1.0	0	1.0
C+16	0	1.5	0	1.0
C+18	0	2.0	0	1.5
C+20	0	1.5	0	1.0
C+30	0.5	1.5	0	1.0
C+40	0	2.0	0	1.0
C+50	1.0	2.0	0	0
C+60	0	0	0	0
C+70	0	1.0	1.0	1.0
C+80	0	1.0	0	1.0
C+90	0	1.0	0	1.0
C+100	0	1.0	1	1.0
C+110	0	2.0	0	1.0
C+120	1.0	2.0	0	1.0
C+130	0	2.0	0	1.0
C+140	0	2.0	0	1.0

TABLE I-1. RAILHEAD WEAR, 15 APRIL 1977,  
TRACK NO. 1 (Cont'd)

STATION SPIRAL & CURVE	WEAR IN UNITS OF 1/16 INCH			
	HIGH RAIL GAGE	HIGH RAIL SURFACE	LOW RAIL GAGE	LOW RAIL SURFACE
C+150	0	2.0	0	1.0
C+160	0	2.0	0.5	1.5
C+170	0.5	2.0	0	1.0
C+180	0	2.0	0	1.0
C+190	0	1.5	0	1.0
C+200	0	2.0	0	0.5
C+220	0	2.0	0	1.0
C+240	0	1.5	0	1.0
C+260	0	1.0	0	1.0
C+280	0	1.5	0.5	1.0
C+300	0	1.0	0.5	1.0
TANGENT				
T+0	0	1.0	0	0
T+25	0	1.0	0	0
T+50	0	1.0	0	1.0
T+75	0	0	0	0.5
T+100	0	0	0	0
T+125	0	0	0.5	0.5
T+150	0	0	0.5	0.5
T+175	0	1.0	0	1.0
T+200	0	0	1.0	1.0

Station distances on tangent are distances in feet from an automatic location detector placed at a convenient location on tangent, T; + is distance south of T; high rail is nominal east rail.

TABLE I-2. RAILHEAD WEAR, 3 MAY 1977  
TRACK NO. 2

WEAR IN UNITS OF 1/16 INCH

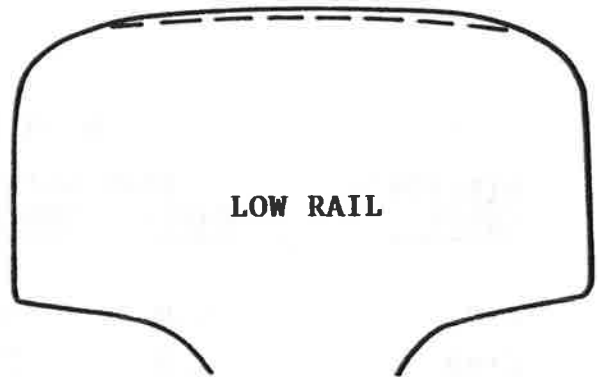
<u>STATION CURVE</u>	<u>HIGH RAIL* GAGE</u>	<u>SURFACE</u>	<u>LOW RAIL GAGE</u>	<u>SURFACE</u>
C+0	5.0	3.0	0	2.0
C+40	4.0	3.0	1.0	3.0
C+100	4.5	2.0	0	3.0
C+240	4.0	2.0	1.0	3.0
C+300	3.5	2.0	0	2.0

Station distances are in feet, railroad south of an automatic location detector placed on track No. 1.

\*The high rail is scheduled to be changed out within a few months.

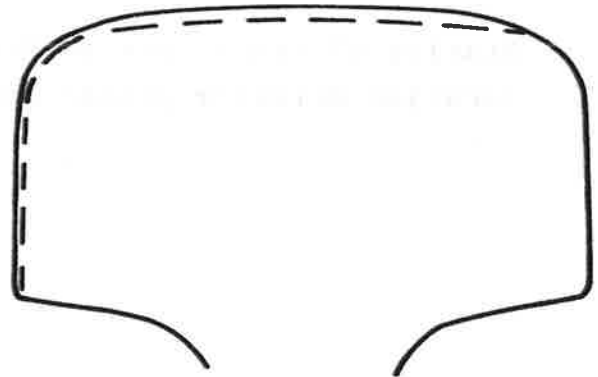
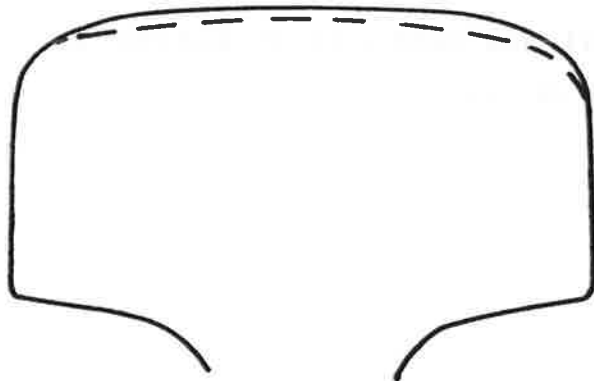


HIGH RAIL



LOW RAIL

STATION C-450



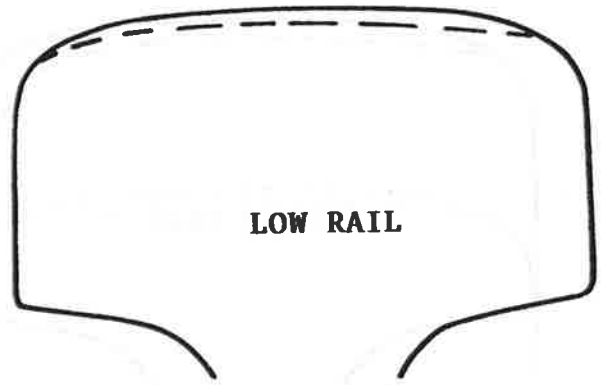
STATION C-400

Station distances in feet from an automatic location detector placed at a convenient location on curve; - North, + South.

FIGURE I-1. RAILHEAD WEAR, 15 APRIL 1977  
TRACK NO. 1

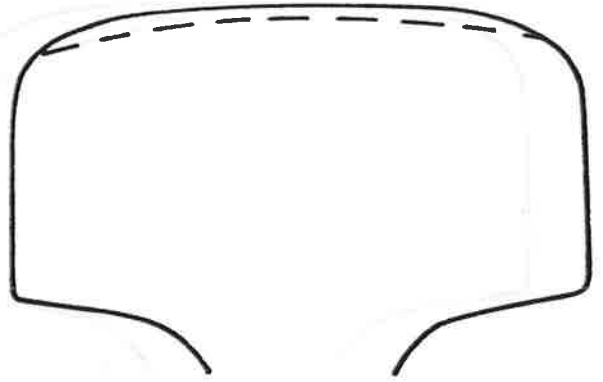
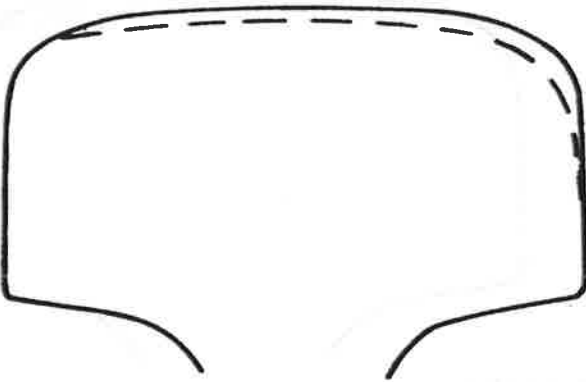


**HIGH RAIL**

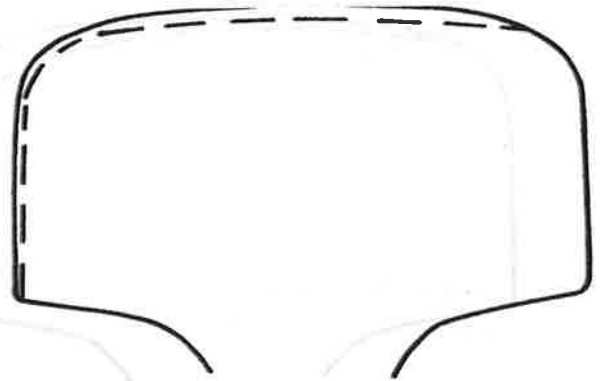
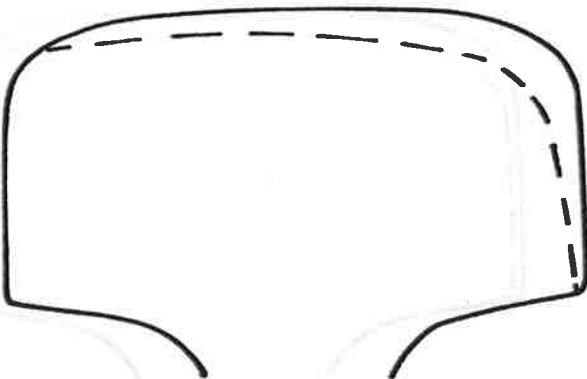


**LOW RAIL**

**STATION C-350**

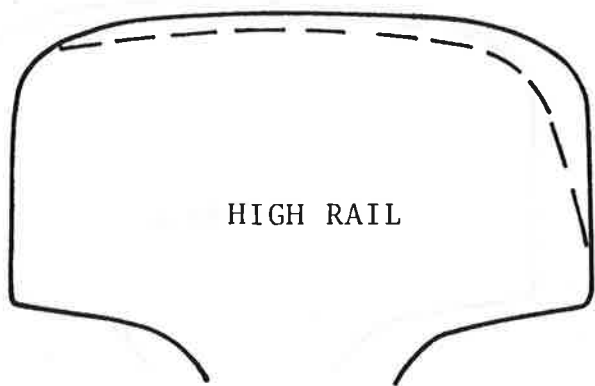


**STATION C-300**

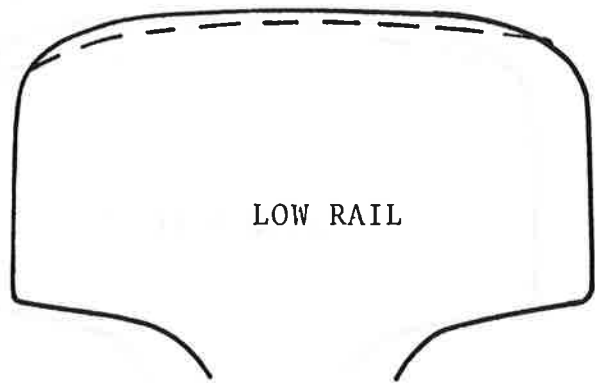


**STATION C-250**

**FIGURE I-1. RAILHEAD WEAR, 15 APRIL 1977  
TRACK NO. 1 (Cont'd)**

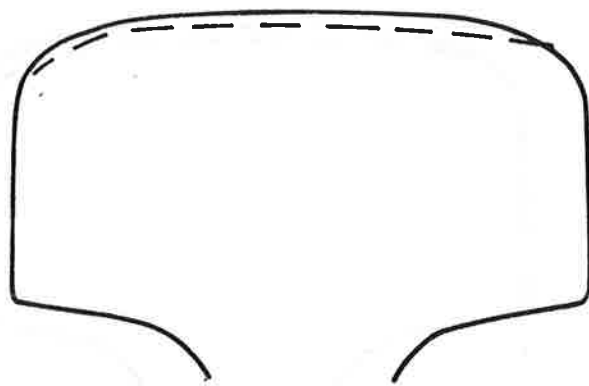
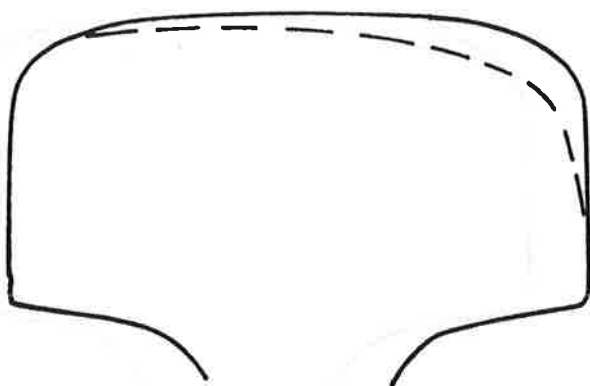


HIGH RAIL

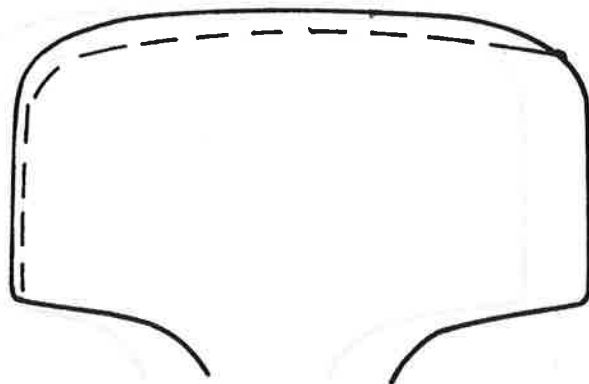
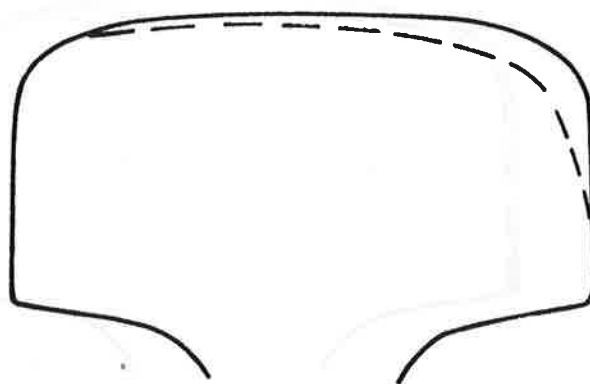


LOW RAIL

STATION C-200

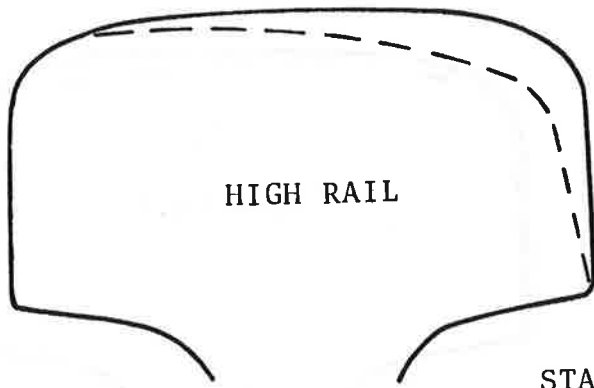


STATION C-160

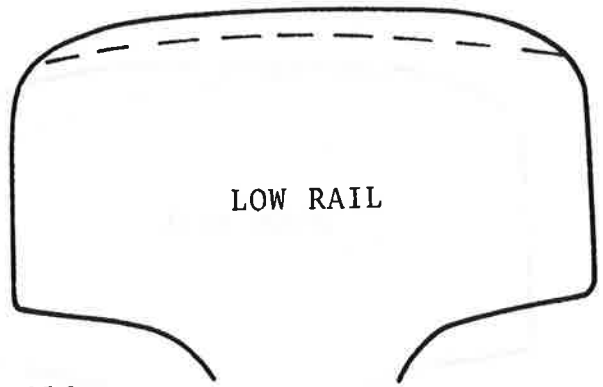


STATION C-140

FIGURE I-1. RAILHEAD WEAR, 15 APRIL 1977  
TRACK NO. 1 (Cont'd)

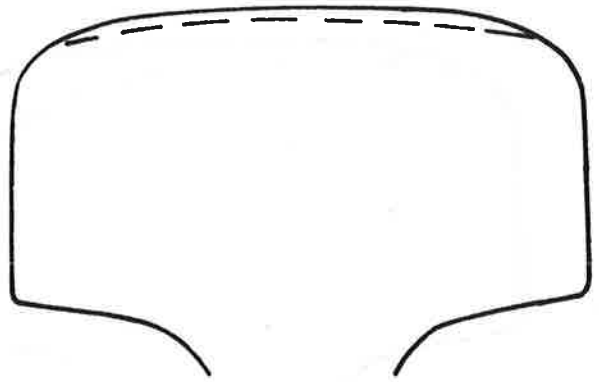
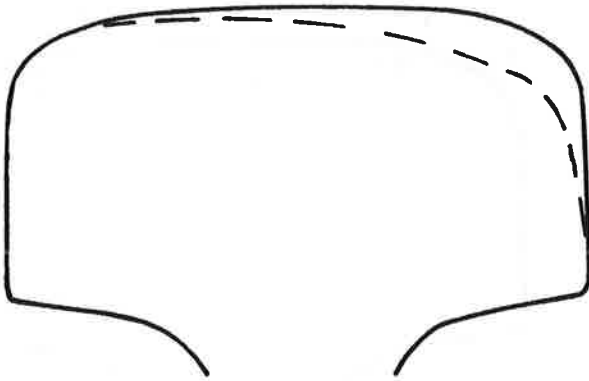


HIGH RAIL

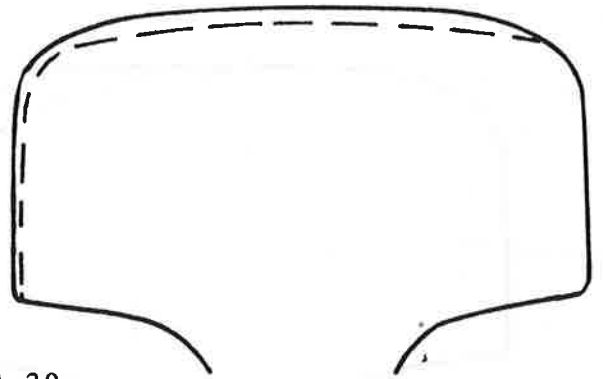
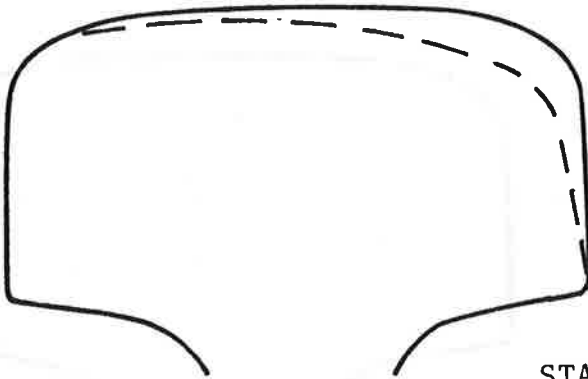


LOW RAIL

STATION C-110

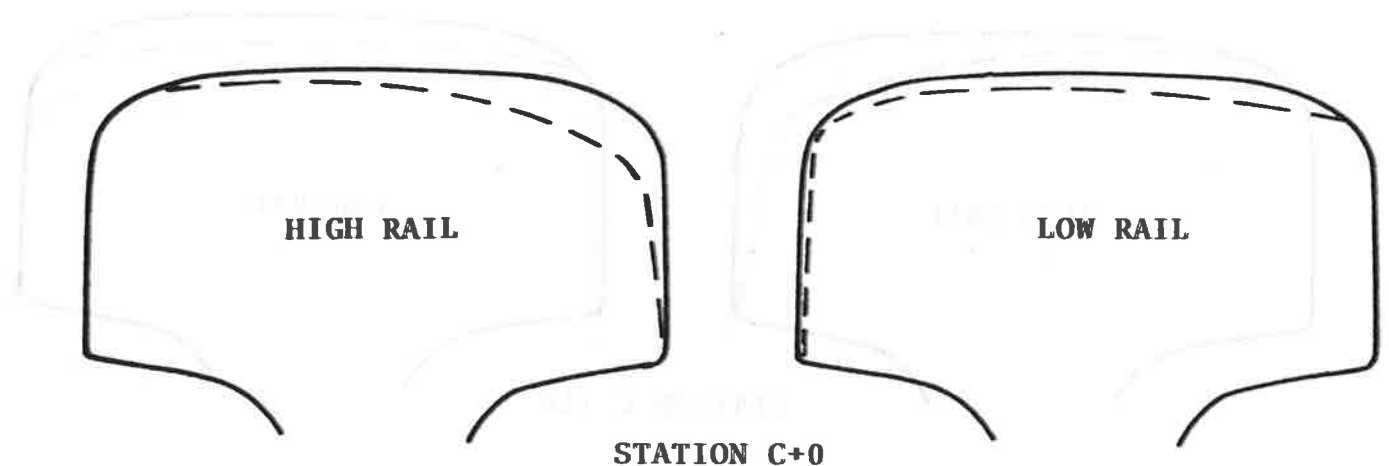


STATION C-60

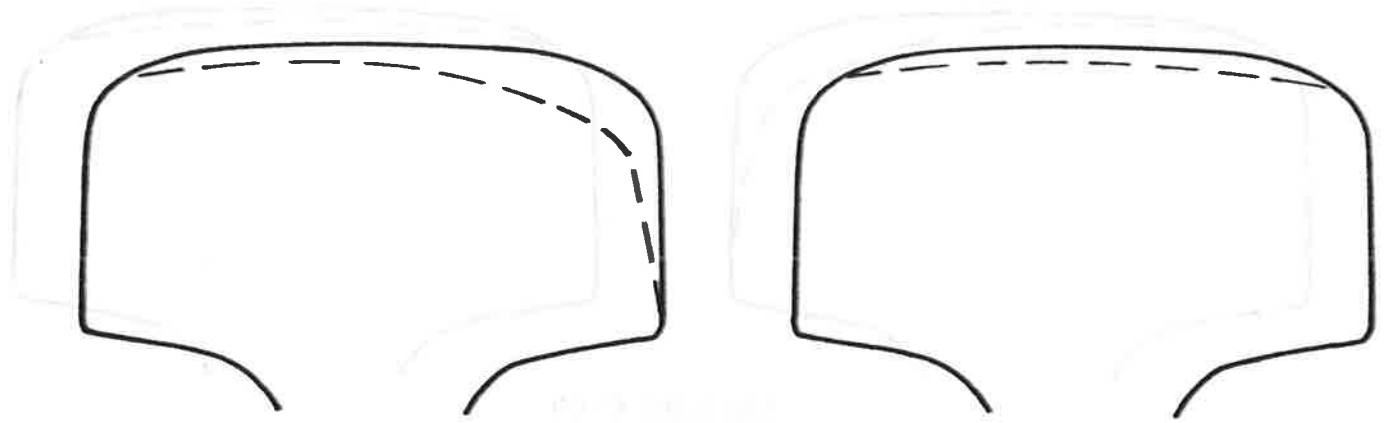


STATION C-20

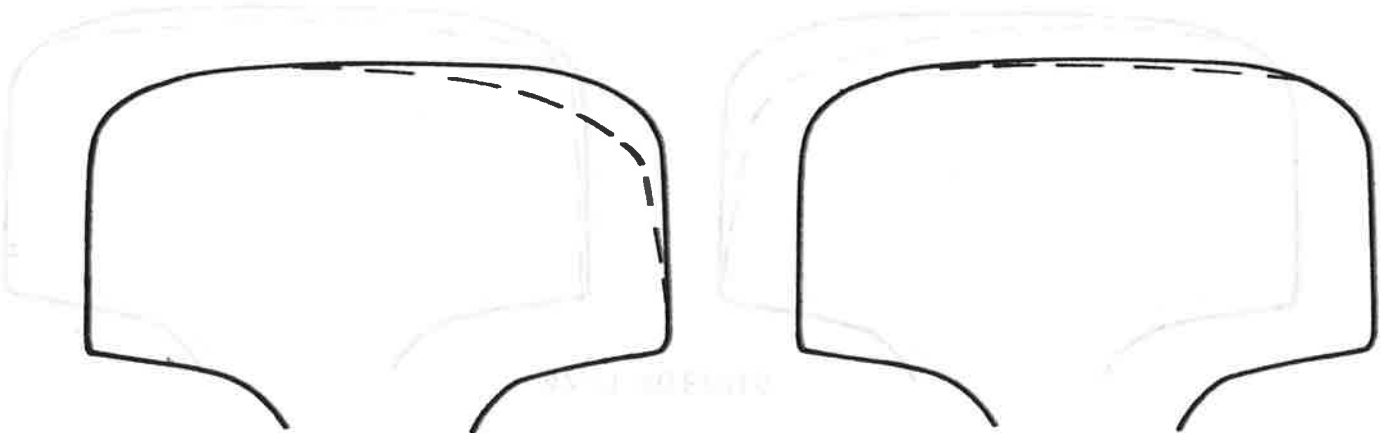
FIGURE I-1. RAILHEAD WEAR, 15 APRIL 1977,  
TRACK NO. 1 (Cont'd)



**STATION C+0**



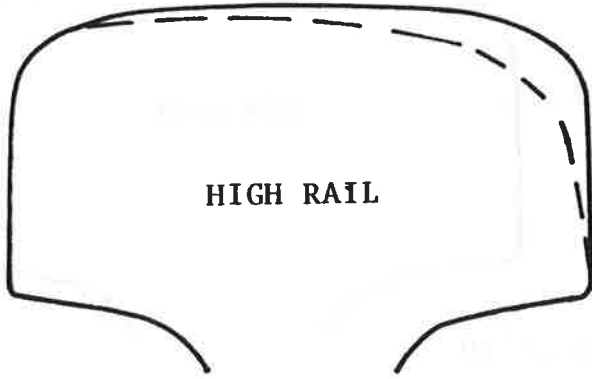
**STATION C+20**



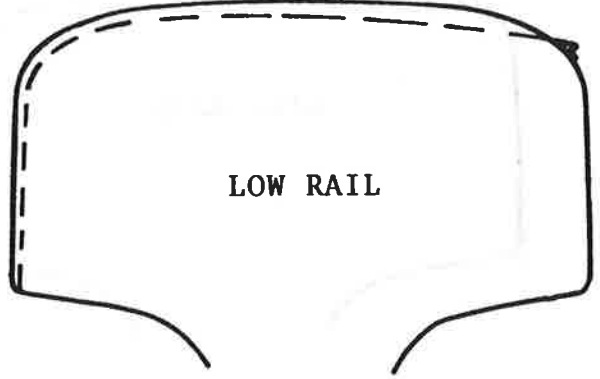
**STATION C+60**

**FIGURE I-1. RAILHEAD WEAR, 15 APRIL 1977, TRACK NO. 1 (Cont'd)**



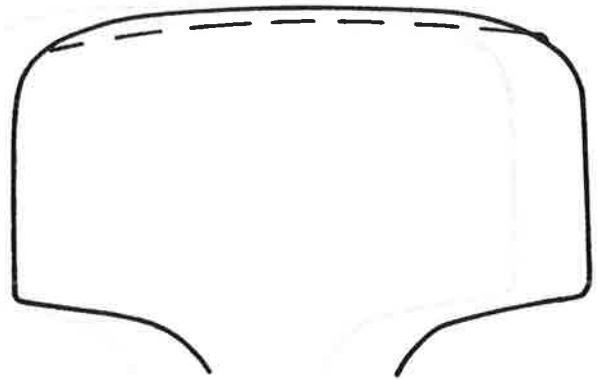
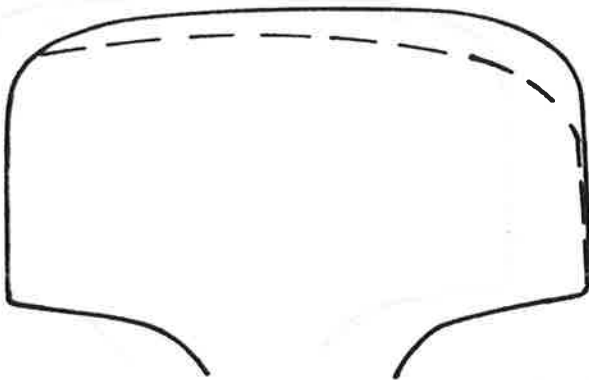


HIGH RAIL

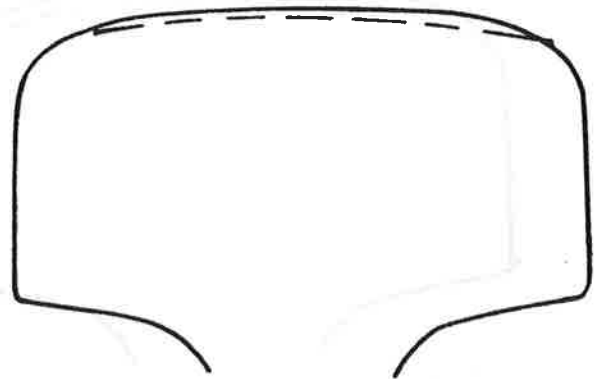
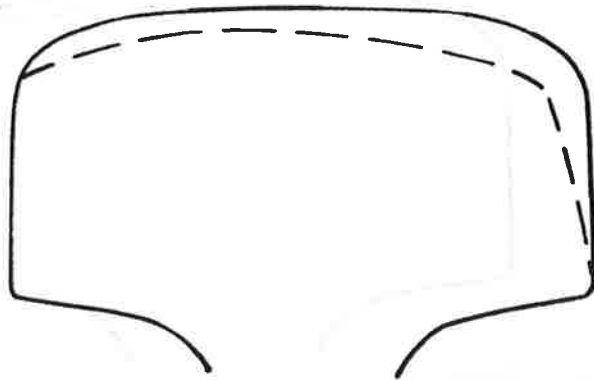


LOW RAIL

STATION C+100

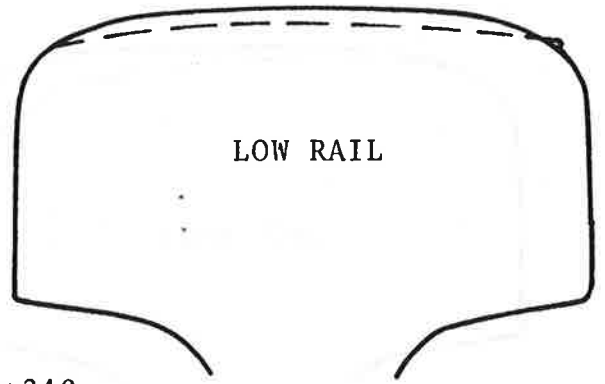
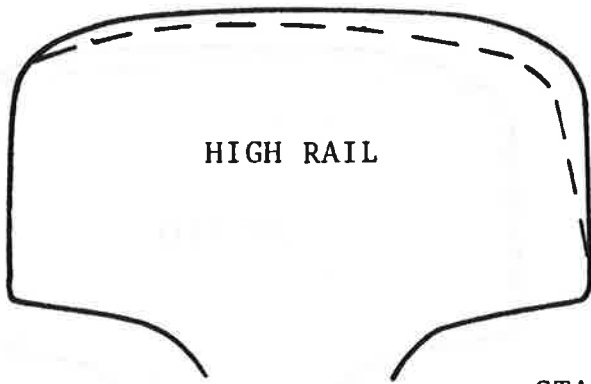


STATION C+150

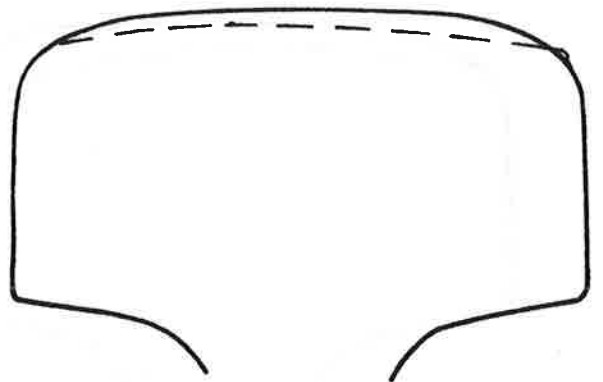
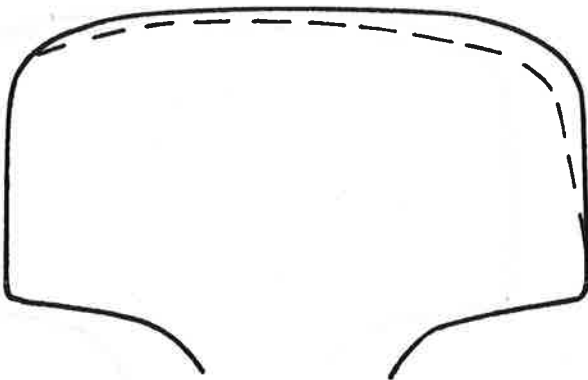


STATION C+200

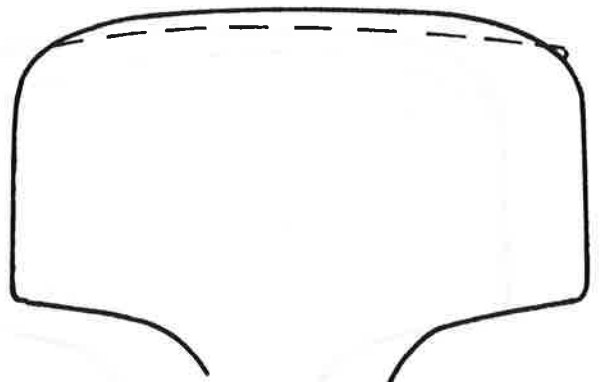
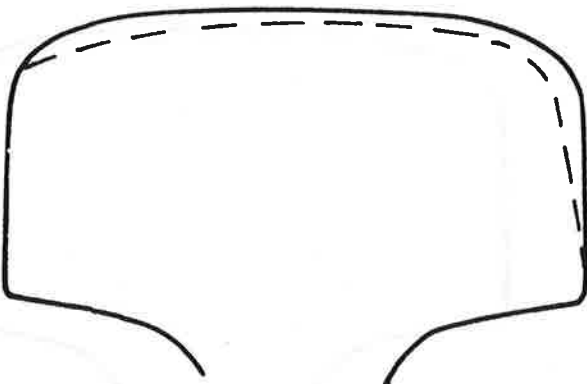
FIGURE I-1. RAILHEAD WEAR, 15 APRIL 1977,  
TRACK NO. 1 (Cont'd)



STATION C+240

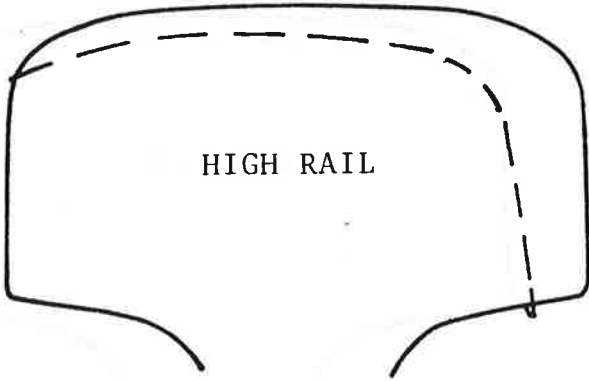


STATION C+260

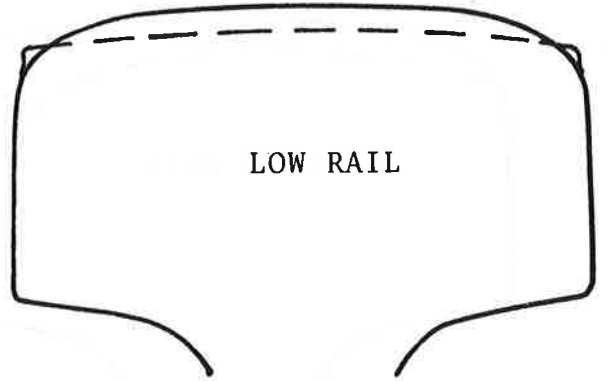


STATION C+300

FIGURE I-1. RAILHEAD WEAR, 15 APRIL 1977  
TRACK NO. 1 (Cont'd)

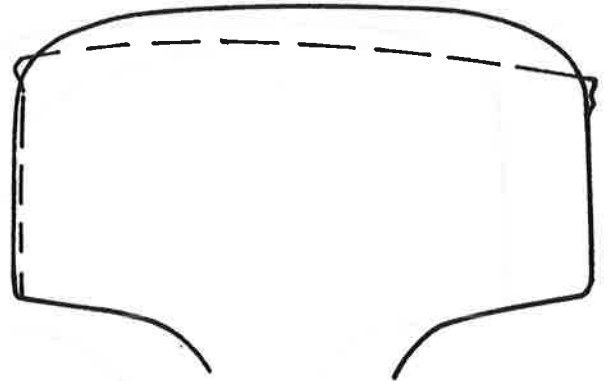
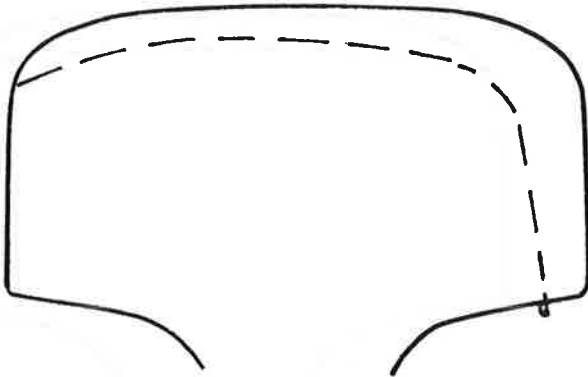


HIGH RAIL

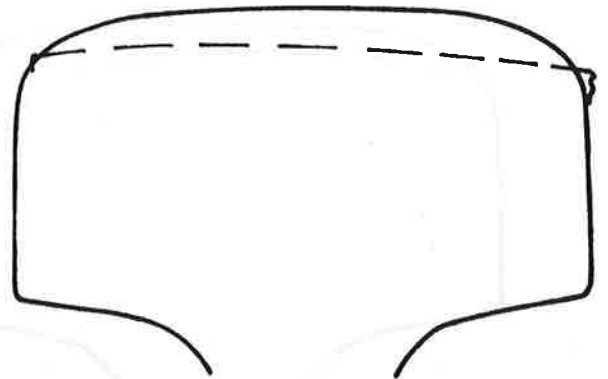
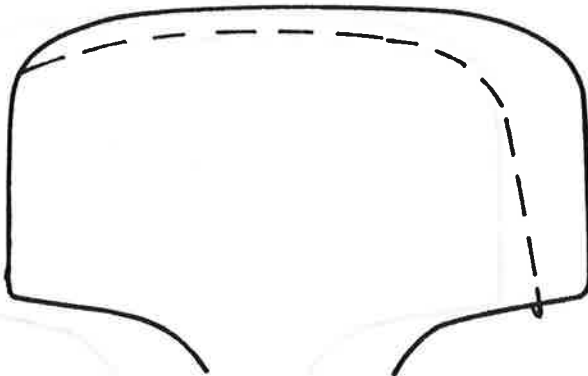


LOW RAIL

STATION C+0



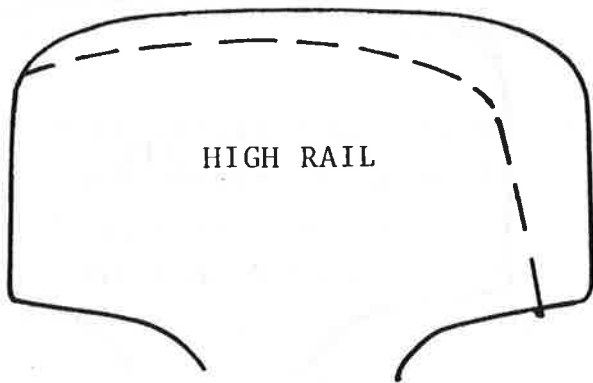
STATION C+100



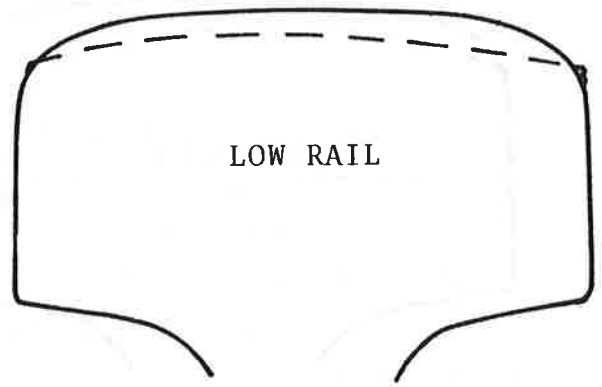
STATION C+140

Station distances in feet from an automatic location detector placed on Track No. 1; + railroad south.

FIGURE I-2. RAILHEAD WEAR, 3 MAY 1977  
TRACK NO. 2

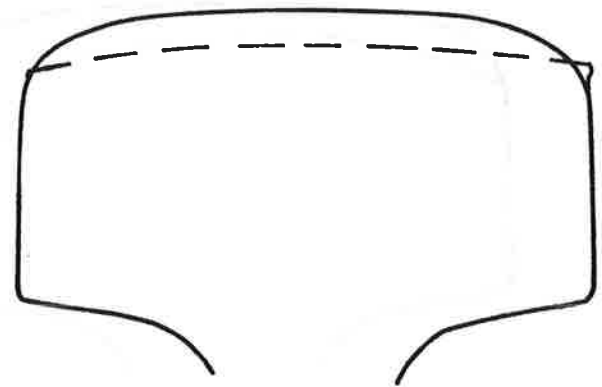
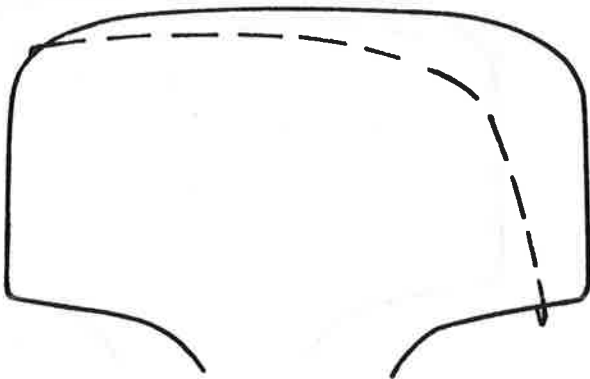


HIGH RAIL

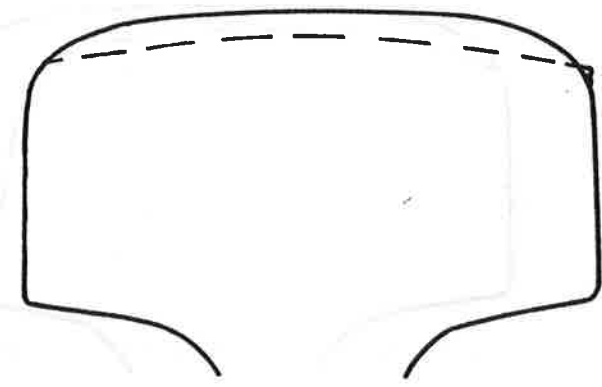
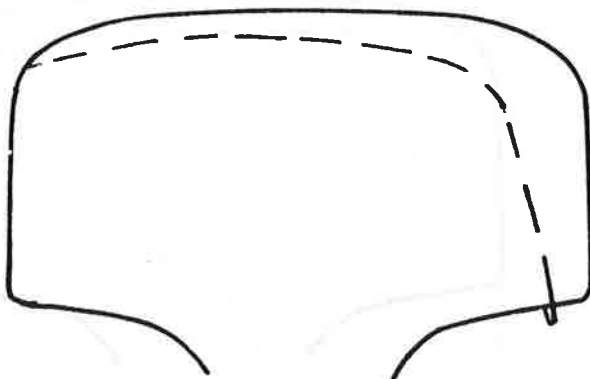


LOW RAIL

STATION C+18



STATION C+240



STATION C+300

FIGURE I-2. RAILHEAD WEAR, 3 MAY 1977  
TRACK NO. 2 (Cont'd)

The lower rail on a curve is heavily loaded when trains move through the curve at slow speeds, well below the speeds for which superelevation was planned. Since the cars are tipped toward the inside of the curve, and the vertical forces are not balanced by centrifugal force, the lower rail carries much more than half of the weight of a car. The tipping of the cars caused by superelevation of the track, plus the regular cant of the rail by the tie plates, results in the wear of the surface of the low rail being more severe toward the field side.

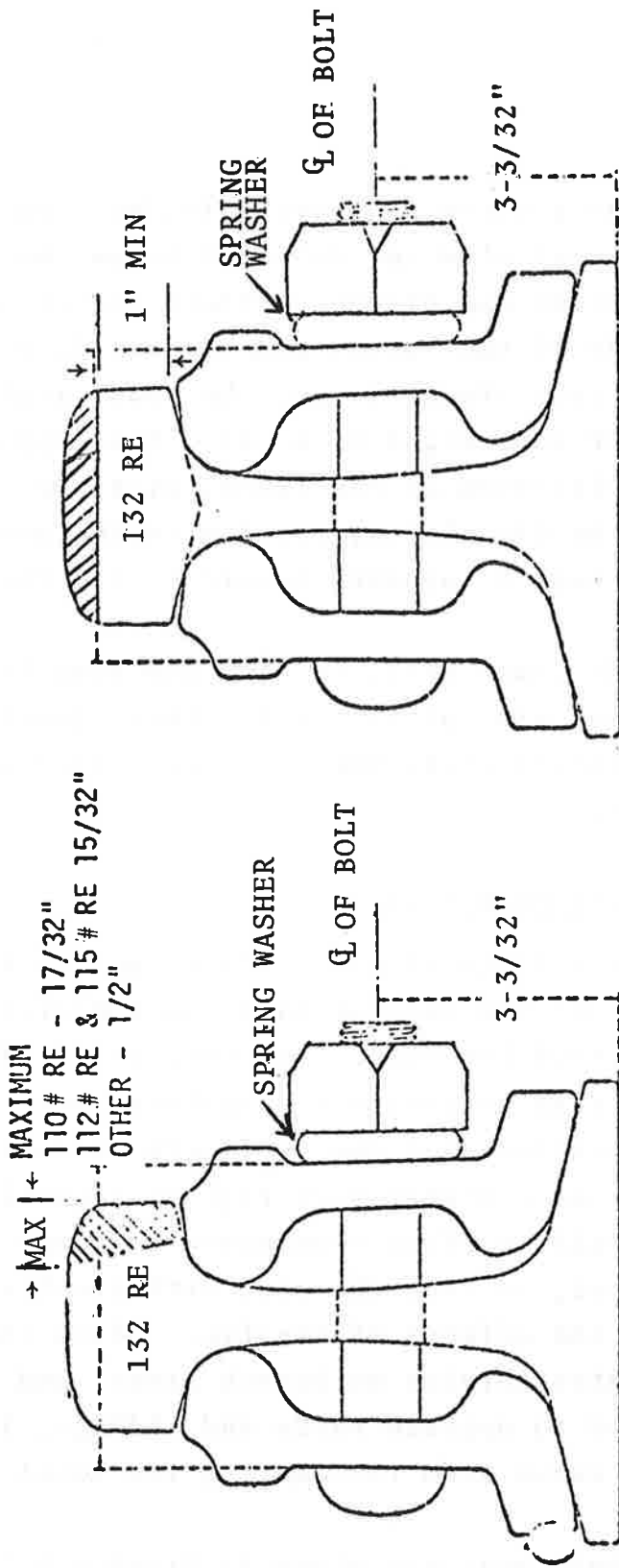
Heavy wheel loads cause metal to flow and form lips on both the gage and field side of the rail. This effect is very pronounced on unhardened rail, but the lips formed on hardened rail are smaller.

### I.3 LIMITS OF RAILHEAD WEAR

Railhead wear is not listed as a rail defect in the Track Safety Standards of the Federal Railroad Administration, nor are limits specified for wear. However, railroads themselves have established limits for railhead wear based on economic considerations and the avoidance of rail defects that would develop if excessively worn rail were continued in heavy service. Worn rail is often transposed from one side of a track to the other, so that the side with greater wear will be less exposed to the effects of traffic. Often the worn rail is moved to lighter service on branch lines, and old branch line rail is used to upgrade yards and sidings, in order to get the maximum value from rail during its total useful life.

Limits for railhead wear are shown in Figures I-3 through I-4 as excerpted from a railroad inspection manual. One measurement only is indicated for wear on the gage side and one for surface wear, as these two measurements are considered sufficient bases for economical decisions on transposing or changing out worn rail. It is noted that gage wear cannot be measured

TOP WEAR



Minimum - any less width requires protection & corrective action.


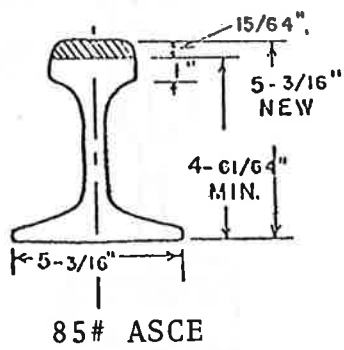
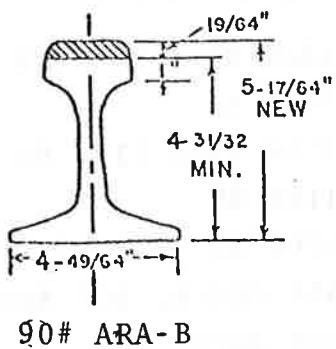
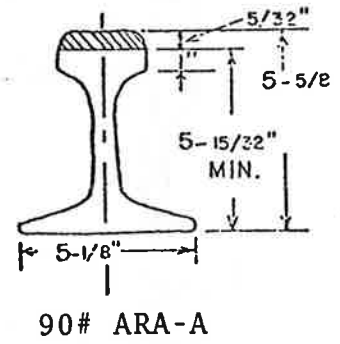
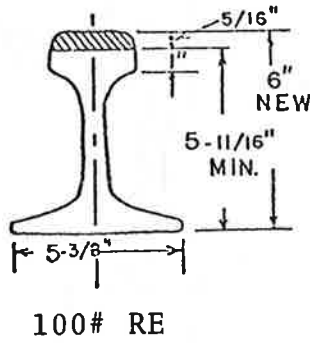
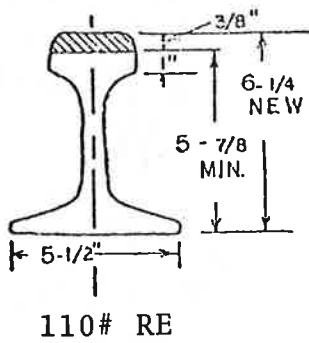
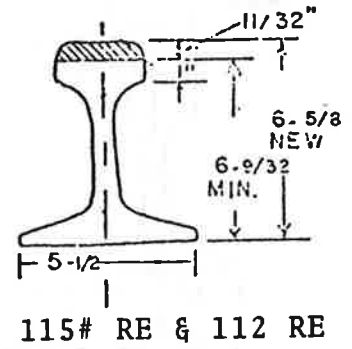
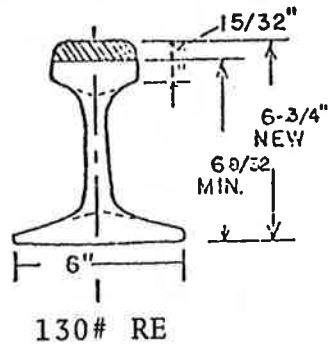
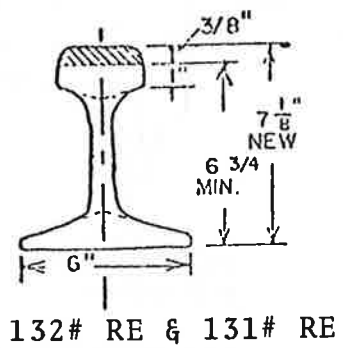
 Area worn away.

FIGURE I-3. MAXIMUM RAIL WEAR AT SPLICE




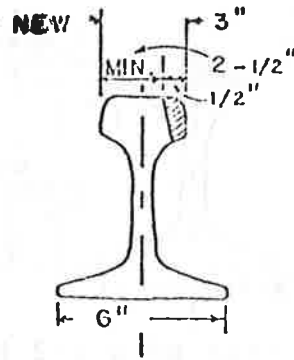
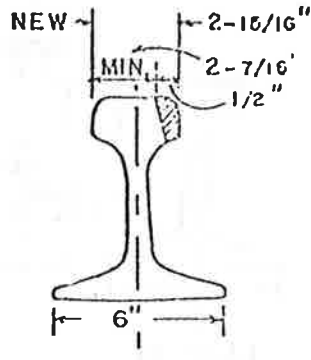
Minimum - any less width requires protection & corrective action.  
 Area worn away.

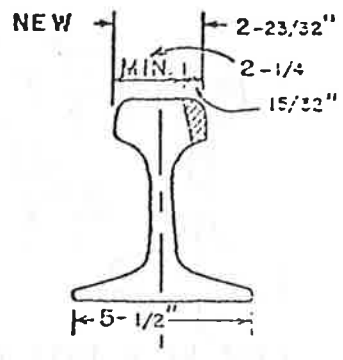
FIGURE I-4. DIMENSIONS FOR MINIMUM RAILHEAD THICKNESS IN COMMON RAIL SECTIONS



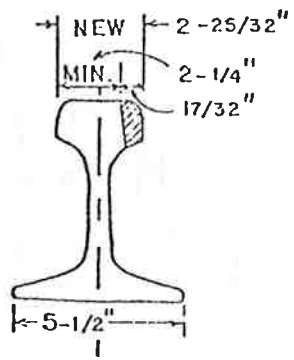
132# RE & 131# RE



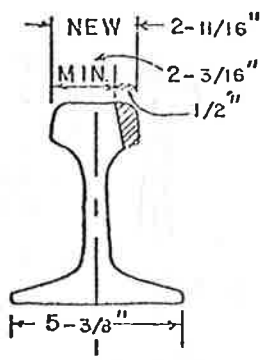
130# RE



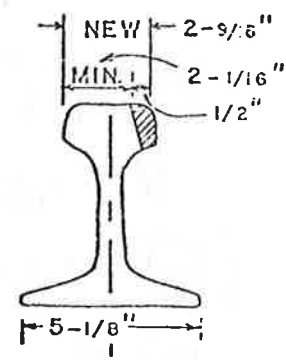
115# RE & 112# RE



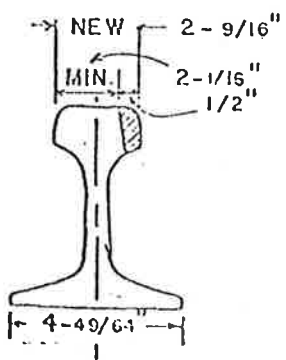
110# RE



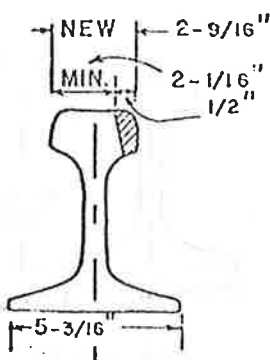
100# RE



90# ARA-A



90# ARA-B



85# ASCE

TRANPOSED RAIL  
MINIMUM WIDTHS

132# RE & 131# RE	→ 2-1/8"
130# RE	→ 2-1/16"
115# RE & 112# RE	→ 1-7/8"
110# RE	→ 1-7/8"
100# RE	→ 1-13/16"
90# ARA-A, 90# ARA-B, &	
85# ASCE	→ 1-11/16"

Minimum - any less width requires protection & corrective action.

Area worn away.

FIGURE I-5. DIMENSIONS FOR MINIMUM HEAD WIDTH IN COMMON RAIL SECTIONS



at the top of rail when surface were also has occurred. However, a measurement made lower on the side of the railhead would be indicative of the same amount of wear, provided that normal wear profiles (transverse) are known.

Typical wear patterns and wear limits used by another major railroad for decisions on transposing or changing out rail are shown in Figure I-6. The wear profiles shown are readily measurable with a headwear tool of the type shown in Figure 78, Volume 1 of this report. The railroad has the following limits for wear so measured.

RAIL WEAR LIMITS  
130, 131 and 132-pound Rail

<u>Top Wear</u>			<u>Side Wear</u>	
0 to 3/8"	Mainline Track		0 to 1/4"	Mainline Track
+3/8" to 1/2"	Secondary Track		+1/4" to 3/8"	Transpose
+1/2" to 3/4"	Yard Track		+3/8" to 5/8"	Secondary Track
Over 3/4"	Scrap		Over 5/8"	Scrap

The same railroad has similar limits for the wear of 100-pound rail except that it is scrapped when top wear exceeds 11/16 inch or side wear exceeds 1/2 inch and is transposed when side wear exceeds 3/16 inch but is less than 3/8 inch.

The wear profiles shown in Figure I-6 are considered reasonable approximations of the wear that occurs under average conditions, with the lips that are formed by metal flow omitted from the illustrations. These profile curves could be characterized as a function of lateral position. However, great variations in wear are found as a result of heavy wheel loads, prevalent wheel conditions and prevalent consists that operate over a given track.

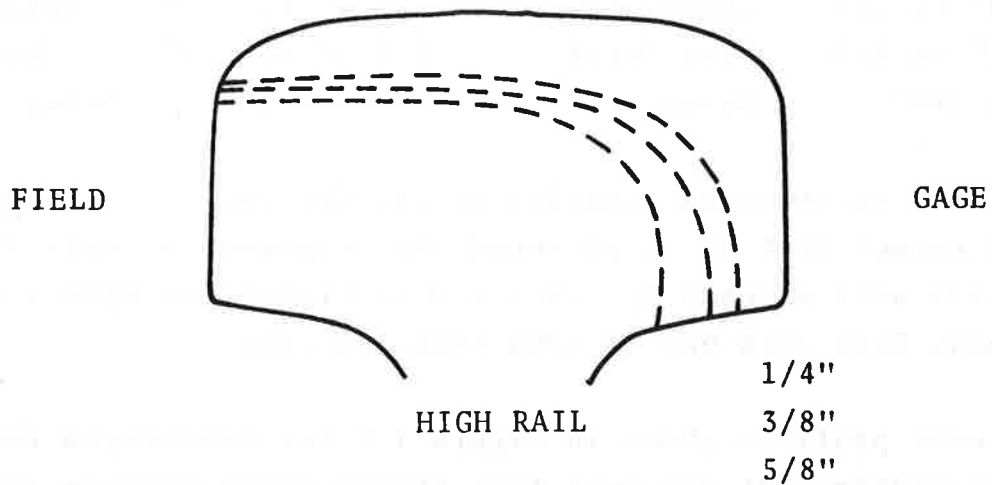
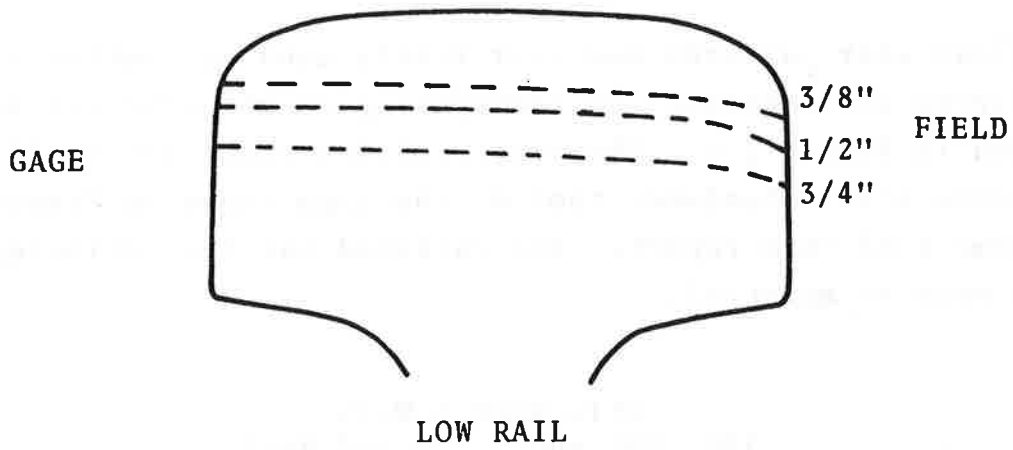


FIGURE I-6. TYPICAL WEAR PATTERNS

APPENDIX J  
REPORT OF NEW TECHNOLOGY

After comprehensive review of the work performed, it was found that two potentially patentable items were produced under this contract. As conceived in this effort, both items are in the form of computer programs and, as such, they are not patentable. However, it is possible to convert these programs into a hard-wired system and, to the extent that this can be done, both are patentable.

The first item, called the Track Parameter Extractor (TPE) related to a method of processing field collected data and identifying the statistical parameters described throughout this report. It evaluates mean joint amplitudes, decay rates, and other statistics that relate to the random behavior concentrated at the joint. It evaluates a roughness amplitude and corner frequencies associated with the stationary random process. It recognizes and flags anomalous occurrences. Further details on the theory of the TPE are to be found in Paragraph 3.6.1.

The second item, called the Track Geometry Simulator (TGS) related to a method of producing geometric records that have all of the essential statistical properties embodied in field data. It does this by utilizing the parametric output of the TPE. As such, the TGS and the TPE complement one another in that one performs the inverse operations of the other.

A new PSD processor for track geometry, program RAINBO, was developed and is fully operational. It accepts data from all existing FRA geometry survey cars and equipment. It

incorporates an adjustable prewhitener, correction for instrument frequency and phase response, and expanded dynamic range, all improvements over previous PSD program. In addition, it generates X-PSD's and coherence functions. A hamming window option is included. Program RAINBO is further described in Paragraph 2.5.2.

A technique for processing ELW PSD's using track chart or global survey data was developed. This is described in Paragraph 2.5.1.

A real time, phase shiftless profileometer algorithm was perfected under this effort. It was incorporated in the software of the FRA track survey car, T-6. This algorithm is described in Paragraph 2.5 and was used to characterize profile joints and anomalies as described in Paragraph 3.5 and Appendices B and C.

110 copies